To the Graduate Council:

I am submitting herewith a dissertation written by Brenda Ann Dougan entitled "Studies of Tungsten Alkyl Alkylidyne Compounds and Iron Porphyrin Derivatives." I have examined the final electronic copy of this dissertation for form and content and recommend that it be accepted in partial fulfillment of the requirements for the degree of Doctor of Philosophy, with a major in Chemistry.

_____
Ziling (Ben) Xue, Major Professor

We have read this dissertation
and recommend its acceptance:

_____
Jamie L. Adcock

_____
George W. Kabalka

_____
Claudia J. Rawn

Accepted for the Council:

_____
Carolyn R. Hodges
Vice Provost and Dean of the
Graduate School

STUDIES OF TUNGSTEN ALKYL ALKYLIDYNE COMPOUNDS AND IRON PORPHYRIN DERIVATIVES

A Dissertation

Presented for the

Doctor of Philosophy Degree

The University of Tennessee, Knoxville

Brenda Ann Dougan

December 2009

DEDICATION

This dissertation is dedicated to Lola Lucy Dougan. Without her bundle of love, happiness, ball of energy, and millions of kisses, I would not have survived the last one and half years of graduate school.

ACKNOWLEDGEMENTS

I would like to acknowledge the people in my graduate career who have willingly given their help and guidance to me. I would first like to thank Professor Zi-Ling (Ben) Xue, my Ph.D. advisor at the University of Tennessee. His help and guidance during my Ph.D. studies will not be forgotten. I will always be grateful for his careful reading of my writings and being very patient with my unique personality.

I would like to acknowledge my committee members: Dr. Jamie L. Adcock, Dr. George W. Kabalka, Dr. Claudia J. Rawn, and Dr. Zi-Ling (Ben) Xue, who agreed to serve on my dissertation committee and to review my Ph.D. work.

The following individuals extended technical support for various aspects of my research at the University of Tennessee, for which I am appreciative: Dr. Carlos Steren at the University of Tennessee for his help with the 400 MHz NMR instrument, Dr. Liguo Song at the University of Tennessee for writing the mass simulation program in Chapter 8, Dr. Xiaoping Wang at the SNS/ORNL (Oak Ridge, TN) for his help on the X-ray structural analysis and determination on the Fe(TPP)Cl (TPP^{2-} = *meso*-tetraphenylporphyrinate) complex, Dr. Garry J. McIntyre at the ILL (Grenoble, France) for his time and effort on the neutron data collection and analysis on the $[Fe(TPP)(HIm)_2]Cl$ (HIm = 1H-imidazole) complex, Dr. Christina M. Hoffmann at the SNS/ORNL (Oak Ridge, TN) for her expertise in X-ray and neutron diffraction, and finally Dr. Yu-Seng Chen at the APS/ANL

(Argonne, IL) for his X-ray structural analysis and data collection on the Fe(TPP)Cl and [Fe(TPP)(HIm)$_2$]Cl complexes on the ChemMatCARS beam line.

I would like to thank my fellow co-workers and colleagues: Dr. Shujian (Jim) Chen, Julia K. C. Abbott, Royce Dansby-Sparks, Bhavna Sharma, Adam Lamb, Julio Gutierrez, and Dave Schneider for helpful discussions about my research projects and allowing me to vent my graduate career frustrations onto them. And last but not least, I am forever grateful for Lola Dougan. I could not have finished this Ph.D. program without her.

I would like to thank the National Science Foundation and the Joint Institute for Neutron Sciences (JINS) fellowship for supporting my graduate research in the past four and half years.

ABSTRACT

This dissertation focuses on two research projects. The first project examines the reactions of tungsten(VI) alkyl alkylidyne and bis-alkylidene complexes with phosphines and water and the studies of thermodynamics and kinetics of the reactions. These studies have been conducted in part to determine the mechanistic pathway in the formation of novel tungsten(VI) species. The second portion of this dissertation focuses on the spin density and structures of biomimetic Fe(III) porphyrin derivatives using neutron and X-ray diffraction techniques. The spin density and magnetic properties of an Fe(III) porphyrin derivative has been determined by polarized neutron diffraction.

In the first portion of this dissertation, reaction of tungsten(VI) alkyl alkylidyne $W(CH_2SiMe_3)_3(\equiv CSiMe_3)$ with $Me_2PCH_2CH_2PMe_2$ (DMPE), a bi-dentate phosphine, has been studied (Chapter 2). The reaction gives a DMPE-alkylidyne adduct, which subsequently undergoes a tautomerization. The tautomeric mixture then converts to an alkyl alkylidene alkylidyne complex**.** Thermodynamic and kinetic studies as well as molecular modeling are used to understand these reactions. In Chapter 3, thermodynamic studies have been conducted of the addition of two mono-dentate phosphines to the tungsten(VI) alkyl alkylidyne complex. A reversible reaction has been observed with the mono-dentate phosphines. The reaction of tungsten(VI) alkyl alkylidyne $W(CH_2CMe_3)_3(\equiv CSiMe_3)$ with H_2O has been pursued. The reaction leads to the

observation of the intermediate $W_2O_2(\mu\text{-}O)(CH_2SiMe_3)_2(CH_2CMe_3)_4$ and subsequent formation of two oxo trimers. NMR spectroscopic studies have been used to determine the mechanistic pathway in formation of these trimeric complexes.

In the second portion of this dissertation, variable-temperature X-ray studies have been conducted of Fe(TPP)Cl (TPP^{2-} = *meso*-tetraphenylporphyrinate) (Chapter 5) and $[Fe(TPP)(HIm)_2]Cl$ (HIm = 1H-imidazole) complexes (Chapter 6). The spin-density in the $[Fe(TPP)(HIm)_2]Cl$ (*S* = 1/2) complex has been probed using polarized neutron diffraction (Chapter 7). The study shows that the spin distribution of the unpaired electron is localized on the Fe(III) center. The Fe(TPP)Cl-d_{28} and $[Fe(TPP)(DIm)_2\text{-}d_{36}]Cl$ complexes have been synthesized and characterized by X-ray diffraction (Chapter 8). A comparison is made between the protonated and per-deuterated X-ray diffraction structures.

TABLE OF CONTENTS

LIST OF FIGURES

LIST OF TABLES

LIST OF SCHEMES

NUMBERING SCHEME FOR COMPOUNDS IN THE TEXT

1	$W(CH_2SiMe_3)_3(\equiv CSiMe_3)$
2a	$W(CH_2SiMe_3)_3(\equiv CSiMe_3)(PMe_3)$
2b	$W(CH_2SiMe_3)_2(=CHSiMe_3)_2(PMe_3)$
3a	$W(CH_2SiMe_3)_3(\equiv CSiMe_3)(PMe_2Ph)$
3b	$W(CH_2SiMe_3)_2(=CHSiMe_3)_2(PMe_2Ph)$
4a	$W(CH_2SiMe_3)_3(\equiv CSiMe_3)$(DMPE-*P*)
4b	$W(CH_2SiMe_3)_2(=CHSiMe_3)_2$(DMPE-*P*)
5a	*syn*-$W(CH_2SiMe_3)(=CHSiMe_3)(\equiv CSiMe_3)(PMe_3)$
5b	*anti*-$W(CH_2SiMe_3)(=CHSiMe_3)(\equiv CSiMe_3)(PMe_3)$
6a	*syn*-$W(CH_2SiMe_3)(=CHSiMe_3)(\equiv CSiMe_3)(PMe_2Ph)$
6b	*anti*-$W(CH_2SiMe_3)(=CHSiMe_3)(\equiv CSiMe_3)(PMe_2Ph)$
7a	*syn*-$W(CH_2SiMe_3)(=CHSiMe_3)(\equiv CSiMe_3)$(DMPE)
7b	*anti*--$W(CH_2SiMe_3)(=CHSiMe_3)(\equiv CSiMe_3)$(DMPE)
8	$W(CH_2CMe_3)_3(\equiv CSiMe_3)$
9	$W_3O_3(\mu{=}O)_3(CH_2CMe_3)_6(THF)_3$
10	$W_3O_3(\mu{=}O)_3(CH_2CMe_3)_6(D_2O)_3$
11	$W_2O_2(\mu\text{-}O)(CH_2SiMe_3)_2(CH_2CMe_3)_4$
11-*d*$_4$	$W_2O_2(\mu\text{-}O)(CD_2SiMe_3)_2(CH_2CMe_3)_4$
12	Fe(TPP)Cl
12-*d*$_{28}$	Fe(TPP)Cl-d_{28}

13 [Fe(TPP)(HIm)$_2$]Cl

13-*d*$_{36}$ [Fe(TPP)(DIm)$_2$-*d*$_{36}$]Cl

14-*d*$_{30}$ *meso*-tetraphenylporphyrin-*d*$_{30}$; D$_2$(TPP-*d*$_{28}$)

15 *meso*-tetraphenylporphyrin; H$_2$TPP

15-*d*$_{28}$ *meso*-tetraphenylporphyrin-*d*$_{28}$; H$_2$(TPP-*d*$_{28}$)

NOMENCLATURE AND ABBERVIATIONS

DMPE	bis(dimethylphosphino)ethane
PR_3	PMe_3, PMe_2Ph, or $Me_2PCH_2CH_2PMe_2$
ANL	Argonne National Laboratory (Argonne, IL, USA)
APS	Advanced Photon Source
DIm	1D-imidazole-d_4
HIm	1H-imidazole
ILL	Institut Laue-Langevin (Grenoble, France)
MS	Mass Spectrum
ORNL	Oak Ridge National Laboratory (Oak Ridge, TN, USA)
ORTEP	Oak Ridge Thermal Ellipsoid Plot
SNS	Spallation Neutron Source
TPP^{2-}	*meso*-tetraphenylporphyrinate
XRD	X-ray Diffraction
PND	Polarized Neutron Diffraction
VT	Variable-Temperature

CHAPTER 1

Introduction

1.1. Chemistry of Bis-alkylidene and Alkyl Alkylidyne Complexes

The first metal-carbon triple bond complex was discovered in 1973 by E. O. Fischer. Fischer carbene and carbyne compounds, e.g., $W(CO)_5[=C(OCH_3)Ph]$ and $Mo(CO)_4(\equiv CEt)Cl$, illustrate low oxidation state metal centers and their carbene/carbyne ligands are electrophilic. The reaction of tungsten (0) carbonyl with an alkyllithium leads to the formation of a tungsten(II) carbene complex (Eq. 1.1). The Fischer carbene can be treated with an electrophile, such as boron trichloride, to produce a Fischer carbyne (Eq. 1.2).

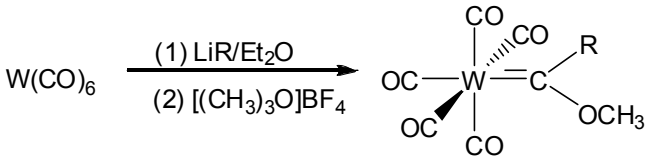

(Eq. 1.1)

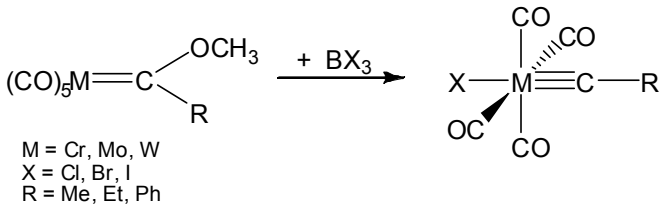

(Eq. 1.2)

After E. O. Fischer's discovery of M-C multiple bonding, R. R. Schrock found that acetylene metathesis occurs by carbyne complexes. Metals in the Schrock carbynes are at high oxidation states, and are typically early transition metals [e.g. W(VI) or Ti(IV)]. The complexes such as $W(CH_2SiMe_3)_3(\equiv CSiMe_3)$ (**1**) are often called alkylidynes, and contain non-π acceptor ligands (nucleophilic)

and non-π donor R groups. Another class of related complexes are called Schrock carbenes or alkylidenes with metal-carbon double bonds. A typical example is $Ta(=CHCMe_3)(CH_2CMe_3)_3$.

The reaction of $TaCl_5$ with $Zn(CH_2CMe_3)_2$ leads to the formation of $Ta(CH_2CMe_3)_3Cl_2$ (Eq. 1.3).[5] After treating $Ta(CH_2CMe_3)_3Cl_2$ with Me_3CCH_2Li (Eq. 1.4), $Ta(=CHCMe_3)(CH_2CMe_3)_3$ is observed.[5]

$$TaCl_5 + Zn(CH_2CMe_3)_2 \longrightarrow Ta(CH_2CMe_3)_3Cl_2 \qquad \text{(Eq. 1.3)}$$

$$Ta(CH_2CMe_3)_3Cl_2 \xrightarrow{2\ LiCH_2CMe_3} Ta(=CHCMe_3)(CH_2CMe_3)_3 \qquad \text{(Eq. 1.4)}$$

When treating $Cl_3W(OMe)_3$ with an excess amount of Me_3SiCH_2Li, the formation of $W(CH_2SiMe_3)_3(\equiv CSiMe_3)$ (**1**) occurs (Eq. 1.5). Alkylidynes may also be prepared *via* metathesis. When $(Me_3CO)_3W\equiv W(OCMe_3)_3$ is treated with 2-butyne, *via* metathesis, $W(\equiv CMe)(OCMe_3)_3$ is yielded (Eq. 1.6). A second metathesis with $Me_3SiC\equiv CSiMe_3$, followed by reaction with Me_3CCH_2Li, gives $W(CH_2CMe_3)_3(\equiv CSiMe_3)$ (**8**) (Eq. 1.7).[6] **1** and **8** are used in Chapters 2, 3, and 4. Studies of the reactions of the tungsten(VI) alkylidynes with phosphines and water were conducted, as summarized below. These studies have led to insightful chemistry and provided a better understanding of their applications in different areas of catalysis.

Our group reported earlier unusual reactions of silanes with d^0 tantalum bis-alkylidene complexes such as $Ta(CH_2SiMe_3)(=CHSiMe_3)_2(PMe_3)_2$.[1] These

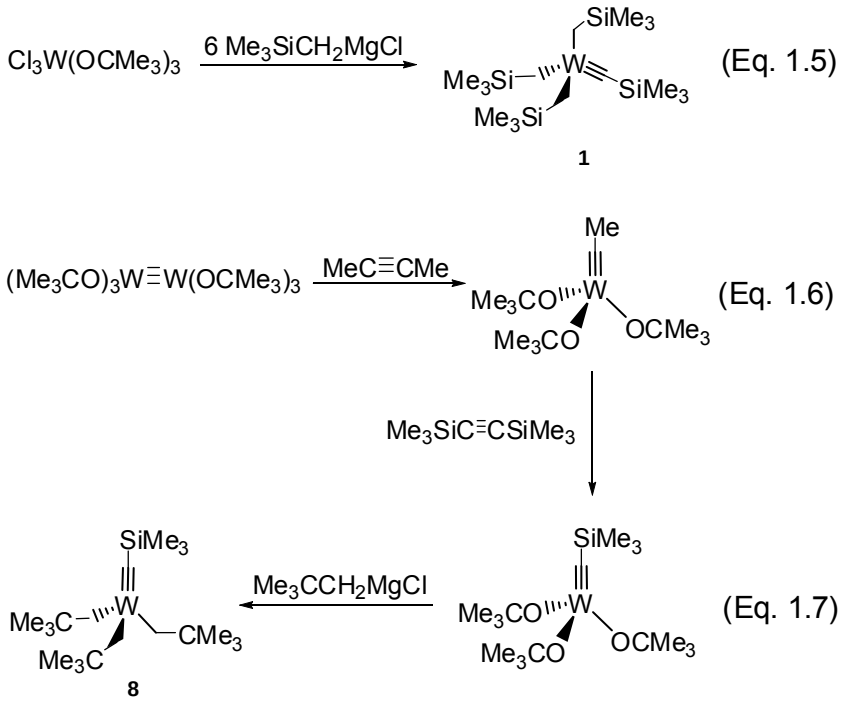

reactions give new tantalum bis-alkylidene complexes. Since then, we have been interested in the reactivities of d^0 tungsten alkylidene alkylidyne complexes containing =CHSiMe$_3$ and ≡CSiMe$_3$ ligands towards silanes. In the reactions of W(CH$_2$SiMe$_3$)$_3$(≡CSiMe$_3$) (**1**) with PR$_3$, our group observed intermediates W(CH$_2$SiMe$_3$)$_3$(≡CSiMe$_3$)(PR$_3$) (**2a**, **3a**) that undergo an exchange with their bis-alkylidene tautomers W(CH$_2$SiMe$_3$)$_2$(=CHSiMe$_3$)$_2$(PR$_3$) (PR$_3$ = PMe$_3$, **2b**; PMe$_2$Ph, **3b**).[2] The tautomeric mixture then reacts with another molecule of PR$_3$ to form tungsten(VI) alkyl alkylidene alkylidyne complexes W(CH$_2$SiMe$_3$)(=CHSiMe$_3$)(≡CSiMe$_3$)(PR$_3$) (PR$_3$ = PMe$_3$, *syn*: **5a**; *anti*: **5b**; = PMe$_2$Ph).[2] Mechanistic studies have been pursued and led to an understanding of the formation of tungsten(VI) complexes containing a single, double, and triple

bond to the same W atom. We have recently expanded the project to examine: (1) Reaction of $W(CH_2SiMe_3)_3(\equiv CSiMe_3)$ (**1**) with bi-dentate phosphine, bis(dimethylphosophino)ethane $Me_2PCH_2CH_2PMe_2$ (DMPE); and (2) The first step of the reactions between $W(CH_2SiMe_3)_3(\equiv CSiMe_3)$ (**1**) and PR_3, i.e., the addition of PR_3 onto **1**, which was not studied earlier.

In addition to the reactions of **1** with phosphines, we have been interested in the reaction of water with alkylidyne complex $W(CH_2CMe_3)_3(\equiv CSiMe_3)$ (**8**). Reactions of metal complexes with water have been used to make microelectronic metal oxide thin films. Silicon oxide has been the most popular gate insulating material mainly because of its easy preparation from silicon wafers. SiO_2 has a low dielectric constant (κ = 3.9), leading to a large leakage current. New generations of electronic devices (Figure 1.1) require scaling of gate insulator thickness to be less than 15 Å. At this thickness, SiO_2 cannot be effective as the insulator material. Metal oxide thin films with large dielectric constants (κ) are needed as the gate insulator. High dielectric constant MO_n gate materials, such as WO_3, have the potential to replace SiO_2. Metal oxides also serve as capacitor materials in electronic devices in the form of dynamic random access memory (DRAM) devices.[3]

Our group studied earlier the reaction of **1** with water and the formation of $O{=}W(CH_2SiMe_3)_3(OSiMe_3)$ from the reaction.[4] We have investigated the reaction of water with $W(CH_2CMe_3)_3(\equiv CSiMe_3)$ (**8**), an analog of **1**. To our surprise, the reaction of **8** with water leads to the formation of two oxo trimers

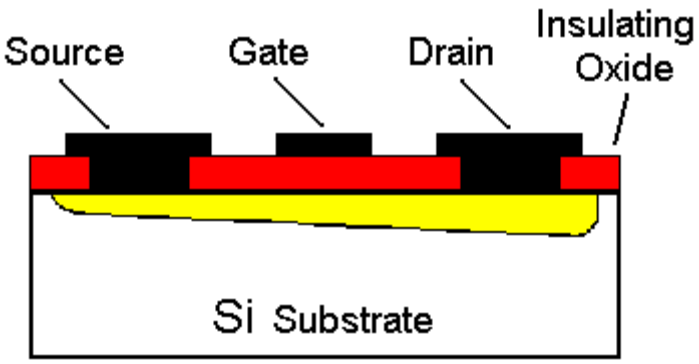

Figure 1.1. Schematic of gate materials in microelectronic devices

$W_3O_3(\mu\text{=}O)_3(CH_2CMe_3)_6L_3$ (L = THF, **9**; D_2O, **10**), demonstrating reactivities different from those of **1**. We have also observed an intermediate $W_2O_2(\mu\text{-}O)(CH_2SiMe_3)_2(CH_2CMe_3)_4$ (**11**) in the formation of **9** and **10**. **11** has been used to postulate a mechanistic pathway in the formation of **9** and **10**.

The reactions of H_2O with transition metal complexes give a comparison to their reactions involving O_2. Reactions of d^n transition metal complexes with O_2 often proceed through different mechanistic pathways than d^0 complexes. Reactivities of Groups 4 and 5 transition metal complexes with O_2 have been studied often with those containing cyclopentadienyl (Cp) or amide groups.[7] We are interested in pursing mechanistic studies of complexes containing no Cp or amide substituents. The reactions and mechanistic studies of tungsten(VI) alkylidyne metal complexes with H_2O and O_2 (studied earlier) will provide an insight into the formation of metal oxides from the reactions.

1.2. Fe(III) Porphyrin Derivatives

Unpaired electrons and magnetic properties of molecular compounds have been extensively studied by multiple spectroscopic methods. For instance, electron paramagnetic resonance (EPR) and nuclear magnetic resonance (NMR) have been used to determine electronic *g*-tensors and magnetic hyperfine interactions in paramagnetic compounds.[7-12] Since unpaired electrons usually reside in valence molecular orbitals, magnetic properties of the compounds that mainly arise from the unpaired electrons are very sensitive to

changes in bonding. The spectroscopic properties, especially EPR, are particularly useful, providing information of the electron configuration of transition metals and spin density distributions in the molecules. While these techniques probe the energetic aspects of the wavefunctions and bonding, polarized neutron diffraction (PND) examines the spatial aspects of the wavefunction and bonding in the compounds, giving different features of the bonding. PND is a unique technique in that it directly provides spin density in a compound.

Polarized neutron diffraction has not been used thus far to study the magnetic properties of biological systems or biomimetic compounds. This is the only known technique that gives the distribution of spin density in compounds. Magnetic properties of metal-containing biological systems or biomimetic compounds have been actively studied with the use of several techniques including magnetization measurements, EPR, NMR, and magnetic circular dichroism (MCD).[7] For example, electron spin distribution in iron porphyrins has been probed by EPR and NMR.[8] Both techniques use magnetic nuclei as local probes, and are limited by nonmagnetic nuclei in a compound.[9] Our interest has focused on paramagnetic metalloproteins such as Fe(TPP)Cl (**12**) and [Fe(TPP)(HIm)$_2$]Cl (TPP^{2-} = *meso*-tetraphenylporphyrinate; HIm = 1H-imidazole, **13**). In these complexes, Fe(III) ions are bound to porphyrin ligands to form complexes containing unpaired electrons. We have used PND to determine unpaired electron density in these biomimetic porphyrin complexes, as summarized below. The structures of the complexes are present in hemoglobin, myoglobin and cytochromes. We have also prepared per-deuterated complexes

for polarized neutron diffraction, as deuterium atoms reduce neutron background scattering and enhance PND signals. Prior to conducting PND experiments, single crystal X-ray diffraction experiments are needed in order to provide structural parameters for the PND experiments. Thus, in-depth structural analysis at variable low temperatures have been conducted.

1.3. Determination of Spin Density by Polarized Neutron Diffraction

It is perhaps best to first discuss the difference between neutron and X-ray diffraction. Before we proceed, however, it is important to understand the fundamental terminology in these techniques such as scattering, diffraction, and elastic and inelastic scattering. Elastic scattering refers to the process when photons or neutrons do not undergo energy transfer and retain their energy, after the incident X-ray or neutron beam penetrates the crystal. Only the direction of the propagation of the incident beam is changed. Some other photons or neutrons transfer energy in the process, and their wavelength become longer. Such scattering is called inelastic scattering. In elastic scattering, when the wavelength of the incident beam is comparable to lattice spacings in the crystal, interference of the scattered photons or neutrons occurs according to Bragg's law (Eq. 1.8).

$$n\lambda = 2d \sin \theta \qquad \text{(Eq. 1.8)}$$

where λ is the X-ray or neutron wavelength, d is the spacing between crystal planes, θ is the scattering angle, and n is an integer.

Such scattering is called diffraction (also known as Bragg scattering or Bragg diffraction). It is the basis of both X-ray or neutron diffraction experiments to determine crystal structures and polarized neutron diffraction experiments to determine spin density discussed here.

X-ray photons are scattered by electron shells of atoms in a crystal. Thus X-ray diffraction gives the electron density distribution of a unit cell of the compound. In contrast, neutrons are particles and show both wave- and particle-like properties. The wave property of neutrons is the basis of neutron diffraction. One unique property of neutrons is that they have a spin 1/2 and a magnetic moment. Thus a neutron beam interacts with both the nuclei and the spins of unpaired electrons in a crystal during neutron scattering. The latter is the basis of spin density studies by neutron scattering that we will review in detail in the next section.

The X-ray and neutron scattering lengths are significantly different.[13-17] Neutron scattering can be advantageous in locating light atoms such as hydrogen, deuterium and helium and to distinguish between atoms with similar atomic numbers such as hydrogen and deuterium or nitrogen and oxygen.[13-17] X-ray and neutron scattering usually complement one another. X-ray diffraction experiments give the electron density distribution in a molecule, and neutron diffraction experiments provide nucleus positions and spin density in the molecule.

The crystal structure of the compound is determined to obtain structural information such as atomic positions and thermal parameters. Both X-ray and

non-polarized neutron diffractions have been used in the current work. While the structures obtained from X-ray and neutron diffraction are quite similar at low temperatures, there are differences between the two.[15]

Polarized neutron diffraction (PND) is a technique that is usually used on single crystals of compounds possessing unpaired electrons (Scheme 1.1). PND is experimentally similar to a neutron diffraction experiment, except that a polarized neutron beam is used.[18-23] To obtain a polarized neutron beam, an unpolarized neutron beam first passes through a spin filter that is made of either a polarizing crystal,[20] which also acts as a monochromator (polarizing monochromator), or a ^{3}He spin filter for pulsed neutrons,[21,22] so that neutrons with, e.g., up spin (m_s = +1/2) are obtained. A polarizing crystal of a ferromagnetic material, such as Heusler alloy Cu_2MnAl, is often used for polarized neutrons generated from reactors.[20] When the polarizing crystal is placed inside a magnet, electron spins are polarized along the magnetic field. When the unpolarized neutron beam is scattered from the polarizing crystal, the Bragg [111] diffraction gives rise to a monochromatic beam of polarized neutrons with spins parallel (↑) to the magnetic field. A ^{3}He spin filter polarizes a broad energy range of neutrons and is thus suitable for pulsed neutrons.[21,22] There are two protons and one neutron in the ^{3}He isotope, and the ^{3}He nuclear polarization is dominated by the unpaired neutron.[22] In an optical cell filled with ^{3}He gas, polarized light is used to optically pump the ^{3}He isotope continuously in order to maintain polarization.[21] The polarized ^{3}He captures neutrons whose spins are antiparallel with the ^{3}He spins, and transmits neutrons whose spins are parallel.

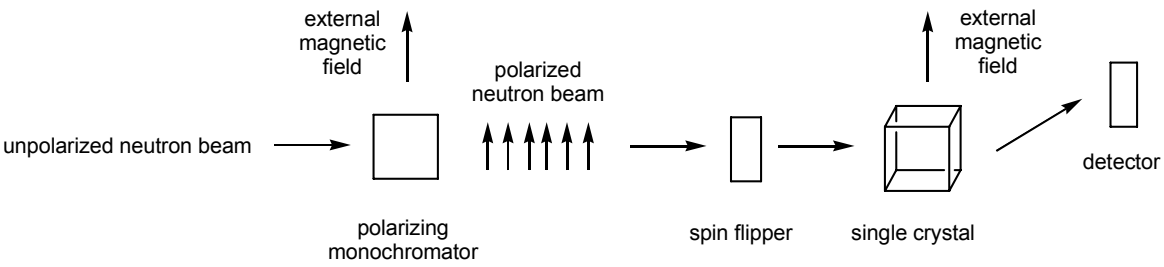

Scheme 1.1. Basic operation of a polarized neutron diffractometer using a reactor neutron source.[18-23] For a diffractometer using pulsed neutrons, the polarizing monochromator (and the external magnetic field to polarize the ferromagnetic material) is replaced by a ^{3}He spin filter.

It is planned to use a ^{3}He spin filter for the TOPAZ single crystal diffractometer at the Spallation Neutron Source (SNS) at the Oak Ridge National Laboratory.

The polarized neutron beam generated by a polarizing crystal/monochromator or ^{3}He spin filter then passes through a spin flipper. When the flipper is turned off, neutrons with up spin (m_s = +1/2) are observed. When the flipper is turned on, the neutrons are re-orientated to spin down (m_s = –1/2). This process gives a polarized neutron beam that is aligned either parallel (↑) or antiparallel (↓) to the external applied magnetic field (Scheme 1.1).

1.4. Current Dissertation

There are two main foci in this Ph.D. dissertation. The first focus is the reactions of tungsten(VI) alkyl alkylidyne and bis-alkylidene complexes with phosphines and water. Thermodynamic and kinetic studies have been conducted to determine the mechanistic pathway that leads to the formation of novel d^0 tungsten complexes. The second focus is study of spin density in Fe porphyrin complexes as well as related preparation of per-deuterated Fe(III) porphyrin derivatives and crystal structure determination of the Fe porphyrin complexes.

1.4.1. Chapter 2

Preparation and characterization of alkyl alkylidyne $W(CH_2SiMe_3)_3(\equiv CSiMe_3)$(DMPE-*P*) (**4a**) and bis-alkylidene $W(CH_2SiMe_3)_2(=CHSiMe_3)_2$(DMPE-*P*) (**4b**) and inter-conversion between the

alkyl alkylidyne (**4a**) and bis-alkylidene (**4b**) complexes were studied. The reaction of $W(CH_2SiMe_3)_3(\equiv CSiMe_3)$ (**1**) with DMPE (DMPE = $Me_2PCH_2CH_2PMe_2$) gives the adduct **4a**. **4a** undergoes a rarely observed reversible transformation to its bis-alkylidene tautomer **4b** through α–H migration. The DMPE ligands in both **4a** and **4b** contain a dangling P atom (*P*). Thermodynamic and kinetic studies of the **4a** $\rightleftharpoons$ **4b** exchange show that it is slightly endothermic with $\Delta H°$ = 5.1(1.1) kcal/mol and $\Delta S°$ = 24(4) eu; $\Delta H_1^{\neq}$ = 4.0(0.9) kcal/mol, $\Delta S_1^{\neq}$ = –51(2) eu for the **4a** $\rightarrow$ **4b** forward reaction; $\Delta H_{-1}^{\neq}$ = 2.0(0.8) kcal/mol, $\Delta S_{-1}^{\neq}$ = –76(1) eu for the **4b** $\rightarrow$ **4a** reverse reaction. Activation entropies are the major contributors to the activation barriers of the exchange: $\Delta G_{1\,278K}^{\neq}$ = 21.7(1.5) kcal/mol and $\Delta G_{-1\,278K}^{\neq}$ = 23.1(1.1) kcal/mol. The **4a** $\rightleftharpoons$ **4b** mixture undergoes α–H abstraction, yielding alkyl alkylidene alkylidyne complexes $W(CH_2SiMe_3)(=CHSiMe_3)(\equiv CSiMe_3)(DMPE)$ (*syn*: **7a**; *anti*: **7b**) containing chelating DMPE ligand with the following activation parameters: $\Delta H_2^{\neq}$ = 13(1) kcal/mol and $\Delta S_2^{\neq}$ = –36(4) eu. The preparation and characterization of **7a** and **7b** has also been studied.

1.4.2. Chapter 3

Addition of two mono-dentate phosphines (PR_3 = PMe_3, PMe_2Ph) to $W(CH_2SiMe_3)_3(\equiv CSiMe_3)$ (**1**), forming $W(CH_2SiMe_3)_3(\equiv CSiMe_3)(PR_3)$ (**2a**, **3a**) and their bis-alkylidene tautomers $W(CH_2SiMe_3)_2(=CHSiMe_3)_2(PR_3)$ (**2b**, **3b**), has been found to be reversible. Variable-temperature NMR studies of the

exchanges give equilibrium constants and enthalpies and entropies of the equilibria: $\Delta H°$ = –10.0(1.1) kcal/mol and $\Delta S°$ = –23(4) eu for **1** + PMe_3 ⇌ **2a**/**2b**, and $\Delta H°$ = –3.0(0.7) kcal/mol and $\Delta S°$ = –6(3) eu for **1** + PMe_2Ph ⇌ **3a**/**3b**. An in-depth discussion of the addition of the two mono-dentate phosphines to **1** is presented in Chapter 3.

1.4.3. Chapter 4

The reactions of alkyl alkylidyne $W(CH_2CMe_3)_3(\equiv CSiMe_3)$ (**8**) with H_2O in THF and with D_2O in benzene-d_6 give two new trimeric oxo complexes: $W_3O_3(\mu{=}O)_3(CH_2CMe_3)_6(THF)_3$ (**9**) and $[W_3O_3(\mu{=}O)_3(CH_2CMe_3)_6(D_2O)_3]\bullet 2C_6D_6$ (**10**), respectively. $W_3O_3(\mu{=}O)_3(CH_2CMe_3)_6(THF)_3$ (**9**) and $W_3O_3(\mu{=}O)_3(CH_2CMe_3)_6(D_2O)_3$ (**10**) have been characterized by NMR spectroscopy and single-crystal X-ray diffraction. The X-ray structures of **9** and **10** illustrate W=O→W bonding which is rare in organometallic complexes. In the reaction with D_2O in THF, an unstable intermediate $W_2O_2(\mu\text{-}O)(CD_2SiMe_3)_2(CH_2CMe_3)_4$ (**11-*d*$_4$**) has been identified and characterized by ^1H, ^2H and ^{13}C NMR spectroscopy. Kinetics of the reactions of **8** with excess H_2O and D_2O in THF-d_8 at 298(1) K, yielding **11** and **11-*d*$_4$**, respectively, has been studied, giving the kinetic isotope effect (KIE) of 3.46(3) for this reaction.

1.4.4. Chapter 5

The crystal preparation and variable-temperature X-ray diffraction studies of Fe(TPP)Cl (**12**) are presented in this chapter. The extensive structural studies show that the thermal motion in the phenyl groups leads to lower symmetry from the *I4/m* space group at 293(2) K to the *I4* space group at 20(2) K. The phenyl groups tilt away from the crystallographic *c* direction (perpendicular to the mirror plane) and lead to the loss of the mirror symmetry. The structural analyses of **12** at 20(2), 143(2), and 293(2) K give a better insight into the vital role the phenyl groups play in the symmetry of **12**.

1.4.5 Chapter 6

Variable X-ray diffraction studies of the structure of [Fe(TPP)$(HIm)_2$]Cl (**13**) are presented in this chapter. The neutron structure of **13** at 20(2) K is also given. A structural comparison is made between the reported X-ray structure and our current work. In contrast to the reported structure, the X-ray structure at 20(2) K illustrates no hydrogen interaction between the N atom (N4) in the imidazole ligand on the Fe1 molecule and the O atom in the water molecule with a N4-O bond distance of 4.332 Å. However, the N4-O bond distance in the 143(2) structure is 2.778 Å. The X-ray structures at 20(2) and 143(2) K show hydrogen bonding between the O atom in the water molecule and the chloride ion. The neutron structure at 20(2) K shows similiar hydrogen interaction as that observed in the two X-ray structures, and the results are discussed. The role of the water molecule in the crystal lattice illustrates a new structural behavior at

low temperature, which was not observed in the reported structure of **13**. An in-depth structural analysis of **13** is presented in Chapter 6.

1.4.6. Chapter 7

Direct measurement of the spin distribution in low-spin (S = 1/2) $[Fe(TPP)(HIm)_2]Cl$ (**13**, TPP^{2-} = *meso*-tetraphenylporphyrinate; HIm = 1H-imidazole) by single-crystal polarized-neutron diffraction shows that the Fe and the N atoms in the porphyrin and imidazole ligands possess +1.15(2) *e* of α-density and -0.02 to -0.07 *e* of β-density, respectively. The total moment delocalized onto the nearest neighbours around each Fe site is 0.20(3) *e*, in an agreement with that suggested by NMR studies. The preparation of crystals of $[Fe(TPP)(HIm)_2]Cl{\bullet}H_2O{\bullet}CHCl_3$ (**13**$\bullet H_2O\bullet CHCl_3$) suitable for PND studies is also reported.

1.4.7. Chapter 8

Neutron scattering studies such as polarized neutron diffraction and inelastic neutron scattering are unique methods to probe magnetic properties of paramagnetic compounds. The use of the deuterated compounds in these studies would reduce background scattering by hydrogen atoms, and enhance the signal/noise ratios. Per-deuterated *meso*-tetraphenylporphyrin-d_{30} D_2(TPP-d_{28}) (**14-*d*$_{30}$**), Fe(TPP)Cl-d_{28} (**12-*d*$_{28}$,** TPP^{2-} = *meso*-tetraphenylporphyrinate), and 1H-imidazole derivative $[Fe(TPP)(DIm)_2$-$d_{36}]Cl$ (**13-*d*$_{36}$**, DIm = 1D-imidazole-d_4)

have been prepared. A mass spectroscopic (MS) method has been developed to calculate the level of deuteration in H_2(TPP-d_{28}) (**15-d_{28}**). Crystal structures of **14-d_{30}** and **12-d_{28}** at 293(2) K and **13-d_{36}** at 173(2) and 293(2) K have been determined.

1.4.8. Chapter 9

Conclusions and suggested future work are presented in this chapter.

CHAPTER 2

Reaction of a Tungsten Alkylidyne Complex with a Chelating Diphosphine. α-Hydrogen Migration in the Intermediates and Formation of an Alkyl Alkylidene Alkylidyne Complex

2.1. Introduction

Bis(dimethylphosphino)ethane (DMPE) has been extensively studied as a bidentate ligand.[24-29] Its reaction with $W(CH_2CMe_3)_3(\equiv CCMe_3)$ gives $W(CH_2CMe_3)(=CHCMe_3)(\equiv CCMe_3)$(DMPE), one of the first alkyl alkylidene alkylidyne complexes reported by Schrock and Clark (Scheme 2.1).[24] The crystal structure of this complex was reported by Churchill and Youngs in 1979.[25] The square pyramidal DMPE complex shows *cis*-coordination of the two P atoms. The NMR spectra of its PMe_3 analog $W(CH_2CMe_3)(=CHCMe_3)(\equiv CCMe_3)(PMe_3)_2$ suggest that the two mono-dentate phosphine ligands take the *trans* axial positions in the trigonal bipyramidal. Both complexes were prepared through direct heating of a solution of $W(CH_2CMe_3)_3(\equiv CCMe_3)$ in liquid phosphine.[24] No intermediate was observed in the formation of the neopentyl neopentylidene neopentylidyne complexes.

We recently found that the reaction of $W(CH_2SiMe_3)_3(\equiv CSiMe_3)$ (**1**), a β–Si analog of $W(CH_2CMe_3)_3(\equiv CCMe_3)$, with PMe_3 or PMe_2Ph under heating yields $W(CH_2SiMe_3)(=CHSiMe_3)(\equiv CSiMe_3)(PR_3)_2$ (PR_3 = PMe_3, **5a-b**; PMe_2Ph, **6a-b**).[2]

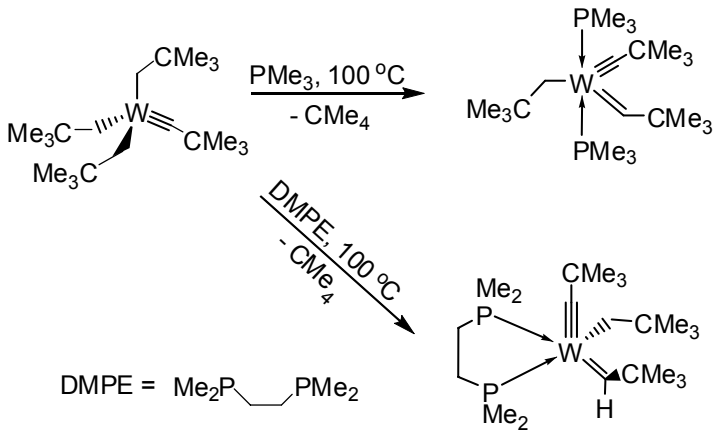

Scheme 2.1. Reported d^0 complexes containing metal-carbon single, double, and triple bonds.[2]

Prior to the formation of **5a-b**/**6a-b**, phosphine adducts **2a**/**3a** were observed as intermediates (Scheme 2.2). **2a**/**3a** undergo reversible α–H migration, giving bis-alkylidene tautomers **2b**/**3b**.[30,31] Kinetic studies reveal that the equilibrium mixtures then react with PR_3 through rate-determining α-H abstraction, followed by PR_3 coordination, to give **5a-b**/**6a-b** (Scheme 2.2).[2,32]

We have recently studied the reaction of $W(CH_2SiMe_3)_3(\equiv CSiMe_3)$ (**1**) with bidentate DMPE. One P atom in DMPE binds with the W atom in **1**, giving an adduct $W(CH_2SiMe_3)_3(\equiv CSiMe_3)$(DMPE-*P*) (**4a**) with a dangling P atom. **4a** then undergoes α–H migration, giving its bis-alkylidene tautomer $W(CH_2SiMe_3)_2(=CHSiMe_3)_2$(DMPE-*P*) (**4b**, Scheme 2.3). To our knowledge, direct observation of such alkyl alkylidyne ⇌ bis-alkylidene exchanges are rare and have been reported in **2a/3a** ⇌ **3b/3b** (Scheme 2.2) and in $W(CH_2CMe_3)_2(\equiv CCMe_3)(SiR_3)$ ⇌ $W(=CHCMe_3)_2(CH_2CMe_3)(SiR_3)$ [SiR_3 = $Si(CMe_3)Ph_2$].[1,8,9] Thermodynamic and kinetic studies of the **4a** ⇌ **4b** exchange have been conducted. The tautomeric mixture **4a** ⇌ **4b**, under heating, undergoes α–H abstraction, yielding alkyl alkylidene alkylidyne complex $W(CH_2SiMe_3)(=CHSiMe_3)(\equiv CSiMe_3)$(DMPE) (*syn*: **7a**; *anti*: **7b**; Scheme 2.3).

This conversion appears to start with the elimination of $SiMe_4$ through α–H abstraction, followed by the coordination of the dangling P atom. Our studies of the reaction of $W(CH_2SiMe_3)_3(\equiv CSiMe_3)$ (**1**) with DMPE, **4a** ⇌ **4b** exchange, and formation of **7a-b** are reported here. These results are compared with those of the reactions of **1** with mono-phosphines PR_3 in Scheme 2.2, offering a deeper

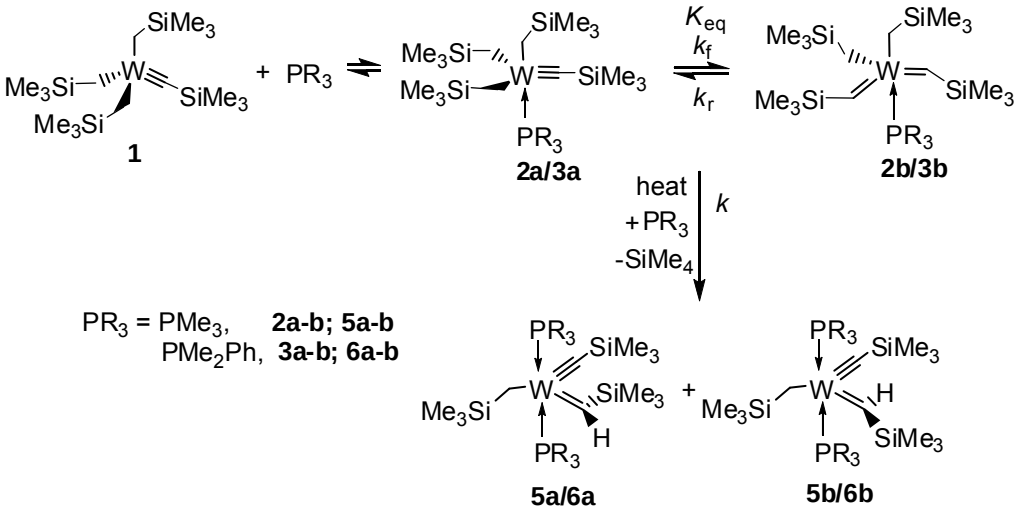

Scheme 2.2. Formation of complexes **5a-b** and **6a-b** from the equilibrium of **2a-b** and **3a-b**.[8,9]

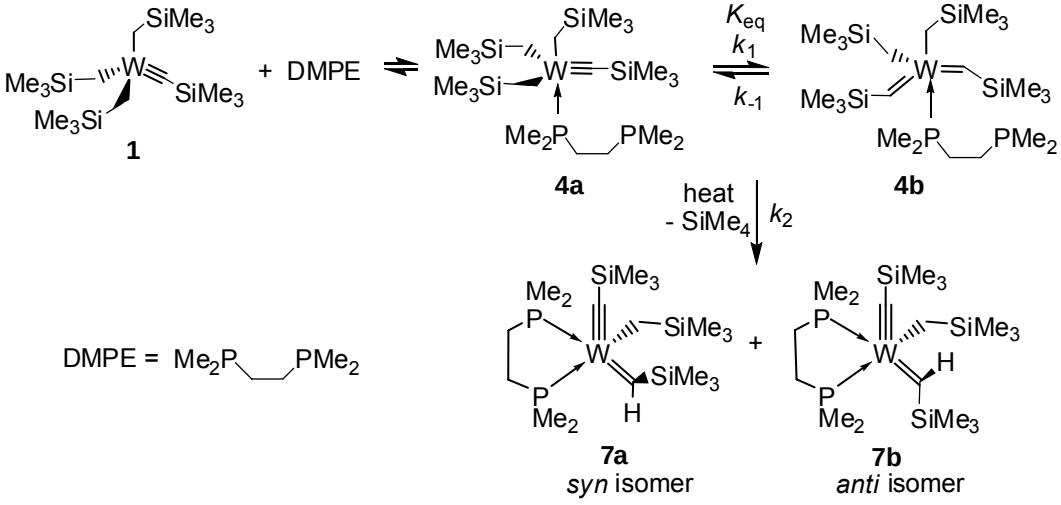

Scheme 2.3. Formation of complexes **7a-b** from the equilibrium of **4a-b**.

insight into the formation of unique alkyl alkylidene alkylidyne complexes containing single, double and triple bonds to one atom in a single molecule.

2.2. Results and Discussion

2.2.1. Preparation and Characterization of the Alkyl Alkylidyne-DMPE Adduct $W(CH_2SiMe_3)_3(\equiv CSiMe_3)$(DMPE-*P*) (4a) and Its Conversion to Bis-alkylidene Tautomer $W(CH_2SiMe_3)_2(=CHSiMe_3)_2$(DMPE-*P*) (4b)

When 1 equiv DMPE was added to a solution of $W(CH_2SiMe_3)_3(\equiv CSiMe_3)$ (**1**) in toluene-d_8 at –78 °C, an immediate formation of the adduct **4a** was observed as the color of the solution changed from yellow to red-orange. The solution was then warmed to –35 °C in a pre-cooled NMR probe. ^{31}P NMR spectrum of **4a** showed two broad resonances, one (1.33 ppm) for the P atom bound to the W atom and the other (–47.17 ppm) for the dangling P atom (Figure A1). A small amount of free DMPE was observed at –49.20 ppm in the ^{31}P NMR spectrum.[32] The ^{31}P peak at –47.17 ppm is close to that of free DMPE. Nadasdi and coworkers have reported $CpTi(SCH_2CH_2S)Cl$(DMPE) in which DMPE is a dangling ligand.[33] This Ti complex reveals two ^{31}P NMR chemical shifts for the DMPE ligand, a pair of doublets at –47.42 and 3.10 ppm ($^3J_{P\text{-}P}$ = 19.5 Hz), indicating inequivalent P atoms in the DMPE ligand. The peak at –47.42 ppm is assigned to the dangling PMe_2 group in the DMPE ligand as it is close to that of free DMPE at –49.20 ppm in ^{31}P NMR spectrum.[33] When the temperature was raised to, e.g., –5 °C, for **4a**, peaks of both bound and dangling P atoms became

broad. During the heating, **4b** was found to gradually form in the NMR solution. At –5 °C, the ^{1}H NMR spectrum (Figure A2) of the solution showed a dynamic process with four broad peaks: 0.92 ppm for the methyl groups on the DMPE ligand and free DMPE, 1.36 ppm for the ethylene protons of the bound and free DMPE, 0.53 ppm for the C*H*$_2$SiMe$_3$ groups, and 0.32 and 0.31 ppm for the –Si*Me*$_3$ groups on –CH$_2$Si*Me*$_3$ and ≡CSi*Me*$_3$, respectively. The observation of one CH$_2$ peak and one methyl peak for W←P(Me$_2$)C*H*$_2$-C*H*$_2$-PMe$_2$ in the ^{1}H NMR spectrum indicates that the bound and dangling parts of the DMPE ligand undergo a fast exchange at –5 °C. At –50 °C, the Si*Me*$_3$ peak split into three peaks of ca. 1:2:1 ratio for the ≡CSi*Me*$_3$ (0.49 ppm), two equatorial –CH$_2$Si*Me*$_3$ (0.36 ppm), and one axial –CH$_2$Si*Me*$_3$ ligand (0.33 ppm), suggesting that the exchanges among the axial and equatorial ligands in **4a** are restricted at this temperature. A broad, overlapping –C*H*$_2$SiMe$_3$ peak was observed at 0.54 ppm. A dangling –PMe$_2$ peak (0.81 ppm) and a bound PMe$_2$ peak (0.91 ppm; $^{2}J_{P\text{-}H}$ = 5.4 Hz) were observed. The two W←PC*H*$_2$-C*H*$_2$-P- resonances also split. These observations suggest a slow rotation of the DMPE ligand W←P(Me$_2$)CH$_2$-CH$_2$PMe$_2$ at -50 °C.

The ^{13}C NMR spectrum of **4a** at –5 °C (Figure A3) shows two broad peaks for the W←P(Me$_2$)CH$_2$-CH$_2$PMe$_2$ ligand, one for P*Me*$_2$ at 13.82 ppm and the other for –*C*H$_2$– groups at 25.89 ppm. The observation is similar to that of the DMPE ligand in ^{1}H NMR spectrum and indicates a fast exchange of the bound and dangling parts of the DMPE ligand. The –CH$_2$Si*Me*$_3$ and ≡*C*Si*Me*$_3$

resonances were observed at 3.27 and 3.20 ppm, respectively. Two broad peaks at 50.53 ppm and 80.94 ppm are assigned to the equatorial and axial $-CH_2SiMe_3$, respectively, as they are close to 49.45 ppm for the equatorial and 81.69 ppm for axial $-CH_2SiMe_3$ in $W(CH_2SiMe_3)_3(\equiv CSiMe_3)(PMe_3)$ (**2a**).[2,32] The alkylidyne carbon resonance of $\equiv CSiMe_3$ is broad at 355.4 ppm.

The alkyl alkylidyne adduct **4a** readily converts to its bis-alkylidene tautomer **4b**, and the reaction is reversible. In other words, inter-conversion between **4a** and **4b** eventually reaches an equilibrium **4a** ⇌ **4b**. Thermodynamics and kinetics of the inter-conversion are discussed below.

The sample for NMR characterization of **4b** was prepared by adding DMPE to a solution of $W(CH_2SiMe_3)_3(\equiv CSiMe_3)$ (**1**) in toluene-d_8 at 23 °C. The sample was kept at room temperature for 5 h to ensure adequate conversion of **4a** to **4b**. NMR [^{1}H, ^{13}C, ^{31}P, ^{1}H-gated-decoupled ^{13}C, and HSQC (Heteronuclear Single Quantum Coherence)] spectra of **4b** were taken at –20 °C to slow the inter-conversion **4a** ⇌ **4b** in order to give better resolution of the NMR spectra. In the ^{31}P NMR spectra (Figure A4), two doublets at –47.77 (dangling) and 11.10 ppm (W-PMe_2-, $^3J_{P\text{-}P}$ = 20.7 Hz) are consistent with the presence of a bound W–PMe_2 and a dangling –PMe_2 in **4b**. In the ^{1}H NMR spectrum (Figure A5), resonances of two overlapping doublets for W-PMe_2 were observed at 1.06 and 1.04 ppm ($^2J_{P\text{-}H}$ = 6.6 Hz). This is due to the two diasterotopic methyl groups in the bound P atom of DMPE (Figure 2.1). The dangling –PMe_2 was observed at 0.81 ppm. Two broad resonances at 1.64 and 1.24 ppm are assigned to the

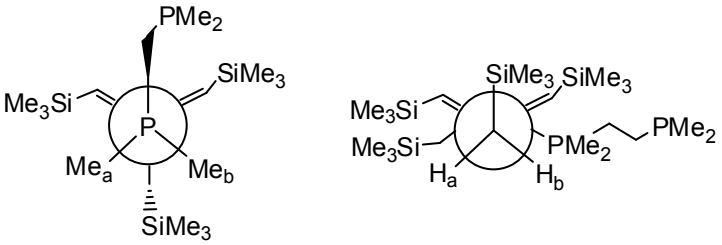

down the P-W-C bond **4b**

down the equatorial alkyl ligand **4b**

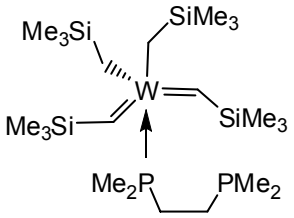

anti, syn-**4b**

Figure 2.1. (Upper) Newman projections of **4b** showing the diastereotopic groups in W-P*Me*$_a$*Me*$_b$- and equatorial W-C*H*$_a$*H*$_b$SiMe$_3$; (Lower) "Pinwheel" *anti,syn* conformation of **4b**.

ethylene protons in W←P(Me_2)CH_2-CH_2PMe_2. The ^{1}H NMR spectrum reveals two doublets of doublets at 0.94 and 0.93 ppm for the inequivalent *eq*-CH_aH_bSiMe_3 group in **4b** (Figure A5). The *ax*-CH_2SiMe_3 group in **4b** was observed at 0.34 ppm. These methylene proton assignments were confirmed by HSQC (Figure A6). Four –Si*Me*$_3$ peaks were observed, and two =C*H*SiMe_3 resonances appear as doublets at 8.01 and 7.23 ppm. These observations are consistent with a "pinwheel" *anti*,*syn* conformation for **4b** with two inequivalent alkylidene ligands (Figure 2.1). Such a conformation was also observed for W(CH_2SiMe_3)$_3$(≡C$SiMe_3$)(PMe_3) (**2a**)[2,32] and Ta(CH_2EMe_3)(=C$HEMe_3$)$_2$(PMe_3)$_2$ (E = C, Si).[1] In the ^{13}C NMR spectrum of **4b** (Figure A7), two doublets at 256.7 and 254.7 ppm ($^2J_{P\text{-}C}$ = 12.5 Hz for both) are observed for the two alkylidene ligands in **4b**. The four –Si*Me*$_3$ groups were observed at 4.88, 2.99, 1.81, and 1.77 ppm. These results are consistent with a "pinwheel" *anti,syn* conformation. Two doublets at 51.16 ppm and at 37.78 ppm for the equatorial and axial –*C*H_2SiMe_3 ligands were also observed. ^{13}C resonances of the DMPE ligand further support the presence of a dangling PMe_2. The α–methyl groups in the W-P*Me*$_2$- moiety were observed as doublets at 14.93 and 14.64 ppm, as they are diastereotopic (Figure A7). The dangling –P*Me*$_2$ appears as a doublet at 13.49 ppm. The P-*C*H_2-*C*H_2-P atoms in the DMPE ligand were observed as two doublets of doublets at 25.11 and 28.10 ppm.

2.2.2. Conversion of the 4a ⇌ 4b Equilibrium Mixture to W(CH_2SiMe_3)(=$CHSiMe_3$)(≡$CSiMe_3$)(DMPE) (7a-b)

Upon heating a solution of **4a** ⇌ **4b** with excess DMPE in toluene-d_8, the mixture undergoes cyclometalation for the dangling DMPE ligand (Scheme 2.3). In the process, α–H abstraction occurs to give alkyl alkylidene alkylidyne complexes **7a** and **7b**. ^{1}H, ^{13}C, ^{31}P, ^{1}H-gated-decoupled ^{13}C and HSQC NMR characterization of **7a** and **7b** reveal that they are likely *syn*- and *anti*-rotamers, as observed in W(CH_2SiMe_3)(=$CHSiMe_3$)(≡$CSiMe_3$)(PR_3)$_2$ (PR_3 = PMe_3, **5a-b**; PMe_2Ph, **6a-b**)[2] and Re(=$CHCMe_3$)(≡$CCMe_3$)(OR)$_2$.[34] In the *syn*-rotamer **7a**, the –$SiMe_3$ group on the alkylidyne ligand points toward the alkylidyne ligand.

The ^{31}P NMR spectrum (Figure A8) of **7a** shows doublets at 40.21 and 23.16 ppm suggesting that the P atoms are inequivalent. Likewise, two doublets at 38.84 and 22.41 ppm in the ^{31}P NMR spectrum of **7b** were found. These chemical shifts are significantly different from those of free DMPE or dangling P atoms in **4a-b** at –45 to –47 ppm, suggesting that both P atoms in the DMPE ligand are bound to the metal atom. The ^{1}H NMR resonances of the alkylidene H atoms in **7a** and **7b** were observed as two overlapping doublets of doublets at 7.95 and 11.14 ppm, respectively (Figure A9). The axial –$CH_2Si\mathit{Me}_3$, =$CHSi\mathit{Me}_3$, and ≡$CSi\mathit{Me}_3$ were observed at 0.43, 0.34, and 0.15 ppm, respectively. Two multiplets for –$C\mathit{H}_a\mathit{H}_bSiMe_3$ were observed at 0.49 and –0.44 ppm as H_a and H_b are diastereotopic (Figure 2.2) and coupled to the two P atoms in the DMPE ligand. 2-D ^{1}H–^{1}H COSY (Correlation Spectroscopy) confirmed the assignment

of the two resonances. 2-D *J*-resolved ^{1}H NMR spectrum of **7a** yields $^{2}J_{H\text{-}H}$ = 12.6 Hz for the –C*H*$_a$*H*$_b$SiMe$_3$ ligand. In **7b**, the –C*H*$_a$*H*$_b$SiMe$_3$ peaks appear at 0.11 and –0.01 ppm, as confirmed by HSQC. The four α–methyl groups in the DMPE ligand for **7a** are inequivalent (Figure 2.2) and observed as four doublets at 1.52, 1.32, 0.88, and 0.71 ppm. Likewise, four doublets for **7b** appear at 1.51, 1.32, 0.96, and 0.76 ppm for its four α–methyl groups. The diastereotopic ethylene protons in the DMPE ligand (Figure 2.2) in **7a** and **7b** were observed as complex multiplets.[35] The assignments of the ethylene proton resonances in the DMPE ligand were confirmed by HSQC (Figure A10). In the ^{13}C NMR spectrum (Figure A11), the alkylidene C resonance of **7a** was observed as a doublet of doublets at 241.14 ppm. One $^{2}J_{P\text{-}C}$ coupling constant (26.5 Hz, P-W=*C*H-) is much larger than the other (12.6 Hz), suggesting that the alkylidene ligand is *trans* to one P atom (with the larger $^{2}J_{P\text{-}C}$) and *cis* to another (with the smaller $^{2}J_{P\text{-}C}$). The ^{13}C resonance of the alkylidene C atom in **7b** was also observed as a doublet of doublets at 237.46 ppm ($^{2}J_{P\text{-}C}$ = 12.1 Hz) in the ^{13}C NMR spectrum. The alkylidyne ^{13}C resonance of **7a** appears as an overlapping doublet of doublets at 326.56 ppm. Likewise, the alkylidyne ^{13}C resonance of **7b** was located as a doublet of doublets at 329.35 ppm. The P-*C*H$_2$-*C*H$_2$-P resonances in **7a** were observed as two doublets of doublets at 31.76 and 29.05 ppm. Likewise, two doublets of doublets in **7b** appear at 34.92 and 27.05 ppm. The four inequivalent α–methyl groups in DMPE for **7a** are observed at 25.26, 19.64, 18.63, and 12.64 ppm, as confirmed by HSQC (Figure A10). In **7b**, these methyl resonances also appear as four doublets at 24.58, 19.28, 18.00, and 12.58 ppm.

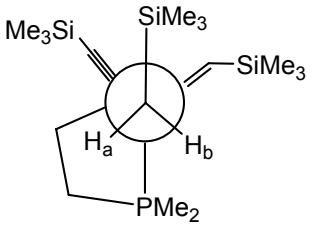

Me groups in one PMe_2 moiety are not shown

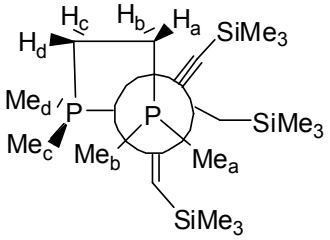

Figure 2.2. Newman projections of **7a** showing the diastereotopic H atoms in $CH_aH_bSiMe_3$ and H and P atoms in the DMPE ligand.

2.2.3. Kinetic and Thermodynamic Studies of the 4a ⇌ 4b Tautomerization – Comparison of PMe_3 and DMPE Ligands

Kinetic and thermodynamic studies of the tautomerization of $W(CH_2SiMe_3)_3(\equiv CSiMe_3)(PR_3)$ (**4a**), adduct between phosphine DMPE and alkyl alkylidyne $W(CH_2SiMe_3)_3(\equiv CSiMe_3)$ (**1**), with its bis-alkylidene isomer $W(CH_2SiMe_3)_2(=CHSiMe_3)_2(PR_3)$ (**4b**) were conducted.

Variable-temperature NMR spectra were taken of the tautomerization **4a** ⇌ **4b** and equilibrium constants, K_{eq} = [**4b**]/[**4a**], were measured between 258 and 283 K. The equilibrium constants ranging from 13.2(0.3) at 283 K to 5.2(0.7) at 258 K (Table 2.1) indicate that the **4b** isomer is favorable at higher temperatures. Decreasing the temperature shifts the equilibrium to the alkylidyne isomer **4a**. The ln K_{eq} vs $1/T$ plot (Figure 2.3) gives the thermodynamic enthalpy and entropy of the **4a** ⇌ **4b** tautomerization. The process **4a** ⇌ **4b** is endothermic with $\Delta H°$ = 5.1(1.1) kcal/mol and $\Delta S°$ = 24(4) eu. $\Delta S° > 0$ reflects the fact that **4a**, with a symmetry plane, is more symmetric than "pinwheel" **4b** (Figure 2.1) with no symmetry.

Variable-temperature ^1H NMR experiments for the **4a** ⇌ **4b** exchange between 258 and 283 K show that the α–H migrations between **4a** and **4b** follow first-order reversible kinetics (Eqs. 2.1 and 2.2).[36]

Table 2.1. Equilibrium (K_{eq}) and rate constants (k_1 and k_{-1}) of the **4a** ⇌ **4b** exchange[a-d]

T (K)	K_{eq}	$k_1 \times 10^5$ (s^{-1})	$k_{-1} \times 10^6$ (s^{-1})
258(1)	5.2(0.7)	1.64(0.03)	3.16(0.05)
263(1)	6.9(0.2)	2.2(0.2)	3.3(0.3)
268(1)	8.4(0.4)	2.7(0.2)	3.3(0.3)
273(1)	9.2(0.2)	3.22(0.14)	3.50(0.16)
278(1)	11.3(0.2)	4.15(0.10)	3.59(0.08)
283(1)	13.2(0.3)	6.69(0.11)	5.09(0.08)

[a] Solvent: toluene-d_8.

[b] The relatively small temperature range of 25 K in the current thermodynamic and kinetic studies leads to relatively large uncertainties in thermodynamic ($\Delta H°$ and $\Delta S°$) and kinetic ($\Delta H^{\neq}$ and $\Delta S^{\neq}$) parameters, as the error calculations in the Experimental Section show.

[c] The largest random uncertainty is $\sigma K_{eq(ran)}/K_{eq}$ = 0.7/5.2 = 13.5%. The total uncertainty $\sigma K_{eq}/K_{eq}$ of 14% was calculated from $\sigma K_{eq(ran)}/K_{eq}$ = 13.5% and the estimated systematic uncertainty $\sigma K_{eq(sys)}/K_{eq}$ = 5% by $\sigma K_{eq}/K_{eq} = [(\sigma K_{eq(ran)}/K_{eq})^2 + (\sigma K_{eq(sys)}/K_{eq})^2]^{1/2}$.

[d] The largest random uncertainties are $\delta k_{1(ran)}/k_1$ = 0.2/2.04 = 9.8% and $\delta k_{-1(ran)}/k_{-1}$ = 0.3/3.25 = 9.2%. The total uncertainties $\delta k_1/k_1$ = 0.110 and $\delta k_{-1}/k_{-1}$ = 0.105 were calculated from $\delta k_{(ran)}/k$ and the estimated systematic uncertainty $\delta k_{(sys)}/k$ = 5% by $\delta k/k = [(\delta k_{(ran)}/k)^2 + (\delta k_{(sys)}/k)^2]^{1/2}$.

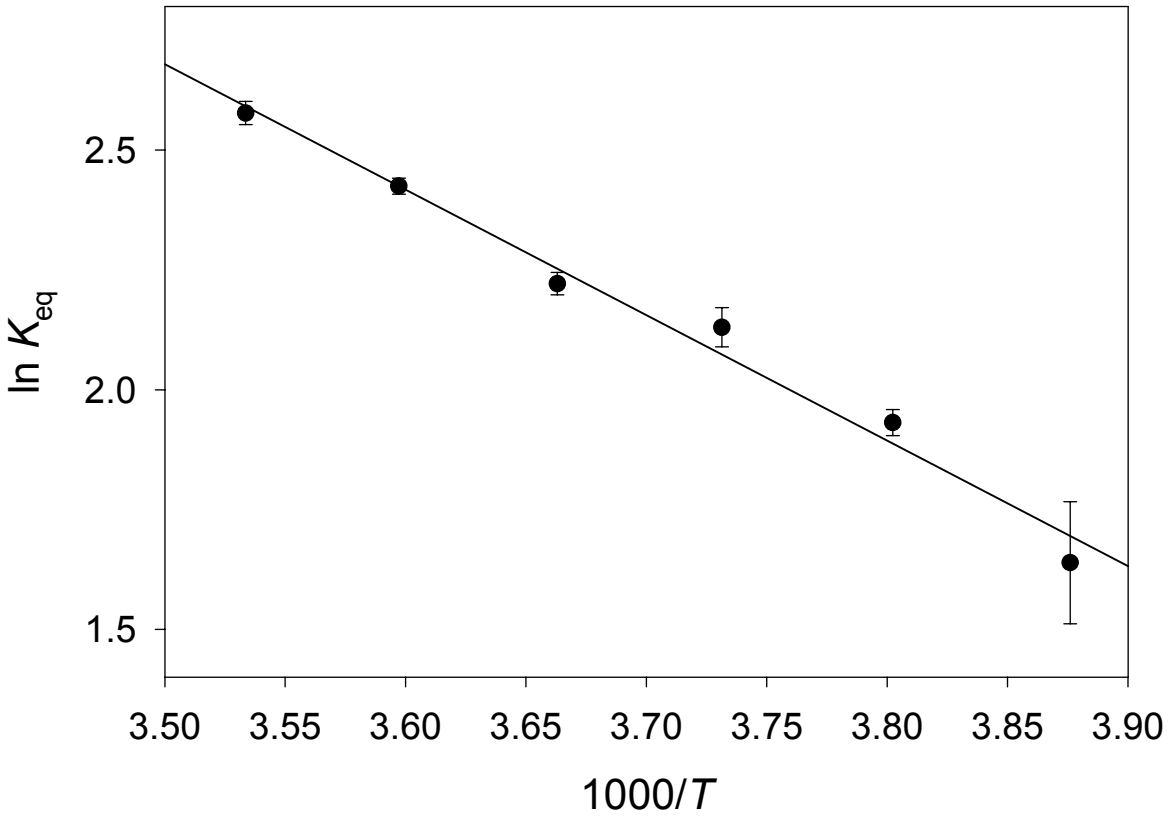

Figure 2.3. A plot of ln K_{eq} vs 1000/T of the equilibrium **4a** ⇌ **4b**.

$$ln \frac{(I_{4be} - I_{4bt})}{(I_{4be} - I_{4b0})} = (k_1 + k_{-1})t \quad \text{(Eq. 2.1)}$$

$$K_{eq} = \frac{k_1}{k_{-1}} = \frac{[\mathbf{4b}]}{[\mathbf{4a}]} \quad \text{(Eq. 2.2)}$$

where I_{4b0}, I_{4bt} and I_{4be} are the integrations of **4b** at time t = 0, t = t, and equilibrium, respectively; k_1 and k_{-1} are the rate constants for the forward and reverse reactions, respectively.

The kinetic plots for the exchange are shown in Figure 2.4, and the rate constants from Eqs. 2.1–2.2 are given in Table 2.1. Eyring plots (Figure 2.5) lead to the activation parameters of the exchange: $\Delta H_1^{\neq}$ = 7.5(0.9) kcal/mol, $\Delta S_1^{\neq}$ = –51(2) eu for the forward reaction **4a** → **4b**, and $\Delta H_{-1}^{\neq}$ = 2.0(0.8) kcal/mol, $\Delta S_{-1}^{\neq}$ = –76(1) eu for the reverse **4b** → **4a** reaction.

It is interesting to compare the thermodynamic and kinetic properties of the current tautomerization with those of the $W(CH_2SiMe_3)_3(\equiv CSiMe_3)(PMe_3)$ (**2a**) ⇌ $W(CH_2SiMe_3)_2(=CHSiMe_3)_2(PMe_3)$ (**2b**) tautomerization that involves PMe_3.[2] The current **4a** ⇌ **4b** exchange is endothermic with $\Delta H°$ = 5.1(1.1) kcal/mol and $\Delta S°$ = 24(4) eu. The equilibrium shifts to **4b** at higher temperatures. The **2a** ⇌ **2b** exchange is a slightly exothermic process with $\Delta H°$ = –2(1) kcal/mol and $\Delta S°$ = –2(2) eu. The **2a** ⇌ **2b** equilibrium shifts to **2a** at higher temperatures. It is not clear what leads to the difference in the thermodynamic parameters, although the equilibrium constants for **4a** ⇌ **4b** [K_{eq} = 11.3(0.2)] and **2a** ⇌ **2b** [K_{eq} = 12.3(0.2)]

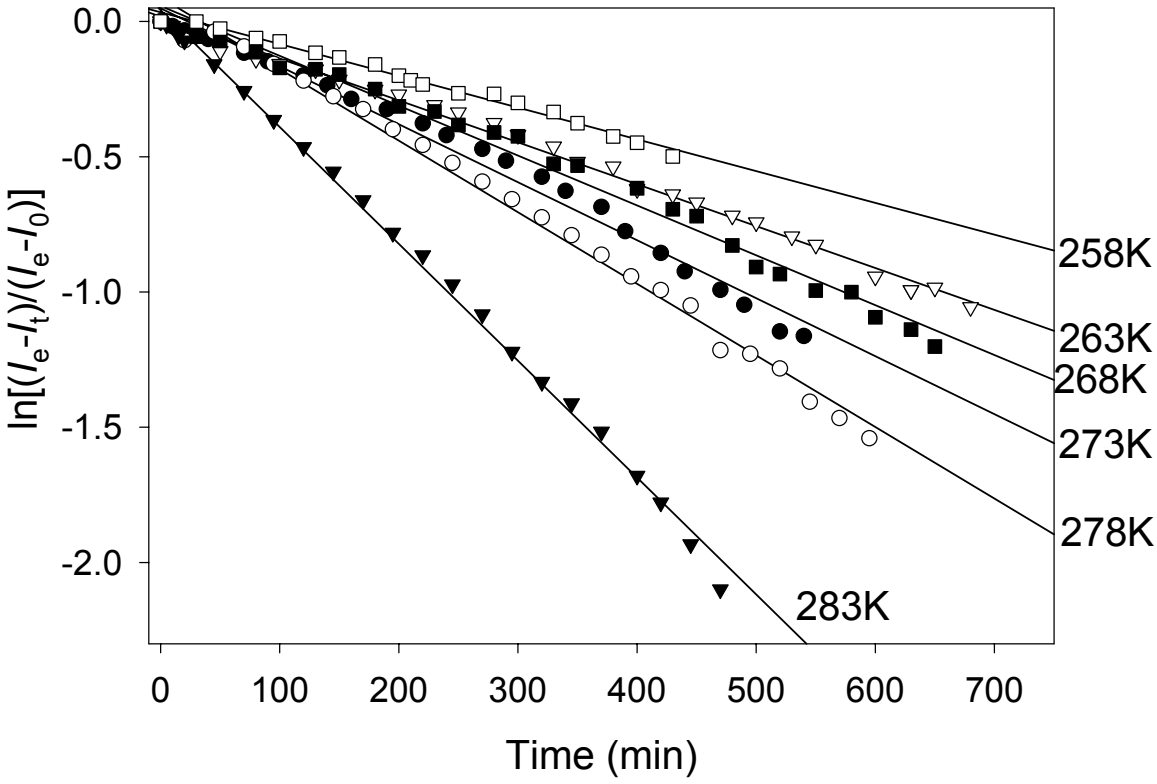

Figure 2.4. Kinetic plots of the reversible reactions **4a** ⇌ **4b**.

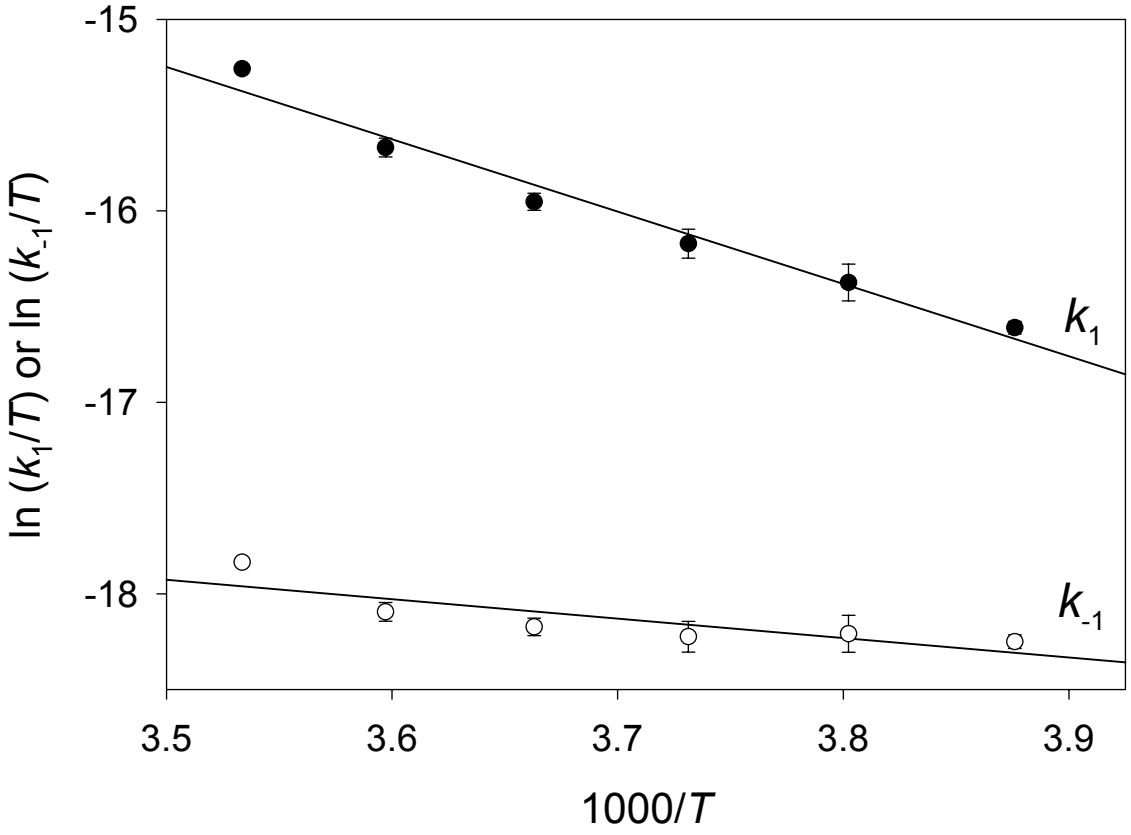

Figure 2.5. Eyring plots for the reversible reactions **4a** ⇌ **4b**.

are similar at 278 K. At temperatures above 283 K, α–H abstraction in **4a** ⇌ **4b** (and formation of **7a-b** from DMPE-containing **4a-b**) becomes fast, and this made monitoring of the **4a** ⇌ **4b** exchange by ^{1}H NMR spectroscopy difficult. Thus, thermodynamic and kinetic studies of the **4a** ⇌ **4b** exchange were only conducted at 258–283 K. In comparison, PMe_3-containing **2a**-**b** seem to be more stable, and no significant conversion from the **2a** ⇌ **2b** equilibrium mixture to $W(CH_2SiMe_3)(=CHSiMe_3)(\equiv CSiMe_3)(PMe_3)_2$ (**5a-b**) was observed <333 K.[2] The **2a** ⇌ **2b** equilibrium was thus studied at 278–303 K.

The rate constants for the **4a** ⇌ **4b** exchange at 278 K, k_1 = 4.1(0.1) × 10^{-5} s^{-1} and k_{-1} = 3.59(0.08) × 10^{-6} s^{-1} are larger than those for the **2a** ⇌ **2b** exchange: k_1 = 1.42(0.02) × 10^{-5} s^{-1} and k_{-1} = 1.160(0.018) × 10^{-6} s^{-1} at 278 K, indicating the former is faster. The activation parameters for the tautomerization involving PMe_3 are: $\Delta H_1^{\neq}$ = 16.2(1.2) kcal/mol, $\Delta S_1^{\neq}$ = –22(4) eu, and $\Delta G_{1\,278K}^{\neq}$ = 22(2) kcal/mol for the forward reaction **2a** → **2b**, and $\Delta H_{-1}^{\neq}$ = 16.2(1.3) kcal/mol, $\Delta S_{-1}^{\neq}$ = –21(4) eu, and $\Delta G_{-1\,278K}^{\neq}$ = 22(2) kcal/mol for the reverse **2b** → **2a** reaction.[2] In both forward and reverse reactions involving **2a** and **2b**, activation enthalpies $\Delta H^{\neq}$ significantly outweigh activation entropies $\Delta S^{\neq}$ in the kinetic barriers $\Delta G_{278K}^{\neq}$. In contrast, in both forward and reverse reactions involving DMPE-containing **4a** and **4b**, activation enthalpies $\Delta H^{\neq}$ [7.5(0.9) and 2.0(0.8) kcal/mol] are minor contributors to $\Delta G_{278K}^{\neq}$. Here activation entropies $\Delta S^{\neq}$ are the dominant factors in the kinetic barriers. In the forward reaction **4a** → **4b**, $\Delta H_1^{\neq}$ = 7.5(0.9) kcal/mol is significantly smaller and activation entropy $\Delta S_1^{\neq}$ = –51(2) eu is much larger

(negative) than those in the reaction **2a** → **2b**. The activation barrier $\Delta G_1^{\neq}{}_{278K}$ = 21.7(1.5) kcal/mol is, however, similar to that in **2a** → **2b**. In the reverse **4b** → **4a** reaction, $\Delta G_{-1}^{\neq}{}_{278K}$ = 23.1(1.1) kcal/mol is slightly larger than either $\Delta G_1^{\neq}{}_{278K}$ for the forward **4a** → **4b** reaction and $\Delta G_{-1}^{\neq}{}_{278K}$ = 22(2) kcal/mol for the reverse **2b** → **2a** reaction. Activation enthalpy $\Delta H_{-1}^{\neq}$ = 2.0(0.8) kcal/mol is small, and the large activation entropy $\Delta S_{-1}^{\neq}$ = –76(1) eu contributes significantly to the kinetic barrier $\Delta G_{-1}^{\neq}{}_{278K}$. Perhaps the dangling phosphine group in **4a**-**b** squeezes other ligands, making it difficult to orient the ligands for α–H migration. Thus activation entropy plays a major role in the **4a** ⇌ **4b** exchange.

2.2.4 Kinetic Study of the Conversion of 4a-b to 7a-b – Comparison of DMPE with PMe_3 and PMe_2Ph

The alkyl alkylidyne and bis-alkylidene tautomers were found to undergo α–H abstraction upon heating the **4a** ⇌ **4b** equilibrium mixture to give **7a**-**b** (Scheme 2.3) and $SiMe_4$. A kinetic study was performed to better understand the conversion.

The conversion of **4a**-**b** containing a dangling phosphine group to bidentate **7a**-**b** is an intramolecular conversion (Scheme 2.3). In comparison, the conversion of **2a**-**b** to **5a**-**b** (and **3a**-**b** → **6a**-**b**) involves the addition of a PMe_3 or PMe_2Ph molecule to **2a**-**b**.[2]

The intramolecular formation of **7a**-**b** follows first-order kinetics. Kinetic plots according to Eq. 2.3 are given in Figures 2.6 and 2.7.[37]

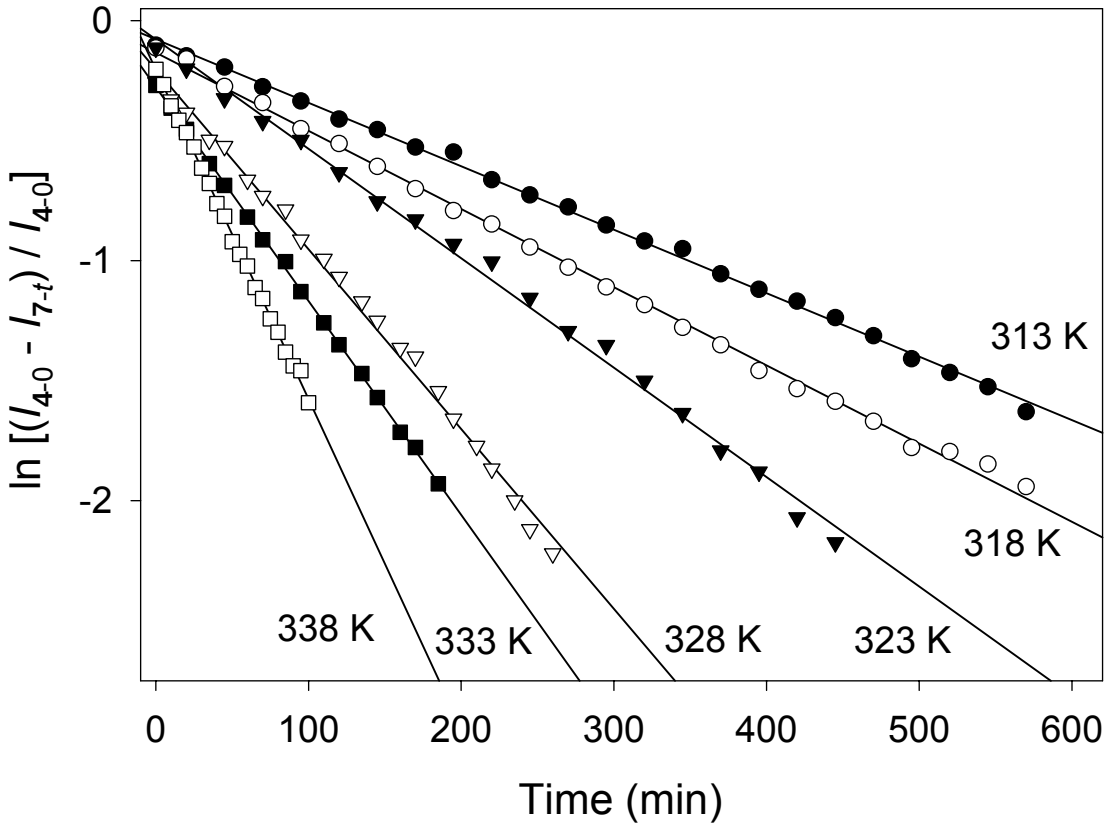

Figure 2.6. Kinetic plots of the formation of **7a-b**.

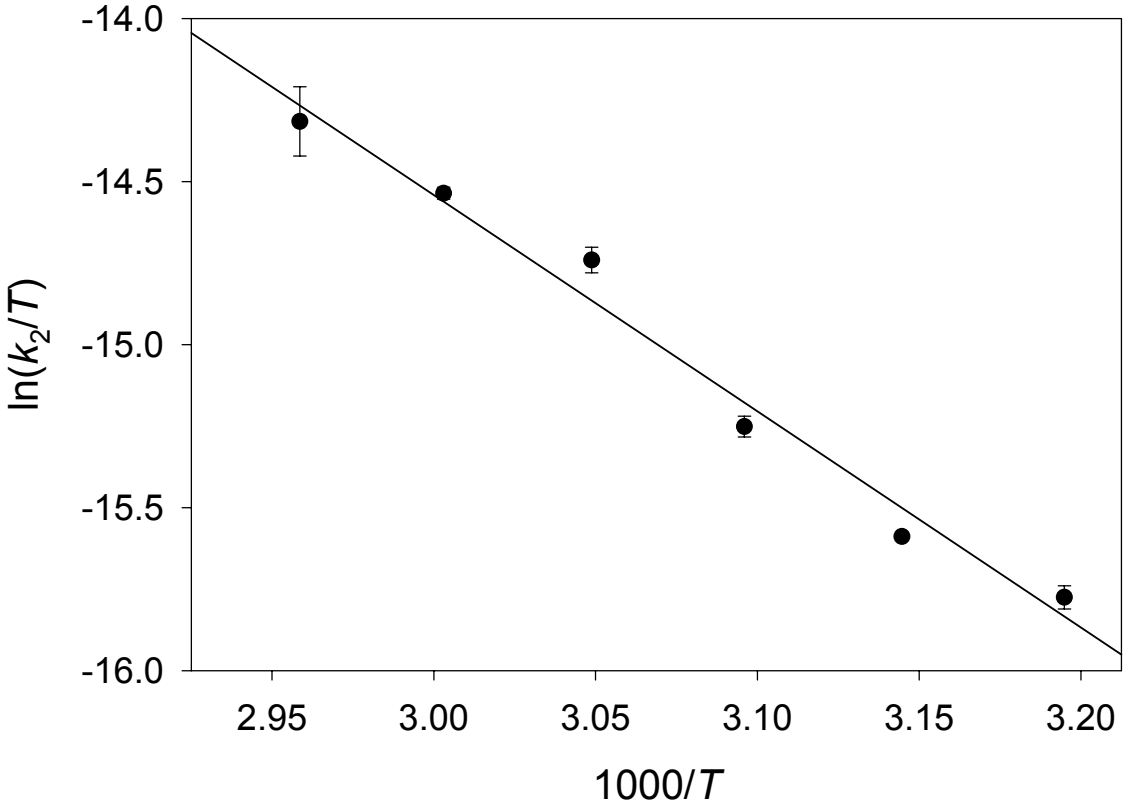

Figure 2.7. Eyring plot of the **4a-b** → **7a-b** conversion.

$$\ln\left[\frac{(I_{4_0} - I_{7_t})}{(I_{4_0})}\right] = -k_2' t \qquad \text{(Eq. 2.3)}$$

The Eyring plot (Figure 2.7) leads to the activation parameters: $\Delta H_2^{\neq}$ = 13(1) kcal/mol, $\Delta S_2^{\neq}$ = –36(4) eu, and $\Delta G_{2\,338K}^{\neq}$ = 25(2) kcal/mol for the **4a-b** → **7a-b** reaction. The relative large negative activation entropy indicates that at the transition state, which involves cyclometalation, the system becomes more ordered. In the **2a-b** → **5a-b** conversion at 333–358 K (Scheme 2.2), the activation parameters $\Delta H^{\neq}$ = 29(2) kcal/mol, $\Delta S^{\neq}$ = 4(1) eu, and $\Delta G_{2\,338K}^{\neq}$ = 28(3) kcal/mol are typical for cyclometalation/α-H abstraction prior to the addition of a second PMe_3 ligand.[38-40] The kinetic barrier $\Delta G_{2\,338K}^{\neq}$ for the DMPE-containing **4a-b** → **7a-b** conversion is lower than that for PMe_3-containing **2a-b** → **5a-b** conversion. Activation entropy $\Delta S_2^{\neq}$ in the former (DMPE) plays a much more significant role in the kinetic barrier than in later (PMe_3). $\Delta H_2^{\neq}$ = 13(1) kcal/mol in the former (DMPE) is significantly lower than $\Delta H^{\neq}$ = 29(2) kcal/mol in the latter (PMe_3), suggesting that steric repulsion by the dangling DMPE ligand drives the α–H abstraction in **4a-b**. The rate constants, k_2, were measured between 313 and 338 K and are listed in Table 2.2. At 338 K, k_2 = 2.1(0.2) × 10^{-4} s^{-1} for the **4a-b** → **7a-b** conversion. In comparison, the rate constant is 8.5(0.6) × 10^{-6} s^{-1} for the **2a-b** to **5a-b** conversion.[2] The conversion of the DMPE complexes **4a-b** is about 25 times faster than the PMe_3 complexes **2a-b**. Our earlier studies of the PMe_2Ph complexes **3a-b** (Scheme 2.2) show that their conversion to

Table 2.2. Rate constants (k_2) for the formation of **7a**-**b**[a]

T (K)[b]	$k_2 \times 10^5$ (s^{-1})[c]
313(1)	4.41(0.17)
318(1)	5.4(0.0)
323(1)	7.7(0.3)
328(1)	13.0(0.5)
333(1)	16.2(0.3)
338(1)	21(2)

[a] Solvent: toluene-d_8.

[b] The relatively small temperature range of 25 K in the current kinetic study leads to relatively large uncertainties in kinetic ($\Delta H^{\neq}$ and $\Delta S^{\neq}$) parameters, as the error calculations in the Experimental Section show.

[c] The largest random uncertainties are $\delta k_{2(\text{ran})}/k_2$ = 2/21 = 9.5%. The total uncertainties $\delta k_2/k_2$ = 0.1076 were calculated from $\delta k_{(\text{ran})}/k$ and the estimated systematic uncertainty $\delta k_{(\text{sys})}/k$ = 5% by $\delta k/k = [(\delta k_{(\text{ran})}/k)^2 + (\delta k_{(\text{sys})}/k)^2]^{1/2}$.

$W(CH_2SiMe_3)(=CHSiMe_3)(\equiv CSiMe_3)(PMe_2Ph)_2$ is about 3.4 times faster than that of PMe_3 complexes **2a-b** at 348.2(0.1) K.[2]

Two possible mechanistic pathways for the intramolecular **4a-b** $\rightarrow$ **7a-b** conversion have been considered. In Path I (Scheme 2.4), **4a-b** undergo rate-determining α–H abstraction to give *Intermediate* **A**, followed by coordination of the dangling PMe_2 group, yielding **7a-b**. In Path II, coordination of the dangling PMe_2 group occurs first to give *Intermediate* **B**. Subsequent α–H abstraction yields **7a-b**. These two pathways are similar to those considered in the formation of bis-PMe_3 **5a-b** from **2a-b**.[2] Kinetic studies of the **2a-b** to **5a-b** conversion reveals that it is independent of the concentration of PMe_3, suggesting that the conversion follows a pathway similar to Path I. In the current intramolecular **4a-b** $\rightarrow$ **7a-b** conversion, kinetics of the first-order reaction does not, however, distinguish between Path I and Path II. It is reasonable to assume that the DMPE complexes **4a-b** follow a similar pathway (Path I) in the formation of **7a-b**, especially considering the fact that the $Me_2PCH_2CH_2PMe_2$ (DMPE) ligand is sterically more demanding than PMe_3. A molecular model of **4b** using SYBYL v. 8.0[41] has been built (Figure 2.8), based on the X-ray crystal structure of **2b**[2] by replacing the PMe_3 ligand in **2b** by a dangling DMPE ligand to see if there is space in **4a-b** for the dangling PMe_2 to bind to the metal atom. A space-filling drawing of the **4b** model reveals that, as in the crystal structure of **2b**, the penta-coordinated DMPE complex **4b** is highly congested with nearly no space for the dangling PMe_2 group to coordinate. Although we are not able to distinguish

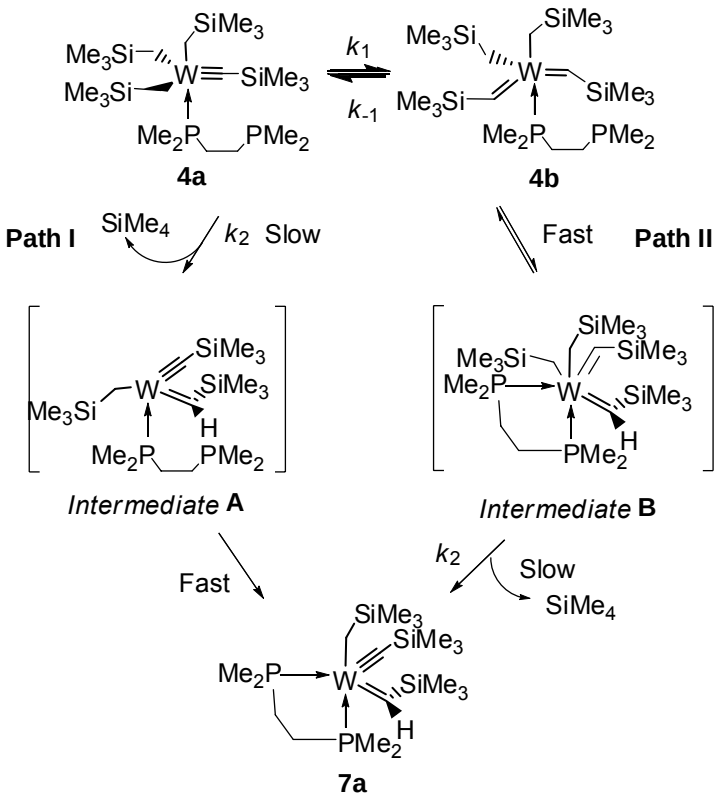

Scheme 2.4. Proposed mechanistic pathways for the formation of **7a**. **7b** is not shown.

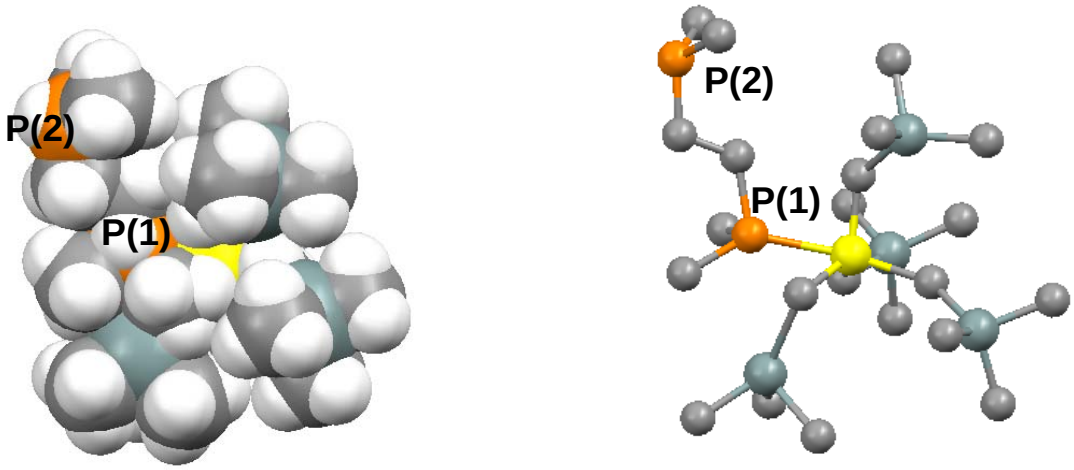

(a) (b)

Figure 2.8. Molecular modeling structure of **4b**: (a) Space-filling mode; (b) A ball and stick display at the *cis* position relative to DMPE. Tungsten atom in **4b** was replaced by a molybdenum atom in the modeling. See Experimental Section for details.

between Path I and Path II in the current work, we think Path I is preferred in the **4a-b** → **7a-b** conversion. As in the **4a** ⇌ **4b** tautomerization, the large, negative activation entropy $\Delta S_2^{\neq}$ = –36(4) eu is a reflection of the presence of the dangling DMPE ligand, making it difficult for other ligands in **4a-b** to orient for α–H abstraction.

2.3. Concluding Remarks

In this chapter, the reaction of $W(CH_2SiMe_3)_3(\equiv CSiMe_3)$ (**1**) with DMPE (DMPE = $Me_2PCH_2CH_2PMe_2$) gives an adduct $W(CH_2SiMe_3)_3(\equiv CSiMe_3)$(DMPE-*P*) (**4a**). **4a** undergoes a rarely observed reversible transformation to its bis-alkylidene tautomer $W(CH_2SiMe_3)_2(=CHSiMe_3)_2$(DMPE-*P*) (**4b**) through α–H migration. The DMPE ligands in both **4a** and **4b** contain a dangling P atom (*P*). Thermodynamic and kinetic studies of the **4a** ⇌ **4b** exchange show that it is slightly endothermic with $\Delta H°$ = 5.1(1.1) kcal/mol and $\Delta S°$ = 24(4) eu; $\Delta H_1^{\neq}$ = 4.0(0.9) kcal/mol, $\Delta S_1^{\neq}$ = –51(2) eu for the **4a** → **4b** forward reaction; $\Delta H_{-1}^{\neq}$ = 2.0(0.8) kcal/mol, $\Delta S_{-1}^{\neq}$ = –76(1) eu for the **4b** → **4a** reverse reaction. Activation entropies are the major contributors to the activation barriers of the exchange: $\Delta G_1^{\neq}{}_{278K}$ = 21.7(1.5) kcal/mol and $\Delta G_{-1}^{\neq}{}_{278K}$ = 23.1(1.1) kcal/mol. The **4a** ⇌ **4b** exchange at 283 K is faster than that of the previously reported PMe_3 analogs $W(CH_2SiMe_3)_3(\equiv CSiMe_3)(PMe_3)$ (**2a**) ⇌ $W(CH_2SiMe_3)_2(=CHSiMe_3)_2(PMe_3)$ (**2b**).[2] The **4a** ⇌ **4b** mixture undergoes an α–H abstraction, yielding alkyl alkylidene alkylidyne complexes $W(CH_2SiMe_3)(=CHSiMe_3)(\equiv CSiMe_3)$(DMPE) (*syn*: **7a**; *anti*:

7b) containing chelating DMPE ligand with the following activation parameters: $\Delta H_2^{\neq}$ = 13(1) kcal/mol and $\Delta S_2^{\neq}$ = –6(4) eu. The formation of **7a-b** is faster than the formation of $W(CH_2SiMe_3)(=CHSiMe_3)(\equiv CSiMe_3)(PR_3)_2$ (PR_3 = PMe_3, **5a-b**; PMe_2Ph, **6a-b**).

2.4. Experimental Section

2.4.1. General Procedures

All manipulations were performed under a dry nitrogen atmosphere with the use of either a dry box or standard Schlenk techniques. Solvents were purified by distillation from potassium/benzophenone ketyl. Benzene-d_6 and toluene-d_8 were dried over activated molecular sieves and stored under nitrogen. WCl_6 was freshly sublimed under vacuum. $W(CH_2SiMe_3)_3(\equiv CSiMe_3)$ (**1**)[42] was prepared from $W(OMe)_3Cl_3$ and 6 equiv of Me_3SiCH_2MgCl.[2] ^1H, ^{13}C, and ^{31}P NMR spectra were recorded on a Bruker AMX-400 spectrometer. DMPE was referenced to an external standard of H_3PO_4 (85% in H_2O) in tolune-d_8 at –20 and –5 °C. Elemental analysis was performed by Complete Analysis Laboratories Inc., Parsippany, NJ.

For the thermodynamic studies, the equilibrium constants K_{eq} were obtained from at least two separate experiments at a given temperature, and their averages are listed in Table 2.1. The maximum random uncertainty in the equilibrium constants were combined with the estimated systematic uncertainty of ca. 5%. The total uncertainties in the equilibrium constants were used in the ln

K_{eq} vs. 1000/T plot in Figure 2.3 and the error propagation calculations. The estimated uncertainty in the temperature measurements for an NMR probe was 1 K. The enthalpy ($\Delta H°$) and entropy ($\Delta S°$) changes were calculated from an unweighted nonlinear least-squares procedure in the SigmaPlot Scientific Graph System. The uncertainties in $\Delta H°$ and $\Delta S°$ were computed from error propagation formulas which were derived from $-RT \ln K_{eq} = \Delta H° - T\Delta S°$, as reported earlier.[31]

For the kinetic studies, the rate constants k_1, k_{-1}, and k_2 were obtained from at least two separate experiments at a given temperature, and their averages are listed. The estimated uncertainty (σT) in the temperature measurements for an NMR probe was 1 K. The enthalpy ($\Delta H^{\neq}$) and entropy ($\Delta S^{\neq}$) were calculated from an unweighted nonlinear least-squares procedure in the SigmaPlot Scientific Graph System. The uncertainties in $\Delta H^{\neq}$ and $\Delta S^{\neq}$ were computed from the error propagation formulas derived by Girolami and coworkers from the Eyring equation.[43] The values of $\sigma k/k$ are given in Tables 2.1 and 2.2.

2.4.2. Preparation of $W(CH_2SiMe_3)_3(\equiv CSiMe_3)(DMPE\text{-}P)$ (4a)

$W(CH_2SiMe_3)_3(\equiv CSiMe_3)$ (**1**, 49.5 mg, 0.093 mmol) and 4,4'-dimethylbiphenyl (an internal standard) were dissolved in toluene-d_8. DMPE (17 μL, 0.10 mmol) was added via a syringe to a J.R. Youngs NMR tube at –78 °C. The NMR probe was pre-cooled at –5 °C. ^{1}H NMR (toluene-d_8, 399.79 MHz, –5 °C) δ 1.36 (broad, 4H, CH_2PMe$_2$), 0.92 (broad, 12H, PMe_2), 0.53 (broad, 6H, *ax*-

CH$_2$SiMe$_3$ and *eq*-*CH*$_2$SiMe$_3$), 0.32 (s, 9H, ≡CSi*Me*$_3$), 0.31 (s, 27H, *ax*-CH$_2$Si*Me*$_3$ and *eq*-CH$_2$Si*Me*$_3$); ^{13}C{^{1}H} (toluene-d_8, 100.54 MHz, –5 °C) δ 355.4 (broad, ≡*C*SiMe$_3$), 80.94 (broad, *ax*-*C*H$_2$SiMe$_3$), 50.53 (broad, *eq*-*C*H$_2$SiMe$_3$), 25.89 (s, *C*H$_2$PMe$_2$), 13.82 (s, P*Me*$_2$), 3.27 (s, *ax*-CH$_2$Si*Me*$_3$ and *eq*-CH$_2$Si*Me*$_3$), 3.20 (s, ≡CSi*Me*$_3$); ^{31}P{^{1}H} (toluene-d_8, 161.84 MHz, –5 °C) δ 1.33 (broad, W-*P*CH$_2$CH$_2$PMe$_2$), –47.17 (broad, W-PCH$_2$CH$_2$*P*Me$_2$).

2.4.3. Preparation of W(CH$_2$SiMe$_3$)$_2$(=CHSiMe$_3$)$_2$(DMPE-*P*) (4b)

W(CH$_2$SiMe$_3$)$_3$(≡CSiMe$_3$) (**1**, 43.8 mg, 0.083 mmol) and 4,4'-dimethylbiphenyl (an internal standard) were dissolved in toluene-d_8. DMPE (~16 μL, 0.094 mmol) was added *via* a syringe to a J.R. Youngs NMR tube. The sample was kept at room temperature for 5 h to ensure the conversion of **4a** to **4b**. NMR probe was the pre-cooled at –20 °C. ^{1}H NMR (toluene-d_8, 399.79 MHz, –20 °C, *J* in Hz) δ 8.01 (d, 1H, =C*H*SiMe$_3$, $^3J_{P\text{-}H}$ = 5.6), 7.23 (d, 1H, =C*H*SiMe$_3$, $^3J_{P\text{-}H}$ = 4.6), 1.64 (broad, 2H, C*H*$_2$PMe$_2$), 1.24 (overlapping free DMPE, 2H, C*H*$_2$PMe$_2$), 1.06 (d, 3H, P*Me*$_2$, $^2J_{P\text{-}H}$ = 6.6), 1.04 (d, 3H, P*Me*$_2$, $^2J_{P\text{-}H}$ = 6.6), 0.94 (dd, 1H, eq-CH$_a$*H*$_b$-SiMe$_3$, $^3J_{P\text{-}H}$ = 33.0, $^2J_{H\text{-}H}$ = 11.0; overlapped with eq-*CH*$_a$H$_b$-SiMe$_3$ peak), 0.93 (dd, 1H, eq-C*H*$_a$H$_b$-SiMe$_3$, $^3J_{P\text{-}H}$ = 33.0, $^2J_{H\text{-}H}$ = 11.8; overlapped with eq-CH$_a$*H*$_b$-SiMe$_3$ peak and P*Me*$_2$), 0.81 (overlapping free DMPE, 6H, P*Me*$_2$), 0.40 (s, 9H, eq-CH$_2$Si*Me*$_3$), 0.37 (s, 9H, *ax*-CH$_2$Si*Me*$_3$), 0.34 (d, 2H, *ax*-C*H*$_2$SiMe$_3$, $^3J_{P\text{-}H}$ = 7.2, overlapped with *ax*-CH$_2$Si*Me*$_3$ peak), 0.30 (s, 9H, =CHSi*Me*$_3$), 0.15 (s, 9H, =CHSi*Me*$_3$); ^{13}C{^{1}H} (toluene-d_8, 100.54 MHz, –20 °C, *J*

in Hz) δ 256.66 (d, =*C*HSiMe$_3$, $^1J_{H\text{-}C}$ = 109.00, $^2J_{P\text{-}C}$ = 12.5), 254.68 (d, =*C*HSiMe$_3$, $^1J_{H\text{-}C}$ = 102.5, $^2J_{P\text{-}C}$ = 12.5), 51.16 (d, *ax*-*C*H$_2$SiMe$_3$, $^1J_{H\text{-}C}$ = 113.3, $^2J_{P\text{-}C}$ = 4.6), 37.78 (d, *eq*-*C*H$_2$SiMe$_3$, $^2J_{P\text{-}C}$ = 30.8, $^1J_{W\text{-}C}$ = 111.0), 28.10 (dd, *C*H$_2$PMe$_2$, $^1J_{H\text{-}C}$ = 124.8, $^1J_{P\text{-}C}$ = 12.3), 25.11 (dd, *C*H$_2$PMe$_2$, $^1J_{H\text{-}C}$ = 123.3, $^1J_{P\text{-}C}$ = 6.2), 14.93 (d, P*Me*$_2$, $^1J_{H\text{-}C}$ = 127.1, $^1J_{P\text{-}C}$ = 23.8), 14.64 (d, P*Me*$_2$, $^1J_{H\text{-}C}$ = 127.1, $^1J_{P\text{-}C}$ = 23.8), 13.49 (d, P*Me*$_2$, $^1J_{H\text{-}C}$ = 129.5, $^1J_{P\text{-}C}$ = 15.4), 4.88 (s, *ax*-CH$_2$Si*Me*$_3$, $^1J_{H\text{-}C}$ = 118.7), 2.99 (s, *eq*-CH$_2$Si*Me*$_3$, $^1J_{H\text{-}C}$ = 117.9), 1.81 (s, =CHSi*Me*$_3$, $^1J_{H\text{-}C}$ = 119.5), 1.77 (s, =CHSi*Me*$_3$, $^1J_{H\text{-}C}$ = 119.5); $^{31}P\{^1H\}$ (toluene-d_8, 161.97 MHz, –20 °C, *J* in Hz) δ 11.10 (d, W-*P*CH$_2$CH$_2$PMe$_2$, $^3J_{P\text{-}P}$ = 20.7), –47.77 (d, W-PCH$_2$CH$_2$*P*Me$_2$, $^3J_{P\text{-}P}$ = 20.7). ^{1}H and ^{13}C NMR assignments were confirmed by low-temperature HSQC and ^{1}H-gated-decoupled ^{13}C NMR experiments.

2.4.4. Preparation of W(CH$_2$SiMe$_3$)(=CHSiMe$_3$)(≡CSiMe$_3$)(Me$_2$PCH$_2$CH$_2$PMe$_2$) (7a-b)

W(CH$_2$SiMe$_3$)$_3$(≡CSiMe$_3$) (**1**, 47.9 mg, 0.09 mmol) was dissolved in benzene-d_6 in a J.R. Young's NMR tube. DMPE (ca. 1.3 equiv, 0.114 mmol) was added *via* a syringe to the room temperature solution. The mixture was kept at room temperature for 24 h, followed by heating at 65 °C for 48 h. All volatiles (SiMe$_4$, unreacted DMPE, and solvent) were removed *in vacuo* at room temperature for 8 h to give a brown solid of **7a**-**b** (21.1 mg, 40% yield). **7a**: ^{1}H NMR (toluene-d_8, 399.97, 23 °C, *J* in Hz) δ 7.95 (dd, 1H, =C*H*SiMe$_3$, $^3J_{P\text{-}H}$ = 6.1, $^3J_{P\text{-}H}$ = 5.3), 1.52 (d, 3H, P*Me*, $^2J_{P\text{-}H}$ = 10.5), 1.43 (m, 1H, C*H*$_2$PMe$_2$), 1.34 (m, 2H,

C*H*$_2$PMe$_2$; overlapping P*Me*), 1.32 (d, 3H, P*Me*, $^2J_{P\text{-}H}$ = 7.6), 1.08 (m, 1H, C*H*$_2$PMe$_2$), 0.88 (d, 3H, P*Me*, $^2J_{P\text{-}H}$ = 7.6), 0.71 (d, 3H, P*Me*, $^2J_{P\text{-}H}$ = 7.3), 0.49 (m, 1H, *ax*-CH$_a$*H*$_b$SiMe$_3$), 0.43 (s, 9H, ≡CSi*Me*$_3$), 0.34 (s, 9H, =CHSi*Me*$_3$), 0.15 (s, 9H, *ax*-CH$_2$Si*Me*$_3$), –0.44 (m, 1H, *ax*-CH$_a$*H*$_b$SiMe$_3$); ^{13}C{^{1}H} (toluene-d_8, 100.54 MHz, 23 °C, *J* in Hz) δ 326.56 (dd, ≡*C*SiMe$_3$, $^2J_{P\text{-}C}$ = 10.7, $^2J_{P\text{-}C}$ = 2.94), 241.14 (dd, =*C*HSiMe$_3$, $^1J_{W\text{-}C}$ = 115.5, $^1J_{H\text{-}C}$ = 97.6, $^2J_{P\text{-}C}$ = 26.5, $^2J_{P\text{-}C}$ = 12.6), 31.76 (dd, *C*H$_2$PMe$_2$, $^1J_{H\text{-}C}$ = 134.5, $^2J_{P\text{-}C}$ = 13.9), 29.05 (dd, *C*H$_2$PMe$_2$, $^1J_{H\text{-}C}$ = 132.5, $^2J_{P\text{-}C}$ = 10.8), 25.26 (dd, P*Me*, $^1J_{H\text{-}C}$ = 135.6, $^1J_{P\text{-}C}$ = 36.7, $^3J_{P\text{-}C}$ = 5.4), 19.72 (*ax*-*C*H$_2$SiMe$_3$), 19.64 (d, P*Me*, $^1J_{H\text{-}C}$ = 123.3, $^1J_{P\text{-}C}$ = 24.7), 18.63 (dd, P*Me*, $^1J_{H\text{-}C}$ = 134.1, $^1J_{P\text{-}C}$ = 17.0, $^2J_{P\text{-}C}$ = 6.2), 12.64 (d, P*Me*, $^1J_{H\text{-}C}$ = 130.2, $^1J_{P\text{-}C}$ = 17.0), 3.91 (s, ≡CSi*Me*$_3$, $^1J_{H\text{-}C}$ = 117.1), 3.36 (s, =CHSi*Me*$_3$, $^1J_{H\text{-}C}$ = 117.1), 2.72 (s, *ax*-CH$_2$Si*Me*$_3$, $^1J_{H\text{-}C}$ = 117.1); ^{31}P{^{1}H} (toluene-d_8, 161.84 MHz, 23 °C, *J* in Hz) δ 40.21 (d, $^2J_{P\text{-}P}$ = 59.3), 23.16 (d, $^2J_{P\text{-}P}$ = 69.1). ^{1}H and ^{13}C NMR assignments were confirmed by room temperature HSQC and ^{1}H-gated-decoupled ^{13}C NMR experiments. **7b**: ^{1}H NMR (toluene-d_8, 399.97, 23 °C, *J* in Hz) δ 11.14 (dd, 1H, =*CH*SiMe$_3$, $^3J_{P\text{-}H}$ = 5.2, $^3J_{P\text{-}H}$ = 4.5), 1.71 (m, C*H*$_2$PMe$_2$), 1.51 (d, 3H, P*Me*, $^2J_{P\text{-}H}$ = 10.5; overlapping with **7a**), 1.32 (d, 3H, P*Me*, $^2J_{P\text{-}H}$ = 7.6; overlapping with **7a**) 1.36 (m, C*H*$_2$PMe$_2$; overlapping with **7a**), 0.96 (d, 3H, P*Me*, $^2J_{P\text{-}H}$ = 6.9), 0.94 (m, C*H*$_2$PMe$_2$, overlapping with **7a**), 0.76 (d, 3H, P*Me*, $^2J_{P\text{-}H}$ = 5.8), 0.17 (s, 9H, –Si*Me*$_3$), 0.16 (s, 9H, -Si*Me*$_3$), 0.11 (m, *ax*-C*H*$_a$H$_b$SiMe$_3$), 0.09 (s, 9H, -Si*Me*$_3$), –0.01 (m, *ax*-CH$_a$*H*$_b$SiMe$_3$, overlapping with **7a**); ^{13}C{^{1}H} (toluene-d_8, 100.54 MHz, 23 °C, *J* in Hz) δ 329.35 (dd, ≡*C*SiMe$_3$, $^2J_{P\text{-}C}$ = 10.4, $^2J_{P\text{-}C}$ = 5.0), 237.46

(dd, =*C*HSiMe$_3$, $^2J_{P\text{-}C}$ = 19.8, $^2J_{P\text{-}C}$ = 12.1), 34.92 (dd, *C*H$_2$PMe$_2$, $^1J_{P\text{-}C}$ = 32.8, $^2J_{P\text{-}C}$ = 17.0), 27.05 (dd, *C*H$_2$PMe$_2$, $^1J_{P\text{-}C}$ = 22.0, $^2J_{P\text{-}C}$ = 10.8), 24.58 (d, P*Me*, $^1J_{P\text{-}C}$ = 5.3), 20.9 (*ax*-*C*H$_2$SiMe$_3$; overlapping with the internal standard and solvent), 19.28 (d, P*Me*, $^1J_{P\text{-}C}$ = 5.2), 18.00 (d, P*Me*, $^1J_{P\text{-}C}$ = 21.5), 12.58 (d, P*Me*, $^1J_{P\text{-}C}$ = 17.0), 4.33 (s, ≡CSi*Me*$_3$, $^1J_{H\text{-}C}$ = 124.1), 2.85 (s, =CHSi*Me*$_3$, $^1J_{H\text{-}C}$ = 115.6), 2.64 (s, *ax*-CH$_2$Si*Me*$_3$, $^1J_{H\text{-}C}$ = 115.6); ^{31}P{^{1}H} (toluene-d_8, 161.84 MHz, 23 °C, *J* in Hz) δ 38.84 (d, $^2J_{P\text{-}P}$ = 59.3), 22.41 (d, $^2J_{P\text{-}P}$ = 59.3). Anal. Calcd: C, 36.48; H, 7.82. Found: C, 36.27; H, 7.85.

2.4.5 Kinetic Study of the Inter-conversion between 4a and 4b

At least two experiments for each temperature were conducted. A mixture of W(CH$_2$SiMe$_3$)$_3$(≡CSiMe$_3$) (**1**), 4,4'-dimethylbiphenyl (an internal standard), and toluene-d_8 in J. R. Youngs NMR tubes in liquid nitrogen were added ca. 3–10 equiv of DMPE through cannula transfer. The samples were kept below –78 °C before insertion into the NMR probe. The NMR probe was pre-cooled to the set temperature. After the NMR tubes were inserted into the probe, the ^{1}H NMR spectra were taken after the temperature was stabilized, and the integrations of **4b**, relative to those of the internal standard, were used as $I_{\mathbf{4b}\text{-}0}$ at t = 0. Once the equilibrium between **4a** and **4b** was reached, the integration of **4b** was used as $I_{\mathbf{4b}\text{-}e}$.

2.4.6 Thermodynamic Study of the Equilibrium between 4a and 4b

Two samples of **4a-b** were prepared with at least 5 equiv of DMPE, and kept at room temperature for 3 h to ensure equilibrium was established. The samples were then placed in a circulation bath at 258.0(1), 263.0(1), 268.0(1), 273.0(1), 278.0(1), or 283.0(1) K for at least 6 h. ^{31}P NMR spectra were taken at −50 °C with a relaxation delay of 10 s. K_{eq} = [**4b**] / [**4a**] = $I_{\mathbf{4b\text{-}e}}$ / $I_{\mathbf{4a\text{-}e}}$ were calculated from the integrations of the two tautomers.

2.4.7 Kinetic Study of the Formation of 7a-b

At least two experiments for each temperature were conducted. A mixture of $W(CH_2SiMe_3)_3(\equiv CSiMe_3)$ (**1**), 4,4'-dimethylbiphenyl (an internal standard), and toluene-d_8 in J. R. Youngs NMR tubes were added ca. 4–8 equiv of DMPE. The sample was then kept at 23 °C for 3 h to establish the **4a** ⇌ **4b** equilibrium. The sample was next placed into the pre-heated NMR spectrometer at the set temperature. After the NMR tubes were inserted into the probe, ^{1}H NMR spectra were taken after the temperature was stabilized, and the integration of **7a** at time t, $I_{\mathbf{7a}\text{-t}}$, relative to those of the internal standard, was recorded. Once the reaction comes to completion, integration of **7a** at the end of the reaction $I_{\mathbf{7a}\text{-f}}$ is used to substitute the integration of **4b** at the start of the reaction $I_{\mathbf{4b}\text{-0}}$.

2.4.8 Molecular Modeling Structure of 4b

Molecular mechanics (MM) calculations were utilized to give molecular modeling structure of **4b**. The initial MM structure was built on the PMe_3 analog $(Me_3SiCH_2)_2W(=CHSiMe_3)_2(PMe_3)$ (**2b**).[2] In the SYBYL v. 8.0 program,[41] the third methyl group in PMe_3 was replaced with $–CH_2CH_2PMe_2$ that was generated by the program. Bond constraint was implemented on the W-P bond, and the bond length was assigned 2.515 Å, similar to the value in **2b**.[2] A Tripos force field constant of 60,000 kcal•mol^{-1}•Å^{-2} was applied to constraint the bond length. For the W-C bonds, a Tripos force field constant of 40,000 kcal•mol^{-1}•Å^{-2} was applied to constrain the bond lengths to the reported alkyl and bis-alkylidene W-C bond values in **2b**.[2] Because the SYBYL program does not recognize tungsten, tungsten atom was substituted with molybdenum atom, which has similar metal radius (Mo: 1.36 Å; W: 1.37 Å) and bond lengths. The energy minimization was achieved using the Powell method.[41]

CHAPTER 3

Thermodynamic Studies of the Reactions of $W(CH_2SiMe_3)_3(\equiv CSiMe_3)$ and Mono-dentate Phosphines

3.1. Introduction

Complexes containing a trimethylsilylmethyl ligand ($-CH_2SiMe_3$) with a β–Si atom often show properties different from those containing its analog neopentyl ligand ($-CH_2CMe_3$). For example, reactions of $W(CH_2CMe_3)_3(\equiv CCMe_3)$ with phosphines PMe_3 and $Me_2PCH_2CH_2PMe_2$ (DMPE) give, through α–H abstraction, bis-phosphine/chelating phosphine products $W(CH_2CMe_3)(=CHCMe_3)(\equiv CCMe_3)(PMe_3)_2$ and $W(CH_2CMe_3)(=CHCMe_3)(\equiv CCMe_3)(DMPE)$.[24,25] $W(CH_2SiMe_3)_3(\equiv CSiMe_3)$ (**1**) reacts with PMe_3, PMe_2Ph and DMPE, forming phosphine adducts $W(CH_2SiMe_3)_3(\equiv CSiMe_3)(PR_3)$ (PR_3 = PMe_3, **2a**; PMe_2Ph, **3a**) (Scheme 3.1) and $W(CH_2SiMe_3)_3(\equiv CSiMe_3)$(DMPE-*P*) (**4a**) (Scheme 3.2) containing one free PMe_2 group.[2,32] These adducts undergo α–H migration to form their bis-alkylidene tautomers $W(CH_2SiMe_3)_2(=CHSiMe_3)_2(PR_3)$ (**2b, 3b**) and $W(CH_2SiMe_3)_2(=CHSiMe_3)_2$(DMPE-*P*) (**4b**). The tautomeric mixtures are in equilibria, and the mixtures undergo α–H abstraction to eliminate $SiMe_4$ and to form, by reacting with free PR_3 and the free PMe_2 group in DMPE-*P* ligand, $W(CH_2SiMe_3)(=CHSiMe_3)(\equiv CSiMe_3)(PR_3)_2$ (**5a**-**b, 6a**-**b**) (Scheme 3.1) and

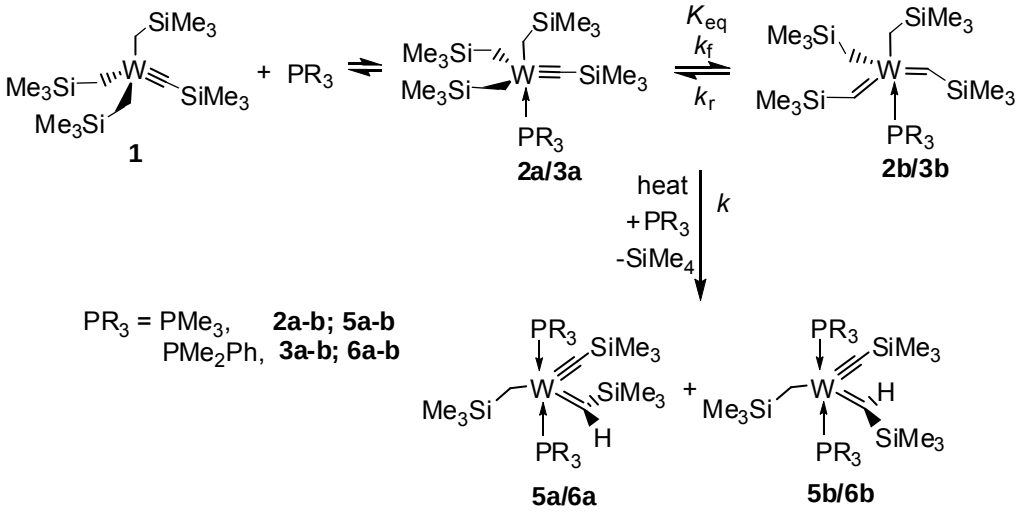

Scheme 3.1. Reaction of mono-dentate phosphines with an alkyl alkylidyne complex.

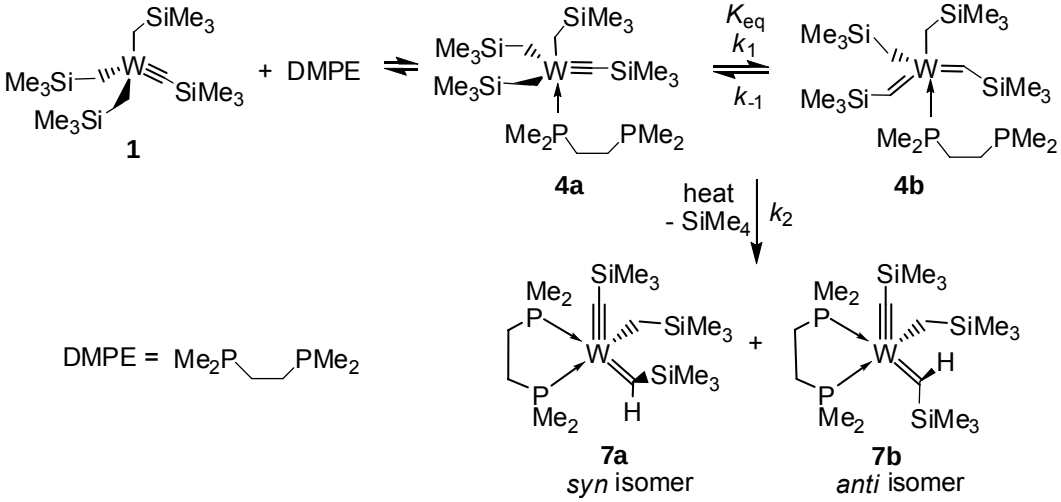

Scheme 3.2. Reaction of a bidentate phosphine with an alkyl alkylidyne complex.

$W(CH_2SiMe_3)(=CHSiMe_3)(\equiv CSiMe_3)(DMPE)$ (**7a**-**b**) (Scheme 3.2) respectively.[30,31,44,45] Another example of the reactivity difference between $-CH_2SiMe_3$ and $-CH_2CMe_3$ ligands is the reactions shown in Scheme 3.3.[1c,e,39,46] $Ta(=CHR)_2(CH_2SiMe_3)(PMe_3)_2$ (R = $SiMe_3$, CMe_3) reacts with silanes to give metallocyclic products. Its neopentyl analog $Ta(=CHCMe_3)_2(CH_2CMe_3)(PMe_3)_2$, in comparison, forms unknown species with the silanes. The reversible addition of PMe_3 and PMe_2Ph to **1** forming **2a** and **3a**, respectively, is studied here in order to understand the unusual chemistry of **1** in detail.

3.2. Results and Discussion

3.2.1 Thermodynamic Study of the Addition of PMe_3 to 1

Alkyl alkylidyne $W(CH_2SiMe_3)_3(\equiv CSiMe_3)$ (**1**) was treated with a various amount of PMe_3 (0.7–1.8 equiv) to probe the addition of phosphine and the equilibrium (Scheme 3.4). The addition was fast and essentially completed by the time NMR spectra were recorded. After the addition, the solution in toluene-d_8 was kept at room temperature for 48 h, however, to ensure that equilibrium was established.

Variable-temperature NMR spectra of the mixture were studied, and the equilibrium constants, K_{eq} = [**2b**]/([**1**] [PMe_3]), measured with a variable amount of PMe_3 between 273 and 303 K are listed in Table 3.1. The peaks of **2a** were very small and ignored in the calculations of K_{eq}. In the **2a** ⇌ **2b** tautomerization, **2b** dominates by a ratio of ca. 9.4–12.3.[2,32] A plot of ln K_{eq} vs 1000/T (Figure 3.1)

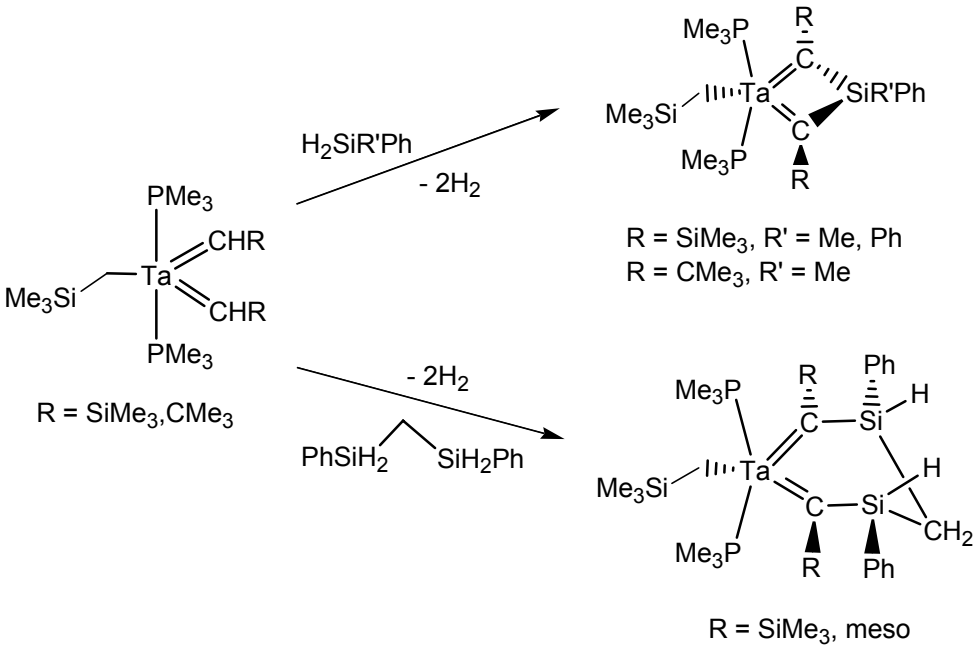

Scheme 3.3. Reactions of $PhR'SiH_2$ (R' = Me, Ph, CH_2SiH_2Ph) with a phosphine alkylidene complex.

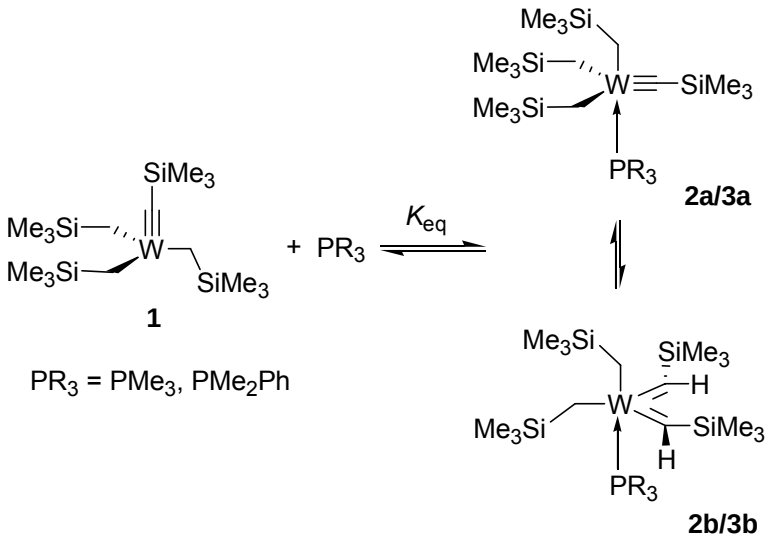

Scheme 3.4. Equilibrium of **1** + PR_3 (PR_3 = PMe_3, PMe_2Ph) ⇌ **2a**/**3a** and **2b**/**3b**.

Table 3.1. Equilibrium (K_{eq}) of the **1** + PMe_3 ⇌ **2a**-**b** exchange

T (K)[b]	K_{eq}[c]
273(1)	$10.8(0.4) \times 10^2$
278(1)	$7.1(0.8) \times 10^2$
283(1)	$5.3(0.3) \times 10^2$
288(1)	$3.6\ (0.3) \times 10^2$
293(1)	$2.83(0.08) \times 10^2$
298(1)	$2.23(0.03) \times 10^2$
303(1)	$1.66(0.07) \times 10^2$

[a] Solvent: toluene-d_8.

[b] The relatively small temperature range of 30 K in the current thermodynamic and kinetic studies leads to relatively large uncertainties in thermodynamic ($\Delta H°$ and $\Delta S°$) as the error calculations in the Experimental Section show.

[c] The largest random uncertainty is $\sigma K_{eq(ran)}/K_{eq}$ = 0.84/7.1 = 12%. The total uncertainty $\sigma K_{eq}/K_{eq}$ of 13% was calculated from $\sigma K_{eq(ran)}/K_{eq}$ = 12% and the estimated systematic uncertainty $\sigma K_{eq(sys)}/K_{eq}$ = 5% by $\sigma K_{eq}/K_{eq} = [(\sigma K_{eq(ran)}/K_{eq})^2 + (\sigma K_{eq(sys)}/K_{eq})^2]^{1/2}$.

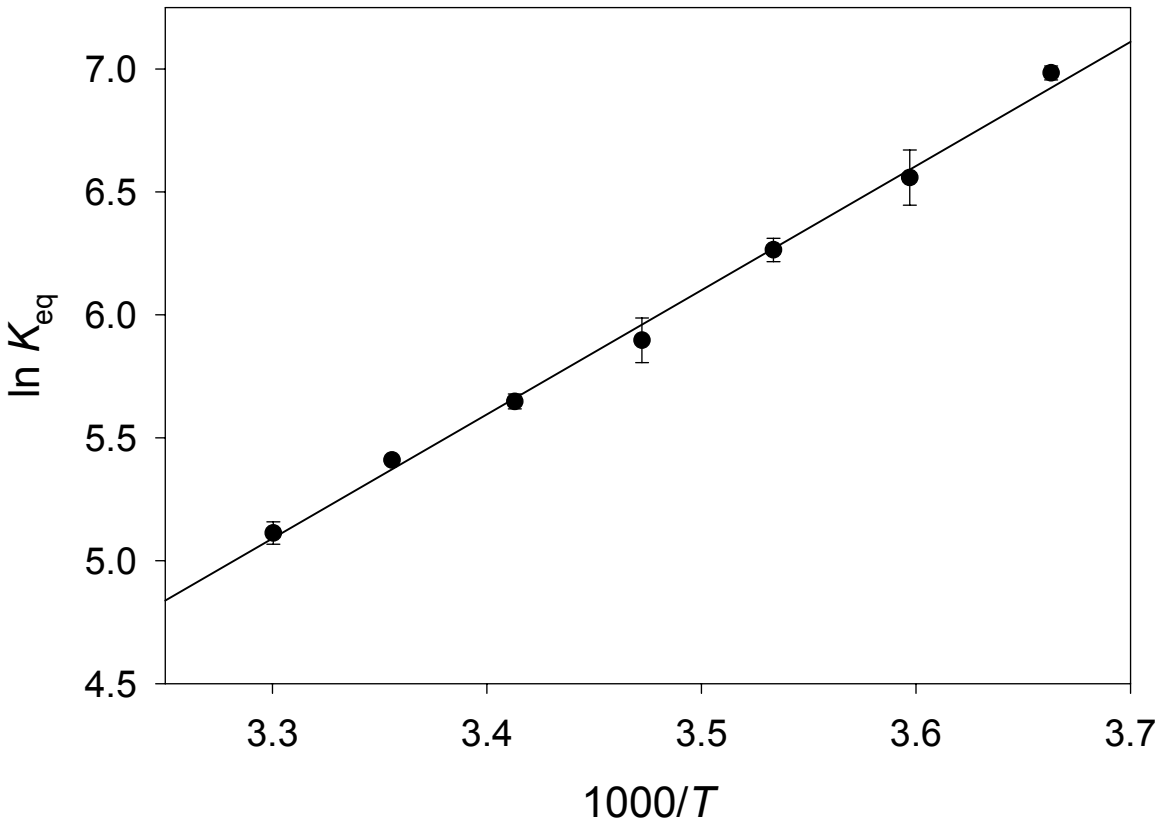

Figure 3.1. A plot of ln K_{eq} vs 1000/T of the equilibrium **1** + PMe_3 ⇌ **2a**-**b**.

gave ΔH° = –10.0(1.1) kcal/mol and ΔS° = –23(4) eu, indicating that the addition is exothermic. The large, negative entropy of the reaction is not surprising, as in the addition, two molecules give one adduct molecule. The equilibrium constants (K_{eq}) range from 10.8×10^2 at 273 K to 1.7×10^2 at 303 K, indicating that the **2a** ⇌ **2b** tautomer are strongly favored. Hence, PMe_3 strongly binds to **1** and disfavors dissociation. At higher temperatures, the equilibrium shifts towards **1** + PMe_3.

3.2.2. Thermodynamic Study of the Addition of PMe_2Ph to 1

PMe_2Ph was utilized for comparison with PMe_3 and DMPE. $W(CH_2SiMe_3)_3(\equiv CSiMe_3)$ (**1**) in toluene-d_8 was added a various amount of ca. 1.0–1.5 equiv of PMe_2Ph *via* syringe. The addition is much slower than that involving PMe_3, and takes about 2-3 days at room temperature to reach the equilibrium. The samples were kept at room temperature for 5 days to ensure that equilibrium was established.

Variable-temperature NMR spectra of the exchange of **1** and PMe_2Ph with **3a**-**b** were studied, and the equilibrium constants, K_{eq} = [**3b**]/([**1**][PMe_2Ph]), measured between 263 and 303 K with a variable amount of PMe_2Ph are listed in Table 3.2. A plot of ln K_{eq} vs 1000/T (Figure 3.2) gave ΔH° = –3.0 (0.7) kcal/mol and ΔS° = –6(3) eu. The equilibrium constants (K_{eq}) range from 16 at 263 K to 8 at 303 K. The much smaller equilibrium constants, in comparison to those of addition of PMe_3 to **1** (Table 3.1), suggest that, although the **3a** ⇌ **3b**

Table 3.2. Equilibrium (K_{eq}) of the **1** + PMe_2Ph ⇌ **3a**-**b** exchange[a]

T (K)[b]	K_{eq}[c]
263(1)	16.4(1.5)
273(1)	12.0(1.7)
283(1)	10.3(0.4)
293(1)	8.8(0.6)
303(1)	7.5(0.5)

[a] Solvent: toluene-d_8.

[b] The relatively small temperature range of 40 K in the current thermodynamic and kinetic studies leads to relatively large uncertainties in thermodynamic ($\Delta H°$ and $\Delta S°$) as the error calculations in the Experimental Section show.

[c] The largest random uncertainty is $\sigma K_{eq(ran)}/K_{eq}$ = 1.7/12 = 14%. The total uncertainty $\sigma K_{eq}/K_{eq}$ of 15% was calculated from $\sigma K_{eq(ran)}/K_{eq}$ = 14% and the estimated systematic uncertainty $\sigma K_{eq(sys)}/K_{eq}$ = 5% by $\sigma K_{eq}/K_{eq} = [(\sigma K_{eq(ran)}/K_{eq})^2 + (\sigma K_{eq(sys)}/K_{eq})^2]^{1/2}$.

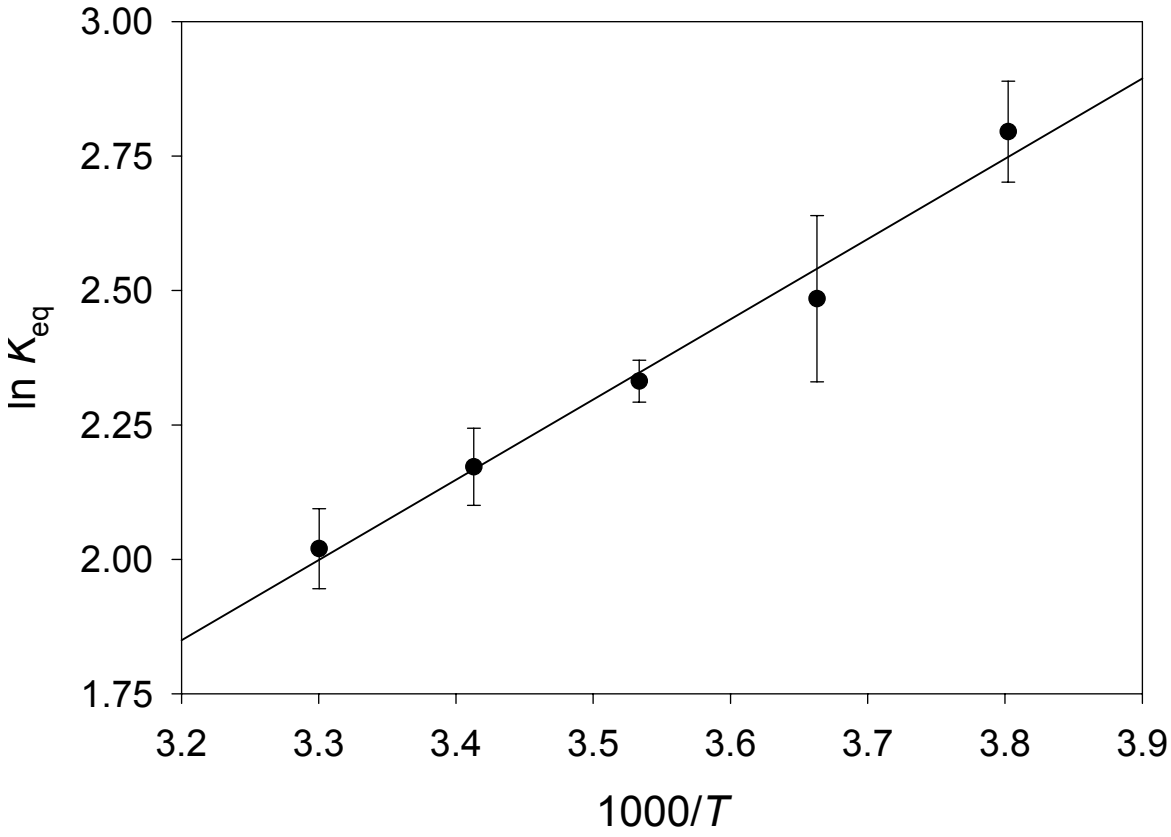

Figure 3.2. A plot of ln K_{eq} vs 1000/T of the equilibrium **1** + PMe_2Ph ⇌ **3a**-**b**.

tautomer and the bis-alkylidene (**3b**) are favored, the binding of PMe_2Ph to **1** is not as strong/favored as the binding of PMe_3. This is also reflected in smaller $\Delta H°$ and thus the release of much less energy in the addition of PMe_2Ph to **1**. Activation entropy is also less negative. Although electronic effect of phenyl group in PMe_2Ph may play a role, sterics involving more bulky phenyl group vs. Me in PMe_3 may be a major factor, especially considering the fact that $W(CH_2SiMe_3)_3(\equiv CSiMe_3)$ (**1**) is very crowded. In other words, the bulkier PMe_2Ph ligand has a lower binding affinity than PMe_3. With decreasing temperature, the equilibrium shifts towards **1**. The **1** + PMe_2Ph $\rightleftharpoons$ **3a**-**b** equilibrium [K_{eq} = 16.4(1.5) at 273 K] is shifted more to the left (**1 +** PMe_2Ph) than the **1 +** PMe_3 $\rightleftharpoons$ **2a**-**b** equilibrium [K_{eq} = 10.8(0.4) $\times$ 10^2 at 273 K].

3.3. Concluding Remarks

Addition of two mono-dentate phosphines (PR_3 = PMe_3 and PMe_2Ph) to $W(CH_2SiMe_3)_3(\equiv CSiMe_3)$ (**1**), forming $W(CH_2SiMe_3)_3(\equiv CSiMe_3)(PR_3)$ (**2a**, **3a**) and their bis-alkylidene tautomers $W(CH_2SiMe_3)_2(=CHSiMe_3)_2(PR_3)$ (**2b**, **3b**), has been found to be reversible. The reaction of excess $W(CH_2SiMe_3)_3(\equiv CSiMe_3)$ (**1**) and $Me_2PCH_2CH_2PMe_2$ (DMPE) appears to be more complicated than those of **1** with the mono-dentate phosphines, and is not pursued in the current work.

3.4. Experimental Section

All manipulations were preformed under a dry nitrogen atmosphere with the use of either a dry box or standard Schlenk techniques. Solvents were purified by distillation from potassium/benzophenone ketyl. Toluene-d_8 was dried over activated molecular sieves and stored under N_2. WCl_6 was freshly sublimed under vacuum. $W(CH_2SiMe_3)_3(\equiv CSiMe_3)$ (**1**)[42] was prepared from $(MeO)_3WCl_3$ and six equiv of Me_3SiCH_2MgCl by a procedure similar to that used in the preparation of $W(CH_2CMe_3)_3(\equiv CCMe_3)$.[6a] ^1H NMR spectra were recorded on a Bruker AMX-400 spectrometer.

For the thermodynamic studies, the equilibrium constants K_{eq} were obtained from at least three separate experiments at a given temperature, and their averages are listed in Tables 3.1 and 3.2. The maximum random uncertainty in the equilibrium constants were combined with the estimated systematic uncertainty of ca. 5%. The total uncertainties in the equilibrium constants were used in the ln K_{eq} vs. 1000/T plot in Figures 3.1 and 3.2 and the error propagation calculations. The estimated uncertainty in the temperature measurements for an NMR probe was 1 K. The enthalpy ($\Delta H°$) and entropy ($\Delta S°$) changes were calculated from an unweighted nonlinear least-squares procedure contained in the SigmaPlot Scientific Graph System. The uncertainties in $\Delta H°$ and $\Delta S°$ were computed from the following error propagation formulas which were derived from $-RT \ln K_{eq} = \Delta H° - T\Delta S°$.

$$(\sigma\Delta H^{\circ})^2 = \frac{R^2\left(T_{max}^2 T_{min}^4 + T_{min}^2 T_{max}^4\right)}{(T_{max} - T_{min})^4}\left[\ln\left(\frac{K_{eq(max)}}{K_{eq(min)}}\right)\right]^2\left(\frac{\sigma T}{T}\right)^2 + \frac{2R^2 T_{max}^2 T_{min}^2}{(T_{max} - T_{min})^2}\left(\frac{\sigma K_{eq}}{K_{eq}}\right)^2 \quad \text{(Eq. 3.1)}$$

$$(\sigma\Delta S^{\circ})^2 = \frac{2R^2 T_{min}^2 T_{max}^2}{(T_{max} - T_{min})^4}\left[\ln\left(\frac{K_{eq(max)}}{K_{eq(min)}}\right)\right]^2\left(\frac{\sigma T}{T}\right)^2 + \frac{R^2(T_{max}^2 + T_{min}^2)}{(T_{max} - T_{min})^2}\left(\frac{\sigma K_{eq}}{K_{eq}}\right)^2 \quad \text{(Eq. 3.2)}$$

T_{min} and T_{max} are the minimum and maximum temperatures in the current studies; T is the mean temperature in the current studies. $K_{eq(min)}$ and $K_{eq(max)}$ are the minimum and maximum equilibrium constants, respectively. $\sigma K_{eq}/K_{eq}$ is given in Tables 3.1 and 3.2.

3.4.1. Thermodynamic Study of the Equilibrium among $W(CH_2SiMe_3)_3(\equiv CSiMe_3)$ (1), PMe_3 and the 2a ⇌ 2b Tautomeric Mixture

At least five experiments were conducted. A mixture of $W(CH_2SiMe_3)_3(\equiv CSiMe_3)$ (**1**, 20.7 mg, 0.04 mmol), 4,4'-dimethylphenyl (an internal standard), and ca. toluene-d_8 (0.65 mL) in J. R. Youngs NMR tubes were added a ca. 0.7–1.8 equiv PMe_3 *via* syringe. The samples were kept at room temperature for 48 h to ensure that equilibrium was established. The NMR probe was pre-cooled or pre-heated to the set temperature. After the NMR tubes were inserted into the probe, the ^{1}H NMR spectra were taken after the temperature was stabilized. K_{eq} = [**1**][PMe_3] / [**2b**] were calculated from the integration of the **1**, PMe_3, and **2b**.

3.4.2. Thermodynamic Study of the Equilibrium among $W(CH_2SiMe_3)_3(\equiv CSiMe_3)$ (1), PMe_2Ph and the 3a ⇌ 3b Tautomeric Mixture

At least three experiments were conducted. A mixture of $W(CH_2SiMe_3)_3(\equiv CSiMe_3)$ (**1**, 29.1 mg, 0.06 mmol), 4,4'-dimethylphenyl (an internal standard), and ca. toluene-d_8 (0.53 mL) in J. R. Youngs NMR tubes were added a ca. 1.0–1.5 equiv PMe_2Ph *via* syringe. The samples were kept at room temperature for 5 days to ensure that equilibrium was established. The NMR probe was pre-cooled or pre-heated to the set temperature. After the NMR tubes were inserted into the probe, the ^1H NMR spectra was taken after the temperature was stabilized. In 30 min after the sample was placed at the set temperature, no change in the NMR spectrum was observed. The samples were, however, kept for 2 h at each temperature, during which NMR spectra were taken every 30 min to ensure no further change was observed. K_{eq} = [**1**][PMe_2Ph] / [**3b**] were calculated from the integration of **1**, PMe_2Ph, and **3b**.

CHAPTER 4

Reaction of a Tungsten Alkylidyne Complex with Water. Formation, Characterization and Crystal Structures of Two Oxo Trimers

4.1. Introduction

Many early transition metal complexes are moisture-sensitive, and reactions of metal complexes with water have been used to make metal oxides in, e.g. microelectronic industry.[47-49] These reactions have attracted much attention. Schrock, Lippard and coworkers reported the formation of $W_2O_3(CH_2CMe_3)_6$,[50-51] and $(NEt_4)[WO_3(CH_2CMe_3)]$[50-51] from the reactions of H_2O with $W(CH_2CMe_3)_3(\equiv CCMe_3)$ and $W(\equiv CCMe_3)(OCMe_3)_3$, respectively (Scheme 4.1). In the former reaction, an alkylidene intermediate, $(Me_3CCH_2)_3W(=CDCMe_3)(OD)$, was proposed, and the reaction yields $W_2O_2(\mu\text{-}O)(CH_2CMe_3)_4(CD_2CMe_3)_2$ containing three alkyl ligands per W atom. Osborn and coworkers prepared $[\{Mo(=NCMe_3)(CH_2CMe_3)_3\}_2(MoO_4)]$ from $(Me_3CCH_2)_2Mo(=CHCMe_3)(=NCMe_3)$ and H_2O.[52] CMe_4 was a product in these reactions. Legzdins and coworkers found that the reactions of a H_2O–O_2 mixture with d^4 $Cp^*M(NO)(CH_2SiMe_3)_2$ (M = Mo, W) yielded $Cp^*M(=O)_2(CH_2SiMe_3)$.[53]

We have studied the reaction of water with $W(CH_2CMe_3)_3(\equiv CSiMe_3)$ (**8**), an analog of $W(CH_2CMe_3)_3(\equiv CCMe_3)$, and found the reaction yields $W_3O_3(\mu{=}O)_3(CH_2CMe_3)_6$ as either a THF (**9**) or D_2O adduct (**10**) (Scheme 4.2)

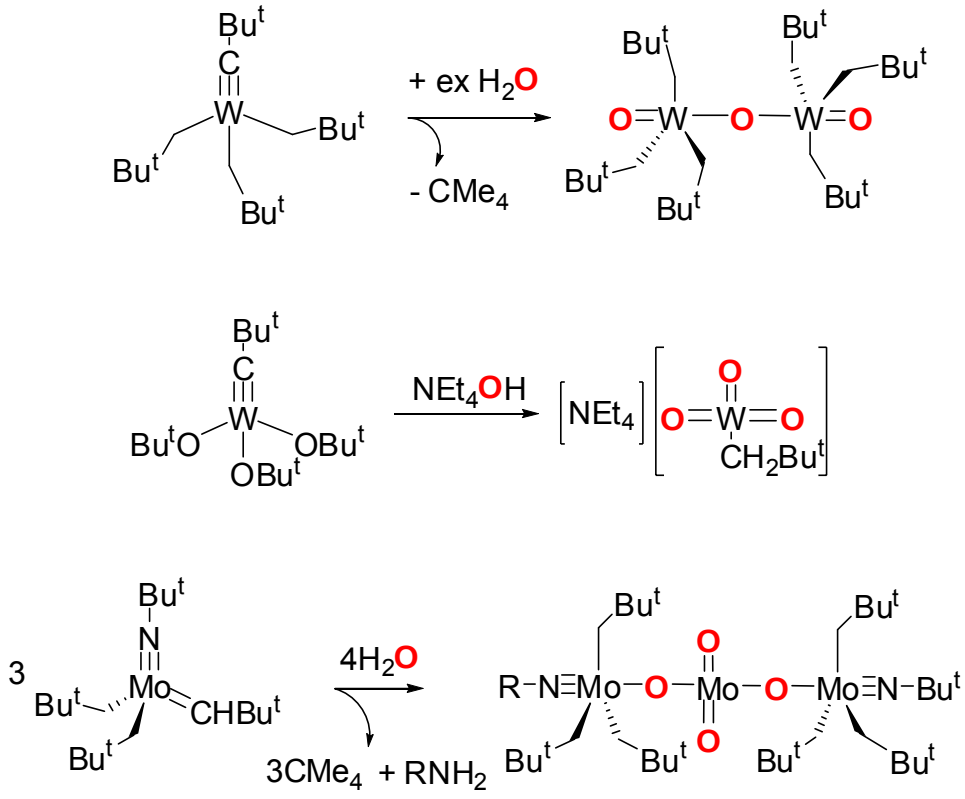

Scheme 4.1. Reaction of Group 6 complexes with H_2O.

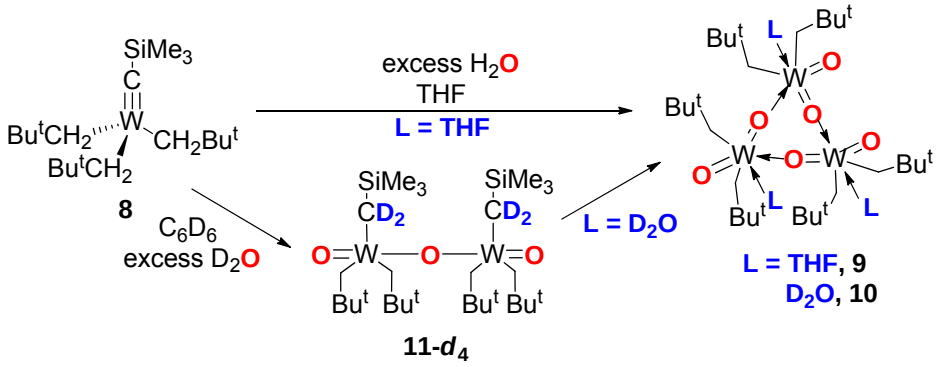

Scheme 4.2. Reaction of $W(CH_2CMe_3)_3(\equiv CSiMe_3)$ (**8**) with H_2O.

containing two neopentyl ligands per W atom in the trimer. X-ray crystal structures of both **9** and **10** have been determined. An intermediate $W_2O_2(\mu$-$O)(CD_2SiMe_3)_2(CH_2Me_3)_4$ (**11-*d*$_4$**), containing one $–CD_2SiMe_3$ and two neopentyl ligands, was observed in the reaction of **8** with D_2O in THF. **11-*d*$_4$** reacts with D_2O to eliminate the $–CD_2SiMe_3$ ligand in **11-*d*$_4$** selectively (as CD_3SiMe_3). Kinetic studies of the reactions of **8** with excess H_2O and D_2O have been studied. Our work is reported here.

4.2. Results and Discussion

4.2.1. Synthesis and Characterization of $W_3O_3(\mu$=O)$_3(CH_2CMe_3)_6(THF)_3$ (9)

When excess H_2O was added to $W(CH_2CMe_3)_3(\equiv CSiMe_3)$ (**8**) in THF at 23 °C, an immediate reaction was observed. When the reaction was monitored by NMR, the starting material **8** disappeared in ca. 3 h. The mixture was kept then at 4–5 °C overnight to ensure the completion of the reaction. Upon the removal of the THF/H_2O solution, the crystals are re-dissolved in THF (~0.5 mL). The solution is cooled to 4–5 °C for 24 h to give crystals of $W_3O_3(\mu$=O)$_3(CH_2CMe_3)_6(THF)_3$ (**9**). We found that the best yield of the yellow hexagonal crystals of **9** was obtained by using a 1:2 mixture of water and THF. A representation of the molecular structure, crystallographic refinement data, and selected bond distances and angles of **9** are given in Figure 4.1 and Tables 4.1 and 4.2, respectively. The terminal O=W bond length is 1.709(4) Å which is similar to the reported O=W bond length of 1.726(10) Å in $W_2O_3(CH_2CMe_3)_6$.[50-51]

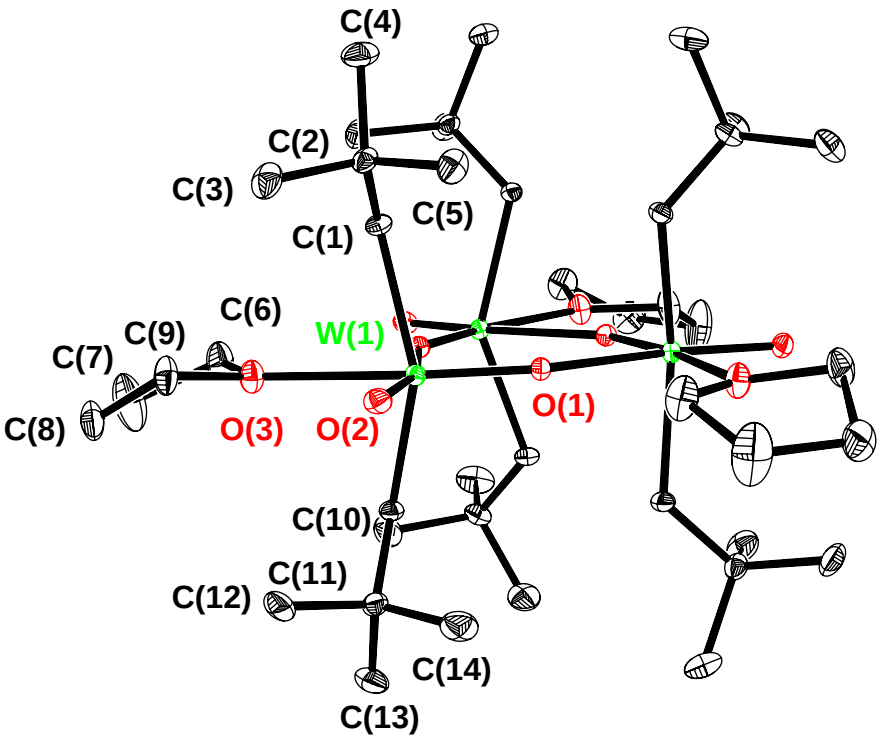

Figure 4.1. ORTEP side-view of **9** showing probability at 30% level. Hydrogen atoms removed for clarity.

Table 4.1. Crystal data and structure refinement for **9** and **10**

Compound No.	**9**	**10**
Empirical formula	$C_{19}H_{80}O_8W_{2.67}$	$C_{36}H_{72}O_9W_3$
Formula weight	1147.28	1200.49
Temperature (K)	163(2)	163(2)
Crystal system	Cubic	Triclinic
Space group	*I*-43d	*P*-1
Unit cell dimensions	*a* = 26.980(3) Å	*a* = 12.044(7) Å
		b = 14.567(8) Å
		c = 14.887(8) Å
		α = 119.207(6)°
		β = 101.221(7)°
		γ = 92.006 (7)°
Volume ($Å^3$)	19639(4)	2210(2)
Z	18	2
Density (calculated) (Mg/m^3)	1.746	1.804
Absorption coefficient (mm^{-1})	7.058	7.832
F(000)	10176	1164
θ range for data collection	1.85 to 28.54°	1.61 to 26.84°

Table 4.1. (continued)

Compound No.	**9**	**10**
Index ranges	$-33 \leq h \leq 33$	$-15 \leq h \leq 15$
	$-35 \leq k \leq 35$	$-18 \leq k \leq 18$
	$-35 \leq l \leq 35$	$-18 \leq l \leq 18$
Reflections collected	97571	20704
Independent reflections	3976 [R_{int} = 0.0619]	9161 [R_{int} = 0.0497]
Completeness to θ = 26.00°	100%	98.7%
Refinement method	Full-matrix least-squares on F^2	Full-matrix least-squares on F^2
Data / restraints / parameters	3976 / 0 / 170	9161 / 0 / 451
Goodness-of-fit on F^2	1.011	1.051
Final R indices [$I > 2\sigma(I)$]	$R1$ = 0.0267, w$R2$ = 0.0653	$R1$ = 0.0568, w$R2$ = 0.1496
R indices (all data)	$R1$ = 0.0301, w$R2$ = 0.0670	$R1$ = 0.0833, w$R2$ = 0.1648
Largest diff. peak and hole (Å^{-3})	3.168, –0.462	5.275, –2.149

[a] $R1 = \Sigma||F_o| - |F_c|| / \Sigma|F_o|$; $wR2 = [\Sigma\, w(F_o^2 - F_c^2)^2 / \Sigma\, w(F_o^2)^2]^{1/2}$;

$w = 1/[\sigma^2(F_o) + (aP)^2 + bP]$; $P = [2F_c^2 + \mathrm{Max}(F_o^2, 0)]/3$

Table 4.2. Bond lengths (Å) and angle (°) comparison between **9**, **10** and $W_2O_3(CH_2CMe_3)_6$.[50-51]

Compound No./Name	$W_2O_3(CH_2CMe_3)_6$	**9**	**10**
	Lengths (Å)		
$W=O_T$	1.708*	1.709(4)	1.723*
$W=O_B$	1.950*	1.773(4)	1.773*
$W\leftarrow O_B$	1.950*	2.214(4)	2.214*
W-C	2.134*	2.186*	2.192*
	Angles (°)		
$W\text{-}O_B\text{-}W$	NA	149.7(2)	151.73*
C-W-C	119.73*	145.9(2)	141.9*
O_T=W-C	92.7	98.6(2)	101.2*

* average

[a] O_T = terminal oxygen

[b] O_B = bridging oxygen

The bridging oxo ligand forms a W=O bond and then uses its lone pair electrons to form a dative bond with anther W atom. The W=O and W←O bond lengths are 1.773(4) and 2.214(4) Å, respectively. The W-C bond lengths are 2.182(5) Å for W(1)-C(1) and 2.189(5) Å for W(1)-C(10). The W-THF [W(1)←O(3)] bond length is 2.413(4) Å, longer than the W←O bond length for the bridging oxo ligand. The neopentyl ligands are in the axial position with an C-W-C angle of 145.9(2)°. The W(μ-O) bond angle of O(1)-W(1)-O(1)#1 is 90.2(2)°. The oxo ligand is found almost perpendicular to the dative bond to THF with a bond angle of 86.45(18)°. A brief comparison of structural features among $W_2O_3(CH_2CMe_3)_6$, **9**, and **10** are given Table 4.2.

^1H, ^{13}C, and variable-temperature (VT) ^1H NMR spectra were taken of **9**. The ^1H NMR spectrum showed a strong singlet at 1.30 ppm and a broad doublet at 3.21 ppm (Figure A12). Thus the two α–H atoms in the neopentyl ligand are diastereotopic (–CH_aH_bCMe_3). However, only one doublet (H_a) is observed at room temperature, and the second doublet overlaps with the –CMe_3 resonance. VT ^1H NMR experiments were conducted to identify second doublet (Figure A13). ^1H NMR spectra were collected at 10 K intervals from 218 to 298 K. At 298 K, only a broad doublet peak (H_a) was observed for one out of the two diastereotopic α–H atoms in the –CH_2CMe_3 ligand. At 278 K, the broad peak became a well-defined doublet ($^2J_{H\text{-}H}$ = 14.5 Hz). As temperature was lowered to 238 K, H_b was observed at 1.45 ppm ($^2J_{H\text{-}H}$ = 14.5 Hz). By 228 K and below, two well-defined doublets at 1.46 and 3.27 ppm were observed in the ^1H NMR

spectrum. The ^{13}C NMR spectrum of **9** was in agreement with its structure (Figure A14). At 33.20 ppm, a singlet was observed for the methyl groups in the $–CH_2C\mathit{Me}_3$ ligand. The tertiary C resonance was located at 36.29 ppm. Further downfield the α–carbon resonance in the $–\mathit{C}H_2CMe_3$ ligands was found at 98.49 ppm.

4.2.2. Synthesis and Characterization of $W_3O_3(\mu\text{=}O)_3(CH_2CMe_3)_6(D_2O)_3$ (10)

Since THF is a ligand in the product (**9**) of the fast reaction between **8** and H_2O in THF, we decided to investigate the reaction of **8** with excess D_2O in benzene-d_6. Since benzene-d_6 is non-polar and there might be a kinetic isotope effect (KIE) using D_2O, we expect to have a slower reaction in hope to observe intermediate(s) prior to formation of the trimeric complex.

^1H NMR of the mixture was monitored, and a slow reaction indeed occurred. The reaction was complete in ca. 24 h. Only one intermediate, identified to be $W_2O_2(\mu\text{-}O)(CD_2SiMe_3)_2(CH_2CMe_3)_4$ (**11-d_4**, Scheme 4.2), containing one $–CD_2SiMe_3$ and two neopentyl ligands per W atom, was observed. **11-d_4** gradually converted to **10**, which was isolated through crystallization.

After the NMR experiment was finished, the J.R. Youngs NMR tube was left at room temperature for ca. 2 days. Several colorless crystals of **10** grew during the period, and they were found to be a mixture of small, single crystals. The crystals of **10** have a low solubility. They were not soluble in benzene-d_6, toluene-d_8, D_2O, THF-d_6, $CDCl_3$, but decomposed in DMSO-d_6.

Figure 4.2 gives an ORTEP plot of **10**, indicating that it is a D_2O adduct. The structure of **10** is similar to that of **9**, except that **10** contains D_2O as a ligand. Three D_2O ligands bind to three W atoms through $D_2O \rightarrow W$ dative bonds. The structural data for **10** differs significantly from those of **9**, as seen in Table 4.1, indicating that the substitution of D_2O for THF has a large effect on the core structure. For instance, in the structure of **10**, the W(1)-O(1) and W(1)-O(3) bond lengths are 2.224(8) and 1.785(8) Å, indicating that the two W oxo bonds are W←O and W=O, respectively. Both bonds are slightly longer than those [1.773(4) and 2.214(4) Å] in **9**. The O-W-O bond angle average is ca. 88°; however in **9** it is 90.2(2)°. The W-O-W bond angle in **9** is 149.7(2)°, and in **10**, the average bond angle is 151.7°, a difference of 2°. The selected bond distances and angles of **10** are given in Table 4.3.

4.2.3. Reaction of 8 with D_2O in THF to Give 9

This study was conducted to confirm that the H atoms in the neopentyl ligands in $W(CCH_2Me_3)_3(\equiv CSiMe_3)$ (**8**) do not undergo scrambling with D atoms in D_2O during the reaction of **8** with excess D_2O in THF. The studies here were conducted in both THF and THF-d_8 which were monitored by ^1H (Figure A15) and ^2H NMR spectroscopy, respectively. In addition, ^{13}C (Figure A17) and VT ^1H NMR experiments were used to characterize the product.

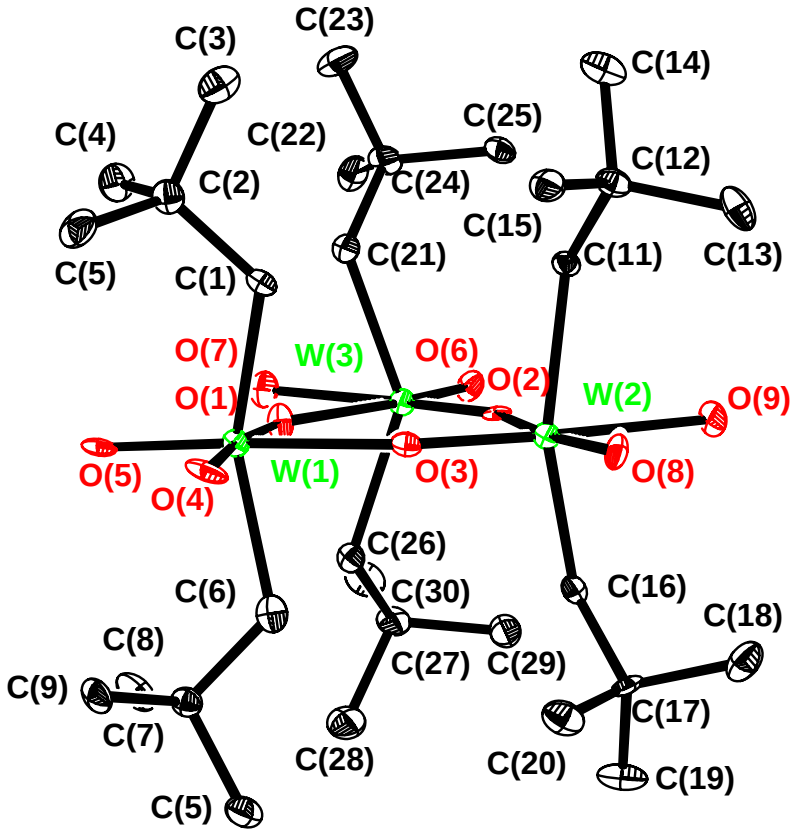

Figure 4.2. ORTEP side-view of **10** showing probability at 30% level. Hydrogen and deuterium atoms omitted for clarity.

Table 4.3. Selected bond lengths (Å) and angles (°) in **10**.

Lengths (Å)			
W(1)-O(1)	2.224(8)	W(2)-O(8)	1.713(9)
W(1)-O(3)	1.785(8)	W(2)-O(9)	2.301(9)
W(1)-O(4)	1.724(9)	W(3)-O(1)	1.765(9)
W(1)-O(5)	2.311(8)	W(3)-O(2)	2.214(9)
W(2)-O(3)	2.203(9)	W(3)-O(6)	1.733(8)
W(2)-O(2)	1.769(8)	W(3)-O(7)	2.331(9)
Angles (°)			
W(1)-O(3)-W(2)	152.4(4)	O(3)-W(1)-O(1)	88.0(3)
W(3)-O(1)-W(1)	151.0(4)	O(2)-W(2)-O(3)	87.9(4)
W(2)-O(2)-W(3)	151.8(5)	O(1)-W(3)-O(2)	88.9(3)
O(4)-W(1)-O(1)	167.7(3)	O(3)-W(1)-C(1)	102.1(4)
O(8)-W(2)-O(3)	167.1(3)	O(2)-W(2)-C(21)	102.0(4)
O(6)-W(3)-O(2)	167.4(4)	(O)(1)-W(3)-C(11)	102.8(4)

These studies show that there was no H-D exchange, and the product in the reaction was **9** with no D incorporation. The VT ^{1}H NMR experiments at 218–298 K here were used to reveal the overlapping H_b peak in the $-CH_aH_bCMe_3$ ligand (Figure A18). In ^{2}H NMR spectra, only CDH_2CMe_3 and CD_3SiMe_3 were observed (Figure A16).

4.2.4. Kinetic and Mechanistic Studies of the Formation of 9

Kinetic studies on the formation of **9** from the reaction of $W(CH_2CMe_3)_3(\equiv CSiMe_3)$ (**8**) with excess D_2O/H_2O were conducted. The formation of **9** follows pseudo first-order kinetics. Kinetic plots according to Eq. 4.1 are given in Figure 4.3,[36] yielding the rate constants k_H = 11.39(3) $\times$ 10^3 s^{-1} and k_D = 3.29(2) $\times$ 10^3 s^{-1}.

$$ln \frac{I_{8-t}}{I_{8-0}} = kt \qquad \text{(Eq. 4.1)}$$

The kinetic isotope effect (KIE = k_H/k_D) is 3.46(3), suggesting that the rate determining step in the reaction involves the breaking of the –OH ligand. Mechanistic considerations of the reaction with H_2O are given below.

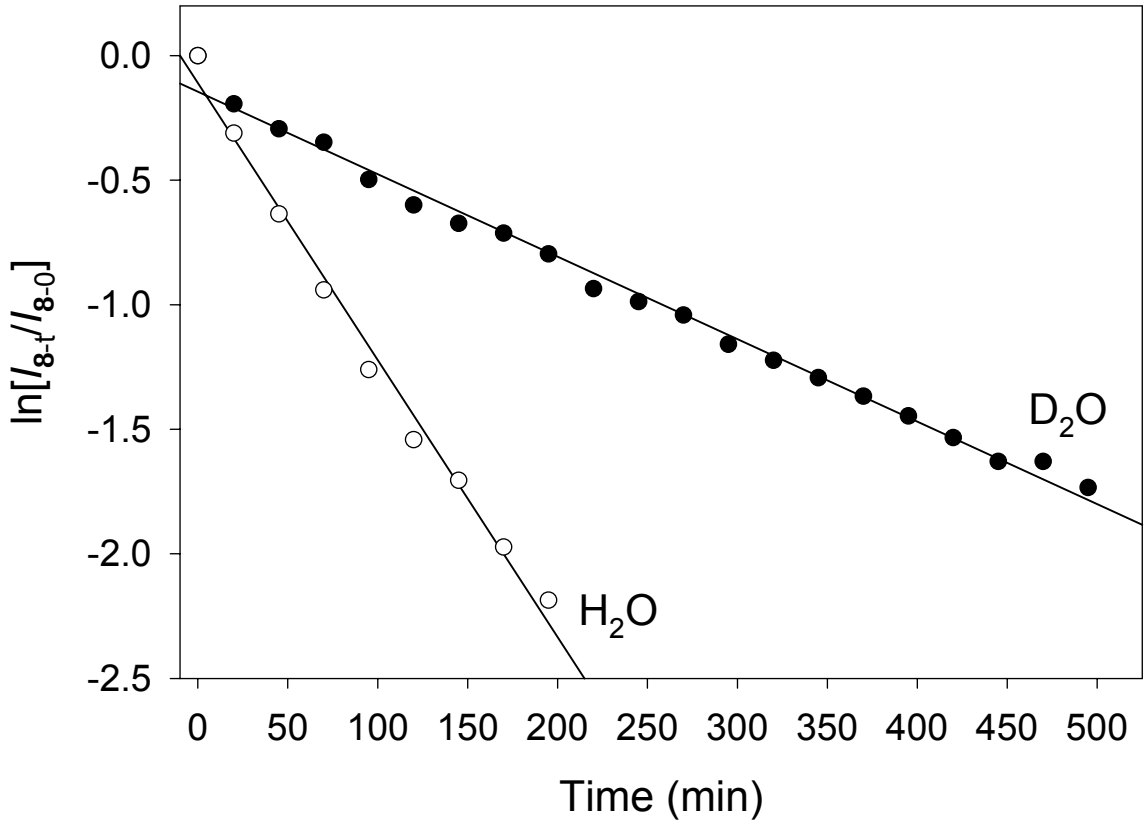

Figure 4.3. Kinetic plots of the formation of **9** by excess H_2O and D_2O in THF-d_8.

4.2.5. Observation and Characterization of Intermediate $W_2O_2(\mu\text{-}O)(CH_2SiMe_3)_2(CH_2CMe_3)_4$ (11) and $W_2O_2(\mu\text{-}O)(CD_2SiMe_3)_2(CH_2CMe_3)_4$ (11-d_4)

When the reaction of **8** with excess H_2O in THF-d_8 was conducted at –40 °C (in a dry ice-ethanol bath), ^{1}H NMR spectroscopy at 23 °C gave resonances that were consistent with $W_2O_2(\mu\text{-}O)(CH_2SiMe_3)_2(CH_2CMe_3)_4$ (**11**). **11** is the major product along with traces of unreacted **8** and product **9**. At this point, THF-d_8 and H_2O were removed *in vacuo* to stop the reaction, and solid was re-dissolved in benzene-d_6 for NMR characterization. In the ^{1}H NMR spectrum, the chemical shift for the methyl groups in the $-CH_2Si\mathit{Me}_3$ ligand was found at 1.40 ppm (Figure A19). The α–H atoms in the $-C\mathit{H}_2SiMe_3$ were observed as a singlet at 0.31 ppm and are equivalent. The methyls in the two $-CH_2C\mathit{Me}_3$ groups were located as a strong singlet at 1.33 ppm. The α–H atoms in the two $-CH_2C\mathit{Me}_3$ groups are diastereotopic and appear at 2.07 ppm as a complex AB system. In the ^{13}C NMR spectrum, two peaks were observed at 1.45 and 62.61 ppm for the C atoms in the $-CH_2SiMe_3$ ligand (Figure A20). The $-CH_2CMe_3$ ligands appear at 32.99, 35.43, and 92.68 ppm. A HSQC experiment confirmed the ^{1}H and ^{13}C NNR assignments. An ESI-MS experiment of the solution gives the parent ion peak of $\mathbf{11}^+$.

Reaction of **8** with D_2O (in THF-d_8) was studied to determine if D_2O adds across the $W{\equiv}CSiMe_3$ bond in **8**. When an excess of D_2O was added to **8** in THF-d_8 at room temperature, formation of $W_2O_2(\mu\text{-}O)(CD_2SiMe_3)_2(CH_2CMe_3)_4$ (**11-d_4**) was observed in ca. 1 h with a trace amount of **8** present. After THF-d_8

and unreacted D_2O were removed, the solid was re-dissolved in benzene-d_6. ^1H, ^2H and ^{13}C NMR spectroscopy studies were used to characterize **11-d_4**. The ^1H NMR studies confirmed the formation of $-CD_2SiMe_3$ ligands (Figure A21). The methyl groups in the $-CD_2Si\mathit{Me}_3$ ligand were observed at 0.31 ppm. One singlet for the methyl groups in the two $-CH_2C\mathit{Me}_3$ ligands was observed at 1.33 ppm, and their respective α–H peaks were found at 2.06 ppm with a complex AB pattern. A broad singlet was found at 1.37 ppm in the ^2H NMR spectrum for the $-C\mathit{D}_2SiMe_3$ ligands (Figure A22). The ^{13}C NMR spectra showed a singlet at 1.52 ppm and was assigned to the methyl carbon atoms in the $-CD_2Si\mathit{Me}_3$ ligand (Figure A23). The α–carbons in the $-\mathit{C}D_2SiMe_3$ ligands were observed at 67.00 ppm as a quintet ($^1J_{C\text{-}D}$ = 22.4 Hz). The neopentyl ligands were observed at 92.60 (as a singlet, $-\mathit{C}H_2-$), 35.45 ($-\mathit{C}-$), and 32.97 ppm ($C\mathit{Me}_3$) in the ^{13}C NMR spectrum.

4.2.6. Mechanistic Considerations

The observation of the intermediate $W_2O_2(\mu\text{-}O)(CD_2SiMe_3)_2(CH_2CMe_3)_4$ (**11-d_4**) suggests that the two D atoms in D_2O add across the W≡C bond in $W(CH_2CMe_3)_3(\equiv CSiMe_3)$ (**8**) with elimination of CH_2DCMe_3. Schrock and coworkers proposed a pathway in the reaction of $W(CH_2CMe_3)_3(\equiv CCMe_3)$ with H_2O, yielding $W_2O_2(\mu\text{-}O)(CH_2CMe_3)_6$.[50-51] A similar pathway may be present in the current reaction to give **11-d_4**. It is surprising that, unlike $W_2O_2(\mu\text{-}O)(CH_2CMe_3)_6$ which is stable to H_2O, **11-d_4** reacts with D_2O to form the oxo

trimer **9** through the selective elimination of the $-CD_2SiMe_3$ ligand as tetramethylsilane CD_3SiMe_3 (Scheme 4.3).

All four elementary steps (two O–D additions to the ≡C bond, and elimination of CH_2DCMe_3 and CD_3SiMe_3) involve the breaking of an O–D bond. Since the kinetic isotope effect (KIE) of 3.46(3) was obtained by monitoring the disappearance of the starting material **8**, the rate determining step is unlikely the last step, the conversion of **11-*d*$_4$** to **9**. We cannot, however, exclude the likelihood that the rate constant k_H, as an *observed* rate constant, includes the contributions of all four elementary steps.

4.3. Concluding Remarks

The reaction of alkyl alkylidyne $W(CH_2CMe_3)_3(\equiv CSiMe_3)$ (**8**) with H_2O in THF and with D_2O in benzene-d_6 gave two new trimeric oxo complexes: $W_3O_3(\mu{=}O)_3(CH_2CMe_3)_6(THF)_3$ (**9**) and $[W_3O_3(\mu{=}O)_3(CH_2CMe_3)_6(D_2O)_3]\bullet 2C_6D_6$ (**10**), respectively. In the reaction with D_2O in THF, an unstable intermediate$W_2O_2(\mu\text{-}O)(CD_2SiMe_3)_2(CH_2CMe_3)_4$ (**11-*d*$_4$**) was identified and characterized by ^1H, ^2H and ^{13}C NMR spectroscopy. Kinetics of the reactions of **8** with excess H_2O and D_2O in THF-d_8 at 298(1) K, yielding **11** and **11-*d*$_4$**, respectively, was studied, giving the kinetic isotope effect (KIE) of 3.46(3) for this reaction.

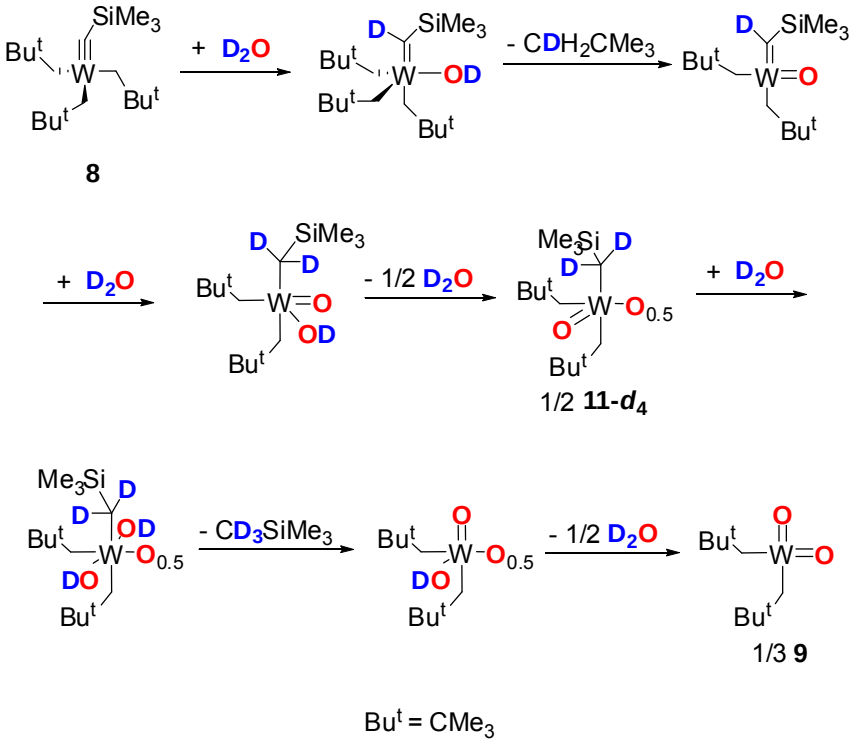

Scheme 4.3. Proposed mechanism of hydrolysis of $W(CH_2CMe_3)_3(\equiv CSiMe_3)$ (**8**).

4.4. Experimental Section

4.4.1 General Procedures

All manipulations were performed under a dry nitrogen atmosphere with the use of either a glovebox or standard Schlenk techniques. THF was purified by distillation from potassium benzophenone ketyl. Benzene-d_6, THF-d_8, and toluene-d_8 were dried and stored over 5 Å molecular sieves. $W(CH_2CMe_3)_3(\equiv CSiMe_3)$ (**8**) was prepared from $W(\equiv CSiMe_3)(OCMe_3)_3$ and >3 equiv. of Me_3CCH_2MgCl using procedures similar to that of Chisholm *et al*.[6b,54] ^1H, ^2H, and $^{13}C\{^1H\}$ NMR spectra were recorded on a Bruker AMX-400 spectrometer. The HSQC was recorded on a Varian Mercury 300 spectrometer. Intermediate **11** was further characterized by using a JEOL (Peabody, MA) JMS-T100LC (AccuTOFTM) orthogonal time-of-flight (TOF) mass spectrometer with an IonSense (Danvers, MA) direct analysis in real time (DART) source. Infared spectra were recorded on a Varian 4100 FT-IR spectrometer. Elemental analysis of **9** was carried out by Complete Analysis Laboratory, Inc., Parsippany, NJ.

4.4.2. Preparation of $W_2O_2(\mu\text{-}O)(CH_2SiMe_3)_2(CH_2CMe_3)_4$ (11)

$W(CH_2CMe_3)_3(\equiv CSiMe_3)$ (**8**, 30.5 mg, 0.063 mmol) was dissolved in THF-d_8 and ~10 equiv. H_2O (~10 μL, 0.56 mmol) was added *via* syringe at room temperature. The reaction mixture was monitored by ^1H NMR spectroscopy at room temperature. After ca. 5 min. at room temperature, intermediate **11** was observed with traces of $W(CH_2CMe_3)_3(\equiv CSiMe_3)$ (**8**) and **9** present. THF-d_8 was

removed *in vacuo* and solid was re-dissolved in benzene-d_6 for NMR characterization. ^{1}H NMR (benzene-d_6, 399.97, 23 °C) δ 2.07 (4H, CH_2CMe$_3$), 1.40 (s, 2H, CH_2SiMe_3), 1.33 (s, 18H, CH_2CMe_3), 0.31 (s, 9H, CH_2SiMe_3); ^{13}C{^{1}H} NMR (benzene-d_6, 100.54 MHz, 23 °C) δ 92.68 (CH_2CMe_3), 62.61 (CH_2SiMe_3), 35.43 (CH_2CMe_3), 32.99 (CH_2CMe_3), 1.45 (CH_2SiMe_3). Selected IR data (cm^{-1}, KBr): 2954 (s), 2864 (s), 1639 (s), 1462 (m), 1406 (m), 1364 (s), 1247 (s), 1155 (s), 1096 (m), 847 (s), 669 (s).

4.4.3. Preparation of $W_2O_2(\mu\text{-}O)(CH_2SiMe_3)_2(CH_2CMe_3)_4$ (11) for Mass Spectrometry

$W(CH_2CMe_3)_3(\equiv CSiMe_3)$ (**8**, 21.2 mg, 0.044 mmol) was dissolved in THF-d_8 and H_2O (~5 μL, 0.28 mmol) was added *via* syringe at room temperature. The reaction mixture was monitored by ^{1}H NMR spectroscopy at room temperature. ESI-MS of the solution (THF-d_8, *m/z*) 875.275 [**11**]$^+$.

4.4.4. Preparation of $W_2O_2(\mu\text{-}O)(CD_2SiMe_3)_2(CH_2CMe_3)_4$ (11-d_4)

In a J. R. Youngs NMR tube containing $W(CH_2CMe_3)_3(\equiv CSiMe_3)$ (**8**, 14.3 mg, 0.030 mmol) and 4,4-dimethylbiphenyl (an internal standard), an excess of D_2O (~10 μL, 0.55 mmol) was added *via* syringe at room temperature to the THF-d_8 solution. The reaction mixture was monitored by ^{1}H NMR spectroscopy at room temperature. After ca. 1 h at room temperature, intermediate **11-d_4** was observed, with traces of **8**. The THF-d_8/D_2O solution was removed *in vacuo* and

the solid was re-dissolved in benzene-d_6 for NMR characterization. ^{1}H NMR (benzene-d_6, 399.97, 23 °C) δ 2.06 (4H, CH_2CMe$_3$), 1.33 (s, 18H, CH$_2$CMe_3), 0.31 (s, 9H, CH$_2$SiMe_3); ^{13}C{^{1}H} NMR (benzene-d_6, 100.54 MHz, 23 °C, J in Hz) δ 92.60 (CH$_2$CMe$_3$), 67.00 (q, $^1J_{C\text{-}D}$ = 22.4, CD$_2$SiMe$_3$), 35.45 (CH$_2C$Me$_3$), 32.97 (CH$_2$CMe_3), 1.52 (CD$_2$SiMe_3); ^{2}H NMR (benzene-d_6, 61.37, 23 °C) δ 1.39 (s, CD$_2$SiMe$_3$).

4.4.5. Preparation of $W_3O_3(\mu{=}O)_3(CH_2CMe_3)_6(THF)_3$ (9) *via* the Reaction of 1 with Excess H_2O

W(CH$_2$CMe$_3$)$_3$(≡CSiMe$_3$) (**8**, 65.2 mg, 0.135 mmol) was dissolved in tetrahydrofuran (~0.40 mL) and a ca. excess of H_2O (0.20 mL, 11.11 mmol) was added to the yellow THF solution. After a ca. 30 min upon standing at room temperature, the brown solution was cooled at 4–5 °C overnight. The THF/H_2O solution was removed *in vacuo* and the white solid was re-dissolved in THF, with heat. After 24 h at 4–5 °C, the crystals were dried *in vacuo*. Yield: 27.1 mg, 56 % yield. ^{1}H NMR (toluene-d_8, 399.71, 23 °C, J in Hz) δ 3.56 (t, 4H, $^2J_{H\text{-}H}$ = $^3J_{H\text{-}H}$ = 6.2, OCH_2) 3.20 (d, 1H, $^2J_{H\text{-}H}$ = 9.4, CH_aH$_b$CMe$_3$), 1.46 (d, overlapping CH_2 peak, CH$_a$$H_bCMe_3$), 1.456 (q, 4H, $^2J_{H\text{-}H}$ = $^3J_{H\text{-}H}$ = 3.3, CH_2), 1.30 (s, 18H, CH$_2$CMe_3); ^{13}C{^{1}H} NMR (toluene-d_8, 100.52 MHz, 23 °C) δ 98.49 (CH$_2$CMe$_3$), 67.77 (OCH$_2$), 36.37 (CH$_2C$Me$_3$), 33.14 (CH$_2$CMe_3), 25.87 (CH$_2$). Anal. Calcd for $W_3C_{30}H_{66}O_6$: C, 33.50, H, 6.15. Found: C, 33.43, H, 6.11. Selected IR data (cm^{-1}, KBr): 2952 (s), 2901 (s), 2863 (s), 1653 (m), 1466 (s), 1363 (s), 1234 (s), 1122(m), 1084 (m),

976 (m), 881 (s), 817 (s), 762 (m), 689 (s).

4.4.6. Preparation of $W_3O_3(\mu\text{=}O)_3(CH_2CMe_3)_6(THF)_3$ (9) *via* the Reaction of 1 with Excess D_2O

$W(CH_2CMe_3)_3(\equiv CSiMe_3)$ (**8**, 50.6 mg, 0.105 mmol) was dissolved in tetrahydrofuran (~0.40 mL). A ca. excess of D_2O (0.20 mL, 11.07 mmol) was added to the THF solution. The yellow solution turned to light brown. The solution was stirred for ca. 5 min and left standing at room temperature overnight. An abundant amount of colorless hexagonal crystals were observed. The solvent was removed (ca. 2 h). The white solid was dissolved in THF, with heat. After 24 h at 4–5 °C, yellow hexagonal crystals of **9** were observed. ^{1}H NMR (toluene-d_8, 399.71, 23 °C) δ 3.56 (m, 4H, OCH_2) 3.21 (broad, CH_aH$_b$CMe$_3$), 1.46 (m, 4H, CH_2), 1.46 (broad, overlapping CH_2 peak, CH$_a$$H_bCMe_3$), 1.31 (s, 18H, CH$_2CMe_3$); ^{13}C{^{1}H} NMR (toluene-d_8, 100.52 MHz, 23 °C) δ 98.67 (CH$_2$CMe$_3$), 67.84 (OCH$_2$), 36.48 (CH$_2$$CMe_3$), 33.20 (CH$_2CMe_3$), 25.94 ($CH_2$).

4.4.7. Kinetic Study of the Formation of 9 by Excess H_2O

At least two experiments were conducted. A mixture of $W(CH_2CMe_3)_3(\equiv CSiMe_3)$ (**8**, 25.4 mg, 0.053 mmol), 4,4'-dimethylbiphenyl (an internal standard), and THF-d_8 in J. R. Youngs NMR tubes were added ca. excess of H_2O (~ 9.5 μL, 0.53 mmol) at –70 °C. The sample was next placed into the pre-cooled NMR probe at 298 K. After the NMR tubes were inserted into

the probe, ^{1}H NMR spectra were taken after the temperature was stabilized, and the integrations of **8**, relative to those of the internal standard, were used as $I_{8\text{-}t}$ at time *t*.

4.4.8. Kinetic Study of the Formation of 9 by Excess D_2O

At least two experiments were conducted. A mixture of $W(CH_2CMe_3)_3(\equiv CSiMe_3)$ (**8**, 14.0 mg, 0.029 mmol), 4,4'-dimethylbiphenyl (an internal standard), and THF-d_8 in J. R. Youngs NMR tubes were added ca. excess of D_2O (~5.25 μL, 0.29 mmol) at –70 °C. The sample was next placed into the pre-cooled NMR probe at 298 K. After the NMR tubes were inserted into the probe, ^{1}H NMR spectra were taken after the temperature was stabilized, and the integrations of **8**, relative to those of the internal standard, were used as $I_{8\text{-}t}$ at time *t*.

4.4.9. Determination of X-ray Crystal Structures of 9 and 10

The X-ray crystal structures of **9** and **10** were determined on a Bruker AXS-Smart 1000 X-ray diffractometer equipped with a CCD area detector and a graphite-monochromated Mo source (K_α radiation, 0.71073 Å) and fitted with an upgraded Nicolet LT-2 low temperature device. Suitable crystals were coated with paratone oil (Exxon) and mounted on a hair loop under a stream of nitrogen at –110(2) °C. The structures of **9** and **10** were solved by direct method. All non-hydrogen atoms were anisotropically refined. All hydrogens were treated as

idealized contributions. Global refinements for the unit cell and data reduction were performed under the SAINT program for data collected.[55a] Cell refinement and data reduction were carried out using the APEX2 program package.[55b] Empirical absorption correction was performed with SADABS.[55c]

CHAPTER 5

Crystal and Molecular Structures of a High-Spin Tetraphenylporphyrin Iron(III) Complex. X-ray Diffraction Studies at 20(2), 143(2), and 293(2) K

5.1 Introduction

Metals such as iron play a vital role in biological hemoglobin and myoglobin.[56] In these proteins, Fe ions are bound to planar porphyrin ligands to form complexes known as hemes. Two forms are distinguished: (1) heme A is the six coordinate complex with an Fe atom bound to O_2 and (2) heme B complex, the oxygen free five coordinated complex (Figure 5.1). A key structural feature of the O_2-free hemes is that the active center, which is responsible for oxygen binding and release in both proteins, contains a five-coordinate Fe-porphyrin with an imidazole ligand. Hemoglobin is mainly responsible for oxygen transport in vertebrates while myoglobin is responsible for oxygen storage and release within the muscles.[56] In both proteins O_2 binds to the iron, which turns the five-coordinate heme into a six-coordinate complex.[56] Five-coordinate Fe-porphyrin systems, such as trigonal pyramidal Fe(TPP)Cl (**12**, TPP^{2-} = *meso*-tetraphenylporphyrinate) (Figure 5.2)[57] have thus been actively studied to give a better insight into physical and chemical properties of the hemes. As a member of the very well-characterized Fe(TPP)X (X = NCS, Cl, Br, I) series, Fe(TPP)Cl (**12**) has been extensively studied by electrochemical analysis, X-ray diffraction,

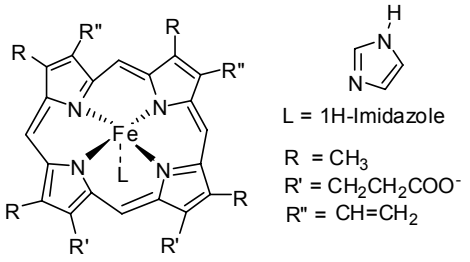

Figure 5.1. Iron porphyrin site in myoglobin.

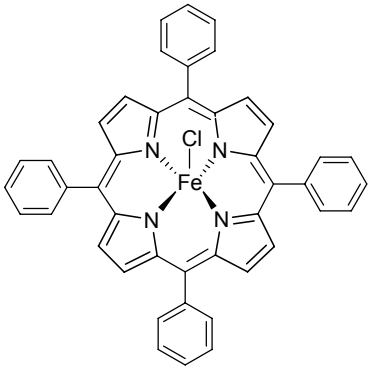

Figure 5.2. Structure of **12**.

NMR, UV-Vis, IR, Mössbauer, and Density Functional Theory calculations.[58,59]

High-spin metal porphyrin complexes have been found to adopt a five-coordinate geometry with the metal ion about 0.3 Å out of the porphyrin plane.[60] The crystal structure of Fe(TPP)Cl (**12**) was first reported incorrectly as Fe(TPP)(OH)•H_2O[61] and solved in the space group *I4*. The reported structure had a six-coordinate Fe(III) ion in the porphyrin plane with H_2O and OH^- ligands at the axial positions along the crystallographic four-fold axis. Three years later, Hoard *et al.* discovered that the two axial ligands, OH^- and H_2O, had been wrongly assigned after the same data were re-analyzed, and the structure was solved in the space group *I4/m* as Fe(TPP)Cl.[58] The high-spin Fe(III) ion in the molecule is five coordinated and sits above or below the porphyrin plane. The axial ligand is indeed a chloride atom, as confirmed by elemental analysis.

The crystals of Fe(TPP)Cl (**12**) used in these earlier studies were obtained either from its solution in a $CHCl_3$/EtOH mixture[58] or in the course of the studies of its reaction with nitrite ion.[62] The crystals obtained from the two processes belong to different crystal systems – the former is in the tetragonal and the latter is in the monoclinic system. The structure of the tetragonal polymorph is the focus of the current studies. The reported X-ray diffraction experiment for the tetragonal polymorph was performed at room temperature.[58] In the current work, the crystal structures of Fe(TPP)Cl at 293(2), 143(2), and 20(2) K are investigated, in particular the temperature dependence of the phenyl groups. This variable-temperature X-ray diffraction study provides a valuable insight into the structural changes and adjustments of the Fe porphyrin complex.

5.2. Results and Discussion

There are two molecules of Fe(TPP)Cl (**12**) in the body-centered tetragonal unit cell, with one-eighth of the molecule in the asymmetric unit in space group *I4/m*, or one quarter in space group *I4*. The Fe(III) ion in the Fe(TPP)Cl molecule is five coordinated. Four bonds are formed to the four nitrogen atoms of the planar porphyrin ring. The fifth, axial ligand is a chlorine atom. Due to the asymmetric coordination, the Fe atom moves about 0.39 Å out of the porphyrin plane towards the Cl atom and the molecule resides at a special position (0,0,0) with C_{4h} point-group symmetry (Figure 5.3). The origin (0,0,0) is also the center of the planar porphyrin, which lies on a mirror plane perpendicular to *c*. The four phenyl rings in Fe(TPP)Cl are oriented perpendicular to the porphyrin plane with half the ring above and half the ring below the mirror plane. Each pair of opposing rings lies on the same plane along the *c*-axis to give a C_{4v} point group symmetry for the molecule (Figure 5.4). The apparently higher C_{4h} site symmetry observed in the crystal structure is contributed to the static disorder of a pair of Fe and Cl atoms on opposite sides of the porphyrin plane. The unusually high symmetry of the molecule with all atoms on the mirror plane and Fe-Cl occupying a special position proved to be an interesting feature for the variable temperature study. This is because only two carbon (and connected hydrogen) atoms of the phenyl ring lie above and below the mirror plane, in general positions, which can respond freely to restraints imposed at low-temperature. [This point is discussed further below (Figure 5.10).)] This proved to be an interesting feature of the compound, which was not understood

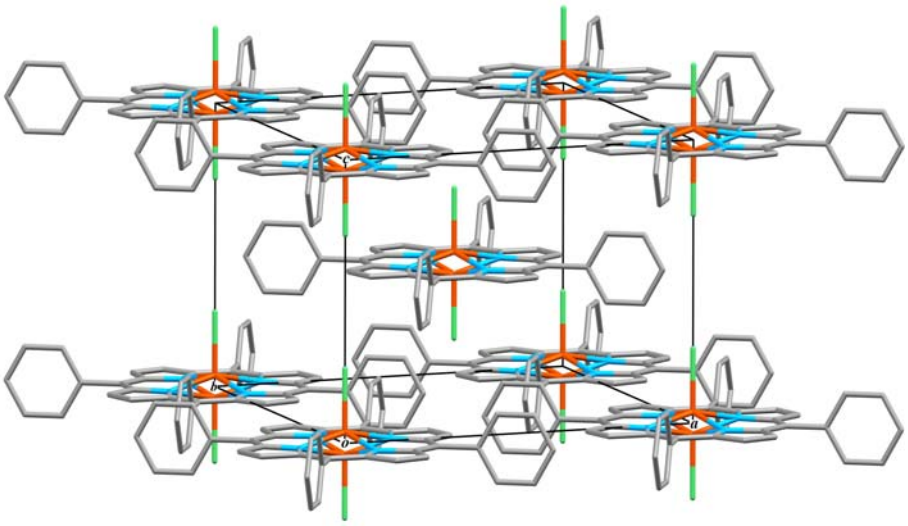

Figure 5.3 Stacking plot of Fe(TTP)Cl (**12**) at 293(2) K.

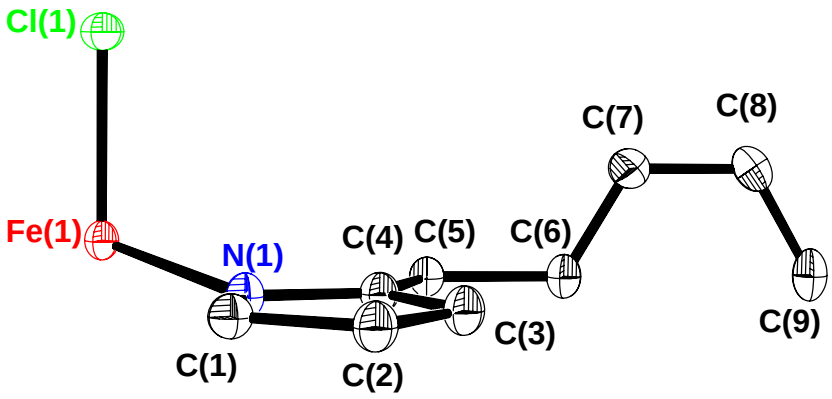

Figure 5.4. ORTEP of the asymmetric unit of **12** at 293(2) K; thermal ellipsoids are at 30% probability level. Hydrogen atoms were omitted for clarity.

previously.

The X-ray structure at 293(2) K (Figure 5.4) was first solved in the *I4/m* space group. The structure at 293(2) K was also refined in the *I4* space group for comparison. As expected from the ADP values for both refinements, the structure models overlap perfectly. A diagram overlapping the *I4* and *I4/m* structures is given in Figure 5.5. Thus the higher symmetry space group *I4/m* describes adequately the structure at 293(2) K. Structural paramters are summarized in Table 5.1.

As can be seen in Tables 5.2 and 5.3, the interatomic distances and angles of our X-ray structure at 293(2) K compare well with the reported structure of Hoard *et al*.[58] For example, Fe...Fe separation in the current structure is 0.782(3) Å vs. reported 0.766(11) Å. Fe1-N1-Cl1 and C3-C4-C5 bond angles here are 126.6(2)° and 124.4(4)° vs. reported 126.6(8)° and 123.8(1.2)°, respectively.

The structure at 143(2) K was also refined in both the *I4/m* and the *I4* space groups. A diagram overlapping the structures refined in the two space groups is given in Figure 5.6. Unlike the overlap diagram at 293(2) K (Figure 5.5), this diagram illustrates a clear distinction between the structures with respect to the phenyl groups. In the *I4* structure, the phenyl groups slightly deviate from the plane perpendicular to the porphyrin plane, leading to a lowering of the point group symmetry of Fe(TPP)Cl from C_{4v} to C_4. The mean plane of the phenyl group tilts 3.2° from the perpendicular to the porphyrin plane**.** The difference between the two structures in the two space groups also has a clear

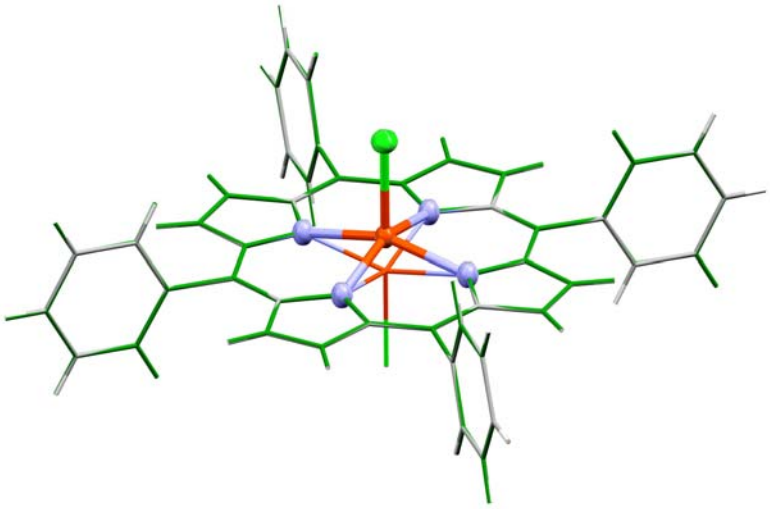

Figure 5.5. Overlap diagram of the *I4* and *I4/m* structures at 293(2) K.

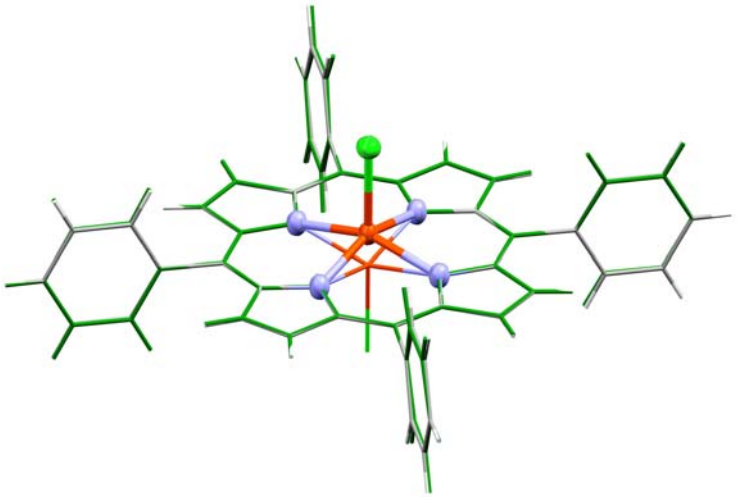

Figure 5.6. Overlap diagram of the *I4* and *I4/m* structures at 143(2) K. The phenyl groups in gray color are in the plane as defined by the *I4/m* structure. The phenyl groups in green color, deviated from the plane, give the lower symmetry *I4* structure.

Table 5.1. Crystal data and structural refinement for **12** at 20(2), 143(2), and 293(2) K.

Temperature (K)	293(2)	143(2)	143(2)	20(2)
Empirical formula	$C_{44}H_{28}ClFeN_4$	$C_{44}H_{28}ClFeN_4$	$C_{44}H_{28}ClFeN_4$	$C_{44}H_{28}ClFeN_4$
Formula weight	704.00	704.00	704.00	704.00
Wavelength (Å)	0.71073	0.71073 Å	0.71073	0.41328
Crystal system	Tetragonal	Tetragonal	Tetragonal	Tetragonal
Space group	*I4/m*	*I4/m*	*I4*	*I4*
Unit cell dimensions (Å)	*a* = 13.5419(3)	*a* = 13.504(3)	*a* = 13.504(3)	*a* = 13.4830(5)
	c = 9.8240(4)	*c* = 9.731(10)	*c* = 9.731(10)	*c* = 9.6849(6)
Volume ($Å^3$)	1801.56(9)	1774.5(19)	1774.5(19)	1760.63(14)
Z	2	2	2	2
Density (calculated) (Mg/m^3)	1.298	1.318	1.307	1.328
Absorption coefficient (mm^{-1})	0.53	0.54	0.53	0.29
F(000)	726	726	726	726

Table 5.1. (continued)

Temperature (K)	293(2)	143(2)	143(2)	20(2)
θ range for data collection	2.56 - 28.02°	2.55 - 27.45°	2.55 - 27.45°	2.75 - 32.14°
Index ranges	$-18 \leq h \leq 17$	$-17 \leq h \leq 16$	$-17 \leq h \leq 16$	$-16 \leq h \leq 33$
	$-17 \leq k \leq 17$	$-17 \leq k \leq 17$	$-17 \leq k \leq 17$	$-24 \leq k \leq 33$
	$-13 \leq l \leq 12$	$-12 \leq l \leq 12$	$-12 \leq l \leq 12$	$-23 \leq l \leq 18$
Reflections collected	9622	7976	7973	36372
Refinement method	Full-matrix least-squares on F^2	Full-matrix least-squares on F^2	Full-matrix least-squares on F^2	Full-matrix least-squares on F^2
Independent Reflections	1154	1106	2002	11751
Completeness to θ = 26.00°	99.9%	99.0%	99.0%	98.9%
Data / restraints / parameters	1154 / 0 / 74	1106 / 0 / 74	2002 / 1 / 117	11751 / 1 / 129
Goodness-of-fit on F^2	1.06	1.23	1.05	1.03

Table 5.1. (continued)

Temperature (K)	293(2)	143(2)	143(2)	20(2)
Final *R* indices [$I > 2\sigma(I)$]	$R1$ = 0.062,	$R1$ = 0.075,	$R1$ = 0.048,	$R1$ = 0.037,
	w$R2$ = 0.147	w$R2$ = 0.221	w$R2$ = 0.148	w$R2$ = 0.112
R indices (all data)	$R1$ = 0.0636,	$R1$ = 0.0814,	$R1$ = 0.0543,	$R1$ = 0.0456,
	w$R2$ = 0.1468	w$R2$ = 0.211	w$R2$ = 0.1487	w$R2$ = 0.1120
Largest diff. peak and hole ($Å^{-3}$)	0.26, –0.26	0.49, –0.36	0.43, –0.32	0.64, –0.54

[a] $R1 = \Sigma||F_o| - |F_c|| / \Sigma|F_o|$; $wR2 = [\Sigma\, w(F_o^2 - F_c^2)^2 / \Sigma\, w(F_o^2)^2]^{1/2}$; $w = 1/[\sigma^2(F_o) + (aP)^2 + bP]$; $P = [2F_c^2 + \mathrm{Max}(F_o^2, 0)]/3$

Table 5.2 Comparison amongst bond lengths (Å) of **12** at 20(2), 143(2), and 293(2) K.

Temp. (K)	293[a]	293(2)	143(2)	143(2)	20(2)
Space Group	*I4/m*	*I4/m*	*I4/m*	*I4*	*I4*
			Lengths (Å)		
Fe-Fe	0.766(11)	0.782(3)	0.792(4)	0.791(2)	0.7888(5)
Fe-Cl1	2.192(12)	2.193(3)	2.190(4)	2.175(5)	2.1979(8)
Fe-N1	2.049(9)	2.052(3)	2.058(4)	2.0518(17)	2.0582(3)
N-C1	1.394(14)	1.386(5)	1.378(6)	1.384(2)	1.3830(5)
N-C4	1.374(15)	1.380(5)	1.380(6)	1.382(2)	1.3833(4)
C3-C4	1.463(17)	1.436(6)	1.446(6)	1.441(2)	1.4432(4)
C4-C5	1.399(16)	1.395(5)	1.398(6)	1.391(3)	1.4015(5)
C5-C6	1.508(17)	1.497(5)	1.501(6)	1.502(2)	1.4991

Table 5.3 Comparison amongst bond angles (°) of **12** at 20(2), 143(2), and 293(2) K.

Temp. (K)	293[a]	293(2)	143(2)	143(2)	20(2)
Space Group	*I4/m*	*I4/m*	*I4/m*	*I4*	*I4*
			Angles (°)		
Fe1-N-C1	126.6(8)	126.6(2)	126.7(3)	126.41(12)	126.24(3)
Fe1-N-C4	126.3(8)	126.2(2)	125.8(3)	126.32(12)	126.31(3)
C1-N-C4	105.6(9)	105.6(3)	105.9(4)	105.72(14)	105.91(3)
C3-C4-C5	123.8(1.2)	124.4(4)	124.1(4)	124.46(16)	124.33(3)
N-C4-C5	126.0(1.1)	125.9(4)	126.2(4)	125.75(15)	125.73(3)
C4-C5-C6	117.5(1.1)	117.7(3)	118.1(4)	118.05(15)	117.95(3)
C5-C6-C7	122	120.8(2)	120.8(2)	120.4(3)	121.9

effect on the refined *R* values. The refined residual values (*R*1 = 0.0814 and w*R*2 = 0.211) in *I4/m* are significantly higher than those in *I4* (*R*1 = 0.0543 and w*R*2 = 0.1487). The *I4* structures at 143(2) and 20(2) K have been refined as inversion twins; the occupations of the two domains refined to 0.50(1) at 20(2) K so that symmetry of the observed diffraction pattern remained *I4/m*. Thus the structure at 143(2) K is better described with the lower symmetry, *I4*, space group.

The bond lengths and angles in the 143(2) K structure are all similar to those at 293(2) K, and it is noteworthy that there is better agreement for the bond lengths between the *I4/m* 293(2) K (Figure 5.7) and the *I4* 143(2) K (Figure 5.8) structures than between the *I4/m* 293(2) K and the *I4/m* 143(2) K structures (Table 5.2). The structure at 143(2) K (Figure 5.7) shows an Fe...Fe separation of 0.791(2) Å [vs. 0.782(3) Å at 293(2) K]. This slightly larger Fe…Fe distance can be attributed to the reduced thermal motion along the Fe-Cl direction.

The structure at 20(2) K was refined against our extensive synchrotron data in both *I4/m* and *I4* space groups with a clear preference for *I4* (Figure 5.9) based on the agreement indices (*R1*, *wR2* [$I > 2\sigma(I)$], *S* of 0.0632, 0.1899, 1.299 in *I4/m vs* 0.0371, 0.1120, 1.030 in *I*4). Henceforth we quote just the results from the refinement in *I4* at 20(2) K. An overlay of the *I4* and *I4/m* structures at 20(2) K is given in Figure 5.10.

One significant difference between the structures at 143(2) and at 20(2) K is that the deviation of the phenyl groups from the plane (σ_v plane in C_{4v}) perpendicular to the porphyrin ring (crystal *ab* plane) becomes more pronounced,

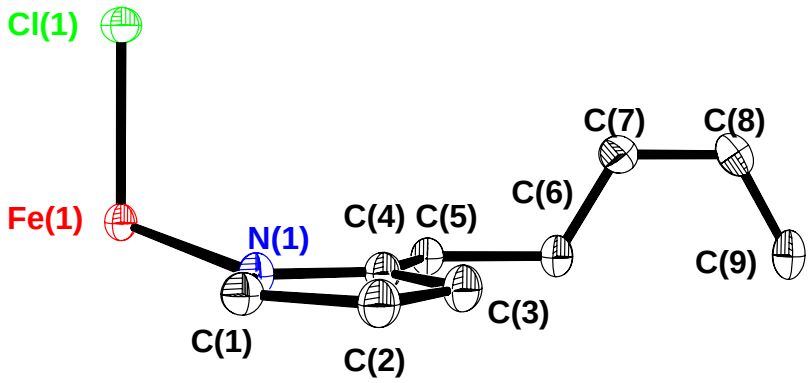

Figure 5.7. ORTEP of the asymmetric unit of **12** at 143(2) K in the *I4/m* space group; thermal ellipsoids are at 30% probability level. Hydrogen atoms were omitted for clarity.

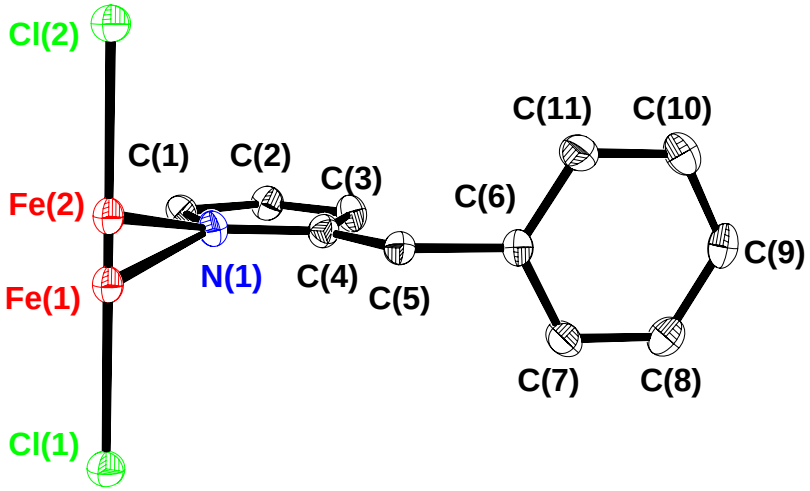

Figure 5.8. ORTEP of the asymmetric unit of **12** at 143(2) K in the *I4* space group; thermal ellipsoids are at 30% probability level. Hydrogen atoms were omitted for clarity.

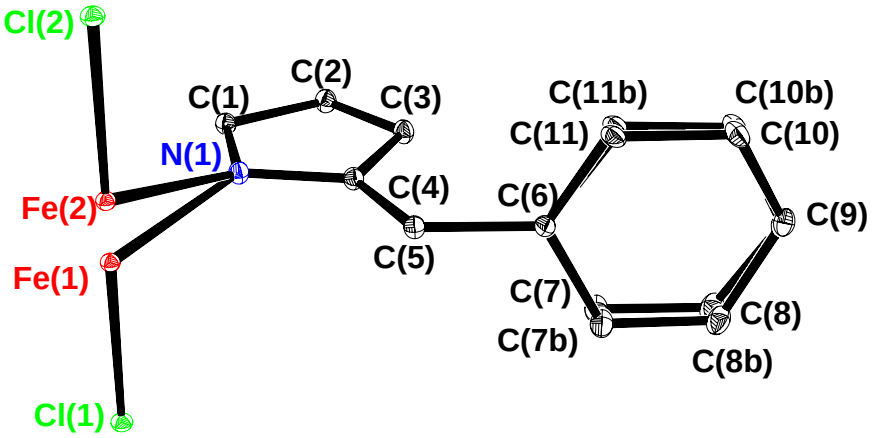

Figure 5.9. ORTEP of the asymmetric unit of **12** at 20(2) K in the *I4* space group showing the slight disorder of the phenyl atoms; thermal ellipsoids are at 30% probability. Hydrogen atoms were removed for clarity.

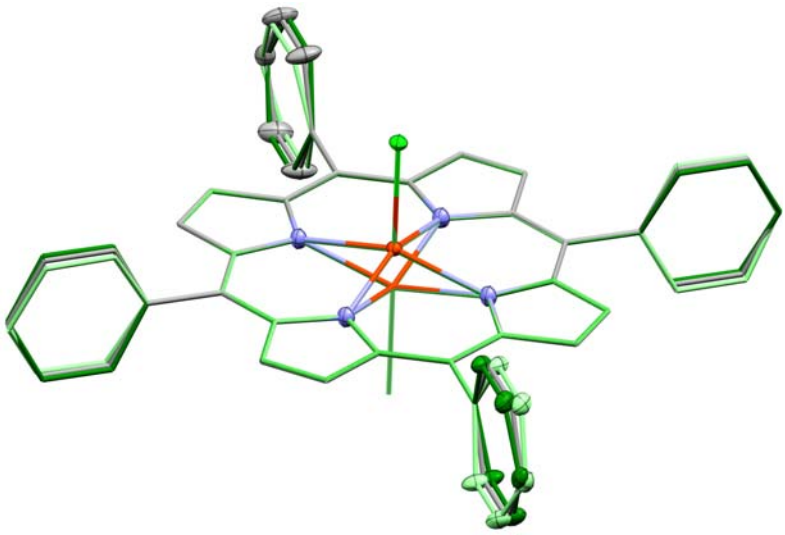

Figure 5.10. Overlap diagram of the *I4* and *I4/m* structures at 20(2) K. The phenyl groups in gray color are in the plane as defined by the *I4/m* structure. The phenyl groups in green color, deviated from the plane, give the *I4* structure.

further confirmed the C_4 point group symmetry observed for Fe(TPP)Cl at 143(2)K. The mean plane of the phenyl group is now tilted 6.2° from being perpendicular to the porphyrin plane**.** The structure at 20(2) K also shows a slight disorder of the phenyl groups, indicating potential loss of the crystallographic four-fold symmetry. This deviation is, however, not significant enough to affect the structure refinement as a whole. As expected, the thermal motion of the Fe and Cl atoms is drastically reduced at such a low temperature as 20(2) K. The Fe...Fe distance was found to be 0.7888(5) Å, very close to the value of 0.791(2) Å observed at 143(2) K. Apart from the tilt of the phenyl plane, the bond lengths and bond angles do not differ significantly from those at 143(2) and 293(2) K.

Our structure at 293(2) K (Figure 5.3) is in full agreement with the previously reported room temperature structure[58] and with the space-group assignment of *I4/m*. However, the crystal structure was found to undergo subtle conformation changes as the temperature was lowered from 293(2) K to 20(2) K leading to a change in the apparent space group and the molecular point group symmetry. The phenyl groups that are attached to the porphyrin ring tilt away from alignment with the crystallographic *c* direction thus violating the mirror symmetry for the Fe(TPP)Cl (**12**) molecule increasingly as a function of decreasing temperature. Figures 5.5, 5.6 and 5.10. demonstrate how the phenyl rings tilt away from the *c*-axis at 293(2), 143(2) K and 20(2) K, respectively, and break the mirror symmetry in the *ab* plane with decreasing temperature.

The atomic positions on the mirror plane are stable with temperature. Despite the loss of mirror symmetry, the porphyrin ring atoms deviate at most 0.063 and 0.14 Å from a common plane, and the common plane tilts only 3.2 and 6.2° from the *ab* plane, at 143(2) and 20(2) K, respectively. The out-of-plane carbon atoms C7 and C8 for *I4/m* and C7, C8, C10 and C11 for *I4* are tilted away from the mirror plane as shown in Figure 5.10. The thermal ellipsoid elongation perpendicular to the mirror plane can be expressed by the ratio of U_{max}/U_{min} which elucidates the trend of distortion of the average structure mode. The ratio in *I4/m* increases from a value of 2.48_{293K} to 2.64_{143K} and significantly higher to 5.34_{20K}. U_{max}/U_{min} in the refinements in space group *I4* remains stable around 2.7 (2.53_{293K}, 2.63_{143K}, 2.83_{20K}) for the measured temperature range as shown in Figure 5.11. This supports a better structure description in space group *I4* with decreasing temperature. This trend can also be described by the distances between C7 and C7′, and between C8 and C8′. There is no apparent separation at 293(2) K, while the distance between C7 and C7′ (as well as C8 and C8′) increases to 0.063 Å at 143(2) K and further to 0.14 Å at 20(2) K. The increase in separation distance $\Delta d(Å)$ with the decrease in temperature is displayed in Figure 5.11.

The temperature variation of the displacement parameters is plotted in Figure 5.11. That the temperature variation of the displacement parameters for C7/C10 and C8/C11 (Table 5.4) from the refinements in *I4* follows the trend shown by other atoms gives further credence to reduction of the symmetry from

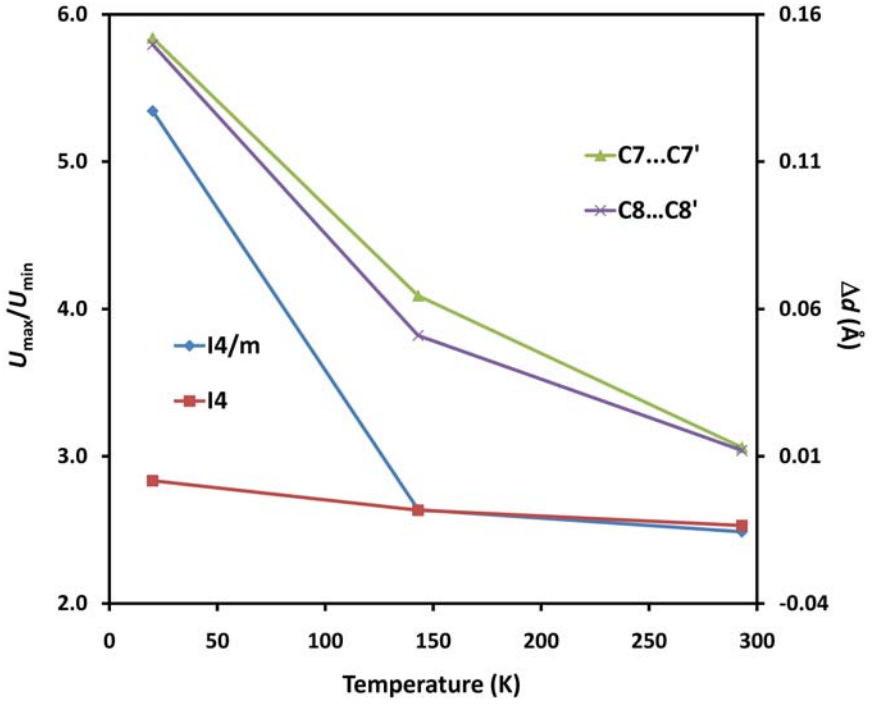

Figure 5.11. Graph showing the change of ratio of thermal ellipsoid distortion with temperature (U_{max}/U_{min}) in space group *I4/m* (blue) and *I4* (red) on the primary axis. The distances C7…C7′ and C8…C8′ of the phenyl ring are shown on the secondary axis.

Table 5.4 Fractional atomic coordinates ($\times 10^{-4}$) and equivalent isotropic displacement parameters ($Å^2 \times 10^{-3}$) of **12** at 293(2) K (upper row, *I4/m*), 143(2) K (middle row, *I4*), and 20(2) K (lower row, *I4*). Fe2, Cl2, C10 and C11 are equivalent to Fe1, Cl1, C7 and C8 respectively in *I4/m* at 293(2) K.

$U_{eq} = (1/3)\Sigma_i\Sigma_j U_{ij} a_i^* a_j^* \mathbf{a}_i.\mathbf{a}_j$

	x	*y*	*z*	U_{eq}
Fe1	0	0	4602(1)	37(1)
	0	0	4602(1)	24(1)
	0	0	4606(1	9(1)
Cl1	0	0	2369(3)	54(1)
	0	0	2366(3)	32(1)
	0	0	2337(1)	11(1)
Fe2	-	-	-	-
	0	0	5414(1)	24(1)
	0	0	5421(1)	9(1)
Cl2	-	-	-	-
	0	0	7675(2)	32(1)
	0	0	7694(1)	11(1)

Table 5.4 (continued)

	x	*y*	*z*	U_{eq}
N1	-380(2)	1438(2)	5000	43(1)
	-372(1)	1445(1)	4998(2)	28(1)
	366(1)	1455(1)	5000(1)	12(1)
C1	248(3)	2247(3)	5000	46(1)
	-1318(1)	1841(1)	5001(3)	28(1)
	-278(1)	2254(1)	4995(1)	12(1)
C2	-314(3)	3138(3)	5000	56(1)
	-1265(1)	2905(1)	4987(4)	33(1)
	275(1)	3170(1)	4994(1)	14(1)
C3	-1277(3)	2883(3)	5000	55(1)
	-298(1)	3154(1)	4996(3)	33(1)
	1254(1)	2924(1)	5006(1)	14(1)
C4	-1323(3)	1823(3)	5000	46(1)
	264(1)	2247(1)	4992(3)	28(1)
	1310(1)	1855(1)	4999(1)	12(1)

Table 5.4 (continued)

	x	*y*	*z*	U_{eq}
C5	1279(3)	2198(3)	5000	43(1)
	1293(1)	2199(1)	4997(3)	29(1)
	2198(1)	1315(1)	4997(1)	12(1)
C6	1838(3)	3151(3)	5000	47(1)
	1862(1)	3155(1)	5004(3)	29(1)
	3154(1)	1883(1)	4994(1)	11(1)
C7	2099(3)	3596(3)	3806(4)	71(1)
	2086(3)	3629(2)	3785(3)	46(1)
	3567(1)	2223(1)	3808(1)	14(1)
C8	2641(3)	4466(3)	3804(4)	79(1)
	2633(3)	4498(2)	3791(3)	51(1)
	4458(2)	2789(2)	3814(2)	14(1)
C9	2917(4)	4896(3)	5000	66(1)
	2939(1)	4914(1)	5006(4)	38(1)
	4928(12)	2907(7)	5000(40)	14(1)

Table 5.4 (continued)

	x	*y*	*z*	U_{eq}
C10	-	-	-	-
	2692(1)	4464(2)	6217(2)	50(1)
	4563(2)	2608(4)	6238(3)	18(1)
C11	-	-	-	-
	2159(2)	3577(2)	6219(2)	46(1)
	3660(2)	2049(3)	6251(4)	16(1)

I4/m to *I4* between 293(2) and 143(2) K.

The cell parameters decrease as expected from 293(2) K, through 143(2) K, to 20(2) K, with the observed *a*-axis, *c*-axis and unit-cell volume observed to be 13.5419(3) Å, 9.8240(4) Å and 1801.56(9) $Å^3$ at 293(2) K, 13.504(3) Å, 9.731(10) Å and 1774.5(19) $Å^3$ at 143(2) K, and 13.4830(5) Å, 9.6849(6) Å and 1760.63(14) $Å^3$ at 20(2) K. The percentage decrease in the *c*-axis [1.4% from 293(2) to 20(2) K] is three times as large as the percentage decrease in the *a*-axis, as a consequence of the tilting of the phenyl rings away from the *c*-axis.

5.3 Concluding Remarks

In summary, the current work reveals that a tilting of the phenyl rings on the porphyrin ring away from the tetragonal *c*-axis leads to a lower symmetry (space group *I4*) of the crystal at 143(2) and 20(2) K which breaks the mirror symmetry in the *ab* plane observed at 293(2) K. The current data do not support unambiguously the possibility of a phase transition. They rather suggest a gradual hardening of the phenyl position into two distinct overlapping configurations. The observation of a decreasing tilt angle with temperature increase implies a static disorder rather than a dynamic disorder. In other words the layered structure (see Figure 5.10) “freezes out” and is stabilized by decreasing the layer distances by tilting the interlayer connecting phenyl rings. We propose a statistical distribution of domains in the structure. Analysis of the hydrogen bonding network will be done using conclusive neutron single crystal diffraction data. This analysis is currently ongoing.

5.4. Experimental Section

5.4.1 Synthesis of Fe(TPP)Cl (12)

Fe(TPP)Cl, purchased from Strem Chemicals, and solvents (Analytical Reagents) were used without further purification. Wet chloroform was prepared by adding water to chloroform (Certified ACS), and the mixture was shaken and then allowed to settle. Wet chloroform at the bottom was removed for the use below.

Fe(TPP)Cl (**12**) was prepared by modified published procedures.[57] Fe(TPP)Cl (**12**, 0.05 mmol) was dissolved in wet chloroform (4 mL), then layered with a 1:3 wet chloroform:ethanol (200 proof) mixture (4 mL), and the sample container was sealed with parafilm. After the layers had completely diffused together - in ca. 5–7 days - the solution was allowed to evaporate very slowly for a further ca. 7 days. Crystals of sizes up to $1 \times 2 \times 2$ mm^3 were observed and collected.

5.4.2 Data Collection

X-ray diffraction data at room temperature [293(2) K] were collected on a Bruker AXS Smart 1000 X-ray diffractometer equipped with a CCD area detector and a graphite-monochromated Mo source (K_α radiation, 0.71073 Å) and fitted with an upgraded Nicolet LT-2 low-temperature device. A suitable crystal of size $0.70 \times 0.20 \times 0.10$ mm^3 was coated with *Paratone-N* oil and mounted on a glass fiber. 9622 reflections were collected. For a refinement in space group *I4/m*, 1099 observed reflections ($I > 2\sigma(I)$) of 1154 unique reflections were used leading to

residual values of R = 0.062, wR = 0.147, GoF = 1.06. The maximum residual electron density was +/-0.26 eÅ^3 (Table 5.1). The unit cell was refined to a = 13.5419(3) Å, c = 9.8240(4) Å, in agreement with literature values.[58]

X-ray diffraction data at 143(2) K were collected on a second crystal (0.50 × 0.20 × 0.10 mm^3) at the same instrument. For the low-temperature experiment, the crystal was coated with Paratone-N oil and mounted on a cryo-loop and measured under an open-flow nitrogen cryo-stream at 143(2) K. 7976 independent reflections were collected. For refinement in space group *I4/m*, 1009 observed reflections ($I > 2\sigma(I)$) of 1106 unique reflections were used leading to residual values of R = 0.075, wR = 0.221, GoF = 1.23. For refinement in space group *I4*, 1772 observed reflections ($I > 2\sigma(I)$) of 2002 unique reflections were used leading to residual values of R = 0.048, wR = 0.148, GoF = 1.05. The maximum residual electron density was +0.44 / –0.31 eÅ^3 for both refinements. The unit cell was refined to a = 13.504(3) Å, c = 9.731(10) Å (Table 5.1).

The lowest temperature X-ray diffraction data were collected on a third crystal at 20(2) K on a Bruker D8 diffractometer on the ChemMatCARS beam line[63] at the Advanced Photon Source/Argonne National Laboratory (APS/ANL). The diffractometer is equipped with a Bruker 6000 CCD detector. The crystal was coated with Paratone-N oil and mounted on a glass fiber and measured under a stream of helium at 20(2) K. 36372 independent reflections were collected. For refinement in space group *I4*, 10231 observed reflections ($I > 2\sigma(I)$) of 11751 unique reflections were used leading to residual values of

R = 0.037*, wR* = 0.112*, GoF* = 1.03. The maximum residual electron density was +0.64 / –0.54 eÅ^3. The unit cell was refined to *a* = 13.4830(5) Å, *c* = 9.6849(6) Å (Table 5.1).

Global refinements for the unit cell and data reduction were performed with the SAINT program[55a] for diffraction data collected at 293(2) K and 143(2) K. Cell refinement and data reduction for data at 20(2) K were carried out using the APEX2 program package.[55b] Empirical absorption correction was performed with SADABS.[55c] The space group for structure solution and refinement was determined from systematic absences using XPREP.[55a]

5.4.3 Structure Determination

The structures of Fe(TPP)Cl at 293(2), 143(2) K and 20(2) K were solved by direct methods using SHELXS and refined using the SHELXTL proprietary software package.[64] All non-hydrogen atoms were refined with anisotropic displacement parameters. Hydrogen atoms were placed at calculated positions, with isotropic displacement parameters constrained to the equivalent isotropic displacement parameters of the connected carbon atoms [U_{iso}(H) = 1.2U_{eq}(C)]. The structures were checked using PLATON.[65]

Chapter 6

X-ray and Neutron Structures of Low-spin Bis(imidazole)iron(III)tetraphenylporphyrin Chloride Complex

6.1. Introduction

In 1987 the structure of the low-spin bis(imidazole)iron(III)tetraphenylporphyrin chloride complex (**13**) (Figure 6.1) at 292 K was published.[66] Over the past 30 years, analysis on the structural and magnetic properties of this complex has been extensively studied using magnetic susceptibility measurements,[67] electron spin resonance (ESR),[68] nuclear magnetic resonance (NMR),[68b,69] Mössbauer spectroscopy,[70] and magnetic circular dichroism (MCD). Density functional theory DFT) calculations[71] and ENDOOR experiments[72] have also been used in obtaining information regarding the magnetic properties of the Fe(III) center. All of these techniques give in-direct results on the electron spin distribution in complexes. Polarized neutron diffraction is the only tool that directly probes the spin density in paramagnetic compounds.[9] We are interested in using polarized neutron diffraction (PND) to obtain spin densities in the Fe porphyrin complexes. In a PND experiment, the crystal of a Fe porphyrin complex is placed at a low temperature (ca. $\leq$20 K) so the spin density in the crystal is aligned by the external magnetic field.[19,73a,74] Low-temperature X-ray diffraction analysis of the Fe porphyrin complex is required in order to provide initial atomic coordinates for neutron structure

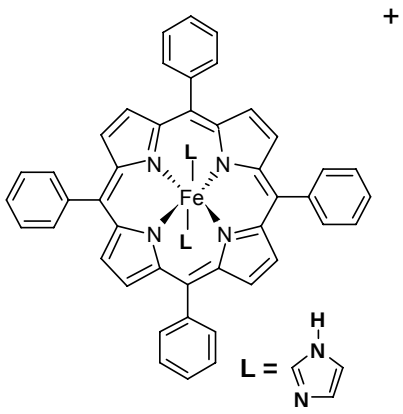

Figure 6.1. Structure of **13**$^{+}$ (L = 1H-imidazole).

determination. In addition, we are interested in observing structural changes of the Fe porphyrin complex at variable temperatures.

We have recently investigated the structural changes of the high-spin iron(III) tetraphenylporphyrin Fe(TPP)Cl (**12**, TPP^{2-} = *meso*-tetraphenylporphyrinate) complex at 20(2), 143(2), and 293(2) K. As temperature was reduced to 20(2) and 143(2) K, the thermal motion of the phenyl groups was reduced. The reduction led to the crystallographic symmetry from *I4/m* at 293(2) K to *I4* space group at 20(2) and 143(2) K.[75] The structural behavior of this Fe(III) porphyrin derivative, with respect to temperature, gives precedent for our current X-ray and neutron studies of $[Fe(TPP)(HIm)_2]Cl$ (HIm = 1H-imidazole) (**13**).

6.2 Results and Discussion

As previously mentioned, the crystal structure of complex **13** at 292 K has been reported.[66] While a unit cell has been obtained at low-temperature,[76] analysis of the low-temperature structure has not been pursued. We have determined the X-ray structures of **13** at 20(2) and 143(2) K and the neutron structure of **13** at 20(2) K. ORTEP plots and unit cell diagrams are given in Figures 6.2 - 6.7. Structural parameters are summarized in Tables 6.1 and 6.2.

The reported structure consists of two independent half Fe ions of $\mathbf{13}^+$ in the triclinic cell. The Fe atom in each ion is located at the inversion center (1/2, 0, 0). Each Fe ion has two imidazole ligands that are parallel to each other. The

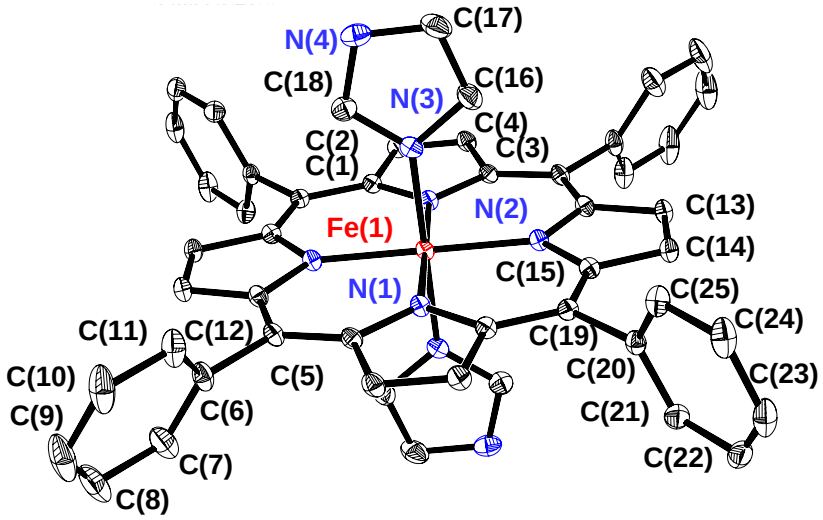

Figure 6.2. ORTEP of the Fe1 molecule in **13**•H_2O•$CHCl_3$ at 143(2) K. Thermal ellipsoids are at 30% probability level. H atoms were moved for clarity.

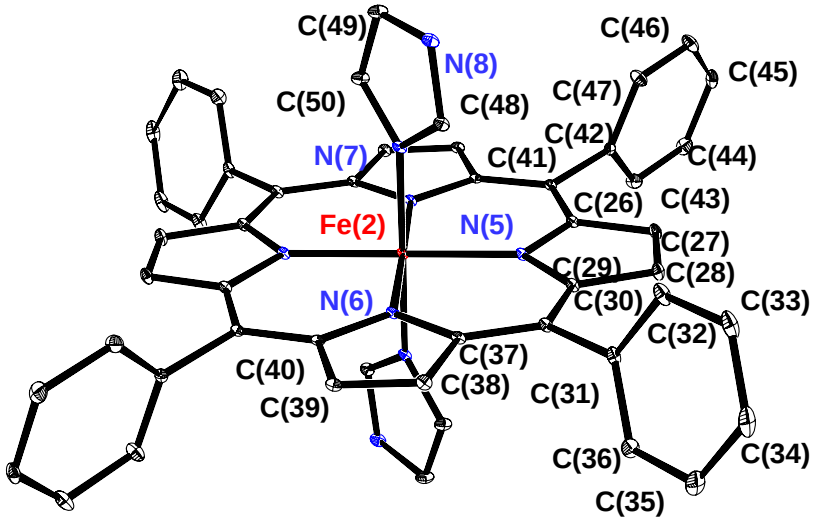

Figure 6.3. ORTEP of the Fe2 molecule in **13**•H_2O•$CHCl_3$ at 20(2) K. Thermal ellipsoids are at 30% probability level. H atoms were moved for clarity.

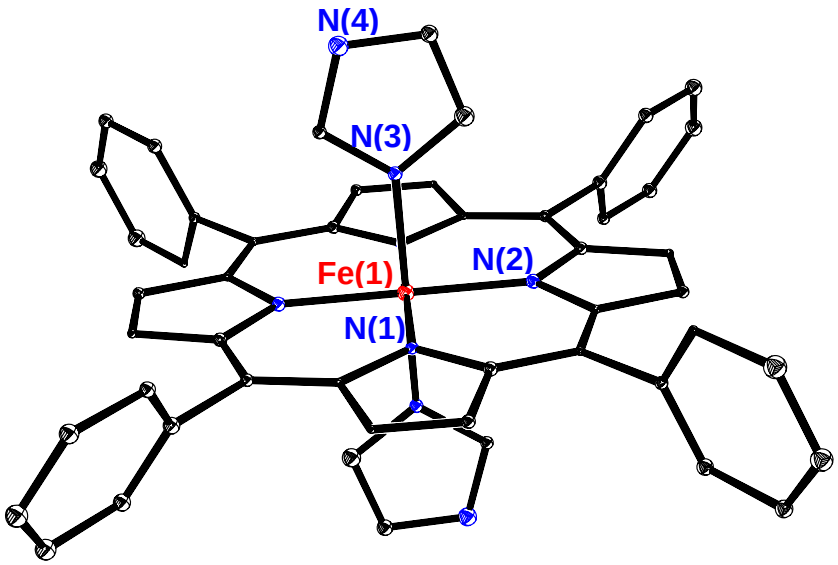

Figure 6.4. Neutron structure of the Fe1 molecule in **13**•H_2O•$CHCl_3$ at 20(2) K. Thermal ellipsoids are at 30% probability level. H atoms were omitted for clarity.

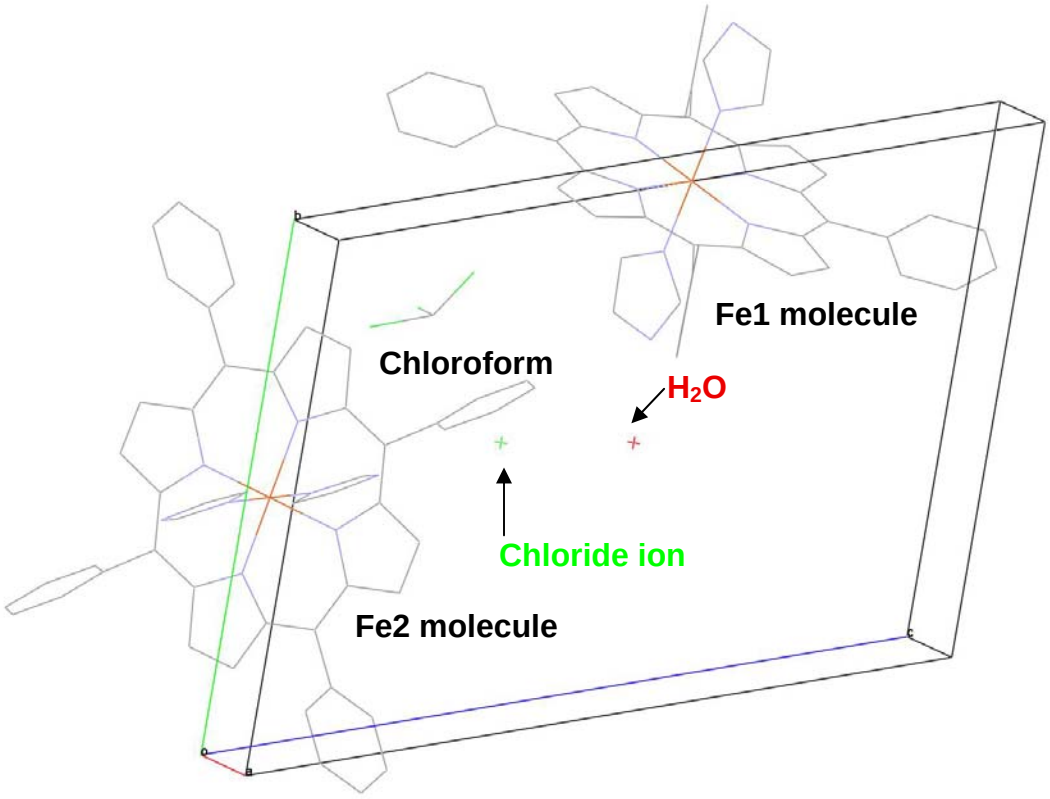

Figure 6.5. Unit cell diagram of the X-ray structure of **13**•H_2O•$CHCl_3$ at 143(2) K. H atoms and disorder were omitted for clarity.

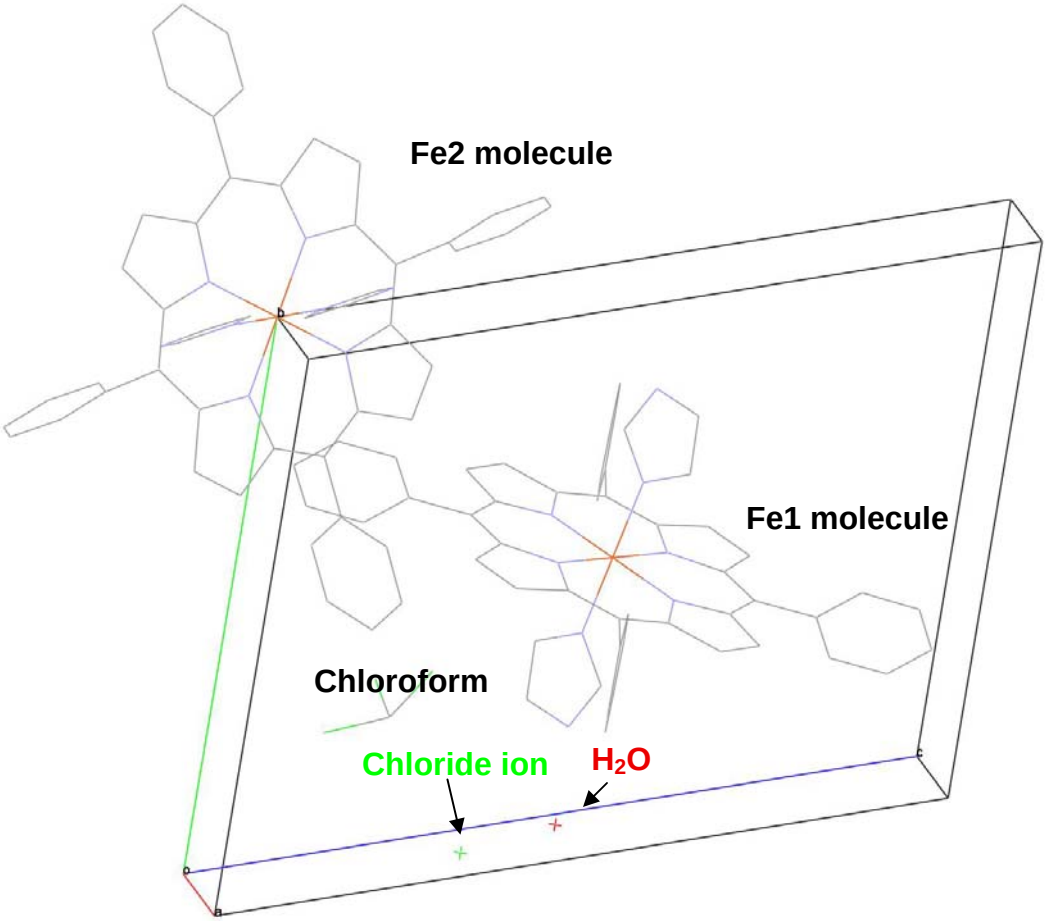

Figure 6.6. Unit cell diagram of the X-ray structure of **13**•H_2O•$CHCl_3$ at 20(2)K. H atoms and disorder were omitted for clarity

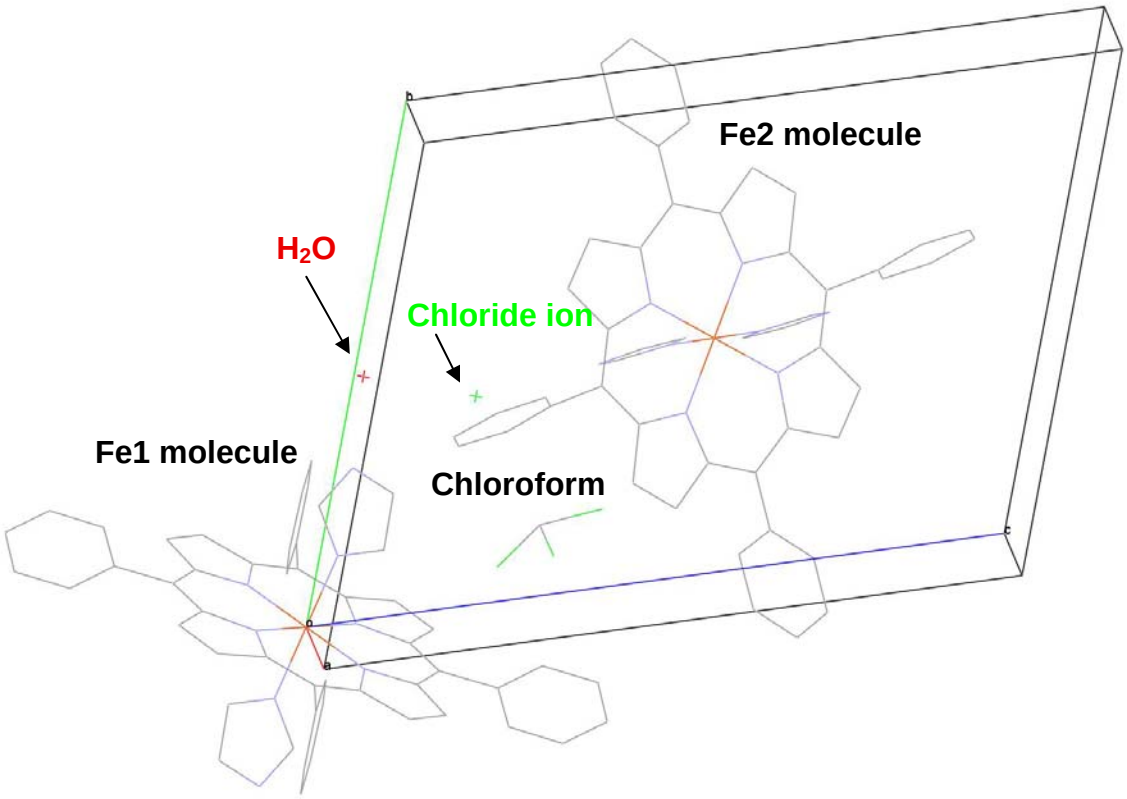

Figure 6.7. Unit cell diagram of the neutron structure of **13**•H_2O•$CHCl_3$ at 20(2) K. H atoms and disorder were omitted for clarity

Table 6.1. X-ray crystal data and structural refinement for **13**•H_2O•$CHCl_3$ at 20(2) and 143(2) K.

Temperature (K)	143(2)	20(2)
Empirical formula	$C_{50}H_{36}FeN_8$•$CHCl_3$•H_2O•Cl	$C_{50}H_{36}FeN_8$•$CHCl_3$•H_2O•Cl
Formula weight	977.55	977.55
Wavelength (Å)	0.71073	0.41320
Crystal system	Triclinic	Triclinic
Space group	*P*-1	*P*-1
Unit cell dimensions	*a* = 11.080(2) Å	*a* = 10.9837(3) Å
	b = 13.156(3) Å	*b* = 13.0500(4) Å
	c = 17.636(4) Å	*c* = 17.5896(5) Å
	α = 69.93(3)°	α = 70.0035(10)°
	β = 72.49(3)°	β = 72.7082(10)°
	γ = 86.21(3)°	γ = 86.4392(10)°
Volume ($Å^3$)	2300.8(10)	2259.97(11)
Z	2	2
Density (cald, Mg/m^3)	1.411	1.437
Abs coeff (mm^{-1})	0.61	0.33
F(000)	1006	1006

Table 6.1. (continued)

Temperature (K)	143(2)	20(2)
θ range (deg)	1.29 - 28.40°	1.13 - 20.30°
Index ranges	$-14 \leq h \leq 14$	$-18 \leq h \leq 18$
	$-17 \leq k \leq 17$	$-21 \leq k \leq 21$
	$-22 \leq l \leq 23$	$-29 \leq l \leq 27$
Reflections collected	24398	145868
Independent reflections	10397	20652
Completeness	99.5% (θ = 26.00°)	92.1% (θ = 21.00°)
Refinement method	Full-matrix least-squares on F^2	Full-matrix least-squares on F^2
Data / restraints / parameters	10397 / 1 / 617	20652 / 4 / 625
Goodness-of-fit on F^2	1.081	1.013
Final R indices [$I > 2\sigma(I)$]	$R1$ = 0.0440, w$R2$ = 0.1039	$R1$ = 0.0564, w$R2$ = 0.1213
R indices (all data)	$R1$ = 0.0621, w$R2$ = 0.1110	$R1$ = 0.0703, w$R2$ = 0.1281

Table 6.1. (continued)

Temperature (K)	143(2)	20(2)
Largest diff. peak and hole ($Å^{-3}$)	0.82, –0.97	0.87, –0.81

[a] $R1 = \Sigma||F_o| - |F_c|| / \Sigma|F_o|$; $wR2 = [\Sigma\, w(F_o^2 - F_c^2)^2 / \Sigma\, w(F_o^2)^2]^{1/2}$; $w = 1/[\sigma^2(F_o) + (aP)^2 + bP]$; $P = [2F_c^2 + \mathrm{Max}(F_o^2, 0)]/3$

Table 6.2. Summary of neutron data for **13** at 20(2) K

Unit cell dimensions	a = 11.000(2) Å	α = 70.253(9)°
	b = 13.058(2) Å	β = 72.852(12)°
	c = 17.604(3) Å	γ = 87.036(13)°
Volume	2270.7 Å^3	
Z	2	
Wavelength	0.8371(2) Å	
No. of reflections for cell parameters	612	
θ range for data collection	4.3 to 19.7°	
Absorption coefficient	0.271 mm^{-1}	
Crystal size	1.5 mm^3	
Reflections collected	2338	
Independent reflections	2193	
R_{int}	0.074	
Index range	$-8 \le h \le 3$, $-10 \le k \le 7$, $-14 \le l \le 13$	
No. of standard reflections	1	
Frequency of standard reflection	50	
Refinement method	F^2	
$R(F)$	0.107	

Table 6.2. (continued)

w$R(F)$	0.126
Goodness-of-fit on F^2	1.699
Data/restraints/parameters	2190/ 0/ 452
Weighting scheme	$w = 1/[\sigma^2(F_o^2) + 0.02F_o^2]$

orientation of the imidazole ligands with respect to the porphyrin ring differ between the two ions. The water molecule, imidazole NH group, and chloride ion illustrate hydrogen bonding. The uncomplexed nitrogen atom (N4) in the Fe1 molecule showed hydrogen interaction to the water molecule with a N4-O distance of 2.774(4) Å. In addition, the water molecule was hydrogen bond to the chloride ion, Cl-O and Cl'-O distances of 3.111(8) and 3.128(5) Å, respectively, around the inversion center. The chloride ion was also hydrogen bond to the uncomplexed nitrogen atom (N8) in the Fe2 molecule with a N8-Cl distance of 3.035(4) Å.[66]

In the current XRD studies, we have monitored behavior of the water molecule and chloride ion at 20(2) and 143(2) K. In the 143(2) K structure, the chloride ion resides near the Fe2 molecule. However, the chloride ion was located near the Fe1 molecule. In both structures the water molecule was found in close proximity to the Fe1 molecule. At 20(2) K, the chloride ion illustrated hydrogen bonding to the water molecule with a Cl-O distance of 3.072 Å. However, in the 143(2) K structure, the Cl-O distance was 3.094 Å. In the 143(2) structure, hydrogen bonding was seen with the uncomplexed nitrogen atom (N4) in the imidazole ligand to the oxygen atom in the water molecule with a N4-O distance of 2.778 Å. In contrast the 20(2) K structure illlustrated no N4-O hydrogen interaction with a N4-O bond distance of 4.332 Å. The uncomplexed nitrogen atom (N8) in the Fe2 molecule had no hydrogen bonding to the water molecule in the 20(2) K and 143(2) K structures, in aggreement with the reported structure. The N8-O average distances were 5.718 and 5.856 Å at 20(2) and

143(2) K, respectively. In the 20(2) K structure, N4 atom did not exhibit a hydrogen bond to the chloride ion with a N4-Cl distance of 3.973 Å and likewise with the 143(2) K structure. In both 20(2) and 143(2) K structures, the chloride ion was hydrogen bonded to the N8 atom in the Fe2 molecule with a distance N8-Cl of 3.043 Å, similar to the reported structure. As expected, the bond lengths and angles in the two independent half Fe ions are similar to those reported in the structure.[66]

The 20(2) and 143(2) K structures are compared to other reported low-spin Fe(III) porphyrin derivatives. For 4[Fe(TPP)$(HIm)_2$]Cl•MeOH (**13**$_4$•MeOH), which crystallizes from a methanol solution,[77] the free chloride ion hydrogen-bonds to oxygen atom in the methanol group, illustrated a Cl-O distance of 3.16 Å. This observation is similiar to those in our 20(2) and 143(2) K X-ray structures. A second hydrogen-bond interaction in the crystal lattice was observed between the chloride ion and the uncomplexed nitrogen atom in the imidazole ligand with a N-Cl distance of 3.07 Å in the reported structure containing MeOH,[77] a difference of a ca. 0.027 Å from our observed N8-Cl distance. In the reported [Fe(OEP)$(2\text{-MeH})_2$]ClO_4 (OEP^{2-} = octaethylporphyrinate; 2-MeH = 2-methylimidazole) crystal structure, hydrogen-bond interaction was observed between the oxygen atom in the water molecule to an uncomplexed nitrogen atom in the 2-methylimidazole ligand in one of the two Fe molecules with a N-O distance of 2.936 Å.[78] Similiary, the oxygen atom in the perchlorate ion illustrated hydrogen-bond interaction to an uncomplexed nitrogen atom in the 2-methylimidazole ligand in the second Fe molecule. The N-

O distance was 3.06 Å.[78] Unlike our 20(2) K structure, $[Fe(OEP)(2\text{-}MeH)_2]ClO_4$ exhibited N-O hydrogen interaction. As previously stated, the 143(2) K structure had a N4-O distance of 2.778 Å, a difference of ca. 0.158 Å from that of $[Fe(OEP)(2\text{-}MeH)_2]ClO_4$.

The neutron structure at 20(2) K was obtained and used in our spin-density studies (Chapter 7). A structural comparison of the neutron structure and the low-temperature X-ray structures are presented. The hydrogen bonding of the oxygen atom in the water molecule to the chloride ion has the same O-Cl distance of 3.072 Å as shown in the 20(2) K X-ray structure. The lack of hydrogen interaction of the uncomplexed nitrogen atom in the Fe1 molecule to the water molecule with a N4-O distance of 4.332 Å is also similar to that observed in the 20(2) K structure. In the contrary, the neutron and 143(2) K X-ray structures both exhibit similar N8-O distances of 5.716 and 5.718 Å, respectively. The presence of a hydrogen bond of the uncomplexed nitrogen atom in the Fe2 molecule and the water molecule was similar to that in both the 20(2) and 143(2) K structures with a N8-Cl distance of 3.045 Å vs. the X-ray N8-Cl distance of 3.043 Å. The chloride ion showed no hydrogen-bond interaction to the uncomplexed nitrogen atom in the Fe1 molecule (N4-Cl distance = 4.150 Å), which is similarly observed in the 20(2) and 143(2) K structures.

6.3 Concluding Remarks

The 20(2) and 143(2) K X-ray structures of the low-spin $[Fe(TPP)(HIm)_2]Cl{\cdot}H_2O{\cdot}CHCl_3$ (TPP^{2-} = *meso*-tetraphenylporphyrinate; HIm =1H-imidazole) (**13**$\bullet H_2O\bullet CHCl_3$) have been determined. The hydrogen bonding network of the water molecule, chloride ion, and uncomplexed nitrogen atoms (N4 and N8) in the imidazole ligand show how temperature can play a vital role in the structural behavior of a complex. The neutron structure of **13**$\bullet H_2O\bullet CHCl_3$ was collected at 20(2) K and its structural parameters were discussed and compared to the X-ray structure of **13**$\bullet H_2O\bullet CHCl_3$.

6.4 Experimental Section

6.4.1 Synthesis of 13

Fe(TPP)Cl (**12**) was purchased from Strem Chemicals. 1H-imidazole was purchased from Aldrich. Solvents (Analytical Reagents) were used without further purification. Wet chloroform was prepared by adding water to chloroform (Certified ACS), and the mixture was shaken and then allowed to settle. Wet chloroform at the bottom was then removed for the use below.

The $[Fe(TPP)(HIm)_2]Cl$ (**13**) complex was prepared by modified literature procedures.[66] Fe(TPP)Cl (**12**) and imidazole were dissolved in wet chloroform (4 mL) and then layered with a 1:3 wet chloroform:hexane mixture (4 mL). Water (40 μL) was added to the diffusion layer. The sample was sealed with parafilm.

Crystals of **13**•H_2O•$CHCl_3$ were observed in 3-5 days.

6.4.2 X-ray Data Collection

X-ray data at 143(2) K were collected on a Bruker AXS Smart 1000 X-ray diffractometer equipped with a CCD area detector and a graphite-monochromated Mo source (K_α radiation, 0.71073 Å) and fitted with an upgrade Nicolet LT-2 low temperature device. Suitable crystals were coated with paratone oil (Exxon) and mounted on a cryo-loop under a stream of nitrogen.

At 20(2) K, X-ray data were collected on a Bruker D8 diffractometer on the ChemMatCARS at the Advanced Photon Source/Argonne National Laboratory (APS/ANL). The diffractometer is equipped with a Bruker 6000 CCD detector and a diamond-monochromated metal alloy source (K_α radiation, 0.413 Å) using an open-flow liquid He cryostat. A suitable crystal was coated with paratone oil (Exxon) and mounted on a glass fiber under a stream of helium at 20(2) K.

Global refinements for the unit cell and data reduction were performed under the SAINT program[55a] for data collected at 293(2) K and 143(2) K. Cell refinement and data reduction for data at 20(2) K were carried out using the APEX2 program package.[55b] Empirical absorption correction was performed with SADABS.[55c] Space groups were determined from systematic absences by XPREP[55a] and further justified by refinement results.

6.4.3 X-ray Structure Determination

The structures of **13**•H_2O•$CHCl_3$ at 143(2) K and 20(2) K were solved by Patterson method and refined using the SHELXTL proprietary software package.[64] All non-hydrogen atoms were refined with anisotropic displacement parameters. Hydrogen atoms were placed at calculated positions with isotropic displacement parameters [U_{iso}(H) = 1.2U_{eq}(C)] in final structural refinement .

6.4.4. Neutron Data Collection

Neutron diffraction data were measured at 20(2) K on the four-circle diffractometer D9 at the Institut Laue-Langevin (ILL), Grenoble, France, in a beam of wavelength 0.8371(2) Å obtained by reflection from a Cu(220) monochromator. D9 is equipped with a small two-dimensional area detector[79] whose main advantage for this measurement was to allow optimal delineation of the peak from the considerable incoherent background due to the large percentage of H in the sample. The sample temperature was maintained by a closed-cycle He refrigerator. Data collection was obtained by using MAD.[80] Cell refinement and integration were performed using RAFD9 and RACER.[81,82a] Refinement of the crystal structure at 20(2) K was performed in the space group *P-1* using SHELX-97[55b] starting from our 143(2) K X-ray atomic coordinates and using the known neutron scattering lengths for Fe, C, N, O, Cl and H.[82b]

6.4.5. Neutron Structure Determination

Initially isotropic thermal displacement parameters were assumed for all atoms, and those of the H atoms were no longer constrained to be related to those of the closest heavier atom. In the final refinement the thermal displacement parameters of the Cl and H atoms on the chloroform molecule and the H atoms in the water molecule were refined as anisotropic.

CHAPTER 7

Spin Distribution in a Low-Spin [Fe(TPP)(HIm)$_2$]Cl Complex by Polarized-Neutron Diffraction

7.1. Introduction

Metals such as iron play important roles in biological systems.[83,84] Fe-containing hemes are involved in, e.g., respiration by hemoglobins, electron transfer, and catalytic reactions. In these metalloproteins, the complexes of Fe ions, porphyrins, and axial histidyl imidazole ligands contain unpaired electrons.[68a,b,83-85] Magnetic properties of and spin distributions in the Fe-containing hemes are believed to play an important role in the biological functions of the hemes including redox chemistry and the binding of the hemes with O_2, a paramagnetic compound in its ground state.

Low-spin (S = 1/2), Fe(III) porphyrin complexes, such as d^5 [Fe(TPP)(HIm)$_2$]Cl (**13**, Figure 6.1 in Chapter 6) containing two axial ligands and one overall unpaired electron, have been extensively studied with the use of several techniques including magnetic susceptibility measurements,[67] electron spin resonance (ESR),[68,72c,80] nuclear magnetic resonance (NMR),[68a,b,69,85a-c,85h,86e,f,87] Mössbauer spectroscopy,[68a,70,85h,86f,i,88] and magnetic circular dichroism (MCD).[85d,e,89] Spin distributions in the complexes have been one focus of the studies. Semi-empirical models have been developed to interpret the ESR and NMR spectra to obtain distributions of the unpaired

electrons, as similarly has been done with Fe(TPP)Cl (**12**).[90] Density function theory (DFT) calculations have also been conducted to probe the Fe porphyrin complexes and their spin density.[88] There is however an apparent contradiction regarding the distribution of the unpaired electron density.[69c,91a] The ESR work shows that the unpaired electron is essentially confined in one of the d_π (d_{xz} or d_{yz}) orbitals of iron, although the spin density is slightly delocalized to the ligands.[68c,72c,86] In other words, the unpaired electron is almost completely localized at the metal center. In contrast, NMR studies reveal that a significant amount of the unpaired electron density (up to 0.2 e) is delocalized to the ligands.[69,87] Recent electron nuclear double resonance (ENDOR) and electron spin echo envelope modulation (ESEEM) spectroscopic studies show that the spin density is slightly delocalized to the porphyrin ligand, although nearly one unpaired electron remains localized in the Fe d_π orbitals.[68a,72,92] The extent of the spin delocalization in the low-spin Fe(III) porphyrin complexes has been investigated.[69c,93] Studies using Fe L-edge X-ray absorption spectroscopy have recently determined the delocalization of the Fe d-electrons into the porphyrin ring in terms of both porphyrin$\rightarrow$Fe σ and π-donation and Fe$\rightarrow$porphyrin π back-bonding.[94] DFT calculations also provide spin density in low-spin Fe porphyrins.[71a,90a] The theoretical studies show that the Fe center and the Fe-N bond axes possess (nearly 1) α and significant β spin, respectively. The β spin in the Fe-N bond axes leads to the presence of additional α spin in the porphyrin and axial ligands. Polarized neutron diffraction (PND) has proven to be a very

powerful tool to determine the spin density in single-molecule magnets, inorganic complexes, and organic radicals.[9,73,95,96] This technique utilizes both the wave- (diffraction) and particle-like (spin) properties of the neutron, and it is the only known technique that directly gives the distribution of spin density in a compound.[9,73,95] In comparison, spectroscopic techniques such as ESR and NMR use magnetic nuclei as local probes, and are limited by nonmagnetic nuclei in a compound. In a PND experiment, a single crystal of a paramagnetic compound is placed inside a magnetic field at a low temperature (ca. 4 K) so the spin density in the crystal is aligned by the external magnetic field.[9,73,95,96e,f] The incident neutron beam is polarized either parallel or antiparallel to the magnetic field. Neutrons are diffracted *via* interactions with the nuclei as well as with the spin density. With a knowledge of the crystal structure magnetic structure factors $F_M(hkl)$ are extracted from the ratios of observed diffracted intensities at the Bragg positions (*hkl*) for the two incident-beam polarizations and are used to give spin density maps in the compound. The $F_M(hkl)$ are Fourier components of the spin density in the crystal, just as X-ray diffraction structure factors are Fourier components of the electron density in the crystal. The principal limitation of the PND technique is the low flux of neutron sources, more so for the increasingly complex structures exhibiting molecular magnetization.

Thus far polarized neutron diffraction has not been used to study the magnetic properties of the biological systems or biomimetics.[93-96] We report here results of our first studies of spin density in [Fe(TPP)(HIm)$_2$]Cl (**13**). Compound **13** was chosen here for our initial PND study mainly because it is considered to

be a classic biomimetic compound.[66,68b,c,70,86c,86e,f,h,i,87b,c]

7.2. Results and Discussion

An in-depth analysis was completed on the spin distribution of the one unpaired electron density on the Fe(III) center. Results were in agreement with the ESR, ENDOR, ESEEM, and DFT calculations – the spin density is mainly localized on the metal center. Thus, our polarized-neutron diffraction study was able to make a concrete conclusion on what all other non-direct methods were proving.

7.2.1. Preparation of Large Crystals of 13•H_2O•$CHCl_3$

As previously mentioned in Chapter 6, Scheidt and coworkers have determined the crystal structure of **13**•H_2O•$CHCl_3$ at 292 K.[66] An identical cell with a slightly smaller volume at 123 K was reported later.[76]

Initially, growing large crystals (>5 mm^3) of **13**•H_2O•$CHCl_3$ was unsuccessful. The preparation consisted of using chloroform (Fisher) and sealing the test tubes. Thus, a minimal amount of moisture was allowed into the system. Small crystals for the reported structure of **13**•H_2O•$CHCl_3$ contained lattice water, and the solution for crystallization was probably left unsealed.[66,76] Thus moisture from the air appears to be a key feature in the crystallization process. Multiple tests were conducted to determine the precise amount of water to be added to the diffusion layer in order to maximize crystal growth. It was

determined that 40 μL of water introduced by washing the chloroform (Fisher) was sufficient to insure that water was incorporated in the crystallization process. Pictures of crystals of **13**•H_2O•$CHCl_3$ thus obtained are shown in Figure 7.1.

7.2.2. Polarized Neutron Diffraction

The magnetization density is the Fourier transform of the magnetic structure factors F_M, which can be experimentally determined by the polarized-neutron diffraction (PND) technique.[9,73c,95,97] In a paramagnetic regime there is no spontaneous magnetization in the sample and magnetic saturation is achieved by the application of a large (vertical) magnetic field at low temperature (in order to minimize thermal fluctuations of the electron spins). Magnetic saturation of the sample was achieved by application of a 9 T magnetic field at ~3 K. While the nuclear contribution to the diffraction intensities is independent of the polarization of the neutron beam, the magnetic contribution varies depending on whether the incident beam is polarized parallel or anti-parallel to the applied field. In a PND experiment the measured quantity is the flipping ratio $R(hkl) = I^+/I^-$, where I^+ and I^- are the diffracted intensities of a Bragg reflection with the incident neutron beam polarization parallel and anti-parallel, respectively, to the applied magnetic field. When the crystal structure is centrosymmetric, as in the present case, both the magnetic structure factor and the nuclear structure factor are real. *R(hkl)* is then given by,

Figure 7.1. Photo of crystals of **13**•H_2O•$CHCl_3$.

$$R(hkl) = \frac{I^+}{I} = \frac{F_N^2 + 2pq^2F_NF_M + q^2F_M^2}{F_N^2 - 2epq^2F_NF_M + q^2F_M^2} \qquad \text{(Eq. 7.1)}$$

where F_N is the nuclear structural factor determined from non-polarized neutron diffraction and q is the sine of the angle between the scattering vector and the magnetic field direction, p is the polarization of the incident beam, and e is the flipping efficiency.[97,98] All quantities except F_M in Eq. 7.1 are known. Thus both the amplitude and the phase of each magnetic structure factor F_M may be determined directly from Eq. 7.1.

Magnetic 'flipping ratios' for 263 unique reflections to $\sin\theta/\lambda$ = 0.40 Å^{-1} were collected using three orientations of the triclinic crystal on D3 in an applied field of 9 T at ~3 K. The observed flipping ratios from 0.61 to 1.43 with generally small statistical error, indicate strong local magnetization in this relatively large structure. Ratios significantly different from 1.0 are also observed for many reflections of type $h + k + l \neq 2n$. This indicates that the magnetization distribution is not body-centered as would be the case if there were just identical magnetization of the two Fe ions which lie on the special positions 0 0 0 and 1/2 1/2 1/2. The sampling of the unique region of reciprocal space is however relatively sparse due to the weakness of the majority of the (nuclear) reflections. Furthermore the observed limit of 0.4 Å^{-1} in $\sin\theta/\lambda$ is well below the value at which the magnetic form factor for Fe(III) falls to zero. These two factors mean that magnetization maps obtained by simple Fourier inversion of the limited data suffer from Fourier truncation errors and are difficult to interpret beyond

identifying that the main magnetization centers are the two iron sites.

Instead, the spin density has been modeled to provide a best fit to the observed magnetic structure factors. This was carried out in a similar way to a conventional structure refinement, except that we could refine against *phased* structure factors, and only the suspected magnetic sites are included with the appropriate magnetic form factors. Refinement of the model was made against the signed observed magnetic structure factors using the program MPLSQ of the Cambridge Crystallographic Subroutine Library.[99] Two models were tried. For the first, the moments were assumed to be spherically distributed on the atomic sites, while in the second, the moment distributions on the Fe sites were modeled by a multipolar expansion of the products of spherical harmonics and radial wavefunctions of the general form:

$$\rho = \sum_{l} \sum_{m} a_{l,m} Y(l,m) < j_l >$$

with l = 0, 2, 4, .., and m = -l, -l+2,..0..,l-2, l for a centrosymmetric site, where $Y(l,m)$ are the spherical harmonics, $<j_l>$ are the radial wavefunctions, and $a_{l,m}$ are the population coefficients. The local axes to describe the spherical harmonics were chosen to put x along Fe-N(nearest porphyrin ring) and z along Fe-N(imidazole). With the scale factor fixed at 1.0, and the magnetic form factors normalized to 1.0 at $\sin\theta/\lambda$ = 0 Å^{-1}, the refined site occupations of the atoms included give the total spin on each site in *e*. In view of the limited number of data and the overall precision, chemically-equivalent, but not necessarily crystallographically-equivalent, atoms across the two porphyrin molecules were

constrained to have the same spin population, which gave only 14 independent atoms, excluding the water and chloroform molecules and all H atoms. Various combinations of sites in addition to the two Fe sites were included in the model and the significance of each added site judged by both the reduction of the goodness of fit and the estimated standard deviation of the refined site occupation. The significance of the various terms in the multipolar expansion of the Fe moments was judged in the same way. Polarized neutron diffraction parameters can be found in Table 7.1. The spin populations on the two Fe molecules are given in Table 7.2. A nuclear map and a spin density map on the Fe1 center are given in Figure 7.2.

The previous *ab initio* DFT calculations and ENDOR studies have indicated that the spin density away from the Fe sites is concentrated on the nearest-neighbor N sites in the planes of the porphyrin rings.[71,90] This was also borne out by the refinements against our observed magnetic structure factors; the spin is located predominantly on the Fe sites (~1.5 *e* on each), with ~0.05 *e* polarized antiparallel on each of the four N sites in each porphyrin ring and ~0.02 *e* also polarized antiparallel on the nearest N atoms of the imidazole ligands, although the latter is barely significant within the errors of our data (Table 7.2). No significant spin density was identified elsewhere in the unit cell. Notably the total moment delocalized onto the nearest neighbours around each Fe site is 0.2 *e* within error, exactly the amount given by the NMR studies.[69,87]

Chapter 9 discusses the preparation of deuterium-labeled [Fe(TPP)(ImH)$_2$-d_{36}]Cl (**13-d_{36}**). The use of the deuterated compounds in neutron diffraction

Table 7.1. Parameters of the polarized neutron data collection

Compound No.	**13**•H_2O•$CHCl_3$
Crystal volume	1.5 mm^3
Temperature	~3 K
Magnetic field	9 T
Monochromator	Cu_2MnAl (111)
Wavelength	0.8371 Å
Polarization	0.975(5)
Flipping efficiency	1.000(5)
$\lambda/2$ ratio	0.004
No. of data	702
$Sin\theta/\lambda_{max}$	0.40 $Å^{-1}$
Index range	$-8 \leq h \leq 8$, $-8 \leq k \leq 6$, $-12 \leq l \leq 12$
No. of independent reflections	263

Table 7.2. Spin populations (*e*) and significant multipole coefficients (*e*) in **13**.

Atom	**Population**	
	Model 1	Model 2
Fe1	1.144(3)	1.136(23)
$a_{2,0}$	-	0.85(18)
$a_{2,1,-}$	-	-0.78(15)
$a_{2,1,+}$	-	0.12(14)
$a_{2,2,-}$	-	-0.26(10)
$a_{2,2,+}$	-	-0.35(17)
N1	-0.018(11)	0.01(2)
N3	0.002(13)	-0.03(2)
N4	0.000(15)	-0.007(14)
C1	-0.020(9)	-0.035(9)
C2	0.017(4)	0.022(4)
C5	0.000(11)	0.004(11)
C6	-0.028(10)	-0.015(10)
C7	0.014(7)	0.008(7)
C8	-0.012(6)	
C9	0.001(7)	-0.000(7)
C16	0.001(14)	0.010(14)
C17	0.002(12)	0.008(12)

Table 7.2. (continued)

Atom	Population	
	Model 1	Model 2
C18	0.018(16)	0.035(16)
χ^2	2.64	2.56

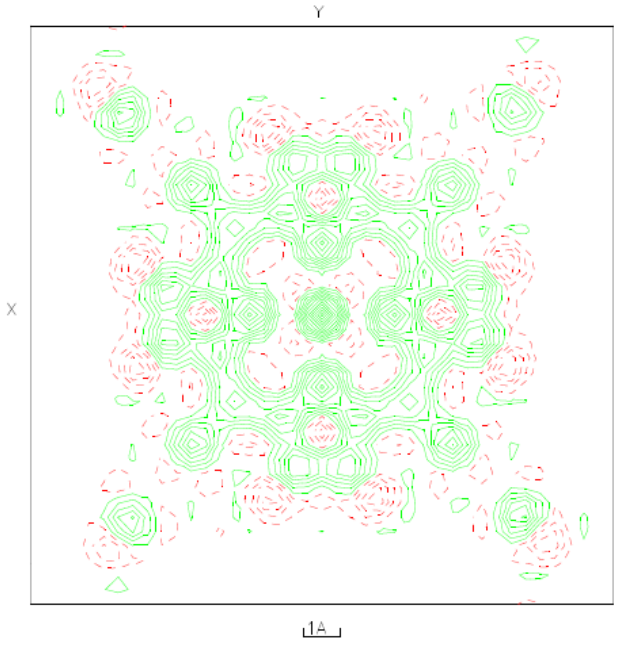

(a)

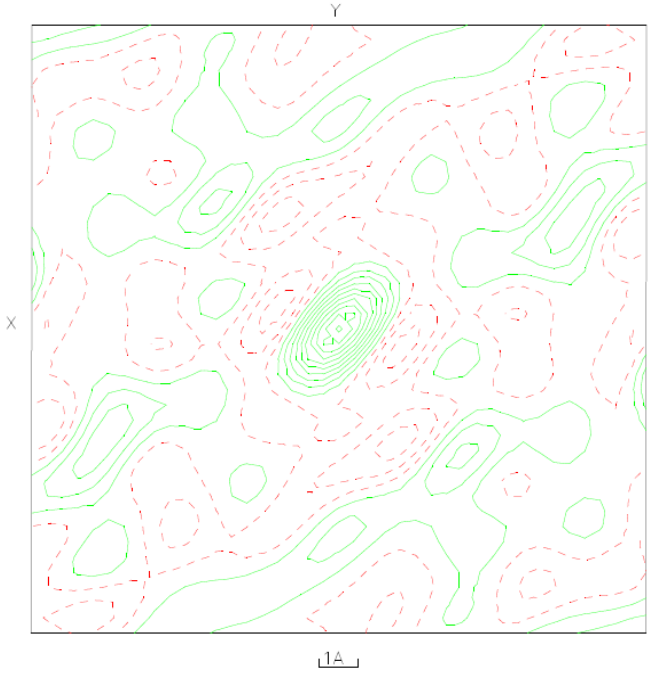

(b)

Figure 7.2. (a) A nuclear map along the Fe1-N1-N2 plane; (b) Spin density map on the Fe1 center.

would reduce background scattering by H atoms, and enhance the signal/noise ratios. Ordinary hydrogen atoms have a large incoherent neutron cross section, which is negligible for D atoms. Thus the deuterated sample is expected to deliver much clearer signals to reveal the spin densities on the C atoms.

7.3. Concluding Remarks

Studies of the spin distribution in low-spin (S = 1/2) [Fe(TPP)(HIm)$_2$]Cl (**13**, TPP^{2-} = *meso*-tetraphenylporphyrinate; HIm = 1H-imidazole) by single-crystal polarized-neutron diffraction show that the Fe atom and the N atoms in the porphyrin and imidazole ligands possess +1.15(2) electron of α-density and –0.02 to –0.07 electron of β–density, respectively. The total moment delocalized onto the nearest neighbors around each Fe site is 0.20(3) e, in agreement with that suggested by NMR studies.

7.4. Experimental Section

7.4.1. General Procedures

Fe(TPP)Cl (**12**) was purchased from Strem Chemicals. 1H-imidazole (99 %) was purchased from Aldrich. Wet chloroform was prepared by adding water to chloroform (Certified ACS), and the mixture was shaken and then allowed to settle. Wet chloroform at the bottom was then removed for the use below.

7.4.2. Preparation of Crystals $[Fe(TPP)(HIm)_2]Cl \bullet H_2O \bullet CHCl_3$ ($13 \bullet H_2O \bullet CHCl_3$)

Crystals suitable for neutron diffraction were prepared by a modified literature procedure.[66] Fe(TPP)Cl (**12**, 35.7 mg, 0.051 mmol, Strem) and imidazole (22.7 mg, 0.333 mmol, Aldrich, 99 %) were mixed in wet chloroform (4 mL) in a 15-mL test tube. A 1:3 chloroform:hexane mixture (4 mL) was then carefully added to form a layer on top of the solution and water drop. A small drop of water (40 μL) was placed between in the diffusion layer. The test tube was capped and kept at 23 ºC for about 3–5 days to give large ($\geq$5 mm^3) single crystals of **13**$\bullet H_2O \bullet CHCl_3$ (22.6 mg, 0.023 mmol, 45% yield).

7.4.3. Crystal Mounting for Polarized Diffraction

The crystal selected for the neutron study was a trapezoidal plate with principal dimensions 2.3 $\times$ 1.5 $\times$ 0.4 mm^3. To protect the crystal from possible strain when cooling and to facilitate changes of mounting it was wrapped in thin Al foil before being glued to an Al sample pin.

7.4.4. Polarized Neutron Diffraction

Spin-flip ratios for spin-up and spin-down polarized incident neutrons were measured at the polarized neutron diffractometer D3 at the ILL. The single crystal was measured in three crystal orientations in a 9 T magnetic field and at 2.3 to 4.8 K. Data collection was obtained by using MAD[80] after cell refinement using RAFNB. Data reduction were performed using ARRNGE, and the

SORGAM of the CCSL suite.[81,99] Structure refinement was completed by MPLSQ of the CCSL suite.[99]

CHAPTER 8

Synthesis and Studies of Deuterated *meso*-Tetraphenylporphyrin Iron(III) Derivatives

8.1. Introduction

Metals such as iron play important roles in biological systems.[56,83,84] In systems such as hemoglobins/myoglobins (for O_2 transport) and cytochrome c (for electron transfer), Fe ions are bound to the porphyrins known as hemes. The Fe ions in the proteins are either five- or six-coordinated. The five-coordinated Fe ions such as those in the myoglobin hemes (see Figure 5.1. in Chapter 5) have a high-spin configuration prior to O_2 binding. The six-coordinated Fe ions often have low-spin configurations. Magnetic properties of these metalloproteins are important to the binding of, e.g., the hemoglobins/myoglobins to paramagnetic O_2 and electron transfer in cytochrome *c*.[85] Several techniques have been used to probe magnetic properties of hemes and their molecular models.[56] *meso*-Tetraphenylporphyrin Fe(III) complexes Fe(TPP)Cl[58] (**12**) and [Fe(TPP)(HIm)$_2$]Cl (HIm: 1H-imidazole) (**13**) are two models for five-coordinated, high-spin and six-coordinated, low-spin hemes, respectively. They have been studied extensively.

Neutron scattering is a unique technique to probe magnetic properties, as spin of neutrons interacts with spin of unpaired electrons in molecules during the scattering processes.[9] Inelastic neutron scattering (INS) leads to magnetic

excitations, while elastic scattering (diffraction) by polarized neutrons is the only known technique to directly give spin (unpaired electron) density distribution in a molecule.[9,73c,95,96] Both INS and polarized neutron diffraction have been recently used to study paramagnetic compounds and single molecular magnets.[9,73c,95,96] The use of neutron scattering in the studies of magnetic properties of biological or biomimetic systems is, however, limited.

Neutron scattering studies often require or prefer the use of deuterated samples in order to reduce background, incoherent scattering by H atoms in the samples. In addition, polarized neutron diffraction of a single crystal is often conducted at a low temperature.[9,73c,95,96] Per-deuterated *meso*-tetraphenylporphyrin Fe(III) derivatives Fe(TPP)Cl-d_{28} (**12-*d*$_{28}$**) and [Fe(TPP)(DIm)$_2$-d_{36}]Cl (DIm: 1D-imidazole-d_4) (**13-*d*$_{36}$**) (Scheme 8.1), to our knowledge, have not been reported. In the current work, D_2(TPP-d_{28}) (**14-*d*$_{30}$**) has been prepared from benzaldehyde-d_6 and pyrrole-d_5 and characterized by mass spectrometry and X-ray diffraction. The two per-deuterated Fe(III) complexes **12-*d*$_{28}$** and **13-*d*$_{36}$** have been prepared from **14-*d*$_{30}$**. The X-ray crystal structure of **12-*d*$_{28}$** has been determined at 293(2) K, and that of **13-*d*$_{36}$** has also been examined at 173(2) and 293(2) K. These studies are presented here.

8.2. Results and Discussion

Preparation of *meso*-tetraphenylporphyrin (H_2TPP, **15**) has been reported using a few well-known methods. In one such procedure, benzaldehyde (1 mol)

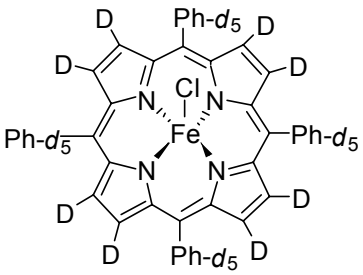

12-d_{28}

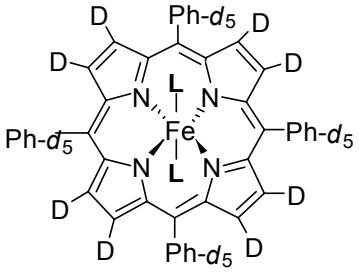

13-d_{36}

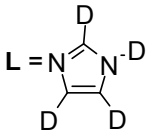

Scheme 8.1. Structures of **12-d_{28}** and **13-d_{36}**.

and pyrrole (1 mol) are added to refluxing propionic acid.[100] If propionic acid is not used, an acid catalyst such as BF_3 or trifluoroacetic acid is added to a mixture of benzaldehyde and pyrrole.[101,102] This reaction to prepare H_2TPP (**15**) is also known to give *meso*-tetraphenylchlorin (H_2TPC) as a byproduct. (See Scheme 8.3 for the structure of deuterated *meso*-tetraphenylchlorin.) After the reaction, the solution is cooled down to room temperature, and a solid containing H_2TPP (**15**) and *meso*-tetraphenylchlorin (H_2TPC) precipitates out of solution. The solid is washed with methanol and filtered. H_2TPC in the mixture is either removed[100a] or converted to H_2TPP (**15**) by adding a quinone oxidant such as 2,3-dichloro-5,6-dicyanobenzoquinone (DDQ) or *p*-chloranil to the solution of the mixture.[100b,101,102] Afterwards, H_2TPP (**15**) in the solution is purified by column chromatography.

8.2.1. Synthesis and Characterization of D_2(TPP-d_{28}) (14-d_{30})

14-d_{30} was prepared in the current work by the procedure shown in Schemes 8.2 and 8.3. Although benzaldehyde-d_6 and pyrrole-d_5 are commercially available, they were prepared by the reactions in Schemes 8.2 and 8.3. The former was yielded from the oxidation of toluene-d_8 by ceric ammonium nitrate.[103] Pyrrole-d_5 was prepared through H-D exchange between pyrrole and propionic acid-d_1 by a procedure reported by Shirazi and Goff.[104] In the reported work, pyrrole-d_5 was then used to react with non-deuterated benzaldehyde to make **14-d_8** with 90% deuteration on the pyrrole positions.

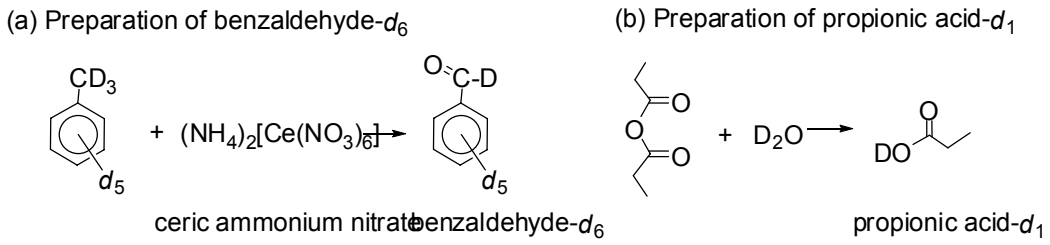

Scheme 8.2. Preparation of benzaldehyde-d_6 and propionic acid-d_1.

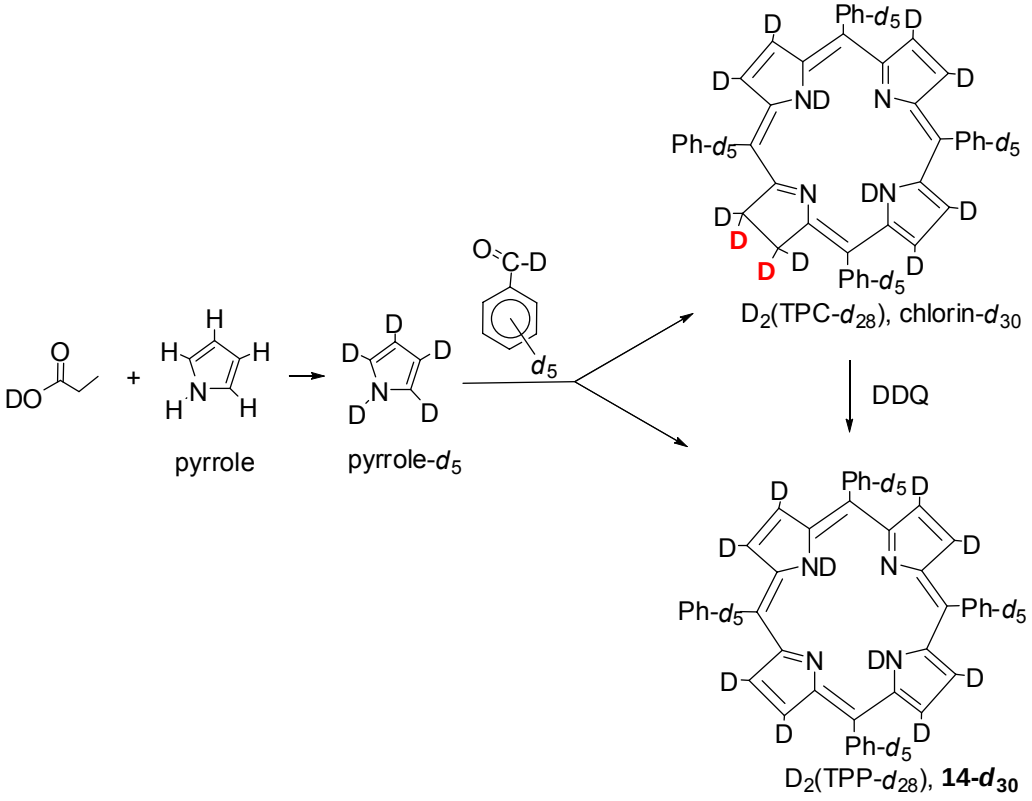

Scheme 8.3. Preparation of **14-d_{30}**.

In the current studies, pyrrole-d_5 containing propionic acid-d_1 and benzaldehyde-d_6 prepared above were mixed to make **14-d_{30}** similar to a procedure by Asano and coworkers, using commercial pyrrole-d_5.[105] This is, to our knowledge, the only report of the preparation of nearly per-deuterated *meso*-tetraphenylporphyrin (**14-d_{30}** with the –N-H positions being partially deuterated), although there have been other reports of synthesis of, e.g., pyrrole-deuterated **14-d_8**.[104] As in the procedure that Asano and coworkers used, DDQ was used as an oxidant to convert *meso*-tetraphenylchlorin-d_{30} D_2(TPC-d_{28}) to **14-d_{30}** (Scheme 8.3).[104,105] The crude dried product was washed with excess methanol prior to silica-gel chromatographic purification.[105] We have found it to be critical to remove all propionic acid-d_1 before the chromatographic separation to obtain pure, crystalline **14-d_{30}**. In comparison, Asano and coworkers washed the product after chromatography. A UV-Vis spectrum of the sample after chromatography shows reported bands that are also observed for H_2TPP (**15**).[100b]

The degree of deuteration in the per-deuterated samples is an interesting point to study and important to neutron scattering experiments using the Fe porphyrin samples. There are several potential sources to introduce H atoms. The deuterated starting materials toluene-d_8 (99.9 atom% D) and D_2O have varied degrees of deuteration. Pyrrole-d_5 was prepared through H-D exchange between pyrrole-h_5 and propionic acid-d_1.[104] The degree of the H-D exchange is not clear. In addition, a small amount of H^+ ions from pyrrole-h_5 through H-D exchange with propionic acid-d_1 may be incorporated into deuterated *meso*-

tetraphenylchlorin. Although kinetic isotope effect (KIE) in the subsequent oxidation by DDQ may preferentially remove H atoms from chlorin, some H atoms are expected to remain in deuterated *meso*-tetraphenylporphyrin. These factors may potentially yield D_2(TPP-d_{20}) (**14-d_{22}**) to D_2(TPP-d_{28}) (**14-d_{30}**). We have developed a mass simulation method to obtain the degree of deuteration in the sample.

MALDI mass spectrometric analysis (Figure 8.1) of the sample after chromatographic separation showed **14-d_{28}** as well as significant amounts of **14-d_{29}** and **14-d_{30}** with deuteration of the pyrrole N atoms. The deuterium atoms in the N-D bonds have undergone a substantial H-D exchange with moisture and residual H_2O in solvent and surface –OH groups in the silica gel used in chromatography, leading to difficulties in MS analysis. We have thus used the exchange with H_2O to convert D_2(TPP-d_n) (**14-d_{n+2}**) to H_2(TPP-d_n) (**15-d_n**, Scheme 8.4) in order to conduct MALDI mass spectrometric (MS) analysis of the sample. A crystal of **14-d_{30}** was dissolved in chloroform, and the solution was added H_2O. The suspension was stirred for 24 h. Afterwards, the top water layer was removed, and H_2O was added to repeat the process. This H-D exchange was found sufficient to give H_2(TPP-d_n), yielding a mixture of H_2(TPP-d_n) (**15-d_n**) containing 1.39% of **15-d_{29}** and 3.13% of **15-d_{30}**, as calculations discussed below show.

The MALDI mass spectrum of $[H_2(TPP\text{-}d_n)+H]^+$ and its respective simulated mass spectrum are given in Figures 8.2 and 8.3. The percentage of

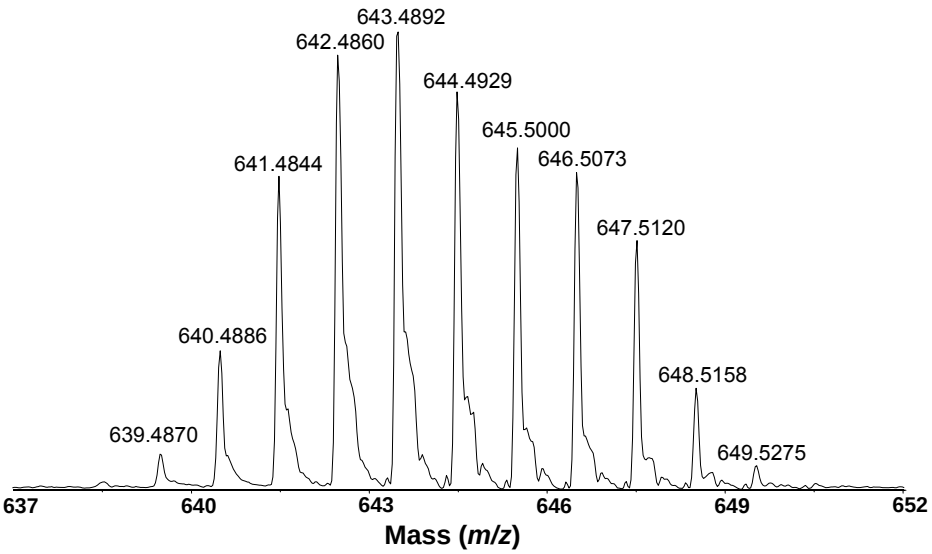

Figure 8.1. MALDI mass spectrum of $[D_2(TPP\text{-}d_n)+H]^+$ $[\mathbf{14}\text{-}\boldsymbol{d}_\mathbf{n}+H]^+$.

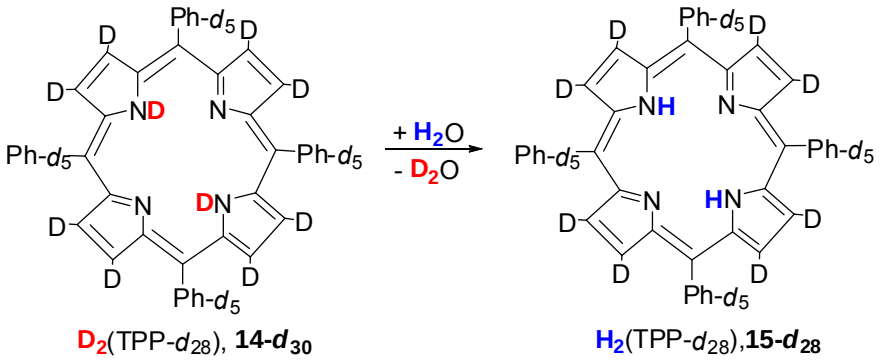

Scheme 8.4. Conversion of **14-d_{30}** to **15-d_{28}** *via* H/D exchange.

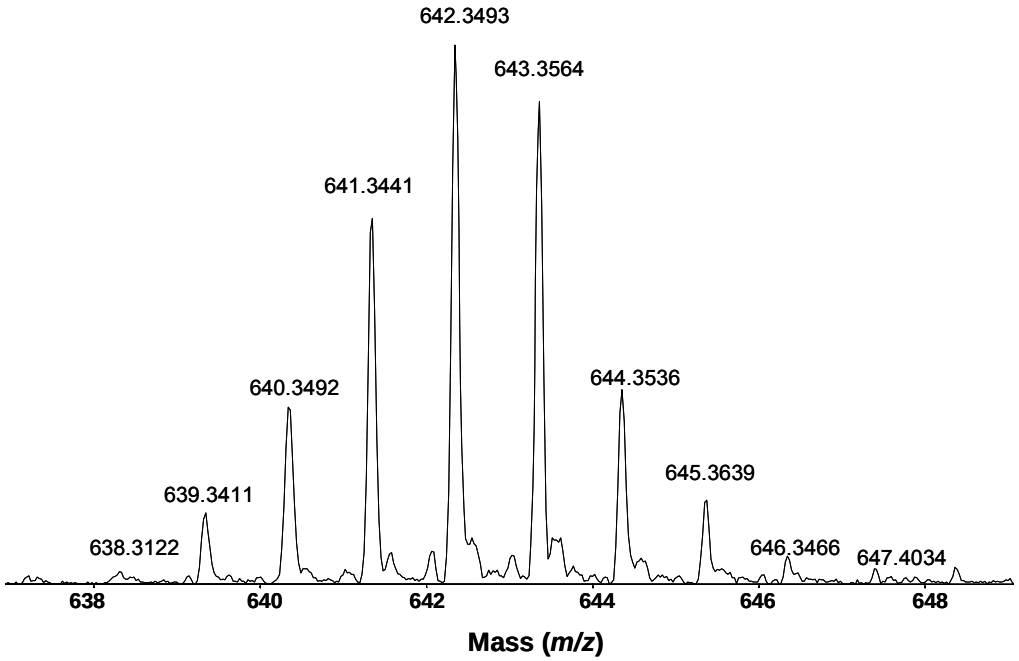

Figure 8.2. MALDI mass spectrum of $[H_2(TPP\text{-}d_n)+H]^+$ $[\mathbf{15}\text{-}\boldsymbol{d}_\mathbf{n}+H]^+$.

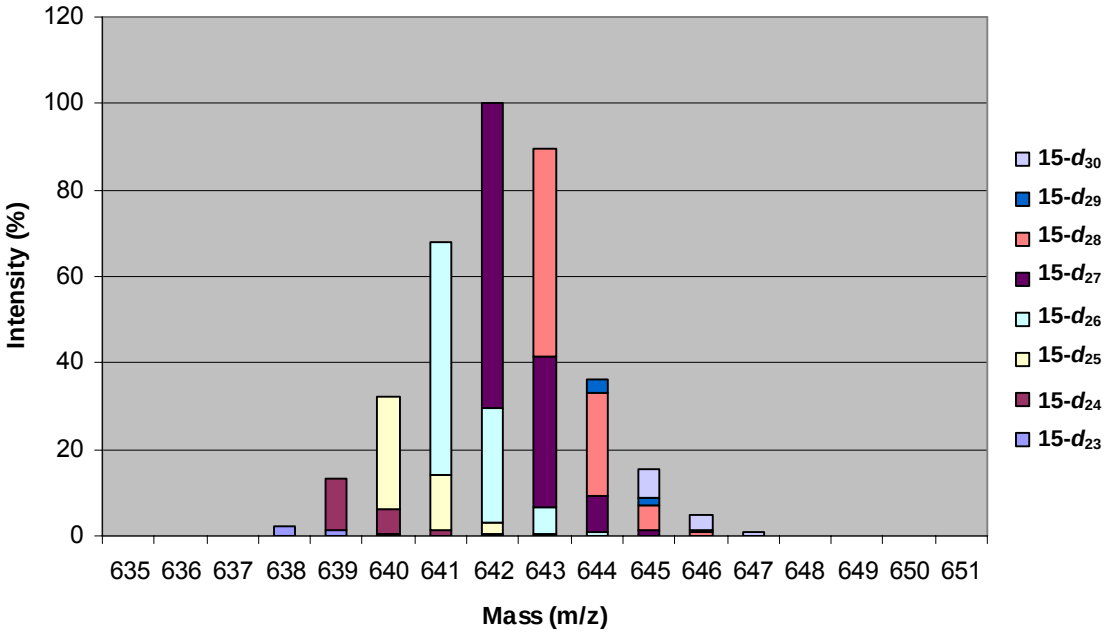

Figure 8.3. Simulated mass spectrum of $[H_2(TPP\text{-}d_n)+H]^+$ $[\mathbf{15}\text{-}\boldsymbol{d}_\mathbf{n}+H]^+$.

deuterium incorporation into the porphyrin ring was calculated using a simulation based on this mass spectrum. The isotope abundances of H_2(TPP-d_{20}) (**15-d_{20}**) through D_2(TPP-d_{28}) (**15-d_{30}**), which did not undergo the H-D exchange, were first obtained using simulated isotope pattern of each isotopologue and its relative MS intensities (Table B54). The simulated isotope patterns of H_2(TPP-d_{23}) (**15-d_{23}**) and H_2(TPP-d_{28}) (**15-d_{28}**) as two examples are given in Tables B55 and B56. One feature of the spectrum of H_2(TPP-d_n) is that the first isotope peak (with the smallest mass) of each isotopologue is the most intense. Thus once its intensity is known, the intensities of other peaks of the isotopologue can be calculated. A simulation program based on this feature was written to determine the intensity of each isotopologue in a mixture. Its use in the current work is given in Table 8.1 and discussed below.

From the experimental MS spectrum in Figure 8.2, the intensities of 638.4 to 647.4 *m/z* were obtained. They are the sums (right column, Table 8.1) of the contributions of each isotopologue to a particular peak. The first observable peak at 638.4 *m/z* with *I* = 2.336% is attributed to **15-d_{23}** and the contributions of **15-d_{23}** to the peaks at 639.4 to 647.4 *m/z* are then calculated from the standard MS of **15-d_{23}**, including *I* = 1.148% to the next peak at 639.4 *m/z*. Deducting 1.148% from the total observed *I* = 13.226% gives *I* = 12.078% which is the first peak of **15-d_{24}**. This process was repeated to give intensity (*I*) for the first peak of each remaining isotopologue (**15-d_{25}** to **15-d_{30}**), and these intensities were used as their relative molar ratios in the mixture. It should be noted that the peaks at 636.4 and 637.4 *m/z* are between 0.91-1.56%, suggesting that the

Table 8.1. Simulation of the MS spectrum for the sample H_2(TPP-d_n) (**15-d_n**) in the current work*

$[M+H]^+$	**15-d_{20}**	**15-d_{21}**	**15-d_{22}**	**15-d_{23}**	**15-d_{24}**	**15-d_{25}**	**15-d_{26}**	**15-d_{27}**	**15-d_{28}**	**15-d_{29}**	**15-d_{30}**	Sum
635.4	0	0	0	0	0	0	0	0	0	0	0	0
636.4	0	0	0	0	0	0	0	0	0	0	0	0
637.4	0	0	0	0	0	0	0	0	0	0	0	0
638.4	0	0	0	2.336	0	0	0	0	0	0	0	2.3336
639.4	0	0	0	1.148079	12.0779	0	0	0	0	0	0	13.226
640.4	0	0	0	0.276047	5.934549	26.0629	0	0	0	0	0	32.8135
641.4	0	0	0	0.043277	1.426581	12.80317	53.55997	0	0	0	0	67.833
642.4	0	0	0	0.004973	0.223586	3.076934	26.30469	70.38982	0	0	0	100
643.4	0	0	0	0.000446	0.02569	0.482138	6.320184	34.56218	48.10586	0	0	89.4974
644.4	0	0	0	3.27E-05	0.002307	0.055384	0.990056	8.302127	23.61498	3.0922	0	36.057
645.4	0	0	0	0	0.000169	0.004978	0.113708	1.30017	5.671152	1.517593	6.95698	15.5644
646.4	0	0	0	0	0	0.000365	0.01023	0.149297	0.887938	0.36436	3.413554	5.18816
647.4	0	0	0	0	0	0	0.00075	0.013374	0.101936	0.057033	0.819365	2.8534
648.4	0	0	0	0	0	0	0	0.000985	0.00914	0.006546	0.128224	0
649.4	0	0	0	0	0	0	0	0	0.000673	0.000588	0.014707	0
650.4	0	0	0	0	0	0	0	0	0	4.33E-05	0.001322	0
651.4	0	0	0	0	0	0	0	0	0	0	9.74E-05	0

* **15-d_n** here refers to H_2(TPP-d_n) after an H-D exchange with H_2O. **14-d_n** refers to D_2(TPP-d_{n-2}).

Table 8.2. Calculation of the percentage of deuteration in the sample

	Intensity (I)[a]	mol% of **15-d_{23}** to **15-d_{30}**	mol% of **15-d_{23}** to **15-d_{28}** only	Weight	Weighted D% for each isotopologue
H_2(TPP-d_{23}) (**15-d_{23}**)	2.336	1.050	1.100	23/28	0.904
H_2(TPP-d_{24}) (**15-d_{24}**)	12.078	5.426	5.683	24/28	4.871
H_2(TPP-d_{25}) (**15-d_{25}**)	26.063	11.709	12.263	25/28	10.949
H_2(TPP-d_{26}) (**15-d_{26}**)	53.560	24.063	25.201	26/28	23.408
H_2(TPP-d_{27}) (**15-d_{27}**)	70.390	31.624	33.120	27/28	31.937
H_2(TPP-d_{28}) (**15-d_{28}**)	48.106	21.613	22.635	28/28 = 1	22.635
HD(TPP-d_{28}) (**15-d_{29}**)	3.092	1.389			
D_2(TPP-d_{28}) (**15-d_{30}**)	6.957	3.126			
sum		100	100		94.704 = 95(5)%[b]

[a] The intensity data are taken from Table 8.1.

[b] The 5% error is estimated based on the combined 4.5 mol% for **15-d_{29}** and **15-d_{30}**.

amounts of **15-d_{20}** to **15-d_{22}** in the mixture are insignificant. A simulated MS from the calculations (Table 8.2) is given in Figure 8.3, and it compares favorably with the experimental spectrum in Figure 8.2.

The percentage of deuteration (e.g., 23/28 = 82.1 atom% D in **15-d_{23}** as its weight of deuteration) for each isotopologue (**15-d_{23}** to **15-d_{30}**) and its relative molar ratio were subsequently used to give an average percentage of deuteration of 95(5)% for the mixture of the isotopologues, as shown in Table 8.2. The estimated error of 5% is based on the combined 4.5 mol% for **15-d_{29}** and **15-d_{30}** that were not fully exchanged with H_2O.

We have also prepared pyrrole-d_5 prepared from H-D exchange between acetic acid-d_1 and pyrrole, a procedure reported by Fajer and coworkers.[103] Pyrrole-d_5 thus prepared was used subsequently to react with benzaldehyde-d_6. For reasons not clear to us, repeated attempts to crystallize the **14-d_{30}** samples thus prepared, using Fajer and coworkers pyrrole-d_5[103] (after drying the samples and chromatographic separation) failed.

X-ray crystal structure of D_2(TPP-d_{28}) (**14-d_{30}**) at 293(2) K has been determined (Figure 8.4), and, as expected, it is similar to that of non-deuterated *meso*-tetraphenylporphyrin reported earlier.[106] Structural parameters are summarized in Table 8.3. Selected bond lengths and angles are given in Table 8.4 with a comparison with those in *meso*-tetraphenylporphyrin (H_2TPP) (**15**).[106]

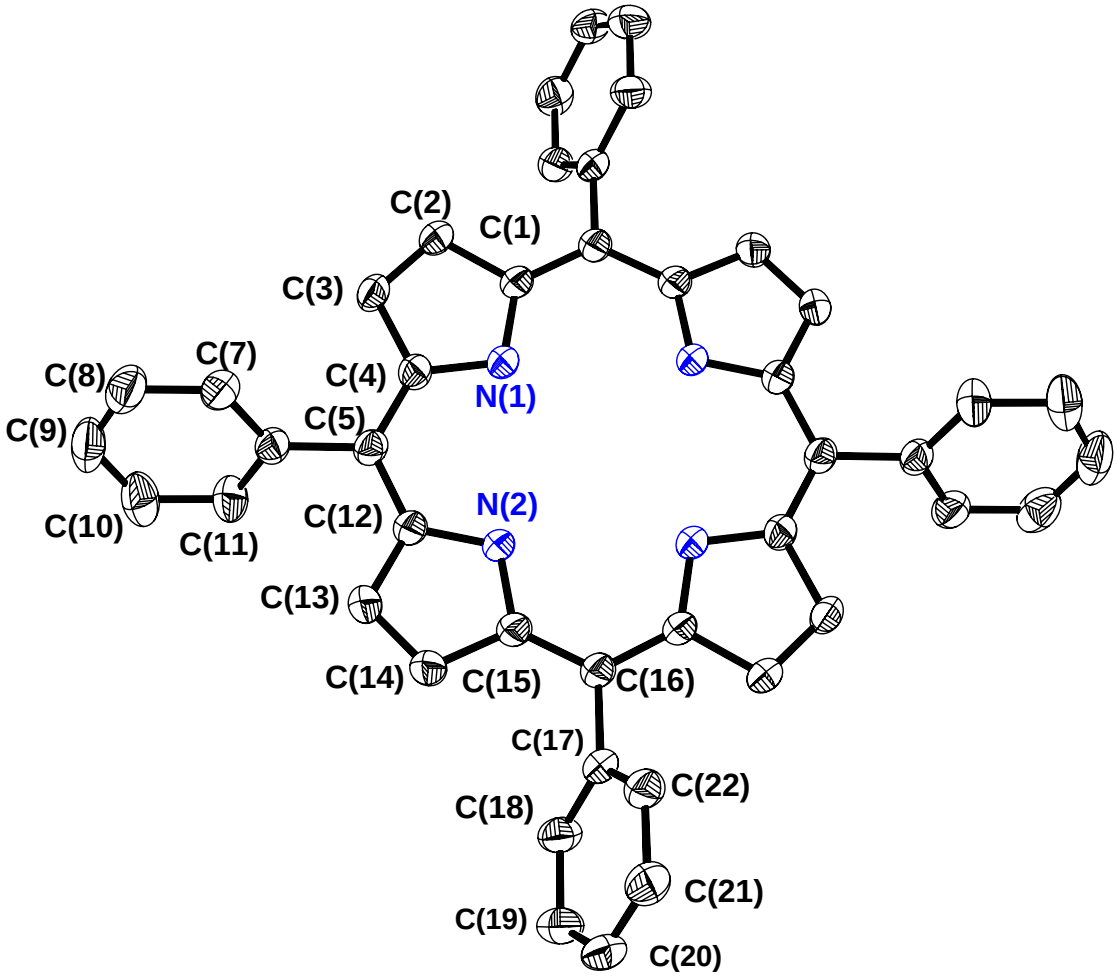

Figure 8.4. ORTEP plot of **14-d_{30}** at 293(2) K; thermal ellipsoids are at 30% probability level. D/H atoms are removed for clarity.

Table 8.3. Crystal data and structure refinement of **12-d_{28}**, **13-d_{36}**, and **14-d_{30}**

	14-d_{30}	**12-d_{28}**	**13-d_{36}**	**13-d_{36}**
Temp (K)	293(2)	293(2)	293(2)	173(2)
Emp. formula	$C_{44}H_2D_{28}N_2$	$C_{44}ClD_{28}$ FeN_4	$C_{51}Cl_4D_{39}FeN_8O$	$C_{51}Cl_4D_{37}FeN_8O$
Formula weight	642.789	732.06	1017.79	1017.79
Crystal system	Triclinic	Tetragonal	Triclinic	Triclinic
Space group	*P*-1	*I4/m*	*P*-1	*P*-1
Unit cell	*a* = 6.4196(2) Å	*a* = 13.5419(19) Å	*a* = 11.2128(3) Å	*a* = 11.093(2) Å
dimensions	*b* = 10.4862(3) Å	*c* = 9.814(2) Å	*b* = 13.3409(3) Å	*b* = 13.130(3) Å
	c = 12.4427(3) Å	α = 90.000°	*c* = 17.7006(4) Å	*c* = 17.625(4) Å
	α = 96.033(2)°		α = 69.6320(10)°	α = 70.07(3)°
	β = 99.311(2)°		β = 72.0360(10)°	β = 72.52(3)°
	γ = 101.010(2)°		γ = 85.3650(10)°	γ = 86.48(3)°
Volume(Å^3)	803.32(4)	1799.7(5)	2360.21(10)	2299.5(8)
Z	1	2	2	2

Table 8.3. (continued)

	14-d_{30}	**12-d_{28}**	**13-d_{36}**	**13-d_{36}**
Density (cald, Mg/m^3)	1.329	1.351	1.432	1.464
Abs coeff (mm^{-1})	0.075	0.530	0.593	0.609
F(000)	322	726	1008	1002
Crystal size (mm^3)	0.40 × 0.30 × 0.10	0.20 × 0.20 × 0.10	0.40 × 0.30 × 0.20	0.40 × 0.30 × 0.30
θ range (deg)	2.42 to 24.03	2.13 to 28.22	1.29 to 33.53	1.29 to 28.31
Index ranges	$-7 \le h \le 8$	$-17 \le h \le 17$	$-17 \le h \le 17$	$-13 \le h \le 14$
	$-14 \le k \le 14$	$-17 \le k \le 17$	$-20 \le k \le 20$	$-15 \le k \le 17$
	$-15 \le l \le 15$	$-12 \le l \le 12$	$-27 \le l \le 24$	$0 \le l \le 23$
Reflns collected	7214	9277	55921	9207
Indep reflns	3354	1128	15956	9207
	[*R*(int) = 0.0299]	[*R*(int) = 0.0149]	[*R*(int) = 0.0358]	[*R*(int) = 0.0000]
Completeness	96.2% (θ = 25.00°)	95.5% (θ = 28.22°)	99.4% (θ = 26.00)	91.9% (θ = 26.00)

Table 8.3. (continued)

	14-d_{30}	**12-d_{28}**	**13-d_{36}**	**13-d_{36}**
Max./min transmn	0.7458 and 0.6882	0.7457 and 0.6935	0.7466 and 0.7000	0.7457 and 0.6709
Data/restraints/params	3354 / 1 / 221	1128 / 0 / 73	15956 / 2 / 625	9207/ 2 / 629
Goodness-of-fit on F^2	1.018	1.079	0.974	1.118
Final *R* indices [$I >$ $2\sigma(I)$]	$R1$ = 0.0487, $wR2$ = 0.1145	$R1$ = 0.0368, $wR2$ = 0.1171	$R1$ = 0.0510, $wR2$ = 0.1236	$R1$ = 0.0511, $wR2$ = 0.1382
R indices (all data)	$R1$ = 0.0778, $wR2$ = 0.1297	$R1$ = 0.0414, $wR2$ = 0.1220	$R1$ = 0.0899, $wR2$ = 0.1466	$R1$ = 0.0663, $wR2$ = 0.1478

[a] $R1 = \Sigma||F_o| - |F_c|| / \Sigma|F_o|$; $wR2 = [\Sigma\, w(F_o^2 - F_c^2)^2 / \Sigma\, w(F_o^2)^2]^{1/2}$; $w = 1/[\sigma^2(F_o) + (aP)^2 + bP]$; $P = [2F_c^2 + \text{Max}(F_o^2, 0)]/3$

Table 8.4. Comparison of bond lengths (Å) and angles (°) between **14-d_{30}** and **15**.[106]

Compound No.	**15**	**14-d_{30}**	Compound	**15**	**14-d_{30}**
Lengths (Å)			Angles (°)		
N1-C1	1.371	1.374(2)	C1-N1-C4	109.2	109.46(14)
N1-C4	1.378	1.374(2)	C12-N2-C15	106.2	106.37(13)
N2-C12	1.369	1.368(2)	N1-C4-C5	126.3	126.08(15)
N2-C15	1.370	1.373(2)	N2-C15-C16	125.8	125.88(14)
C5-C6	1.506	1.501(2)	C4-C5-C6	116.5	116.61(15)
C16-C17	1.502	1.496(2)	C15-C16-C17	118.2	118.39(14)

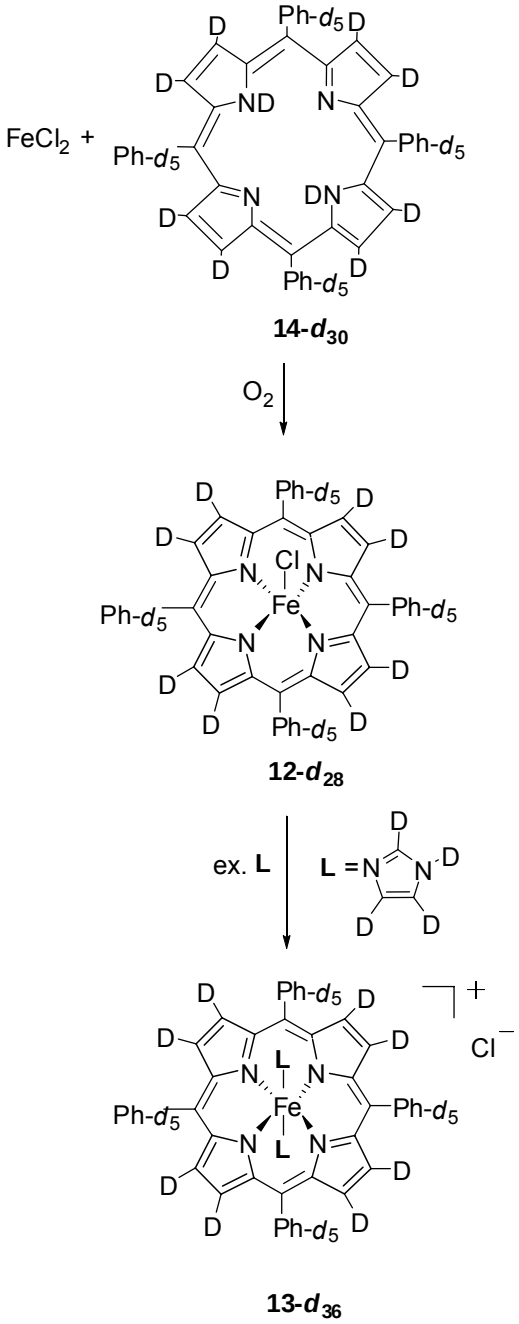

Scheme 8.5. Preparation of Fe(TPP)Cl-d_{28} (**12-*d*$_{28}$**) and [Fe(TPP)(DIm)$_2$-d_{36}]Cl (**13-*d*$_{36}$**).

8.2.2. Synthesis and Characterization of Fe(TPP)Cl-d_{28} (12-d_{28})

Fe(TPP)Cl (**12**) has been prepared from ferrous chloride $FeCl_2$ and H_2TPP (**15**), using air to oxidize Fe(II) to Fe(III) in the reaction.[107] We have followed this procedure to prepare **12-*d*$_{28}$**. Crystallization in chloroform readily yielded single crystals of **12-*d*$_{28}$** in 78% yield (Scheme 8.5). We have also explored the synthesis of **12-*d*$_{28}$** from the reaction of ferric chloride $FeCl_3$ with H_2TPP (**15**). Since no oxidation of the metal ions was needed, the reaction was conducted under nitrogen atmosphere. The procedure also gave crystalline **12-*d*$_{28}$**. The yield was, however, only half of the procedure using ferrous chloride. MALDI mass spectra of Fe(TPP)Cl-d_{28} was obtained (Figure 8.5). The results confirmed that all deuterium incorporation remained intact after addition of $FeCl_3{\cdot}6H_2O$ to **12-*d*$_{28}$**. Peaks at 696.3 (*I* = 100%) and 695.3 (*I* = 100%) *m/z* were assigned to Fe(TPP)-d_{28}^+. A fragment at 643.2 *m/z* was also observed for [(**14-*d*$_{28}$**)+H]$^+$. Asano *et al.* indicate that after metalation, using Cu(II) or Zn(II), with **14-*d*$_{28}$**, the deuterium content remains intact.[105] No change in the deuterium content is expected in the current reactions to make **12-*d*$_{28}$**.

The crystal structure of Fe(TPP)Cl (**12**) was initially reported as Fe(TPP)(OH)•H_2O and solved in the space group *I4*.[61] The six-coordinate Fe ion is coordinated with H_2O and OH^- ligands at the axial positions along the crystallographic four-fold axis. Later, Hoard and coworkers reported that the two axial ligands, H_2O and OH^-, had been wrongly assigned after the same data were re-analyzed.[58] The structure was then solved in the space group *I4/m* as

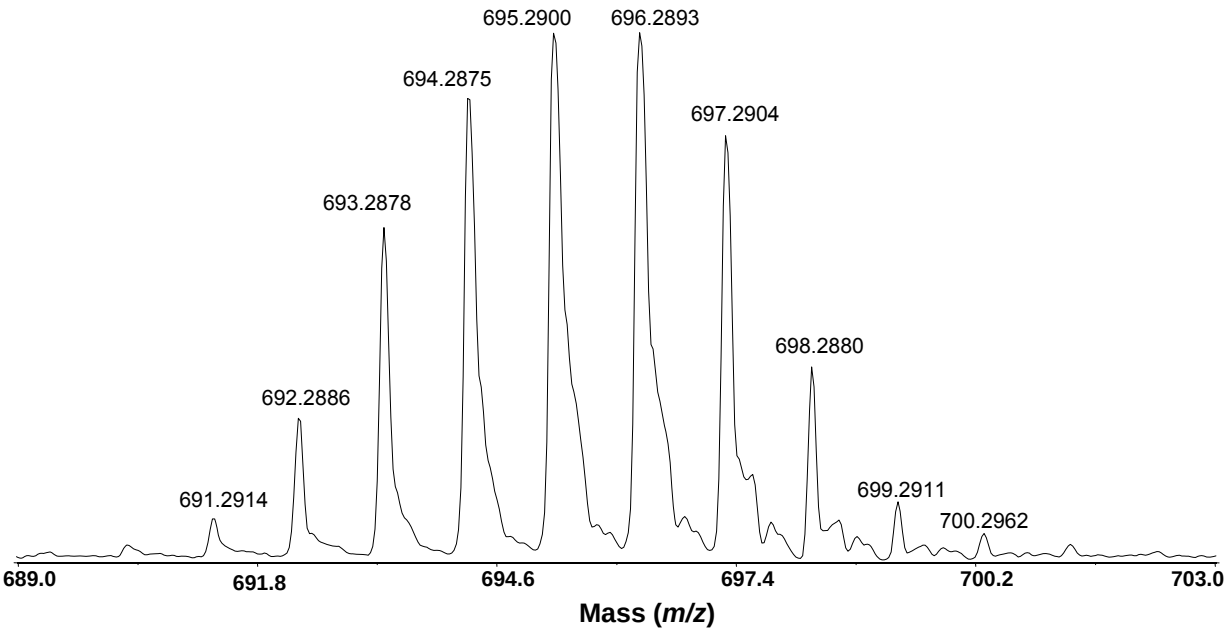

Figure 8.5. MALDI mass spectrum of $[(\text{FeTPP-}d_n)+\text{H}]^+$.

Fe(TPP)Cl (**12**). The Fe ion is five coordinated with an axial chloride ligand, and Fe ion sits out of the porphyrin plane with a 50% disorder. In other words, a statistically averaged molecule has half atoms of Fe and Cl on the *c*-axis. The axial ligand is indeed Cl atom, as confirmed by elemental analysis.[58] The molecule resides on a special position (0,0,0) with a C_{4h} point group symmetry. The ancillary phenyl groups are aligned along the [001] direction and perpendicular to the mirror plane defined by the porphyrin ring atoms. We have recently investigated the X-ray crystal structures of Fe(TPP)Cl (**12**) at 20(2), 143(2), and 293(2) K.[75] Thermal motion of the phenyl groups was found to be reduced at 20(2) and 143(2) K, leading to the reduction of the crystallographic symmetry from *I4/m* at 293(2) K to *I4* space group at 143(2) and 20(2) K.[75] Single crystal diffraction studies of **12-*d*$_{28}$** were conducted at 293(2) K. The 293(2) K data were refined in the space group *I4/m*. As expected, the structures are similar to the reported structures of protio-Fe(TPP)Cl (**12**).[58] The structure of **12-*d*$_{28}$** at 293(2) K is given in Figure 8.6.

8.2.3. Synthesis and Characterization of [Fe(TPP)(DIm)$_2$-*d*$_{36}$]Cl (13-*d*$_{36}$)

[Fe(TPP)(DIm)$_2$-*d*$_{36}$]Cl (**13-*d*$_{36}$**) was synthesized using modified published procedures for protio [Fe(TPP)(HIm)$_2$]Cl (**13**) (Scheme 8.5).[66] In $CDCl_3$, 1D-imidazole-d_4 and Fe(TPP)Cl-d_{28} (**12-*d*$_{28}$**) were mixed. Then a mixture of $CDCl_3$ and hexanes (1:3 volume) containing a small amount of D_2O was layered on the top of the $CDCl_3$ solution, yielding crystals (~0.20 mm^3) of [Fe(TPP)(DIm)$_2$-*d*$_{36}$]Cl•$CDCl_3$•D_2O (**13-*d*$_{36}$**•D_2O•$CDCl_3$) in 1-2 days. We have found that, if

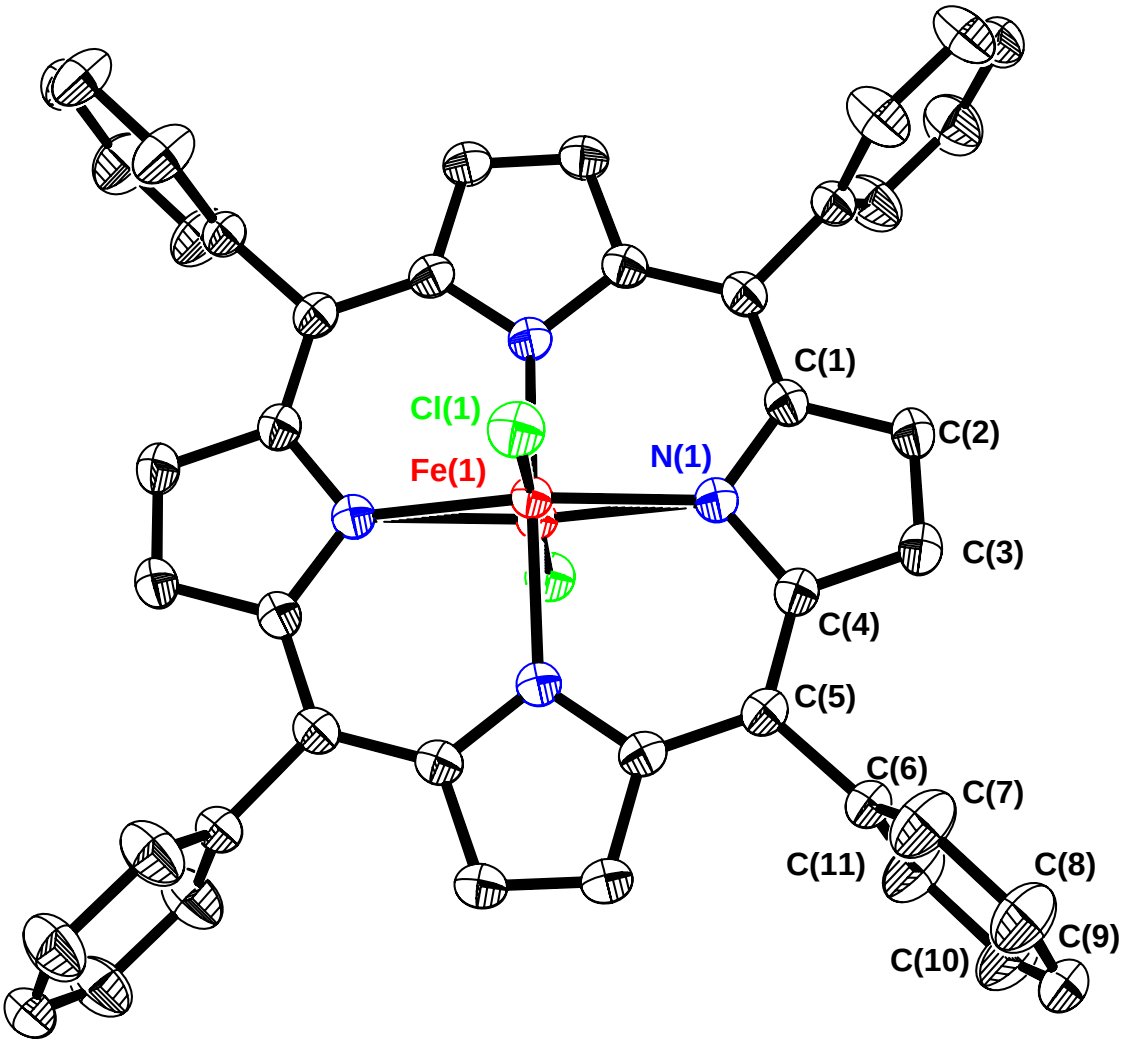

Figure 8.6. ORTEP of **12-d_{28}** at 293(2) K; thermal ellipsoids are at 30% probability level. Deuterium atoms removed for clarity.

crystals of the deuterated complex are left in solution for more than one week, they become a non-crystalline powder. MALDI mass spectra of a single crystal of **13-*d*$_{36}$** was obtained. Observation of Fe(TPP)-d_{28}^+ and $[H_2(TPP\text{-}d_{28})+H]^+$. were observed. However, the parent ion peak of $[Fe(TPP)(DIm)_2\text{-}d_{36}]^+$ $(\mathbf{13}\text{-}d_{36})^+$ was absent. We conclude that the axial ligand 1D-imidazole-d_4 dissociates when $[Fe(TPP)(DIm)_2\text{-}d_{36}]^+$ $(\mathbf{13}\text{-}d_{36})^+$ is ionized, resulting in the observed Fe(TPP)-d_{28}^+.

X-ray diffraction studies were conducted at 173(2) and 293(2) K for **13**-***d*$_{36}$**•D_2O•$CDCl_3$ and ORTEPs are given in Figures 8.7 and A24. Structural parameters are given in Table 8.3. For simplicity purposes, the two Fe molecules were labeled and numbered in the same manner as the published X-ray structure.[66] In the reported structure of protio-$[Fe(TPP)(HIm)_2]Cl$ (**13**), the chloride ion and water molecule were found near the inversion center at (1/2,0,0). The water molecule was involved in hydrogen bonding to an uncomplexed nitrogen atom (N4) in the imidazole ligand with a N4-O distance of 2.774 Å. The second uncomplexed nitrogen atom (N8) and chloride ion give a distance of 3.035 Å, indicating that a strong hydrogen bond is present. In the current structure of **13-*d*$_{36}$**, the bond lengths of **13-*d*$_{36}$** at 173(2) and 293(2) K are very similar to the reported structure (Table 8.5). In Table 8.5, selected bond angles of **13-*d*$_{36}$** are given. There are two independent molecules of **13-*d*$_{36}$** in a unit cell with different orientations of the imidazole rings with respect to the porphyrin ring. In both molecules, the imidazole rings are, however, nearly parallel to each other as shown in Figures 8.7 and A24. The water molecule showed hydrogen

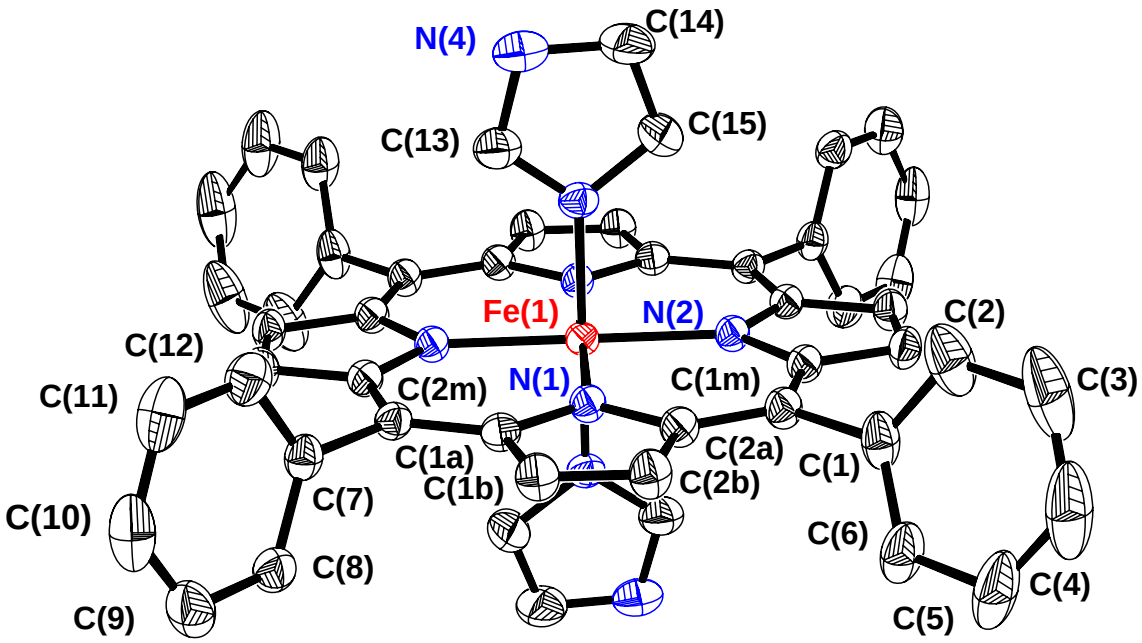

Figure 8.7. ORTEP drawing of Fe1 molecule in **13-d_{36}** at 293(2) K; thermal ellipsoids are at 30% probability level. Deuterium atoms, deuterium oxide, and chloroform-d_1 were removed for clarity.

Table 8.5. Selected bond lengths (Å) and angles (°) in **13**-d_{36}.

Temp. (K)	293(2)	173(2)		293(2)	173(2)
			Lengths (Å)		
Fe1-N1	1.9897(14)	1.987(2)	Fe2-N5	2.0006 (14)	1.990(2)
Fe1-N2	2.0029(16)	2.000(2)	Fe2-N6	1.9927(14)	1.992(2)
Fe1-N3	1.9789(16)	1.974(2)	Fe2-N7	1.9681(16)	1.963(2)
N1-C1a	1.382(2)	1.380(3)	N5-C5a	1.378(2)	1.379(3)
N1-C2a	1.379(2)	1.383(3)	N5-C6a	1.380(2)	1.379(3)
N2-C3a	1.379(2)	1.383(3)	N6-C7a	1.378(2)	1.377(3)
N2-C4a	1.377(2)	1.373(3)	N6-C8a	1.373(2)	1.378(3)
N3-C13	1.309(3)	1.317(4)	N7-C28	1.323(2)	1.326(3)
N3-C15	1.369(3)	1.379(3)	N7-C30	1.373(3)	1.373(3)
			Angles (°)		
N1-Fe1-N2	89.72(6)	89.51(8)	N5-Fe2-N6	89.26(6)	89.26(8)
N1-Fe1-N3	89.49(6)	89.67(9)	N5-Fe2-N7	89.19(6)	88.78(9)
N2-Fe1-N3	90.06(7)	89.81(9)	N6-Fe2-N7	90.30(6)	90.47(9)

bonding to N4. The 173(2) and 293(2) K structures give ca. N4-O distances of 2.764 and 2.783 Å, respectively. The water molecule forms a hydrogen bond to the chloride ion with distances of 3.105 and 3.106 Å at 173(2) and 293(2) K. In the Fe2 molecule, the uncomplexed nitrogen atom (N8) in the imidzaole ligand forms a strong hydrogen bond to the chloride ion with distances of 3.044 Å and 3.037 Å at 173(2) and 293(2) K, respectively.

8.3. Concluding Remarks

In summary, crystalline per-deuterated Fe(III) porphyrin complexes Fe(TPP)Cl-d_{28} (**12-d_{28}**) and [Fe(TPP)(DIm)$_2$-d_{36}]Cl (DIm = 1D-imidazole-d_4) (**13-d_{36}**) have been prepared from D_2(TPP-d_{28}) (**14-d_{30}**). The deuterated porphyrin **14-d_{30}** and two per-deuterated Fe(III) porphyrin complexes have been characterized by MALDI mass spectrometry, and the MALDI mass spectra gave a deuterium incorporation percentage of 95(5)%. X-ray structures of **12-d_{28}**, **13-d_{36}**, and Fe-free porphyrin **14-d_{30}** have been determined.

8.4. Experimental Section

8.4.1. General Procedures

1D-imidazole-d_4 was purchased from Aldrich (98 atom% D). Solvents were used without further purification. Pyrrole (Acros) was purified by distillation prior to use. Toluene-d_8 (Cambride Isotope Laboratories, 99.9 atom% D), propionic anhydride (Alfa Aesar), acetic anhydride (Fisher Scientific), D_2O (Cambridge Isotope Laboratories, 99.9 atom% D), ceric ammonium nitrate

(Fisher Scientific), chloroform-d_1 (Cambride Isotope Laboratories, 99.8 atom% D), 2,3-dichloro-5,6-dicyanobenzoquinone (DDQ) (Aldrich), $FeCl_3 \bullet 6H_2O$ (Fisher Scientific), and $FeCl_2 \bullet 4H_2O$ (Fisher Scientific). Benzaldehyde-d_6 was prepared by previously published methods.[103] Wet chloroform-d_1 was prepared by adding D_2O to chloroform-d_1, and the mixture was shaken and then allowed to settle. Wet chloroform-d_1 at the bottom was then removed for the use below. The mass spectra of **12-d_{28}**, **13-d_{36}**, and **14-d_{28}** were taken using an ABI (Foster City, CA) Voyager-DETM PRO matrix assisted laser desorption ionization time-of-flight (MALDI/TOF) mass spectrometer.

8.4.2. Synthesis of D_2(TPP-d_{28}) (14-d_{30})

Following the reported procedure, propionic anhydride (125 mL, 664 mmol) was added D_2O (17.5 mL, 969 mmol) under nitrogen. The solution was refluxed for 30 min. Pyrrole-h_5 (2.04 g, 30.4 mmol) was added and the solution was refluxed for 1 h. Benzaldehyde-d_6 (3.00 g, 26.8 mmol) was added and the solution was refluxed for 1 h. Solution was cooled to room temperature overnight. Propionic-d_1 acid was distilled off under reduced pressure. The crude product was washed with an excess amount of methanol (500 mL). Next the crude black residue was dissolved in dichloromethane and applied to silica-gel column chromatography. Solvent was removed *via* rotary evaporator. The crude product was treated with DDQ.[100b] The deuterated porphyrin was purified by silica-gel column chromatography (chloroform) to removed chlorin. Solvent was

removed *via* rotary evaporator at 40 °C to give crystalline **14-d_{30}**. Yield: 275 mg, 0.428 mmol, 6.4%.

8.4.3. Preparation of H_2(TPP-d_{28}) (15-d_{28}) for MALDI

A single crystal of D_2(TPP-d_{28}) (**14-d_{30}**) was dissolved in chloroform (~1 mL). Water (~2 mL) was added to the chloroform solution. The mixture was stirred for 24 h. After 24 h, the water was removed and fresh water (~2 mL) was added to the chloroform solution. Over a period of two days, the chloroform solution was washed twice. An aliquot of the chloroform solution was used for the MALDI mass spectrometry experiment. MALDI mass spectrum of the sample is given in Figure 8.2.

8.4.4. Synthesis of Fe(TPP)Cl-d_{28} (12-d_{28})

12-d_{28} was prepared by using modified procedures.[58,61] An excess amount of $FeCl_2 \bullet 4H_2O$ (1.00 g, 5.03 mmol) was added to a refluxing solution of crystalline D_2(TPP-d_{28}) (**14-d_{30}**, 275 mg, 0.428 mmol) in DMF (60 mL) under N_2. Solution was refluxed for 10 h and then chilled in an ice-water bath for 45 min. An excess amount of chilled water (200 mL) was added to the chilled solution. Solution was filtered and purple precipitate was left to dry overnight. The purple **12-d_{28}** was purified by silica-gel chromatography using chloroform. Solvent was then removed *via* a rotary evaporator. The solid was dissolved in chloroform, and crystals of **12-d_{28}** observed after 1-2 days. Yield: 243.1 mg, 0.332 mmol, 78%. FeTPP-d_{28}^+ mass spectra (*m/z*): 692.3 (*I* = ~27%), 693.3 (*I* = ~63%), 694.3

(I = ~88%), 695.3(I = 100%), 696.3 (I = 100%), 697.3 (I = ~81%), and 698.3 (I = ~37%).

8.4.5. Synthesis of [Fe(TPP)(DIm)$_2$-d_{36}]Cl (13-d_{36})

13-d_{36} was prepared by using modified procedures.[66] Crystalline Fe(TPP)Cl-d_{28} (**12-d_{28}**, 36.5 mg, 0.0499 mmol) and 1D-imidazole-d_4 (25.7 mg, 0.356 mmol) were dissolved in wetted chloroform-d_1 (4 mL). The chloroform-d_1 layer was diffused with a 1:3 chloroform-d_1:hexanes (4 mL) mixture. D_2O (~40 μL) was added to the diffusion layer. Sample was sealed and kept at room temperature. Crystals were obtained in ca. 3-4 days. Yield: 33.0 mg, 0.038 mmol, 11.3%.

8.4.6 Determination of X-ray Crystal Structures of 12-d_{28}, 13-d_{36}, and 14-d_{30} at 173(2) and 293(2) K

X-ray data at 293(2) K were collected on a Bruker AXS Smart 1000 X-ray diffractometer equipped with a CCD area detector and a graphite-monochromated Mo source (K_α radiation, 0.71073 Å) and fitted with an upgrade Nicolet LT-2 low temperature device. Suitable crystals were coated with paratone oil (Exxon) and mounted on a glass fiber. X-ray data at 173(2) K were collected in the same manner as the 293(2) K. However, suitable crystal was coated with paratone oil (Exxon) and mounted on a cryo-loop under a stream of nitrogen at 173(2) K.

Global refinements for the unit cell and data reduction were performed under the SAINT program[55a] for data collected at 173(2) and 293(2) K. Empirical absorption correction was performed with SADABS.[55c] Space groups were determined from systematic absences by XPREP[55a] and further justified by refinement results. The structures were solved by Patterson method and refined using the SHELXTL proprietary software package.[64] All non-hydrogen atoms were refined with anisotropic displacement parameters. Hydrogen atoms were placed at calculated positions with isotropic displacement parameters [U_{iso}(H) = 1.2U_{eq}(C)] in final structural refinement.

CHAPTER 9

Conclusion and Future Studies

9.1 Conclusion

In Chapter 2, the reaction of $W(CH_2SiMe_3)_3(\equiv CSiMe_3)$ (**1**) with DMPE (DMPE = $Me_2PCH_2CH_2PMe_2$) was presented. The reaction gives an adduct $W(CH_2SiMe_3)_3(\equiv CSiMe_3)$(DMPE-*P*) (**4a**), which then undergoes a transformation to its bis-alkylidene tautomer $W(CH_2SiMe_3)_2(=CHSiMe_3)_2$(DMPE-*P*) (**4b**) through α–H migration. The **4a** $\rightleftharpoons$ **4b** mixture undergoes α-H abstraction, yielding alkyl alkylidene alkylidyne complexes $W(CH_2SiMe_3)(=CHSiMe_3)(\equiv CSiMe_3)$(DMPE) (*syn*: **7a**; *anti*: **7b**). In Chapter 3, thermodynamic studies of the addition of mono-dentate phosphines (PR_3 = PMe_3, PMe_2Ph) to $W(CH_2SiMe_3)_3(\equiv CSiMe_3)$ (**1**) was presented. In Chapter 4, the reactions of alkyl alkylidyne $W(CCH_2Me_3)_3(\equiv CSiMe_3)$ (**8**) with H_2O in THF and with D_2O in benzene-d_6 lead to the formation of two trimeric oxo complexes: $W_3O_3(\mu{=}O)_3(CH_2CMe_3)_6(THF)_3$ (**9**) and $[W_3O_3(\mu{=}O)_3(CH_2CMe_3)_6(D_2O)_3]\bullet 2C_6D_6$ (**10**), respectively. In Chapters 5 and 6, the X-ray structures of the high-spin Fe(TPP)Cl (**12**) and low-spin $[Fe(TPP)(HIm)_2]Cl$ (**13**) were analyzed at variable temperatures. In Chapter 7, studies of the spin distribution in low-spin (S = 1/2) $[Fe(TPP)(HIm)_2]Cl$ (**13**) were conducted. In Chapter 8, the synthesis of the per-deuterated Fe(TPP)Cl-d_{28} (**12**-$\boldsymbol{d_{28}}$, TPP^{2-} = *meso*-tetraphenylporphyrinate) and its 1D-imidazole-d_4 derivative

[Fe(TPP)(DIm)$_2$-d_{36}]Cl (**13**-$\boldsymbol{d_{36}}$, DIm = 1D-imidazole-d_4) were presented and the compounds will be used in spin density studies in the future.

9.2. Organometallic Chemistry

From the studies conducted in this dissertation, we discovered that the reactions of W(CH_2SiMe_3)$_3$(≡$CSiMe_3$) (**1**)[4] and W(CCH_2Me_3)$_3$(≡$CSiMe_3$) (**8**) with O_2 and H_2O lead to the formation of new tungsten(VI) oxo complexes. Further investigation into other reported alkylidyne tungsten(VI) complexes with O_2 and H_2O can be pursued. The combination of these new metal oxides and our current work would give a better understanding of the mechanistic pathway of the reactions of d^0 transition metal complexes with H_2O and/or O_2.

Alcohol groups are excellent oxygen donors. Thus, the reactions of alkyl alkylidyne tungsten(VI) complexes with alcohol groups can be explored. These reactions in comparison to our H_2O and O_2 reactions would give an insight into the d^0 transition metal chemistry.

From our results in Chapters 2 and 3, additional kinetic and thermodynamic studies can be pursued of the reactions of **1** with DMPE and other multi-dentate phosphines. The phosphine complexes have the potential to undergo hydrosilylation. If the complexes undergo hydrosilylation, they would be more applicable and versatile in other realms of science.

9.3. Polarized Neutron Diffraction

Polarized neutron diffraction experiments can be pursued of other paramagnetic complexes [e.g. Cu(TPP)Cl]. Such complexes would make a nice comparison between two different metal centers, such as Fe(TPP)Cl (**12**) and Cu(TPP)Cl. From our results in Chapter 7, additional spin density studies can be explored on Fe(III) porphyrin derivatives. Exploring compounds with similar structural similarities but different spin states is worth investigating. PND studies on new small molecular magnetics (SMMs) and organic radical compounds can also be looked into.

While there are several systems that can be pursued by PND, charge density studies can also be conducted. Non-complex systems (i.e., small-molecules) exhibiting excellent refinement (e.g. $R1 \sim 0.01$), minimal disorder, and no twinning issues would be the best candidates to pursue electron density studies. The electron and spin distribution studies are complementary techniques that would give information about the electronic and magnetic properties within a complex.

REFERENCES

1. (a) Fellmann, J. D.; Schrock, R. R.; Rupprecht, G. A. *J. Am. Chem. Soc.* **1981**, *103*, 5752. (b) Fellmann, J. D.; Rupprecht, G. A.; Wood, C. D.; Schrock, R. R. *J. Am. Chem. Soc.* **1978**, *100*, 5964. (c) Diminnie, J. B.; Xue, Z. *J. Am. Chem Soc.* **1997**, *119*, 12657. (d) Diminnie, J. B.; Hall, H. D.; Xue, Z. *J. Chem. Soc., Chem. Commun.* **1996**, 2383. (e) Diminnie, J. B.; Blanton, J. R.; Cai, H.; Quisenberry, K. T.; Xue, Z-L. *Organometallics* **2001**, *20*, 1504.
2. (a) Morton, L. A.; Wang, R.; Yu, X.; Campana, C. F.; Guzei, I. A.; Yap, G. P. A.; Xue, Z. *Organometallics* **2006**, *25*, 427. (b) Morton, L. A.; Chen, S.; Qiu, H.; Xue, Z.-L. *J. Am. Chem. Soc.* **2007**, *129*, 7277.
3. Scott, J. F. *Annu. Rev. Matter. Sci.* **1998**, *28*, 79.
4. Morton, L. A. *Ph.D Dissertation*; The University of Tennessee: Knoxville, 2005.
5. Schrock, R. R.; Fellmann, J. D. *J. Am. Chem. Soc.* **1978**, *100*, 3359.
6. (a) Schrock, R. R.; Sancho, J.; Pederson, S. F. *Inorg. Synth.* **1989**, *26*, 45. (b) Chisholm, M. H.; Huffman, J. C.; Klang, J. A. *Polyhedron* **1990**, *9*, 1271.
7. Becini A, Gatteschi D. *EPR of Exchange Coupled Systems.* Springer-Verlag: Berlin, 1990.
8. Willett, R. D.; Gatteschi, D.; Kahn, O. In *Magneto-Structural Correlations in Exchange Coupled Systems,* Reidel: Dordrecht, 1985; p. 207.
9. Gatteschi, D. J. *J Phys Chem B.* **2000**, *104*, 9780.
10. Sharp, R. R. *Nucl. Mag. Res.* **2005**, *34*, 553.

11. Bertini, I.; Luchinat, C.; Parigi, G.; Pierattelli, R. *Dalton Trans.* **2008**, *29*, 3782.

12. Hoffman, B. M. *Acc. Chem. Res.* **2003**, *36*, 522.

13. Wilson, C. C. In *Single Crystal Neutron Diffraction from Molecular Materials*. World Scientific: Singapore, 2000.

14. Larese, J. Z. In *Applications of Physical Methods to Inorganic and Bioinorganic Chemistry*, Scott, R. A., Lukehart, C. M. Eds.; Wiley: Chichester, UK, 2007; p. 291.

15. Long, G. J. In *Comprehensive Coordination Chemistry II*, McCleverty, J. A.; Meyer, T. J. Eds. Elsevier: Amsterdam, 2003; pp. 83-90.

16. Dianoux, A-J.; Lander, G. In *Neutron Data Booklet*; 2nd ed.; Old City Publishing: Philadelphia, 2003.

17. McIntyre, G. J.; Lemee-Cailleau, M. H.; Wilkinson, C. *Physica B*, **2006**, *385-386* (Pt. 2), 1055.

18. Nathans, R.; Pigott, M. T.; Shull, C. G. *J Phys Chem Solids*, **1958**, *6*, 38.

19. Lelievre-Berna, E.; Bourgeat-Lami, E.; Gibert, Y.; Kernavanois, N.; Locatelli, J.; Mary, T.; Pastrello, G.; Petukhov, A.; Pujol, S.; Rouques, R.; Thomas, F.; Thomas, M.; Tasset, F. *Physica B*, **2005**, *356*, 141.

20. Courtois, P.; Hamelin, B.; Andersen, K. H. *Nucl Instrum Meth A*, **2004**, *529*, 157.

21. Jones, G. L.; Dias, F.; Collett, B.; Chen, W. C.; Gentile, T. R.; Piccoli, P. M. B.; Miller, M. E.; Schultz, A. J.; Yan, H.; Tong, X.; Snow, W. M.; Lee, W. T.; Hoffmann, C.; Thomison, J. *Physica B*, **2006**, *385-386* (Pt. 2), 1131.

22. Hussey, D. S.; Rich, D. R.; Belov, A. S.; Tong, X.; Yang, H.; Bailey, C.; Keith, C. D.; Hartfield, J.; Hall, G. D. R.; Black, T. C.; Snow, W. M.; Gentile T. R.; Chen, W. C.; Jones, G. L.; Wildman, E. *Rev. Sci. Instrum.* **2005**, *76*, 053503/1-053503/12.

23. The Yellow Book 2008, Cicognani, G. Ed. Institut Laue-Langevin, France, 2008, pp. 34-35.

24. Clark, D. N.; Schrock, R. R. *J. Am. Chem. Soc.* **1978**, *100*, 6774.

25. Churchill, M. R.; Youngs, W. J. *Inorg. Chem.* **1979**, *18*, 2454.

26. Sterenberg, B. T.; Senturk, O. S.; Udachin, K. A.; Carty, A. J. *Organometallics* **2007**, *26*, 925.

27. Algarra, A. G.; Basallote, M. G.; Castillo, C. E.; Corao, C.; Llusar, R.; Fernandez-Trujillo, M. J.; Vicent, C. *Dalton Transactions* **2006**, 5725.

28. Zou, F.; Furno, F.; Fox, T.; Schmalle, H. W.; Berke, H.; Eckert, J.; Chowdhury, Z.; Burger, P. *J. Am. Chem. Soc.* **2007**, *129*, 7195.

29. Suzuki, T.; Tsukuda, T.; Kiki, M.; Kaizaki, S.; Isobe, K.; Takagi, H. D.; Kashiwabara, K. *Inorg. Chim. Acta* **2005**, *358*, 2501.

30. Schrock, R. R. *Chem. Rev.* **2002**, *102*, 145.

31. (a) Chen, T.-N.; Zhang, X.-H.; Wang, C.-S.; Chen, S.-J.; Wu, Z.-Z.; Li, L.-T.; Sorasaenee, K. R.; Diminnie, J. B.; Pan, H.-J.; Guzei, I. A.; Rheingold, A. L.; Wu, Y.-D.; Xue, Z.-L. *Organometallics* **2005**, *24*, 1214. (b) Chen, T.-N.; Wu, Z.-Z.; Li, L.-T.; Sorasaenee, K. R.; Diminnie, J. B.; Pan, H.-J.; Guzei, I. A.; Rheingold, A. L.; Xue, Z.-L. *J. Am. Chem. Soc.* **1998**, *120*, 13519. (c) Xue, Z.; Chuang, S.-H.; Caulton, K. G.; Chisholm, M. H. *Chem.*

Mater. **1998**, *10*, 2365. (d) Caulton, K. G.; Chisholm, M. H.; Streib, W. E.; Xue, Z. *J. Am. Chem. Soc.* **1991**, *113*, 6082. (e) Xue, Z.; Caulton, K. G.; Chisholm, M. H. *Chem. Mater.* **1991**, *3*, 384.

32. Morton, L. A.; Zhang, X.; Wang, R.; Lin, Z.; Wu, Y.; Xue, Z. *J. Am. Chem. Soc.* **2004**, *126*, 10208.

33. Nadasdi, T. T.; Huang, Y.; Stephan D. W. *Inorg. Chem.* **1993**, *32*, 347.

34. (a) Toreki, R.; Schrock R. R.; Davis, W. M. *J. Am. Chem. Soc.* **1992**, *114*, 3367. (b) Edwards, D. S.; Biondi, L. V.; Zillen, J. W.; Churchill, M. R.; Schrock, R. R. *Organometallics* **1983**, *2*, 1505. (c) LaPointe, A. M.; Schrock, R. R. *Organometallics* **1995**, *14*, 1875. (d) LaPointe, A. M.; Schrock, R. R.; Davis, W. M. *J. Am. Chem. Soc.* **1995**, *117*, 4802. (e) Toreki, R.; Vaughan, G. A.; Schrock, R. R.; Davis, W. M. *J. Am. Chem. Soc.* **1993**, *115*, 127.

35. In the ^{1}H NMR spectra of **7a-b**, the ethylene protons in the DMPE ligand give rise to a complex second-order pattern.

36. Espenson, J. H. In *Chemical Kinetics and Reaction Mechanism*; 2nd ed.; McGraw-Hill: New York, 1995; pp. 46-49.

37. Fettinger, J. C.; Mattamana, S. P.; Poli, R.; Rogers, R. D. *Organometallics* **1996**, *15*, 4211.

38. Li, L.; Hung, M.; Xue, Z. *J. Am. Chem. Soc.* **1995**, *117*, 12746.

39. Yu, X.; Morton, L. A.; Xue, Z-L. *Organometallics* **2004**, *23*, 2210.

40. Wood, C. D.; McLain, S. J.; Schrock, R. R. *J. Am. Chem. Soc.* **1979**, *101*, 3210.

41. SYBYL (with modules Sybyl Basic and Biopolymer), v. 8.0, Tripos Associates, St. Louis, MO.

42. Andersen, R. A.; Chisholm, M. H.; Gibson, J. F.; Reichert, W. W.; Rothwell, I. P.; Wilkinson, G. *Inorg. Chem.* **1981**, *20*, 3934.

43. Morse, P. M.; Spencer, M. D.; Wilson, S. R.; Girolami, G. S. *Organometallics* **1994**, *13*, 1646.

44. (a) Schrock, R. R. *Chem. Rev.* **2002**, *102*, 145. (b) Schrock, R. R. *Chem. Comm.* **2005**, 2773. (c) Current interest: Basuli, F.; Bailey, B. C.; Watson, L. A.; Tomaszewski, J.; Huffman, J. C.; Mindiola, D. J. *Organometallics* **2005**, *24*, 1886. Hoffmann, R. *Interdisciplinary Science Reviews* **1991**, *16*, 301. Kim, H. P.; Angelici, R. J. *Adv. Organomet. Chem.* **1987**, *27*, 51. (d) Mayr, A.; Hoffmeister, H. *Adv. Organomet. Chem.* **1991**, *32*, 227. (e) Schubert, U. In *Carbyne Complexes*, VCH: New York, **1988**, 39. (f) Nugent, W. A.; Mayer, J. M. In *Metal-Ligand Multiple Bonds*, Wiley: New York, 1988.

45. Dougan, B. A.; Xue, Z-L. *Organometallics* **2009**, *28*, 1295.

46. (a) Blanton, J. R.; Chen, T.-N.; Diminnie, J. B.; Cai, H.; Wu, Z.-Z.; Li, L.-T.; Sorasaenee, K. R.; Quisenberry, K. T.; Pan, H.-J.; Wang, C.-S.; Choi, S.-H.; Wu, Y.-D.; Lin, Z.-Y.; Guzei, I. A.; Rheingold, A. L.; Xue, Z.-L. *J. Mol. Catal. A: Chem.* **2002**, *190*, 101. (b) Diminnie, J. B.; Liu, X.-Z.; Cai, H.; Wu, Z.-Z.; Blanton, J. R.; Tuinman, A. A.; Quisenberry, K. T.; Vallet, C. E.; Zuhr, R. A.; Beach, D. B.; Peng, Z.-H.; Wu, Y.-D.; Concolino, T. E.; Rheingold, A. L.; Xue, Z.-L. *Pure Appl. Chem.* **2001**, *73*, 331.

47. (a) Wallace, R. M.; Wilk, G. D. *Crit. Rev. Solid State Mater. Sci.* **2003**, *28*, 231. (b) Smith, R. C.; Ma, T.; Hoilien, N.; Tsung, L. Y.; Bevan, M. J.; Colombo, L.; Roberts, J.; Campbell, S. A.; Gladfelter, W. L. *Adv. Mater. Opt. Electron.* **2000**, *10*, 105. (c) Kelly, P. V.; *et al.* Adv. Mater. Opt. Electron, **2000**, *10*, 115. (d) Senzaki, Y.; Hochberg, A. K.; Norman, J. A. T. *Adv. Mater. Opt. Electron.* **2000**, *10*, 93. (e) Lucovsky, G.; Phillips, J. C. *MRS Symp. Proc.* **1999**, *567* (Ultrathin SiO_2 and High-κ Materials for ULSI Gate Dielectrics), 201.

48. (a) Bastianini, A.; Battiston, G. A.; Gerbasi, R.; Porchia, M.; Daolio, S. J. *Phys. IV* **1995**, *5*, C5-525. (b) Ohshita, Y.; Ogura, A.; Hoshino, A.; Hiiro, S.; Machida, H. *J. Cryst. Growth* **2001**, *233*, 292. (c) Hendrix, B. C.; Borovik, A. S.; Xu, C.; Roeder, J. F.; Baum, T. H.; Bevan, M. J.; Visokay, M. R.; Chambers, J. J.; Rotondaro, A. L. P.; Bu, H.; Colombo, L. *Appl. Phys. Lett.* **2002**, *80*, 2362. (d) Vaartstra, B. A. U.S. Patent 2004040501, **2004**.

49. Son, K.-A.; Mao, A. Y.; Sun, Y.-M.; Kim, B. Y.; Liu, F.; Kamath, A.; White, J.M.; Kwong, D. L.; Roberts, D. A.; Vrtis, R. N. *Appl. Phys. Lett.* **1998**, *72*, 1187.

50. Feinstein-Jaffe, I.; Pedersen, S. F.; Schrock, R. R. *J. Am. Chem. Soc.* **1983**, *105*, 7176.

51. Feinstein-Jaffe, I.; Gibson, D.; Lippard, S. J.; Schrock, R. R.; Spool, A. *J. Am. Chem. Soc.* **1984**, *106*, 6305.

52. Schoettel, G.; Kress, J.; Fischer, J.; Osborn, J. A. *J. Chem. Soc., Chem. Comm.* **1988**, 914-915.

53. Legzdins, P.; Phillips, E. C.; Rettig, S. J.; Sanchez, L.; Trotter, J.; Yee, V. C. *Organometallics* **1988**, *7*, 1877-1878.

54. (a) Listermann, M. L.; Schrock, R. R. *Organometallics*, **1985**, *4*, 74. (b) Chisholm, M. H.; Cotton, F. A.; Extine, M.; Stults, B. R. *J. Am. Chem. Soc.* **1976**, *98*, 4477. (c) Akiyama, M.; Chisholm, M. H.; Cotton, F. A.; Extine, M. W.; Haitko, D. A.; Little, D.; Fanwick, P. E. *Inorg. Chem.* **1979**, *18*, 2266.

55. (a) Bruker SAINT-PLUS, Version 6.02 (including XPREP). Bruker AXS Inc. (b) Bruker. APEX2. Version 2.14. Bruker AXS Inc., Madison, Wisconsin, USA, 2007. (c) Sheldrick, G. M. SADABS. University of Göttingen, Germany, 2003.

56. Lippard, S. J.; Berg, J. M. In *Principles of Bioinorganic Chemistry*, University Science Press: CA, 1994.

57. (a) Behere, D. V.; Birdy, R.; Mitra, S. *Inorg. Chem.* **1982**, *21*, 386. (b) D'Angelo, P.; Lapi, A.; Migliorati, V.; Arcovito, A.; Benfatto, M.; Roscioni, O. M.; Meyer-Klaucke, W.; Della-Longa, S. *Inorg. Chem.* **2008**, *47*, 9905. (c) Scheidt, W. R.; Gouterman, M. *Iron Porphyrins, Part* One, Lever, A. B. P., Gray, H. B. Eds.; Addison-Wesley: Reading, MA, 1983; p. 89.

58. Hoard, J. L.; Cohen. G. H.; Glick, M. D. *J. Am. Chem. Soc.* **1967**, *89*, 1992.

59. (a) Cheng, R. J.; Chen, P. Y.; Lovell, T.; Liu, T.; Noodleman, L.; Case, D. A. *J. Am. Chem. Soc.* **2003**, *125*, 6774. (b) Mao, J.; Zhang, Y.; Oldfield, E. *J. Am. Chem. Soc.* **2002**, *124*, 13911. (c) Collman, J. P.; Hoard, J. L.; Kim, N.; Lang, G.; Reed, C. A. *J. Am. Chem. Soc.* **1975**, *97*, 2676. (d) Eaton, D. R.; LaLancette, E. A. *J. Chem. Phys.* **1964**, *41*, 3534.

60. Cheng, B.; Scheidt, W. R. *Acta Cryst.* **1996**, *C52*, 361.

61. Fleischer, E. B.; Miller, C. K.; Webb, L. E. *J. Am. Chem. Soc.* **1964**, *86*, 2342.

62. Scheidt, W. R.; Finnegan, M. G. *Acta Cryst.* **1989**, *C45*, 1214.

63. Schultz, D., Cookson, D., Gebhardt, J., Graber, T., Lin, B., Meron, M., Viccaro, P. J. *Abstracts of Papers, 228th ACS National Meeting*, Philadelphia, PA, August 22-26, 2004, Pages ANYL-018, Accession Number: 2004:655371.

64. Sheldrick, G. M. *Acta Cryst.* **2008**, *A64*, 112.

65. Spek, A. L. *J. Appl. Cryst*. **2003**, *36*, 7.

66. Scheidt, W. R.; Osvath, S. R.; Lee, Y. J. *J. Am. Chem. Soc.* **1987**, *109*, 1958.

67. Mitra, S. *Phys. Bioinorg. Chem. Series,* **1983**, *2* (Iron Porphyrins, Pt. 2), 1.

68. (a) Walker, F. A. *Coord. Chem. Rev.* **1999**, *185-186*, 471. (b) Walker. F. A. *Inorg. Chem.* **2003**, *42*, 4526. (c) Soltis, S. M.; Strouse, C. E. *J. Am. Chem. Soc.* **1988**, *110*, 2824.

69. (a) Tan, H.; Simonis, U.; Shokhirev, N. V.; Walker, F. A. *J. Am. Chem. Soc.* **1994**, *116*, 5784. (b) Goff, H. M. *J. Am. Chem. Soc.* **1981**, *103*,

3714. (c) Horrocks, W. D.; Greenberg, E. S. *Biochim. Biophys. Acta*, **1973**, *322*, 38.

70. Epstein, L. M.; Straub, D. K.; Maricondi, C. *Inorg. Chem.* **1967**, *6*, 1720.

71. Johansson, M. P.; Sundholm, D.; Gerfen, G.; Wikström, M. *J. Am. Chem. Soc.* **2002**, *124*, 11771.

72. (a) Scholes, C. P.; Falkowski, K. M.; Chen, S.; Bank, J. *J. Am. Chem. Soc.* **1986**, *108*, 1660. (b) Shokhirev, N. V.; Walker, F. A. *J. Phys. Chem.* **1995**, *99*, 17795. (c) Astashkin, A. V.; Raitsimring, A. M.; Walker, F. A. *J. Am. Chem. Soc.* **2001**, *123*, 1905.

73. (a) Dougan, B. A.; Xue, Z. L. *Sci Chi Chem.* **2009**, *52*, 2083. (b) Gillon, B. Spin Distributions in Molecular Systems with Interacting Transition Metal Ions. In *Magnetism Molecules to Materials,* Miller, J. S., Drillon, M., Eds.; Wiley-VCH: New York, 2001; p. 357. (c) Schweizer, J.; Ressouche, E. In *Magnetism Molecules to Materials*, Miller, J. S., Drillon, M., Eds.; Wiley-VCH: New York, 2001; p. 325.

74. Spaldin, N. A. In *Magnetic Materials*, University Press: Cambridge, 2003; p. 46.

75. See Chapter 5 on the X-ray structure analyses of Fe(TPP)Cl (**12**) at 20(2), 143(2), and 293(2) K.

76. Silver, J.; Marsh, P. J.; Symons, M. C. R.; Svistunenko, D. A.; Frampton, C. S.; Fern, G. R. *Inorg. Chem.* **2000**, *39*, 2874.

77. Collins, D. M.; Countryman, R.; Hoard, J. L. *J. Am. Chem. Soc.* **1972**, *94*, 2066.

78. Scheidt, W. R.; Kirner, J. F.; Hoard, J. L. Reed, C. A. *J. Am. Chem. Soc.* **1987**, *109*, 1963.

79. Lehmann, M. S.; Kuhs, W.; Allibon, J.; Wilkinson, C.; McIntyre, G. J. *J. Appl. Cryst.* **1989**, *22*, 562.

80. Barthélemy, A. *ILL Technical Report*, lLL84BA15T. **1984**.

81. Filhol, A. *ILL Technical Report*, lLL87FI19T. **1987**.

82. (a) Wilkinson, C.; Khamis, H. W.; Stansfield, R. F. D.; McIntyre, G. J. *J. Appl, Cryst.* **1988**, *21*, 471. (b) Sears, V. G. Methods of Experimental Physics. In *Neutron Scattering*, Sköld, K., Price, D. L., Eds.; Vol. 23A; Academic Press: Orlando, 1986; p. 521.

83. (a) Bertini, I.; Gray, H. B.; Stiefel, E. I.; Valentine, J. S. In *Biological Inorganic Chemistry. Structure and Reactivity*, University Science Books: CA, 2007. (b) Kaim, W.; Schwederski, B. In *Bioinorganic Chemistry: Inorganic Elements in the Chemistry of Life. An Introduction and Guide*, Wiley: New York, 1994; p. 84.

84. (a) Collman, J. P.; Boulatov, R.; Sunderland, C. J.; Fu, L. *Chem. Rev.* **2004**, *104*, 561. (b) Scheidt, W. R.; Gouterman, M. *Phy. Bioinorg. Chem. Series* **1983**, *1* (Iron Porphyrins, Pt. 1), 89. (c) Suslick, K. S.; Reinert, T. J. *J. Chem. Edu.* **1985**, *62*, 974. (d) Groves, J. T. *J. Inorg. Biochem.* **2006**, *100*, 434. (e) Momenteau, M.; Reed, C. A. *Chem. Rev.* **1994**, *94*, 659. (f) Cheek, J.; Dawson, J. H. In *Handbook of Proteins,* Cox, M. M., Phillips, G. N. Eds.; Vol. 1, 2007; pp. 569-576. (g) Balch, A. L. *Inorg. Chim. Acta* **1992**, *198-200*, 297.

85. (a) Bertini, I.; Turano, P.; Vila, A. J. *Chem. Rev.* **1993**, *93*, 2833. (b) La Mar, G. N.; Satterlee, J. D.; De Ropp, J. S. In *Porphyrin Handbook,* Kadish, K. M., Smith, K. M., Guilard, R. Eds.; Vol. 5, 2000; pp. 185-298. (c) Nakamura, M. *Coord. Chem. Rev.* **2006**, *250*, 2271. (d) Pavel, E. G.; Solomon, E. I. *ACS Symp. Series* **1998**, *692*, 119. (e) Dawson, J. H.; Dooley, D. M. *Phys. Bioinorg. Chem. Series* **1989**, *4* (Iron Porphyrins, Pt. 3), 93. (f) Hersleth, H.-P.; Ryde, U.; Rydberg, P.; Goerbitz, C. H.; Andersson, K. K. *J. Inorg. Biochem.* **2006**, *100*, 460. (g) Rivera M.; Caignan G. A. *Anal. Bioanal. Chem.* **2004**, *378*, 1464. (h) Debrunner, P. G. *Phys. Bioinorg. Chem. Series* **1989**, *4* (Iron Porphyrins, Pt. 3), 137.

86. (a) Blumberg, W. E.; Peisach, J. *Adv. Chem. Ser.* **1971**, *100*, 271. (b) Peisach, J.; Blumberg, W. E.; Adler, A. *Ann. N. Y. Acad. Sci.* **1973**, *206*, 310. (c) Walker, F. A.; Reis, D.; Balke, V. L. *J. Am. Chem. Soc.* **1984**, *106,* 6888. (d) Quinn, R.; Strouse, C. E.; Valentine, J. S. *Inorg. Chem.* **1983**, *22*, 3934. (e) La Mar, G. N.; Walker, F. A. *J. Am. Chem. Soc.* **1973**, *95*, 1782. (f) Tabard, A.; Cocolios, P.; Lagrange, G.; Gerardin, R.; Hubsch, J.; Lecomte, C.; Zarembowitch, J.; Guilard, R. *Inorg. Chem.* **1988**, *27*, 110. (g) Jiao, X. D.; Huang, J. W.; Liu, J. F.; Ji, L. N. *Chinese Chem Lett.* **1994**, *5*, 615. (h) Quinn, R.; Nappa, M.; Valentine, J. S. *J. Am. Chem. Soc.* **1982**, *104*, 2588. (i) Zhu, Z.; Ma, Y.; Chen, R.; Zhang, Y.; Jiang, D. *Chinese J. Inorg. Chem.* **1991**, *7*, 153. (j) Quinn, R.; Valentine, J. S.; Byrn, M. P.; Strouse, C. E. *J. Am. Chem. Soc.* **1987**, *109*, 3301.

87. (a) Mao, J.; Zhang, Y.; Oldfield, E. *J. Am. Chem. Soc*. **2002**, *124*, 13911.

(b) Yamamoto, Y.; Nanai, N.; Chujo, R.; Inoue, Y. *Bull. Chem. Soc. Jpn.* **1991**, *64*, 3199. (c) Xia, X.; Zhu, Z.; Chen, R. *Chinese J. Inorg. Chem.* **1992**, *8*, 367.

88. Zhang, Y.; Mao, J.; Oldfield, E. *J. Am. Chem. Soc*. **2002**, *124*, 7829.

89. Praneeth, V. K. K.; Neese, F.; Lehnert, N. *Inorg. Chem.* **2005**, *44*, 2570.

90. (a) Johansson, M. P.; Sundholm, D. *J. Chem. Phys.* **2004**, *120*, 3229. (b) Chen, H.; Ikeda-Saito, M.; Shaik, S. *J. Am. Chem. Soc.* **2008**, *130*, 14778. (c) Jensen, K. P.; Ryde, U. *J. Biol. Chem.* **2004**, *279*, 14561.

91. (a) McConnell, H. M.; Chesnut, D. B. *J. Chem. Phys*. **1958**, *28*, 107. (b) Kaiser, E. T.; Kevan, L. In *Radical Ions*, Wiley-Interscience: New York, 1968. (c) Bertini, I.; Luchinat, C.; Parigi, G. *Eur. J. Inorg. Chem*. **2000**, 2473. (d) Bertini, I.; Luchinat, C.; Parigi, G. In *Solution NMR of Paramagnetic Molecules*, Elsevier: Amsterdam, 2001.

92. (a) Mun, S. K.; Mallick, M. K.; Mishra, S.; Chang, J. C.; Das, T. P. *J. Am. Chem. Soc.* **1981**, *103*, 5024. (b) Magliozzo, R. S.; Peisach, J. *Biochemistry* **1992**, *31*, 189.

93. (a) Rigby, S. E. J.; Moore, G. R.; Gray, J. C.; Gadsby, P. M. A.; George, S. J.; Thomson, A. J. *Biochem. J*. **1988**, *256*, 571. (b) Axe, F. U.; Flowers, C.; Loew, G. H.; Waleh, A. *J. Am. Chem. Soc*. **1989**, *111*, 7333.

94. Hocking, R. K.; Wasinger, E. C.; Yan, Y.-L.; de Groot, F. M. F.; Walker, F. A.; Hodgson, K. O.; Hedman, B.; Solomon, E. I. *J. Am. Chem. Soc.* **2007**, *129*, 113.

95. (a) Brown, P. J.; Forsyth, J. B.; Mason, R. *Philos. Trans. R. Soc. London,*

B **1980**, *290*, 481. (b) Ressouche, E. *Physica B*, **1999**, *267-268*, 27.

96. (a) Pontillon, Y.; Caneschi, A.; Gatteschi, D.; Sessoli, R.; Ressouche, E.; Schweizer, J. ; Lelievere-Berna, E. *J. Am. Chem. Soc*. **1999**, *121*, 5342. (b) Baron, V.; Gillon, B.; Plantevin, O.; Cousson, A.; Mathoniere, C.; Kahn, O.; Grand, A.; Oehrstroem, L.; Delley, B. *J. Am. Chem. Soc*. **1996**, *118*, 11822. (c) Gillon, B.; Goujon, A.; Willemin, S.; Larionova, J.; Desplanches, C.; Ruiz, E.; Andre, G.; Stride, J. A.; Guerin, C. *Inorg. Chem.* **2007**, *46*, 1090. (d) Zheludev, A.; Grand, A.; Ressouche, E.; Schweizer, J.; Morin, B. G.; Epstein, A. J.; Dixon, D. A.; Miller, J. S. *J. Am. Chem. Soc.* **1994**, *116*, 7243. (e) Figgis, B. N.; Reynolds, P. A.; Mason, R. *J. Am. Chem. Soc.* **1983**, *105*, 440. (f) Luzon, J.; Campo, J.; Palacio, F.; McIntyre, G. J.; Goeta, A. E.; Pask, C. M.; Rawson, J. M. *Polyhedron* **2003**, *22*, 2301.

97. Nathans, R.; Shull, C. G.; Shirane, G.; Andresen, A. *J. Phys. Chem. Solids,* **1959**, *10*, 138.

98. Brown, P. J.; Forsyth, J. B. *Brit. J. Appl. Phys.* **1964**, *15*, 1529.

99. Matthewman, J. C.; Thompson, P.; Brown, P. J. *J. Appl. Cryst.* **1982**, *15*, 167.

98. Fajer, J.; Borg, D. C.; Forman, A. *Ann. N.Y. Acad. Sci.* **1973**, *206*, 349.

99. Shirazi, A.; Goff, H. M. *J. Am. Chem. Soc.* **1982**, *104*, 6318.

100. (a) Adler, A. D.; Longo, F. R.; Finarelli, J. D.; Goldmacher, J.; Assour, J. Koraskoff, L. *J. Org. Chem.* **967**, *32*, 476. (b) Barnett, G. H.; Hudson, M. F.; Smith, K. M. *J. Chem. Soc., Perkin Trans. I* **1975**, 1401.

101. (a) Lindsey, J. S.; Schreiman, I. C.; Hsu, H. C.; Kearney, P. C., Maguerettaz, A. M. *J. Org. Chem.* **1987**, *52*, 827. (b) Lindsey, J. S.; Hsu, H. C.; Schriman, I. C. *Tetrahedron Lett.* **1986**, *27*, 4969.

102. (a) MacCrum, K. A.; Tyhonas, J. S.; Chuang, Y.-Y. Lindsey, J. S. *J. Org. Chem.* **1994**, *59*, 579. (b) Geier, G. R.; Lindsey, J. S. J. *Porphyrins Phthalocyanines*, **2002**, *6*, 1599.

103. Fajer, J.; Borg, D. C.; Forman, A. *Ann. N.Y. Acad. Sci.* **1973**, *206*, 349.

104. Shirazi, A.; Goff, H. M. *J. Am. Chem. Soc.* **1982**, *104*, 6318.

105. Asano, M. S.; Abe, H.; Kaizu, Y. *J. Label. Compd. Radiopharm.* **2006**, *49*, 595.

106. Silvers, S. J.; Tulinksy, A. *J. Am. Chem. Soc.* **1967**, *89*, 3331.

107. Adler, A. D.; Longo, F. R.; Kampas, F.; Kim, J. *J. Inorg. Nuc. Chem.* **1970**, *32*, 2443.

APPENDIX

APPENDIX A

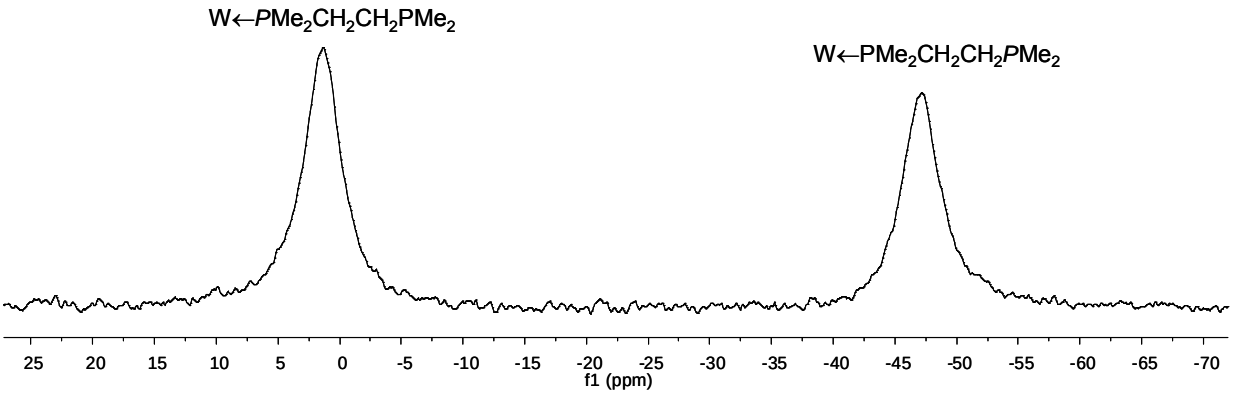

Figure A1. ^{31}P NMR spectrum of **4a** at -5 °C.

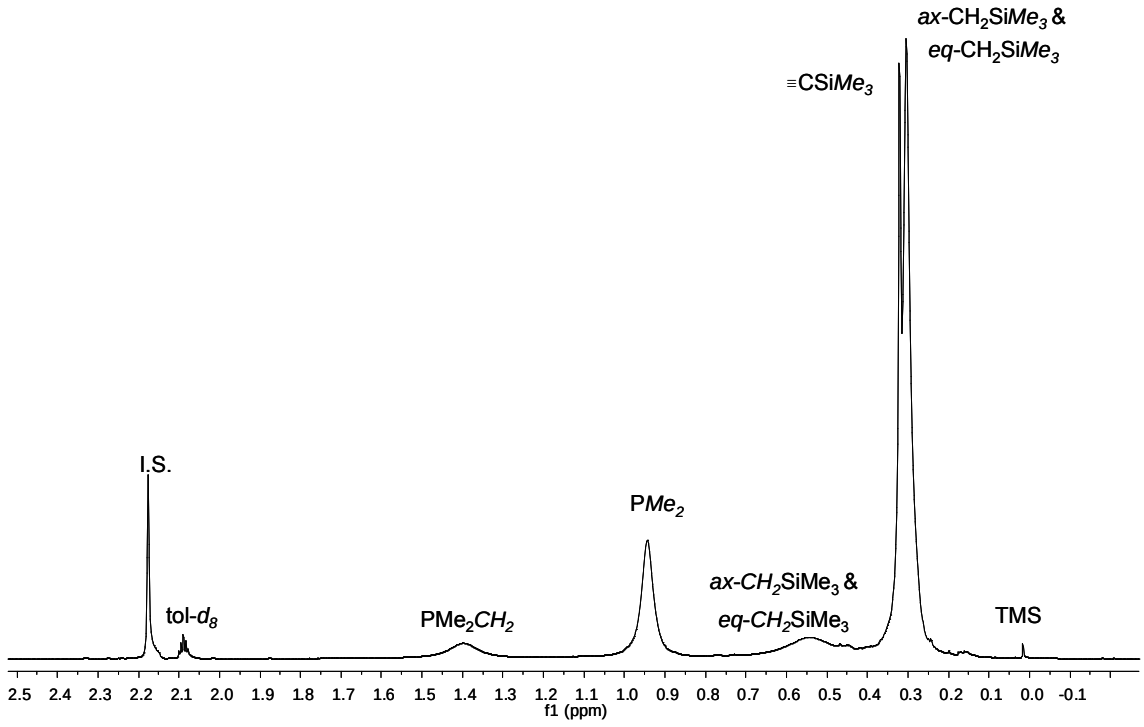

Figure A2. ^{1}H NMR spectrum of **4a** at -5 °C (I.S. = 4,4'-dimethylbiphenyl).

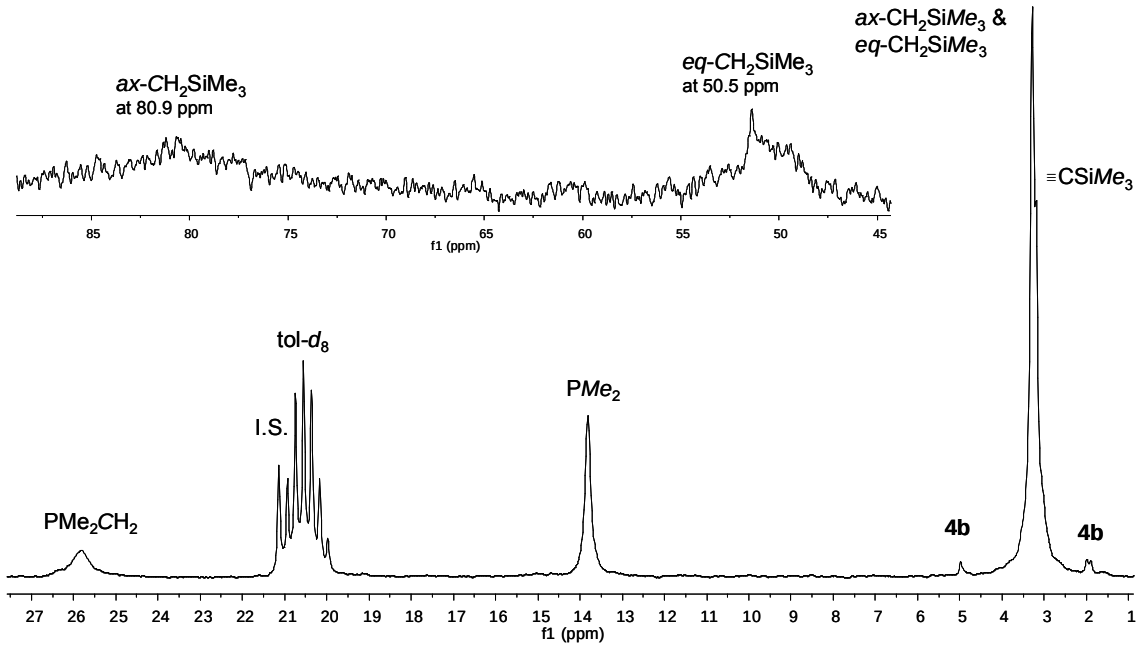

Figure A3. ^{13}C NMR spectrum of **4a** at -5 °C (I.S. = 4,4'-dimethylbiphenyl).

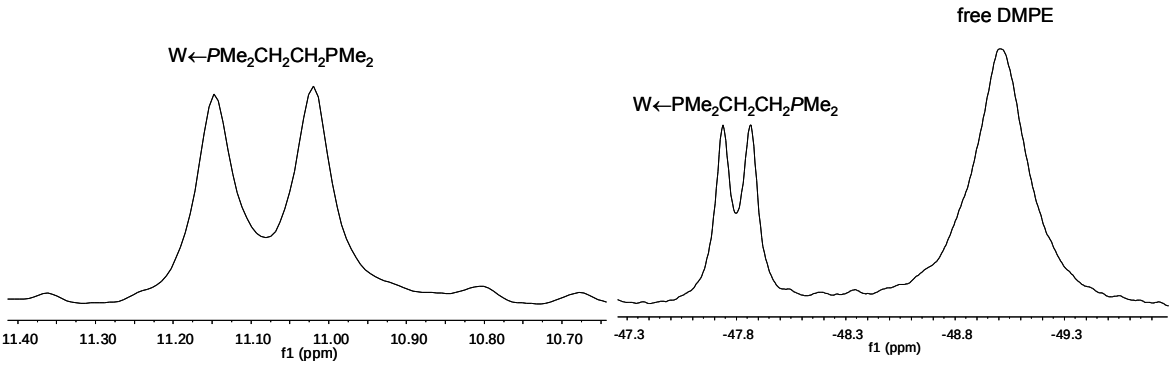

Figure A4. ^{31}P NMR spectrum of **4b** at -20 °C.

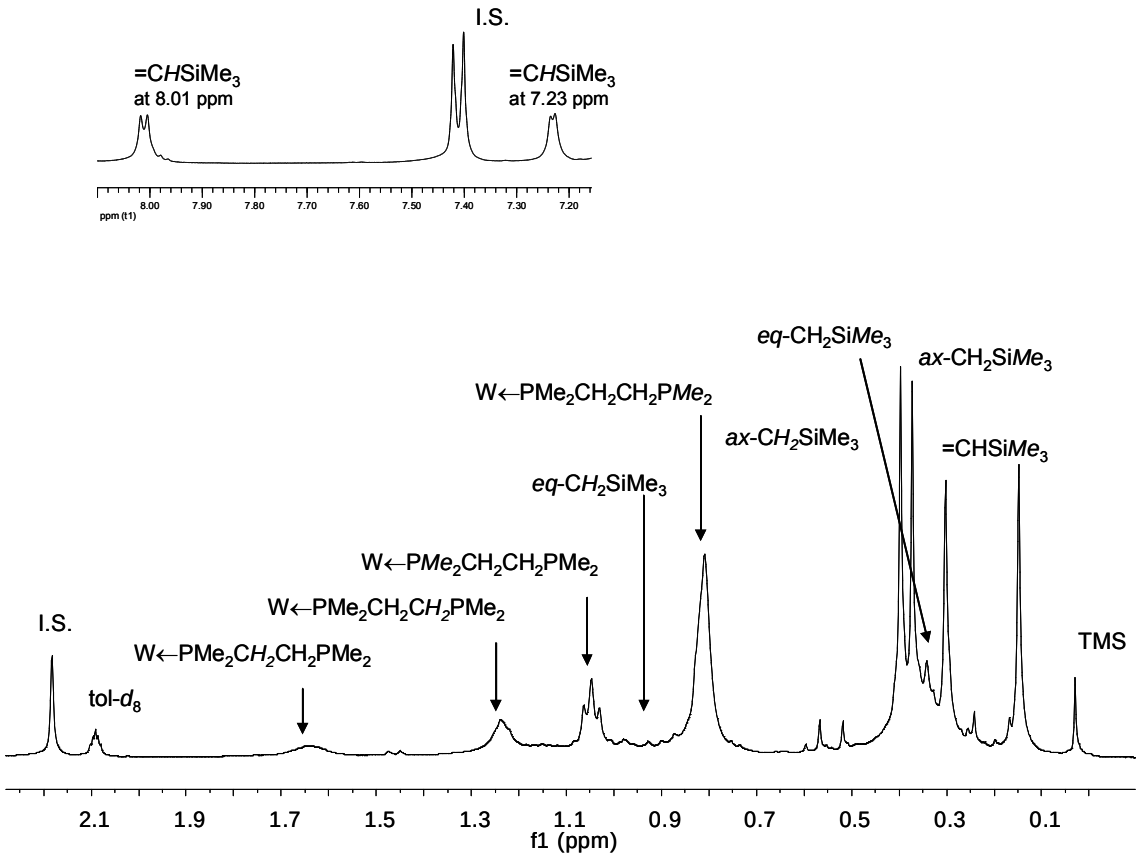

Figure A5. ^{1}H NMR spectrum of **4b** at -20 °C.

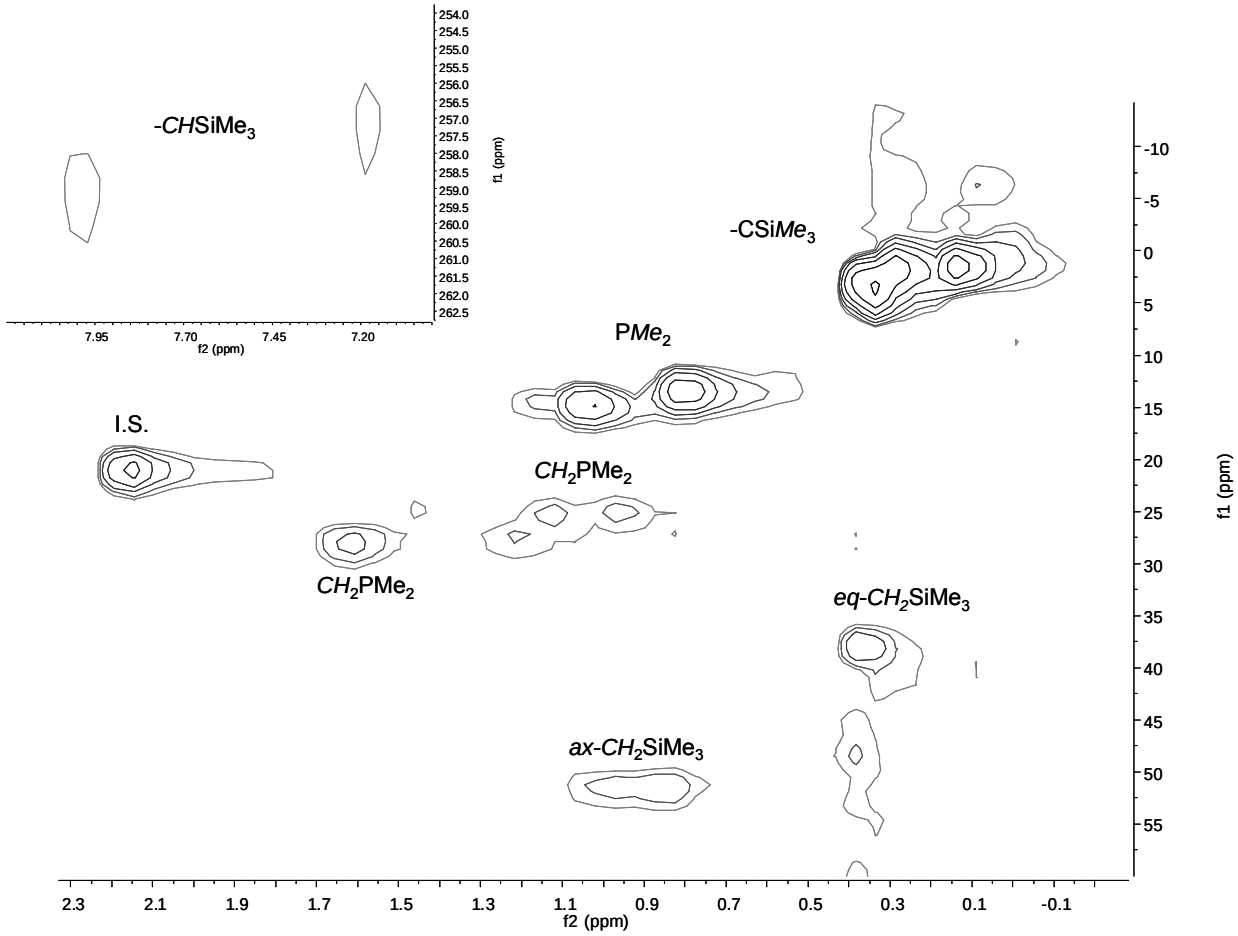

Figure A6. HSQC of **4b** at -20 °C.

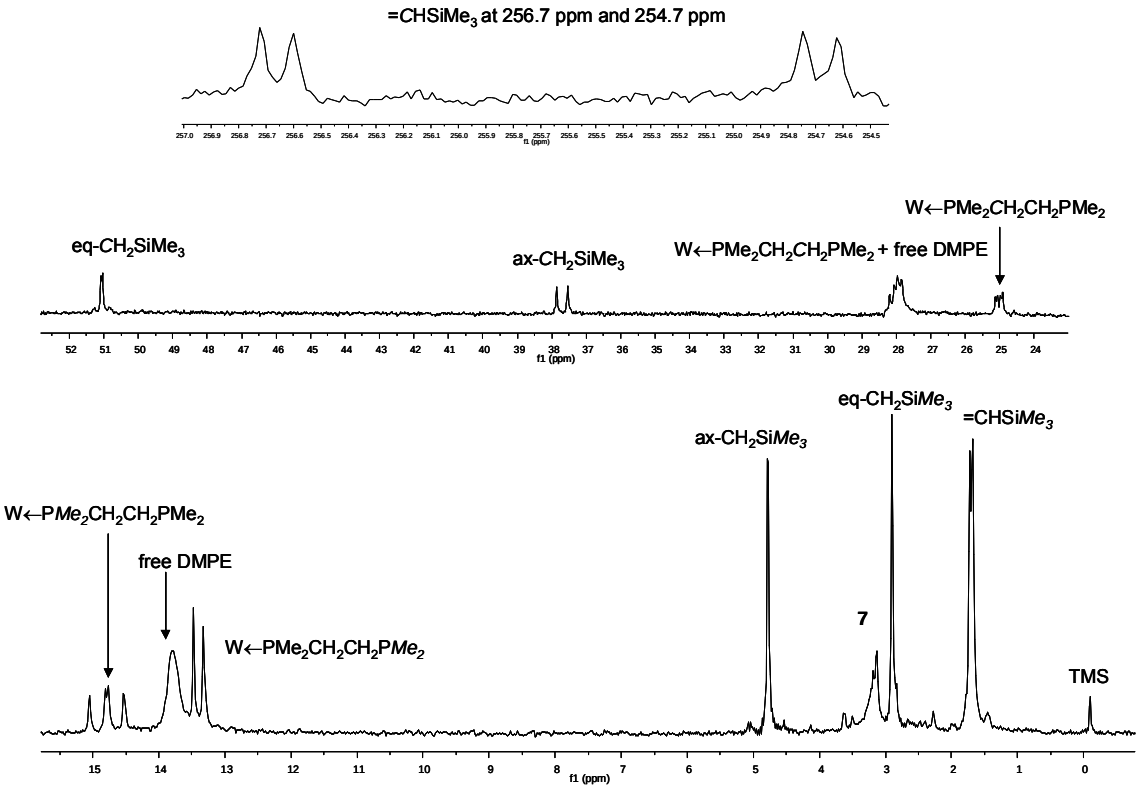

Figure A7. ^{13}C NMR spectrum of **4b** at -20 °C.

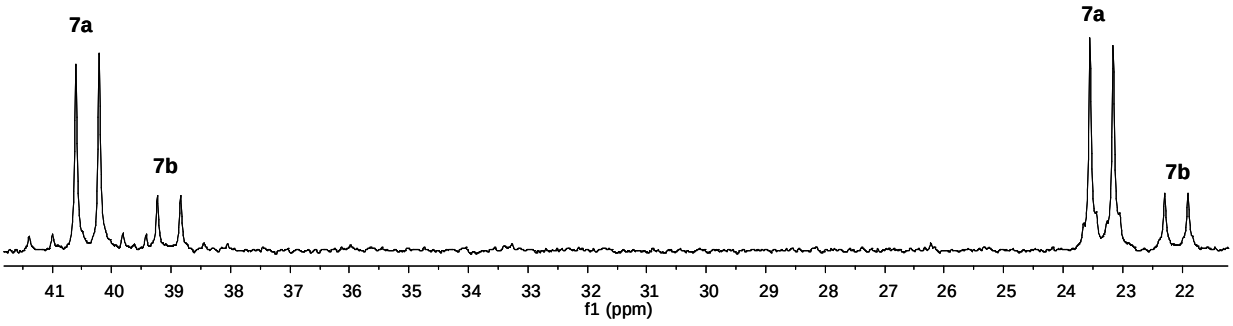

Figure A8. ^{31}P NMR spectrum of **7a** and **7b** at room temperature.

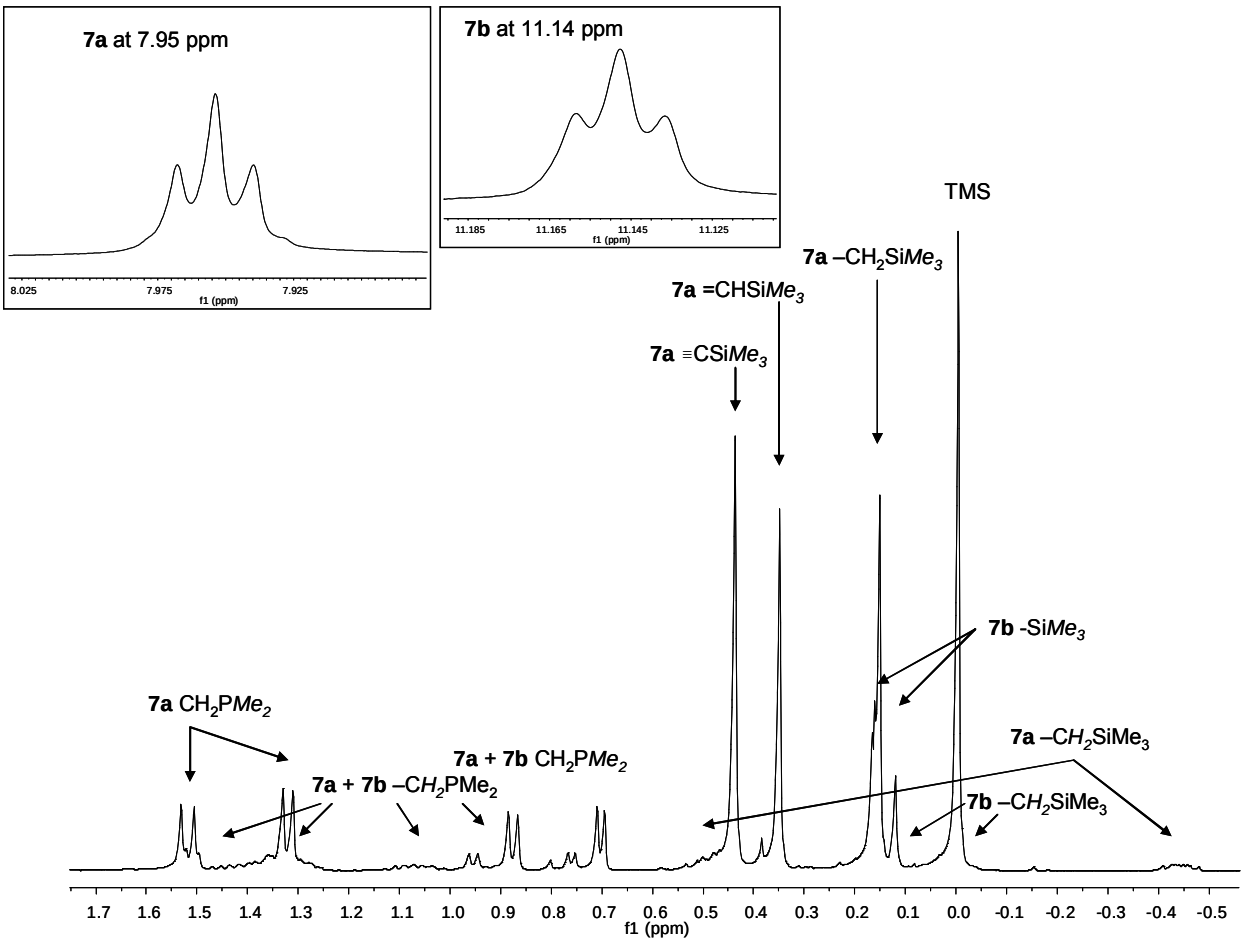

Figure A9. ^{1}H NMR spectrum of **7a** and **7b** at room temperature.

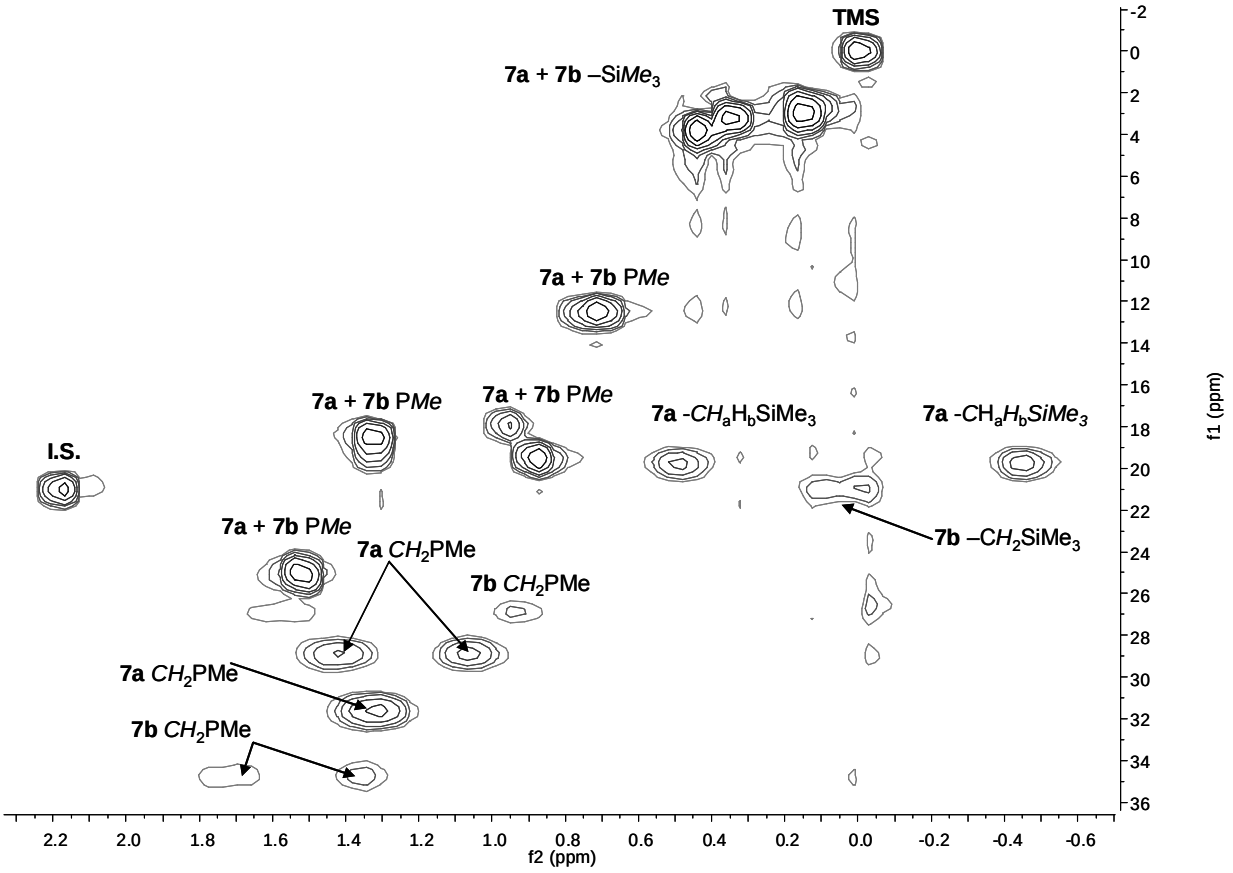

Figure A10. HSQC of **7a** and **7b** at room temperature (I.S. = 4,4'-dimethylbiphenyl).

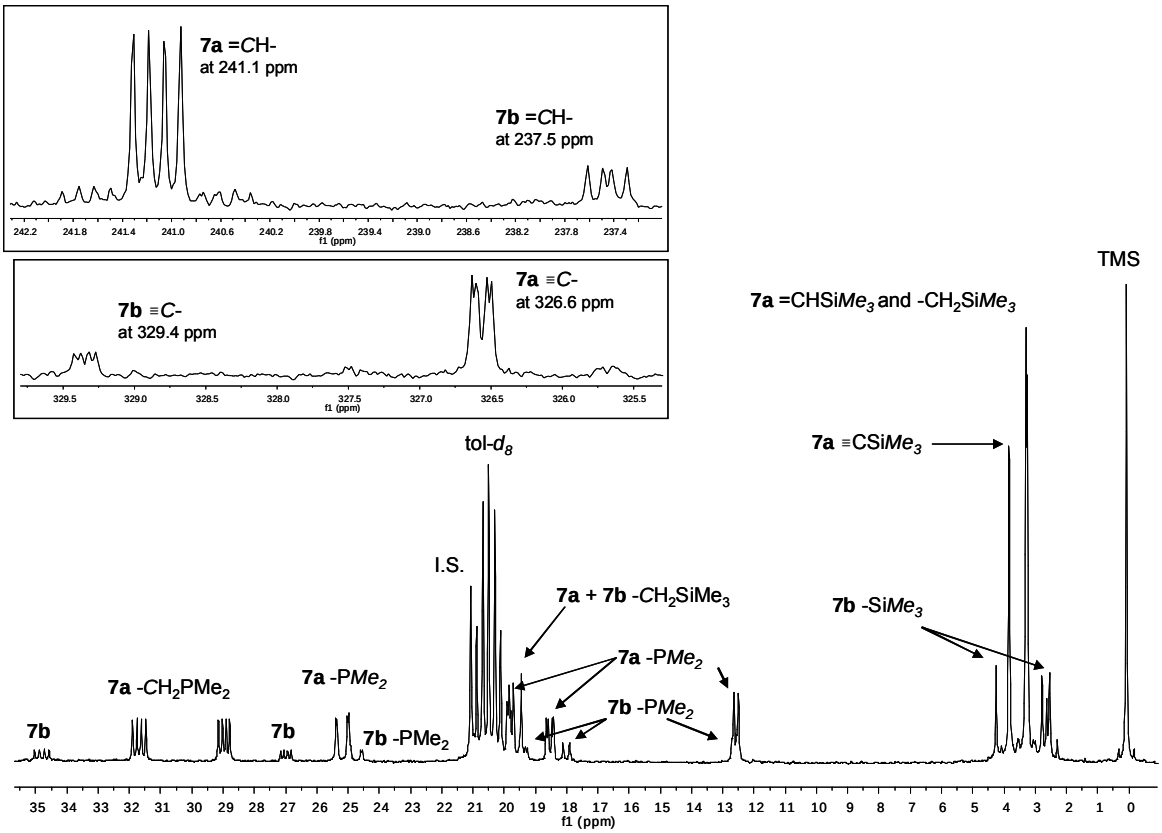

Figure A11. ^{13}C NMR spectrum of **7a** and **7b** at room temperature (I.S. = 4,4'-dimethylbiphenyl).

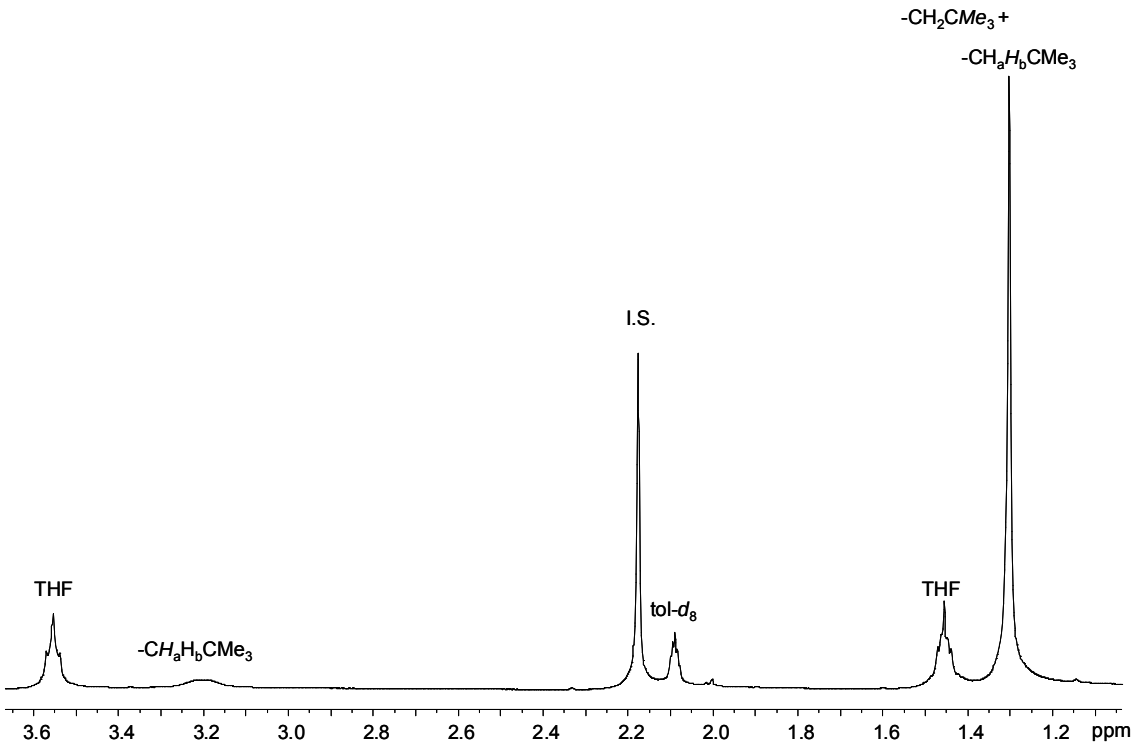

Figure A12. ^{1}H NMR spectrum of **9** at room temperature.

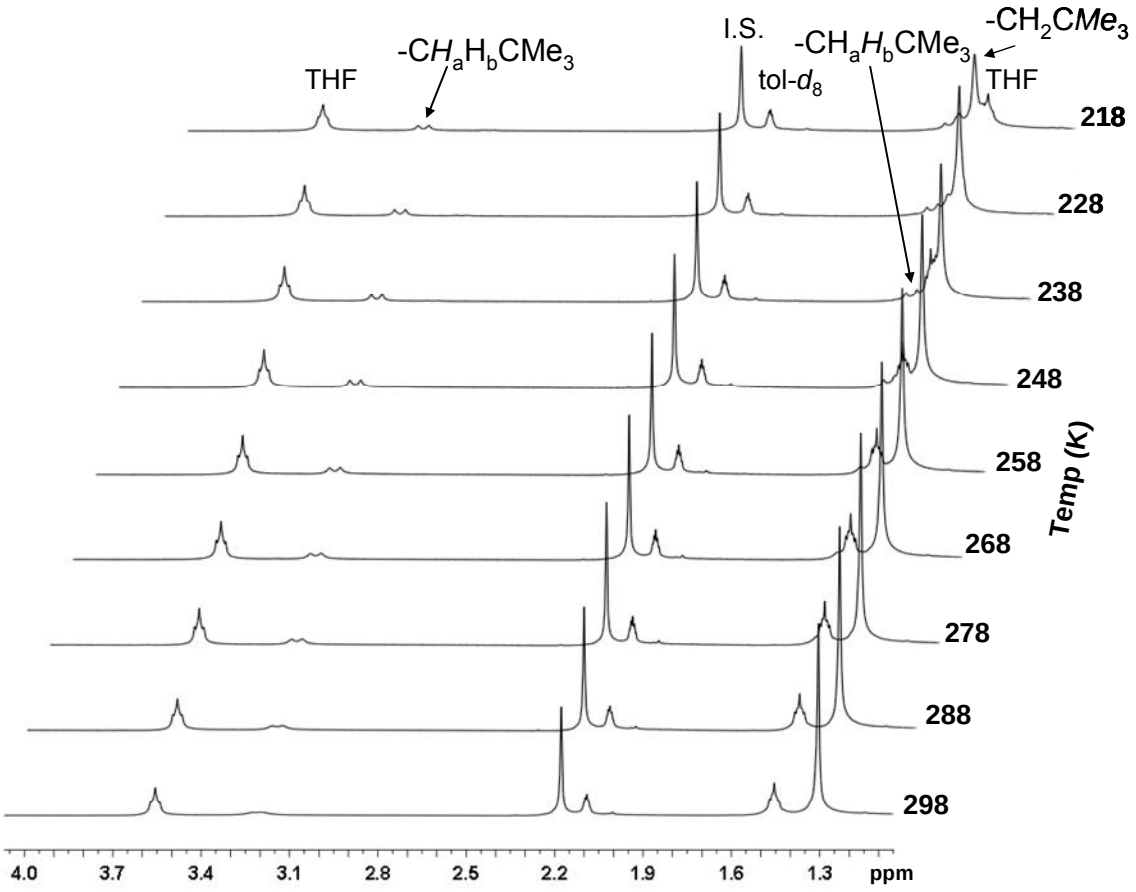

Figure A13. Variable-temperature ^{1}H NMR spectra of **9** in toluene-d_8 (I.S. = 4,4'-dimethylbiphenyl).

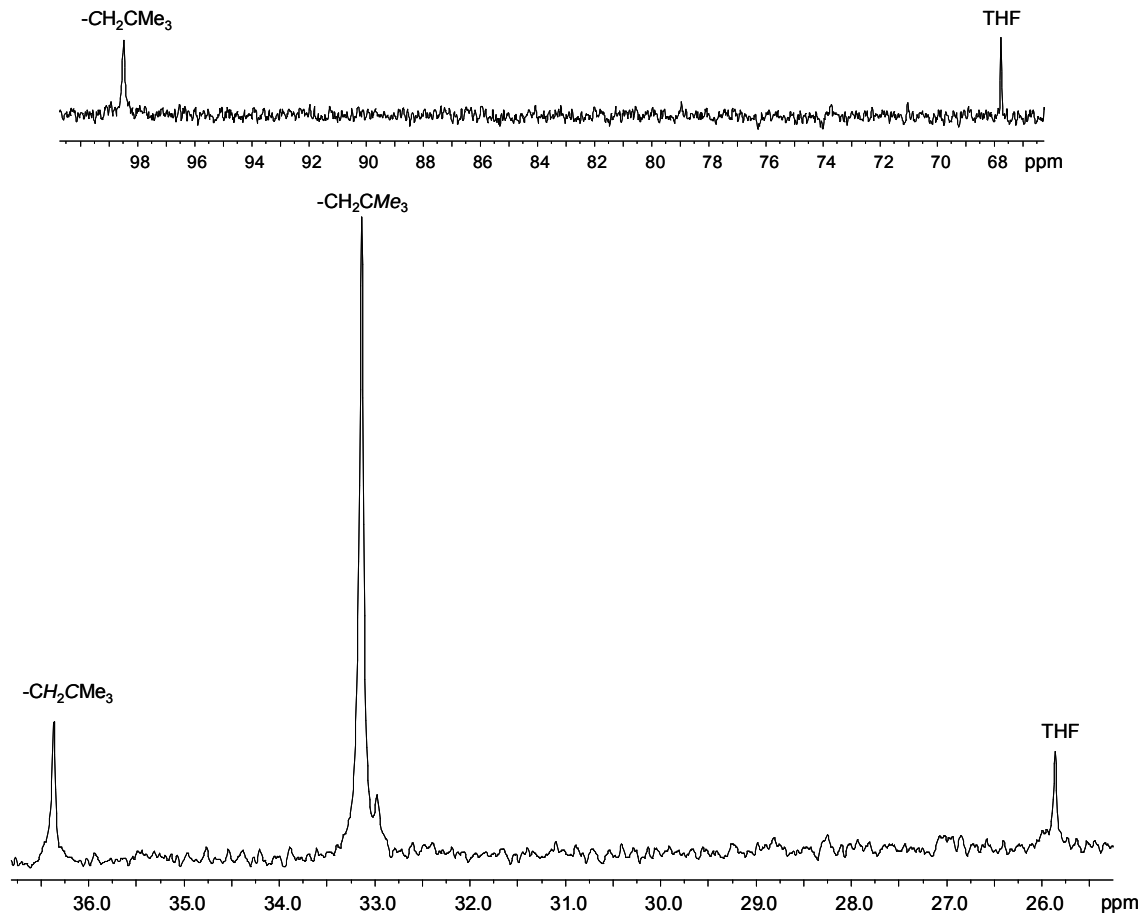

Figure A14. ^{13}C NMR spectrum of **9** at room temperature.

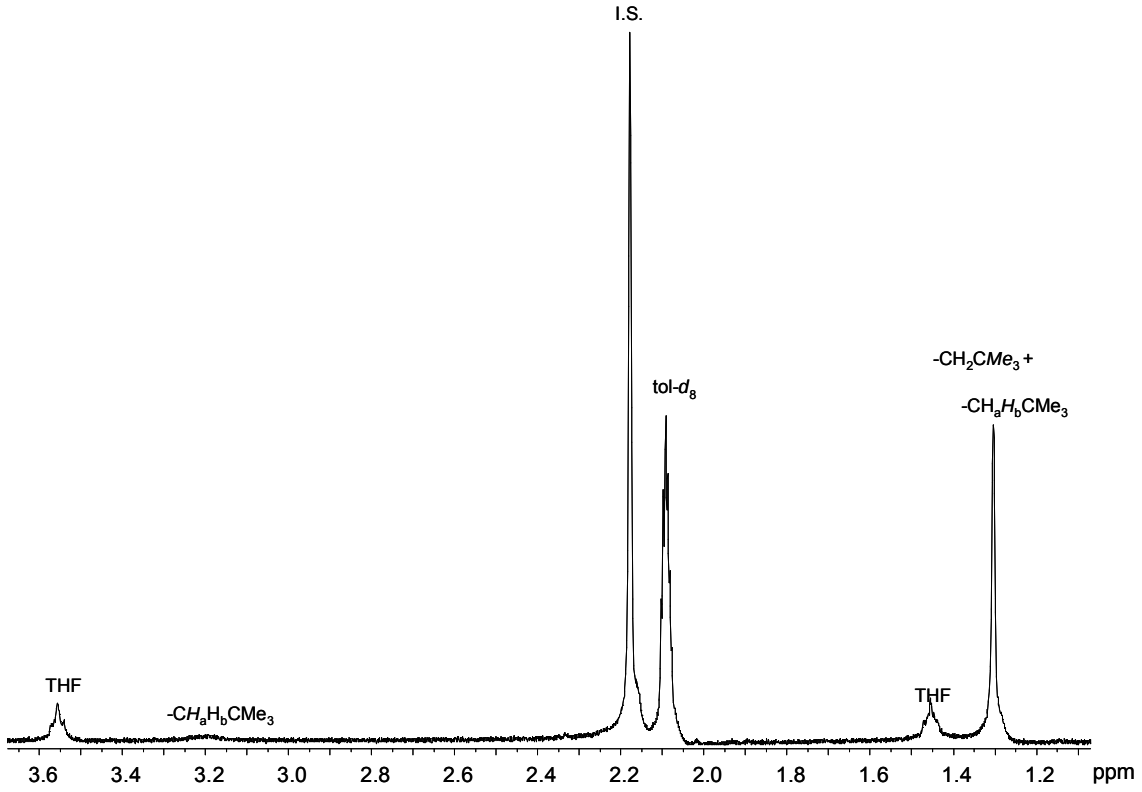

Figure A15. ^{1}H NMR spectrum of the reaction of $W(CH_2CMe_3)_3(\equiv CSiMe_3)$ (**8**) + excess D_2O at room temperature.

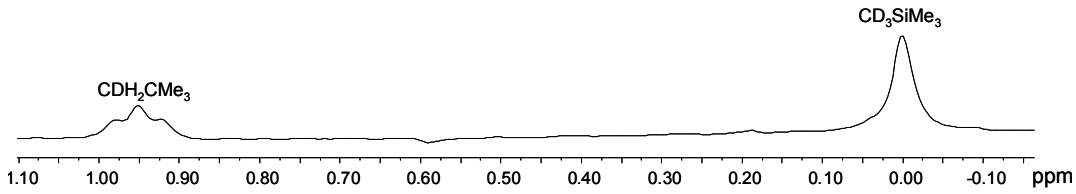

Figure A16 ^{2}H NMR spectrum of the reaction of $W(CH_2CMe_3)_3(\equiv CSiMe_3)$ (**8**) + excess D_2O at 218 K. Non-deuterated THF solvent was used with three drops of THF-d_8 as reference.

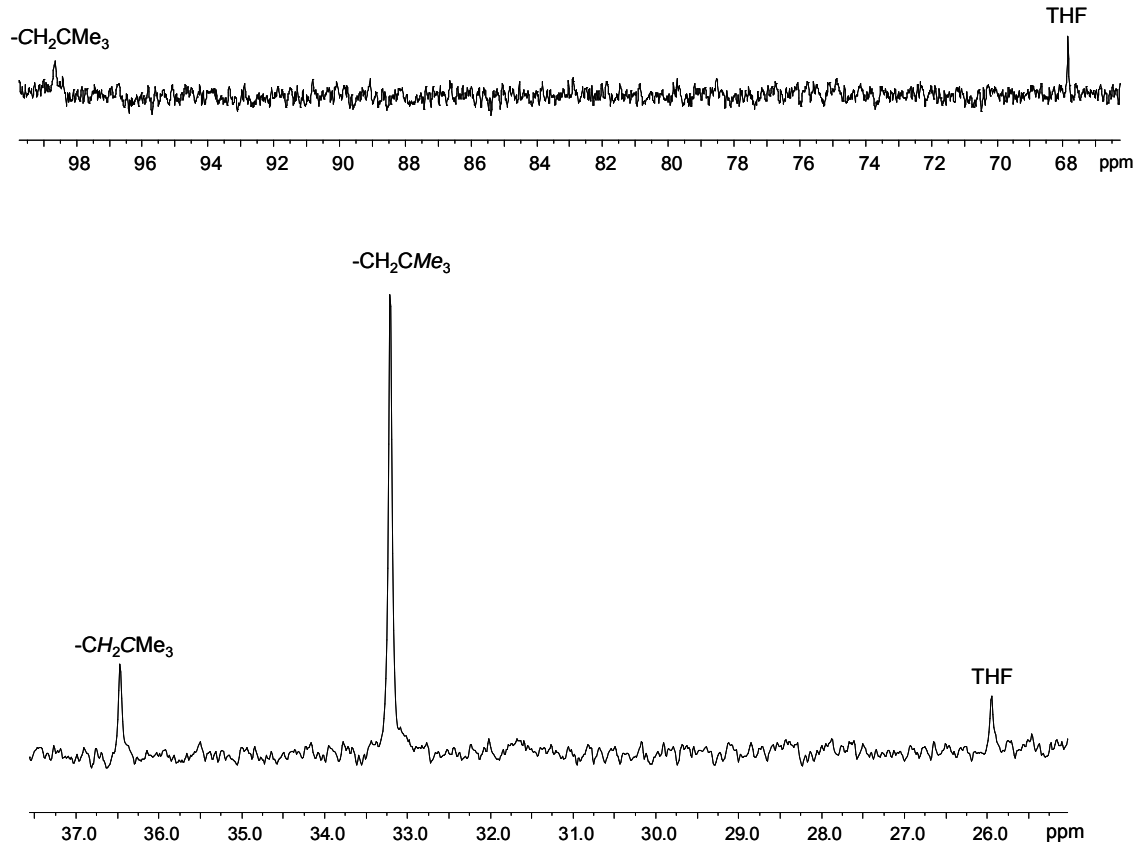

Figure A17. ^{13}C NMR spectrum of the reaction of $W(CH_2CMe_3)_3(\equiv CSiMe_3)$ (**8**) + excess D_2O at room temperature.

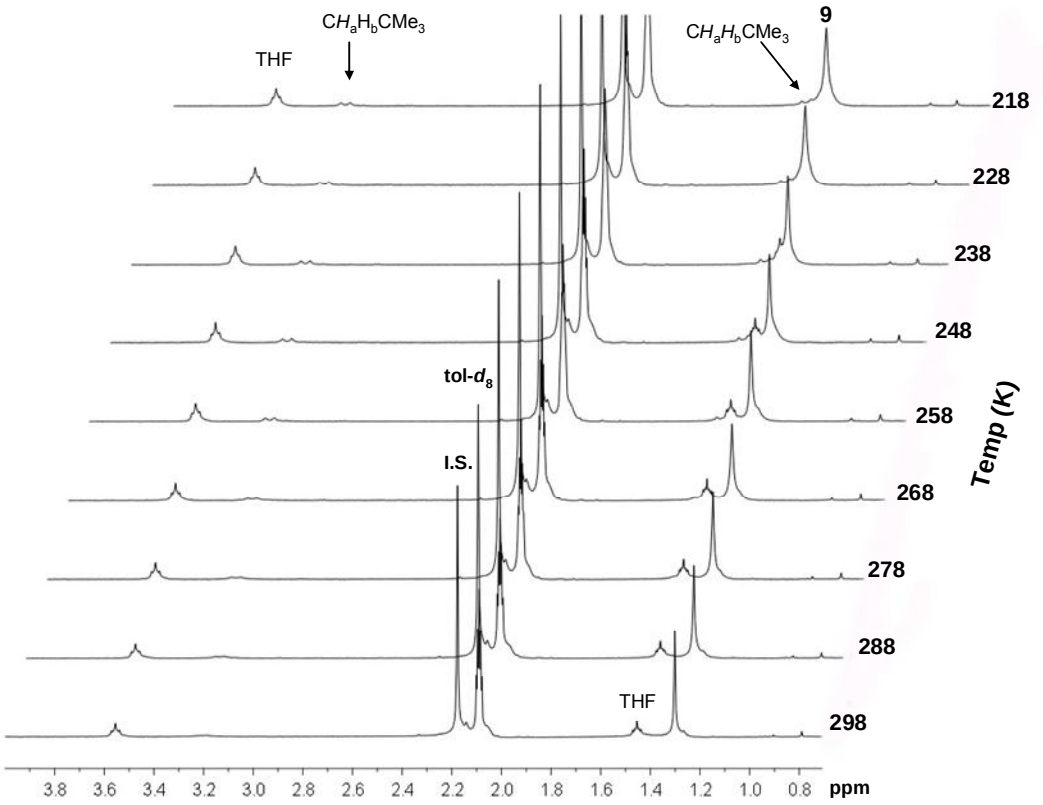

Figure A18. Variable-temperature ^{1}H NMR spectra of the reaction of $W(CH_2CMe_3)_3(\equiv CSiMe_3)$ (**8**) + excess D_2O in tol-d_8 (I.S. = 4,4'-dimethylbiphenyl).

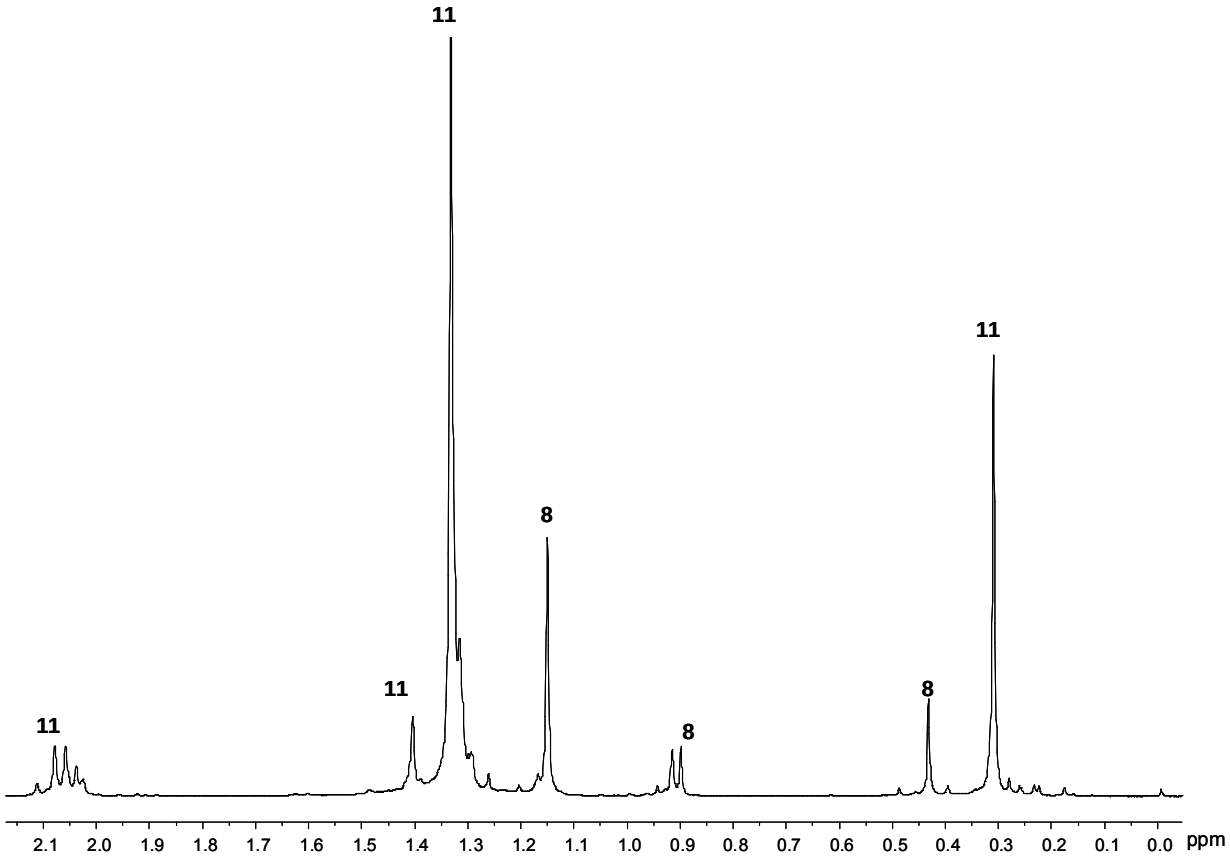

Figure A19. ^{1}H NMR spectrum of **11** at room temperature (with presence of **9** and **10**) (I.S. = 4,4'-dimethylbiphenyl).

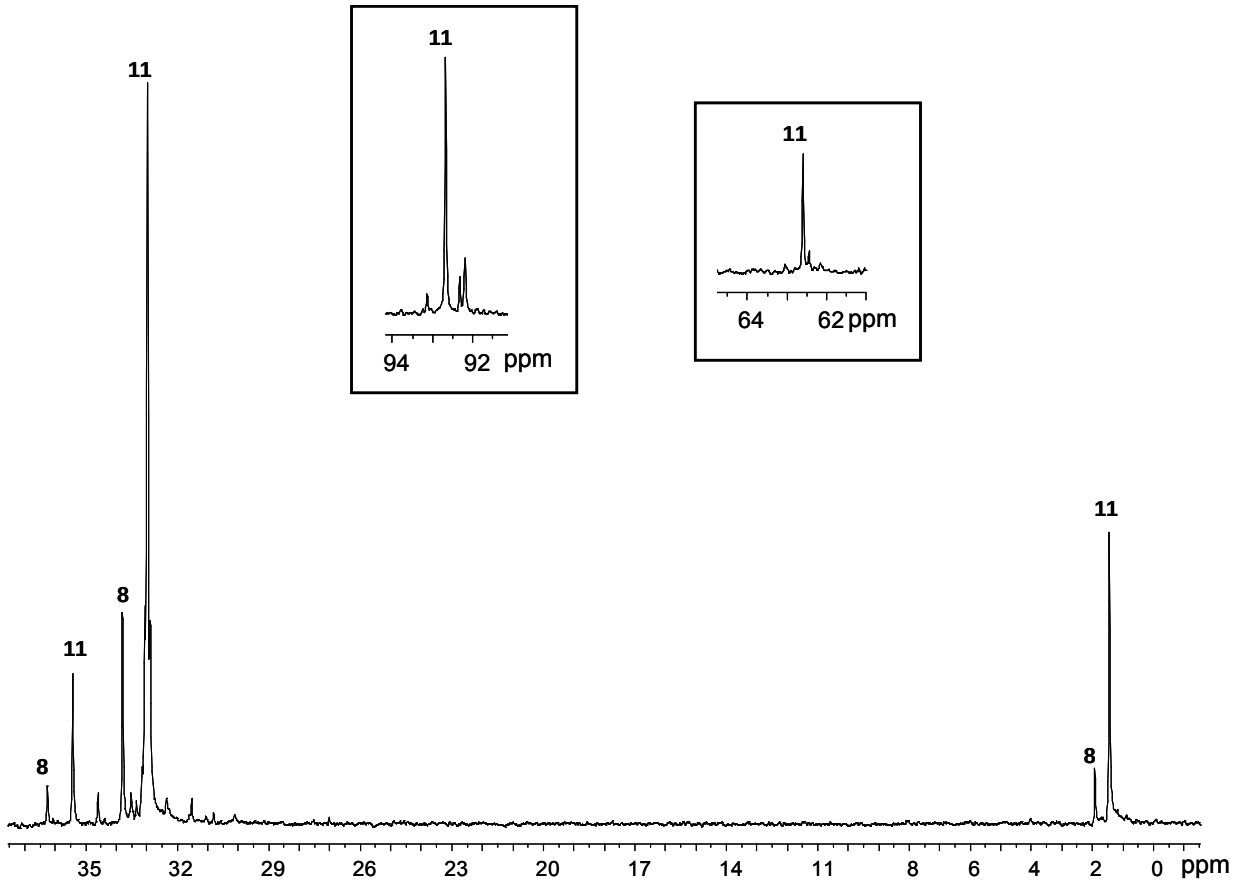

Figure A20. ^{13}C NMR spectrum of **11** at room temperature (with presence of **9** and **10** (I.S. = 4,4'-dimethylbiphenyl).

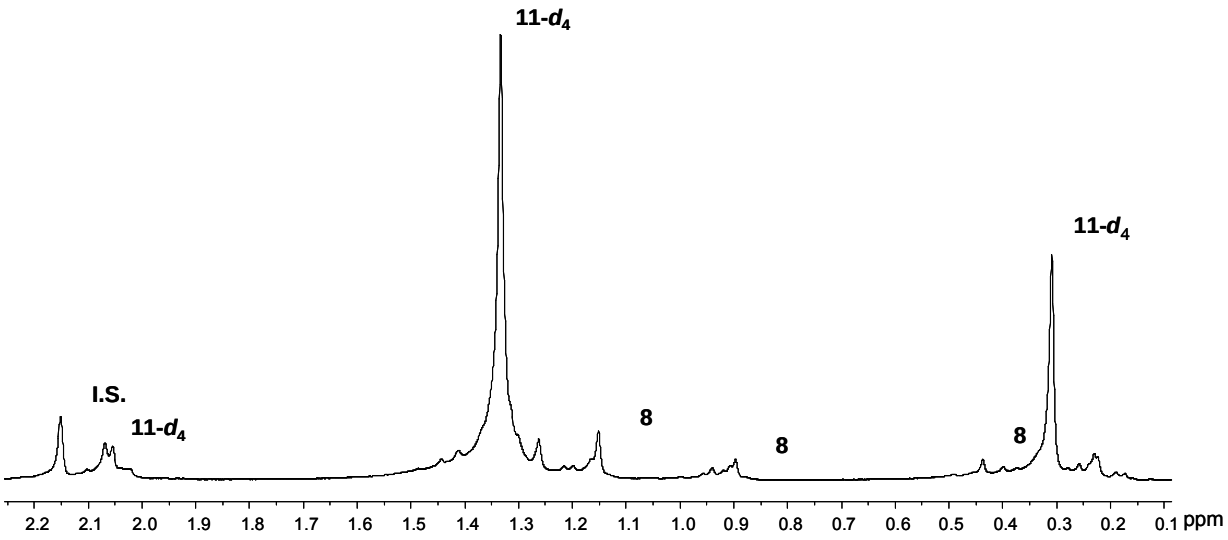

Figure A21. ^{1}H NMR spectrum of **11-d_4** at room temperature (I.S. = 4,4'-dimethylbiphenyl).

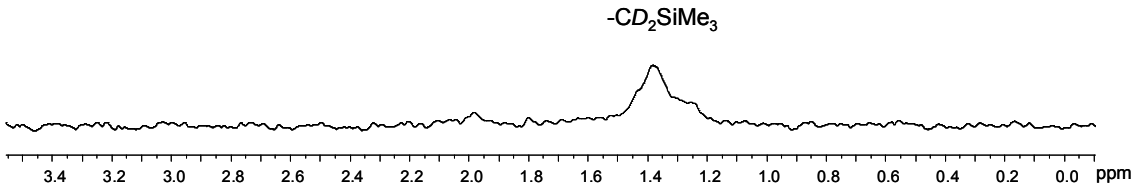

Figure A22. ^{2}H NMR spectrum of **11-d_4** at room temperature.

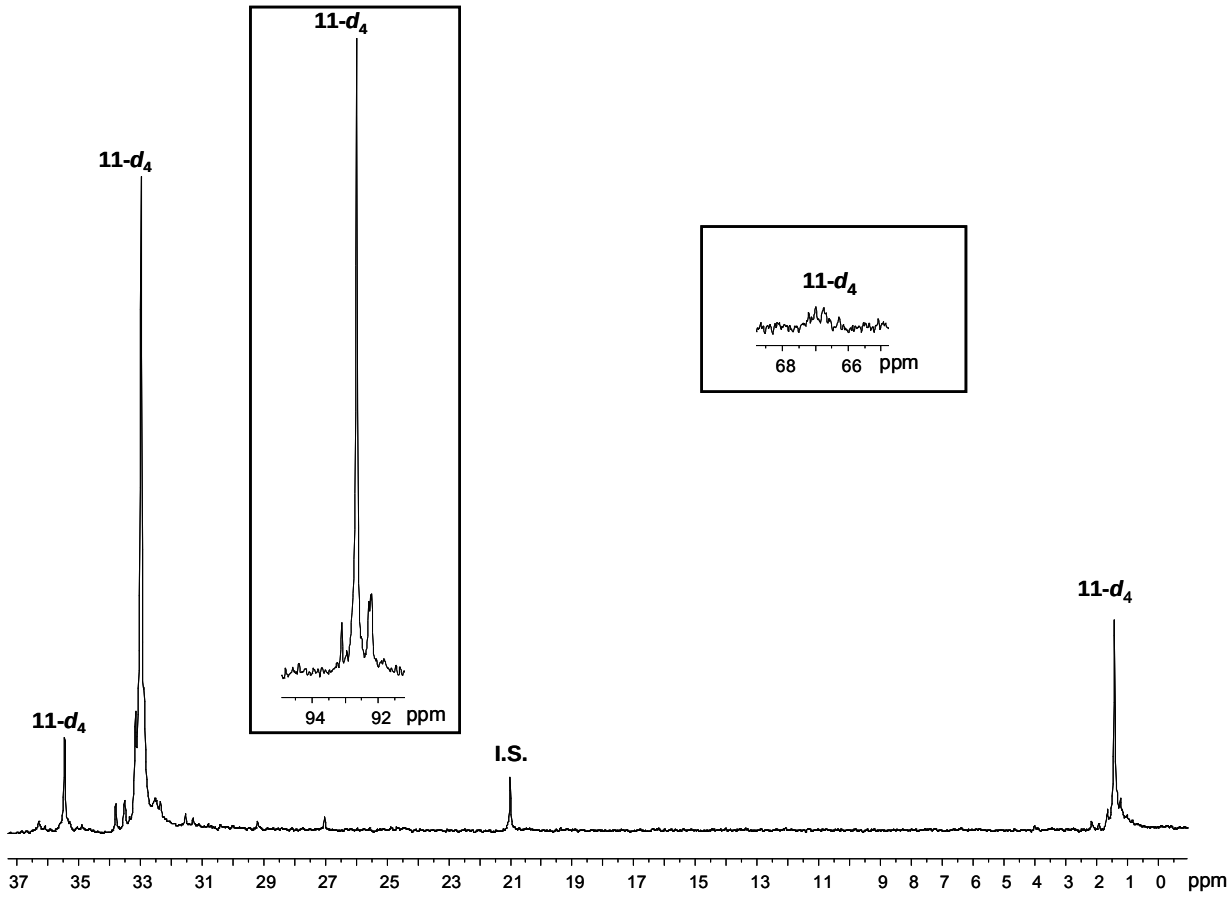

Figure A23. ^{13}C NMR spectrum of **11-d_4** at room temperature (I.S. = 4,4'-dimethylbiphenyl).

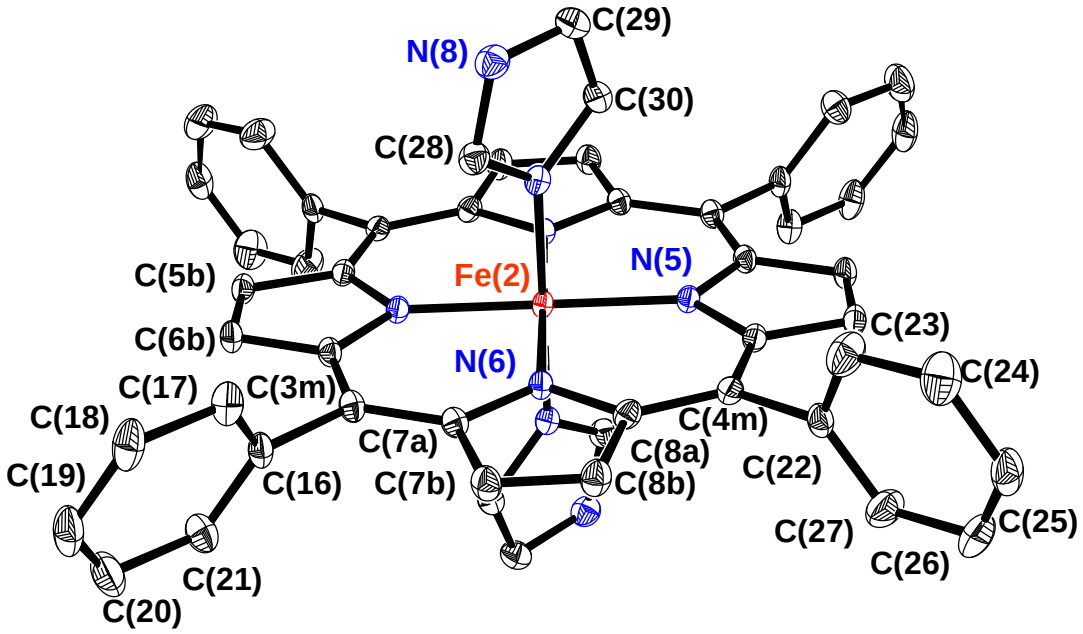

Figure A24. ORTEP of Fe2 molecule in **13-d_{36}**•D_2O•$CDCl_3$ at 173(2) K; thermal ellipsoids are at 30% probability level. Deuterium atoms, deuterium oxide, and chloroform-d_1 are removed for clarity.

APPENDIX B

Table B1. Atomic coordinates (x 10^4) and equivalent isotropic displacement parameters (Å^2 x 10^3) in **9**. *U*(eq) is defined as one third of the trace of the orthogonalized U^{ij} tensor

	x	y	z	*U*(eq)
W(1)	194(1)	4410(1)	9451(1)	15(1)
O(1)	494(2)	4636(1)	9991(1)	17(1)
O(2)	535(2)	3909(2)	9266(2)	22(1)
O(3)	-329(2)	4244(2)	8745(2)	28(1)
C(1)	434(2)	4935(2)	8884(2)	20(1)
C(2)	896(2)	4841(2)	8554(2)	24(1)
C(3)	1360(3)	4753(3)	8873(3)	39(2)
C(4)	978(3)	5304(3)	8243(3)	40(2)
C(5)	823(3)	4410(3)	8203(3)	41(2)
C(6)	-340(3)	3806(3)	8438(3)	37(2)
C(7)	-542(3)	3978(3)	7942(3)	42(2)
C(8)	-844(4)	4425(4)	8069(4)	71(3)
C(9)	-762(3)	4524(3)	8599(3)	39(2)
C(10)	-434(2)	4015(2)	9779(2)	19(1)
C(11)	-386(2)	3471(2)	9945(2)	22(1)
C(12)	-369(3)	3115(2)	9510(3)	36(2)

Table B1. (continued)

	x	y	z	*U*(eq)
C(13)	-860(3)	3352(3)	10249(3)	36(2)
C(14)	64(2)	3382(2)	10280(3)	31(1)

Table B2. Bond angles (°) in **9**

Angles			
O(2)-W(1)-O(1)	105.4(2)	C(6)-O(3)-C(9)	104.7(5)
O(2)-W(1)-C(1)	98.6(2)	C(6)-O(3)-W(1)	128.1(4)
O(1)-W(1)-C(1)	102.6(2)	C(9)-O(3)-W(1)	126.3(4)
O(2)-W(1)-C(10)	98.6(2)	C(2)-C(1)-W(1)	122.3(4)
O(1)-W(1)-C(10)	100.9(2)	C(5)-C(2)-C(4)	107.6(6)
C(1)-W(1)-C(10)	145.9(2)	C(5)-C(2)-C(3)	109.7(6)
O(2)-W(1)-O(1)#1	164.36(18)	C(4)-C(2)-C(3)	108.6(6)
O(1)-W(1)-O(1)#1	90.2(2)	C(5)-C(2)-C(1)	112.3(5)
C(1)-W(1)-O(1)#1	76.99(18)	C(4)-C(2)-C(1)	107.4(5)
C(10)-W(1)-O(1)#1	78.58(18)	C(3)-C(2)-C(1)	111.0(5)
O(2)-W(1)-O(3)	86.45(18)	O(3)-C(6)-C(7)	105.2(6)
O(1)-W(1)-O(3)	168.15(17)	C(8)-C(7)-C(6)	104.0(6)
C(1)-W(1)-O(3)	74.96(19)	C(9)-C(8)-C(7)	106.6(7)
C(10)-W(1)-O(3)	77.01(19)	O(3)-C(9)-C(8)	107.0(6)
O(1)#1-W(1)-O(3)	77.92(14)	C(11)-C(10)-W(1)	121.1(4)
W(1)-O(1)-W(1)#2	149.7(2)	C(12)-C(11)-C(14)	109.4(6)

Table B2. (continued)

Angles			
C(12)-C(11)-C(10)	112.3(5)	C(14)-C(11)-C(13)	107.9(5)
C(14)-C(11)-C(10)	113.0(5)	C(10)-C(11)-C(13)	106.4(5)
C(12)-C(11)-C(13)	107.5(5)		

Symmetry transformations used to generate equivalent atoms:

#1 y-1/2,-z+3/2,-x+1 #2 -z+1,x+1/2,-y+3/2

Table B3. Bond lengths (Å) in **9**

Lengths			
W(1)-O(2)	1.709(4)	C(2)-C(5)	1.514(8)
W(1)-O(1)	1.773(4)	C(2)-C(4)	1.520(9)
W(1)-C(1)	2.182(5)	C(2)-C(3)	1.538(9)
W(1)-C(10)	2.189(5)	C(6)-C(7)	1.517(10)
W(1)-O(1)#1	2.214(4)	C(7)-C(8)	1.495(12)
W(1)-O(3)	2.413(4)	C(8)-C(9)	1.472(11)
O(1)-W(1)#2	2.214(4)	C(10)-C(11)	1.539(7)
O(3)-C(6)	1.444(7)	C(11)-C(12)	1.519(9)
O(3)-C(9)	1.444(8)	C(11)-C(14)	1.531(8)
C(1)-C(2)	1.554(8)	C(11)-C(13)	1.553(9)

Symmetry transformations used to generate equivalent atoms:

#1 y-1/2,-z+3/2,-x+1 #2 -z+1,x+1/2,-y+3/2

Table B4. Anisotropic displacement parameters ($Å^2$ x 10^3) in **9**. The anisotropic displacement factor exponent takes the form: $-2\pi^2[h^2a^{*2}U^{11} + ... + 2 hka^*b^*U^{12}]$

	U^{11}	U^{22}	U^{33}	U^{23}	U^{13}	U^{12}
W(1)	16(1)	15(1)	16(1)	-1(1)	0(1)	1(1)
O(1)	18(2)	18(2)	16(2)	-1(1)	-2(1)	-2(1)
O(2)	21(2)	21(2)	25(2)	-4(2)	6(2)	1(2)
O(3)	27(2)	29(2)	28(2)	-8(2)	-5(2)	5(2)
C(1)	23(3)	19(3)	19(3)	2(2)	4(2)	-4(2)
C(2)	21(3)	24(3)	26(3)	-7(2)	5(2)	-5(2)
C(3)	27(3)	50(4)	40(4)	0(3)	9(3)	7(3)
C(4)	40(4)	54(5)	25(3)	8(3)	8(3)	-5(3)
C(5)	51(4)	44(4)	29(3)	-16(3)	18(3)	-10(3)
C(6)	49(4)	28(3)	33(4)	-12(3)	-10(3)	-1(3)
C(7)	57(5)	41(4)	28(3)	-11(3)	-11(3)	-5(4)
C(8)	83(7)	81(7)	48(5)	-17(5)	-33(5)	41(6)
C(9)	30(4)	49(4)	36(4)	-11(3)	-12(3)	13(3)
C(10)	18(3)	15(2)	24(3)	3(2)	2(2)	-1(2)
C(11)	24(3)	16(3)	26(3)	5(2)	-5(2)	-4(2)

Table B4. (continued)

	U^{11}	U^{22}	U^{33}	U^{23}	U^{13}	U^{12}
C(12)	46(4)	21(3)	41(4)	-1(3)	-8(3)	-5(3)
C(13)	34(3)	34(4)	41(4)	17(3)	1(3)	-7(3)
C(14)	31(3)	27(3)	37(4)	7(3)	-12(3)	2(3)

Table B5. Atomic coordinates (x 10^4) and equivalent isotropic displacement parameters (Å^2 x 10^3) in **10**. *U*(eq) is defined as one third of the trace of the orthogonalized U^{ij} tensor

	x	y	z	*U*(eq)
W(1)	402(1)	7936(1)	2906(1)	17(1)
W(2)	316(1)	7130(1)	5019(1)	18(1)
W(3)	304(1)	4987(1)	2152(1)	18(1)
O(1)	355(6)	6181(6)	2117(6)	16(2)
O(2)	294(8)	5916(7)	3851(7)	24(2)
O(3)	370(7)	7935(6)	4099(6)	18(2)
O(4)	442(8)	9253(7)	3253(7)	24(2)
O(5)	417(8)	7614(7)	1227(6)	28(2)
O(6)	304(8)	4024(7)	868(7)	25(2)
O(7)	201(9)	3588(7)	2491(7)	29(2)
O(8)	287(7)	6787(6)	5964(6)	19(2)
O(9)	346(7)	8844(7)	6347(7)	29(2)
C(1)	2177(11)	7723(10)	2805(10)	22(3)
C(2)	3120(10)	8672(10)	3173(11)	22(3)
C(3)	4256(12)	8242(13)	3086(13)	41(4)
C(4)	3214(13)	9526(11)	4344(12)	35(3)

Table B5. (continued)

	x	y	z	*U*(eq)
C(5)	2862(14)	9174(12)	2479(12)	38(4)
C(6)	-1370(10)	7274(9)	1979(10)	20(3)
C(7)	-2262(11)	8013(10)	1956(11)	25(3)
C(8)	-1943(14)	8589(11)	1370(11)	34(3)
C(9)	-2343(12)	8854(12)	3088(11)	29(3)
C(10)	-3422(13)	7302(12)	1345(13)	37(4)
C(11)	2063(11)	5091(10)	2999(10)	23(3)
C(12)	2977(12)	4520(11)	2386(12)	30(3)
C(13)	3148(13)	4901(13)	1621(12)	36(3)
C(14)	4097(13)	4857(14)	3251(13)	43(4)
C(15)	2654(14)	3321(11)	1804(12)	37(4)
C(16)	-1485(11)	4714(10)	2164(9)	21(3)
C(17)	-2400(12)	3944(11)	1134(10)	29(3)
C(18)	-2446(12)	4256(12)	283(11)	31(3)
C(19)	-3563(12)	4043(13)	1429(12)	38(4)
C(20)	-2200(14)	2796(12)	708(11)	36(4)
C(21)	2112(12)	7864(10)	5509(10)	26(3)
C(22)	3020(11)	7815(10)	6374(10)	24(3)

Table B5. (continued)

	x	y	z	*U*(eq)
C(23)	4193(12)	8361(13)	6449(12)	38(4)
C(24)	2721(12)	8448(12)	7460(10)	29(3)
C(25)	3094(14)	6674(12)	6121(12)	36(4)
C(26)	-1432(10)	7447(9)	4680(9)	17(2)
C(27)	-2382(12)	7157(10)	5099(10)	26(3)
C(28)	-2171(13)	7868(13)	6307(12)	36(4)
C(29)	-3518(13)	7355(12)	4586(13)	35(3)
C(30)	-2494(14)	5985(11)	4789(12)	34(3)
C(31)	5610(20)	10210(20)	9423(15)	78(8)
C(32)	5717(17)	9352(19)	9530(19)	75(8)
C(33)	5140(20)	9128(18)	10080(20)	80(9)
C(34)	8998(17)	10329(17)	10327(14)	60(5)
C(35)	8970(15)	9669(16)	9216(13)	54(5)
C(36)	10012(18)	9418(16)	8942(14)	56(5)

Table B6. Bond angles (°) in **10**.

Angles			
O(4)-W(1)-O(3)	104.3(4)	O(2)-W(2)-C(26)	101.5(4)
O(4)-W(1)-C(6)	101.6(4)	O(8)-W(2)-C(21)	100.6(4)
O(3)-W(1)-C(6)	101.9(4)	O(2)-W(2)-C(21)	102.0(4)
O(4)-W(1)-C(1)	100.8(4)	C(26)-W(2)-C(21)	141.8(5)
O(3)-W(1)-C(1)	102.1(4)	O(8)-W(2)-O(3)	167.1(3)
C(6)-W(1)-C(1)	141.8(5)	O(2)-W(2)-O(3)	87.9(4)
O(4)-W(1)-O(1)	167.7(3)	C(26)-W(2)-O(3)	75.2(4)
O(3)-W(1)-O(1)	88.0(3)	C(21)-W(2)-O(3)	76.0(4)
C(6)-W(1)-O(1)	75.3(4)	O(8)-W(2)-O(9)	85.5(4)
C(1)-W(1)-O(1)	76.3(4)	O(2)-W(2)-O(9)	169.6(4)
O(4)-W(1)-O(5)	85.8(4)	C(26)-W(2)-O(9)	75.7(4)
O(3)-W(1)-O(5)	169.9(3)	C(21)-W(2)-O(9)	75.8(4)
C(6)-W(1)-O(5)	75.1(4)	O(3)-W(2)-O(9)	81.6(3)
C(1)-W(1)-O(5)	76.1(4)	O(6)-W(3)-O(1)	103.7(4)
O(1)-W(1)-O(5)	81.9(3)	O(6)-W(3)-C(16)	101.3(4)
O(8)-W(2)-O(2)	104.9(4)	O(1)-W(3)-C(16)	101.1(4)
O(8)-W(2)-C(26)	101.9(4)	O(6)-W(3)-C(11)	101.0(5)

Table B6. (continued)

Angles			
O(1)-W(3)-C(11)	102.8(4)	C(3)-C(2)-C(1)	107.5(11)
C(16)-W(3)-C(11)	142.1(5)	C(4)-C(2)-C(1)	110.5(11)
O(6)-W(3)-O(2)	167.4(4)	C(7)-C(6)-W(1)	121.0(8)
O(1)-W(3)-O(2)	88.9(3)	C(10)-C(7)-C(9)	109.0(11)
C(16)-W(3)-O(2)	75.9(4)	C(10)-C(7)-C(6)	106.9(11)
C(11)-W(3)-O(2)	75.6(4)	C(9)-C(7)-C(6)	112.0(11)
O(6)-W(3)-O(7)	86.0(4)	C(10)-C(7)-C(8)	109.5(12)
O(1)-W(3)-O(7)	170.2(3)	C(9)-C(7)-C(8)	109.4(11)
C(16)-W(3)-O(7)	75.7(4)	C(6)-C(7)-C(8)	110.0(11)
C(11)-W(3)-O(7)	75.8(4)	C(12)-C(11)-W(3)	121.4(9)
O(2)-W(3)-O(7)	81.4(3)	C(15)-C(12)-C(13)	110.9(13)
W(3)-O(1)-W(1)	151.0(4)	C(15)-C(12)-C(14)	109.4(12)
W(2)-O(2)-W(3)	151.8(5)	C(13)-C(12)-C(14)	109.1(12)
W(1)-O(3)-W(2)	152.4(4)	C(15)-C(12)-C(11)	111.2(12)
C(2)-C(1)-W(1)	122.2(9)	C(13)-C(12)-C(11)	110.9(11)
C(5)-C(2)-C(3)	109.9(12)	C(14)-C(12)-C(11)	105.0(11)
C(5)-C(2)-C(4)	109.3(11)	C(17)-C(16)-W(3)	121.5(8)
C(3)-C(2)-C(4)	108.7(12)	C(20)-C(17)-C(18)	110.6(11)
C(5)-C(2)-C(1)	110.8(11)	C(20)-C(17)-C(19)	108.3(12)

Table B6. (continued)

Angles			
C(18)-C(17)-C(19)	108.2(12)	C(30)-C(27)-C(28)	110.2(12)
C(20)-C(17)-C(16)	111.5(12)	C(30)-C(27)-C(29)	108.6(11)
C(18)-C(17)-C(16)	111.4(11)	C(28)-C(27)-C(29)	107.9(12)
C(19)-C(17)-C(16)	106.7(11)	C(30)-C(27)-C(26)	111.2(11)
C(22)-C(21)-W(2)	122.9(9)	C(28)-C(27)-C(26)	111.4(11)
C(25)-C(22)-C(24)	109.1(12)	C(29)-C(27)-C(26)	107.4(11)
C(25)-C(22)-C(21)	112.0(11)	C(32)-C(31)-C(33)#1	117(2)
C(24)-C(22)-C(21)	109.7(11)	C(33)-C(32)-C(31)	122(2)
C(25)-C(22)-C(23)	110.2(12)	C(32)-C(33)-C(31)#1	120(2)
C(24)-C(22)-C(23)	108.1(11)	C(36)#2-C(34)-C(35)	119.4(17)
C(21)-C(22)-C(23)	107.7(11)	C(36)-C(35)-C(34)	117.7(16)
C(27)-C(26)-W(2)	122.0(9)	C(34)#2-C(36)-C(35)	122.5(16)

Symmetry transformations used to generate equivalent atoms:

#1 -x+1,-y+2,-z+2 #2 -x+2,-y+2,-z+2

Table B7. Bond lengths (Å) in **10**

Lengths			
W(1)-O(4)	1.724(9)	C(1)-C(2)	1.552(16)
W(1)-O(3)	1.785(8)	C(2)-C(5)	1.53(2)
W(1)-C(6)	2.192(12)	C(2)-C(3)	1.527(19)
W(1)-C(1)	2.193(13)	C(2)-C(4)	1.55(2)
W(1)-O(1)	2.224(8)	C(6)-C(7)	1.554(18)
W(1)-O(5)	2.311(8)	C(7)-C(10)	1.529(19)
W(2)-O(8)	1.713(9)	C(7)-C(9)	1.552(19)
W(2)-O(2)	1.769(8)	C(7)-C(8)	1.560(19)
W(2)-C(26)	2.187(12)	C(11)-C(12)	1.565(18)
W(2)-C(21)	2.194(14)	C(12)-C(15)	1.52(2)
W(2)-O(3)	2.203(9)	C(12)-C(13)	1.53(2)
W(2)-O(9)	2.301(9)	C(12)-C(14)	1.54(2)
W(3)-O(6)	1.733(8)	C(16)-C(17)	1.550(17)
W(3)-O(1)	1.765(9)	C(17)-C(20)	1.52(2)
W(3)-C(16)	2.182(12)	C(17)-C(18)	1.533(19)
W(3)-C(11)	2.204(13)	C(17)-C(19)	1.538(19)
W(3)-O(2)	2.214(9)	C(21)-C(22)	1.550(19)
W(3)-O(7)	2.331(9)	C(22)-C(25)	1.525(19)

Table B7. (continued)

Lengths			
C(22)-C(24)	1.547(18)	C(31)-C(33)#1	1.39(4)
C(22)-C(23)	1.553(19)	C(32)-C(33)	1.31(3)
C(26)-C(27)	1.543(18)	C(33)-C(31)#1	1.39(4)
C(27)-C(30)	1.528(19)	C(34)-C(36)#2	1.35(3)
C(27)-C(28)	1.536(19)	C(34)-C(35)	1.44(2)
C(27)-C(29)	1.54(2)	C(35)-C(36)	1.40(3)
C(31)-C(32)	1.35(4)	C(36)-C(34)#2	1.35(3)

Symmetry transformations used to generate equivalent atoms:

#1 -x+1,-y+2,-z+2 #2 -x+2,-y+2,-z+2

Table B8. Anisotropic displacement parameters ($Å^2$ x 10^3) in **10**. The anisotropic displacement factor exponent takes the form: $-2\pi^2[h^2a^{*2}U^{11} + ... + 2 hka^*b^*U^{12}]$

	U^{11}	U^{22}	U^{33}	U^{23}	U^{13}	U^{12}
W(1)	19(1)	15(1)	16(1)	6(1)	4(1)	3(1)
W(2)	20(1)	15(1)	15(1)	5(1)	5(1)	4(1)
W(3)	22(1)	14(1)	16(1)	5(1)	5(1)	3(1)
O(1)	5(4)	26(4)	5(4)	-2(3)	3(3)	-1(3)
O(2)	38(5)	20(4)	20(5)	10(4)	15(4)	15(4)
O(3)	17(4)	11(4)	14(4)	0(3)	-1(3)	-3(3)
O(4)	30(5)	29(5)	23(5)	18(4)	15(4)	8(4)
O(5)	38(6)	29(5)	7(4)	4(4)	0(4)	-6(4)
O(6)	31(5)	23(5)	16(4)	4(4)	10(4)	-1(4)
O(7)	41(6)	24(5)	21(5)	8(4)	14(4)	8(4)
O(8)	10(4)	16(4)	17(4)	0(3)	-5(3)	-2(3)
O(9)	16(5)	34(5)	16(5)	1(4)	-7(4)	4(4)
C(1)	23(7)	26(7)	18(6)	13(5)	2(5)	4(5)
C(2)	10(6)	24(7)	37(8)	17(6)	9(5)	1(5)
C(3)	19(7)	38(9)	43(9)	7(7)	-1(6)	4(6)
C(4)	34(8)	26(7)	35(8)	11(6)	-1(6)	3(6)

Table B8. (continued)

	U^{11}	U^{22}	U^{33}	U^{23}	U^{13}	U^{12}
C(5)	46(9)	30(8)	33(8)	11(7)	14(7)	-9(7)
C(6)	18(6)	18(6)	21(6)	10(5)	-1(5)	-2(5)
C(7)	21(7)	22(7)	28(7)	11(6)	2(5)	6(5)
C(8)	49(9)	28(7)	25(7)	14(6)	6(7)	20(7)
C(9)	24(7)	39(8)	24(7)	13(6)	9(6)	8(6)
C(10)	30(8)	30(8)	39(9)	12(7)	-3(7)	7(6)
C(11)	26(7)	24(7)	17(6)	7(5)	9(5)	8(5)
C(12)	22(7)	34(8)	36(8)	18(7)	11(6)	18(6)
C(13)	30(8)	52(10)	36(8)	27(8)	15(7)	17(7)
C(14)	29(8)	57(11)	45(10)	24(8)	15(7)	15(7)
C(15)	41(9)	22(7)	33(8)	4(6)	8(7)	16(6)
C(16)	23(7)	25(7)	12(6)	4(5)	10(5)	9(5)
C(17)	26(7)	28(7)	14(6)	0(5)	-2(5)	-4(6)
C(18)	24(7)	38(8)	24(7)	16(6)	-8(6)	-8(6)
C(19)	25(8)	42(9)	33(8)	8(7)	11(6)	-8(6)
C(20)	41(9)	34(8)	24(7)	10(6)	5(6)	-11(7)
C(21)	37(8)	20(6)	18(6)	4(5)	12(6)	10(5)
C(22)	24(7)	23(7)	20(7)	8(5)	4(5)	3(5)

Table B8. (continued)

	U^{11}	U^{22}	U^{33}	U^{23}	U^{13}	U^{12}
C(23)	25(8)	54(10)	35(8)	24(8)	2(6)	6(7)
C(24)	32(8)	37(8)	13(6)	8(6)	5(5)	8(6)
C(25)	40(9)	32(8)	31(8)	13(7)	2(7)	21(7)
C(26)	18(6)	14(6)	14(6)	3(5)	0(5)	6(4)
C(27)	31(7)	21(7)	22(7)	8(5)	3(6)	-1(5)
C(28)	35(8)	43(9)	32(8)	15(7)	20(7)	7(7)
C(29)	33(8)	28(8)	48(9)	19(7)	17(7)	7(6)
C(30)	39(9)	29(8)	36(8)	17(7)	9(7)	6(6)
C(31)	75(17)	100(20)	24(10)	18(11)	-7(10)	-47(15)
C(32)	34(11)	53(13)	71(15)	-13(11)	-2(10)	6(9)
C(33)	90(18)	50(13)	84(17)	52(14)	-56(15)	-37(13)
C(34)	51(12)	87(15)	30(9)	17(10)	20(9)	21(10)
C(35)	33(9)	81(14)	22(8)	11(8)	-3(7)	6(9)
C(36)	79(14)	64(12)	29(9)	20(9)	31(9)	13(10)

Table B9. Atomic coordinates (x 10^4) and equivalent isotropic displacement parameters (Å^2 x 10^3) in **12** at 293(2) K in *I4/m* space group. *U*(eq) is defined as one third of the trace of the orthogonalized U^{ij} tensor

	x	y	z	*U*(eq)
Fe(1)	0	0	4602(1)	37(1)
Cl(1)	0	0	2369(3)	54(1)
N(1)	-380(2)	1438(2)	5000	43(1)
C(1)	248(3)	2247(3)	5000	46(1)
C(2)	-314(3)	3138(3)	5000	57(1)
C(3)	-1277(3)	2883(3)	5000	55(1)
C(4)	-1323(3)	1823(3)	5000	46(1)
C(5)	1279(3)	2198(3)	5000	43(1)
C(6)	1838(3)	3151(3)	5000	47(1)
C(7)	2099(3)	3596(3)	3806(4)	71(1)
C(8)	2641(3)	4466(3)	3804(4)	79(1)
C(9)	2917(4)	4896(3)	5000	66(1)

Table B10. Bond angles (°) in **12** at 293(2) K

Angles			
Fe(1)#1-Fe(1)-N(1)	79.01(4)	C(4)-N(1)-Fe(1)	126.2(2)
Fe(1)#1-Fe(1)-N(1)#2	79.01(4)	C(1)-N(1)-Fe(1)	126.6(2)
N(1)-Fe(1)-N(1)#2	87.917(16)	N(1)-C(1)-C(5)	125.1(4)
Fe(1)#1-Fe(1)-N(1)#3	79.01(4)	N(1)-C(1)-C(2)	110.0(4)
N(1)-Fe(1)-N(1)#3	87.919(16)	C(5)-C(1)-C(2)	125.0(4)
N(1)#2-Fe(1)-N(1)#3	158.02(8)	C(3)-C(2)-C(1)	107.4(4)
Fe(1)#1-Fe(1)-N(1)#1	79.01(4)	C(2)-C(3)-C(4)	107.3(4)
N(1)-Fe(1)-N(1)#1	158.02(8)	N(1)-C(4)-C(5)#3	125.9(4)
N(1)#2-Fe(1)-N(1)#1	87.918(16)	N(1)-C(4)-C(3)	109.7(4)
N(1)#3-Fe(1)-N(1)#1	87.918(16)	C(5)#3-C(4)-C(3)	124.4(4)
Fe(1)#1-Fe(1)-Cl(1)	180.000(1)	C(4)#2-C(5)-C(1)	124.7(4)
N(1)-Fe(1)-Cl(1)	100.99(4)	C(4)#2-C(5)-C(6)	117.7(3)
N(1)#2-Fe(1)-Cl(1)	100.99(4)	C(1)-C(5)-C(6)	117.7(3)
N(1)#3-Fe(1)-Cl(1)	100.99(4)	C(7)-C(6)-C(7)#4	118.4(4)
N(1)#1-Fe(1)-Cl(1)	100.99(4)	C(7)-C(6)-C(5)	120.8(2)
C(4)-N(1)-C(1)	105.6(3)	C(7)#4-C(6)-C(5)	120.8(2)
C(4)-N(1)-Fe(1)#1	126.2(2)	C(6)-C(7)-C(8)	120.8(4)
C(1)-N(1)-Fe(1)#1	126.6(2)		

Table B10. (continued)

Angles			
C(9)-C(8)-C(7)	120.4(4)	C(8)#4-C(9)-C(8)	119.0(4)

Symmetry transformations used to generate equivalent atoms:

#1 -x,-y,-z+1 #2 y,-x,-z+1 #3 -y,x,z #4 x,y,-z+1

Table B11. Bond lengths (Å) in **12** at 293(2) K

Lengths			
Fe(1)-Fe(1)#1	0.782(3)	C(2)-C(3)	1.348(6)
Fe(1)-N(1)	2.052(3)	C(3)-C(4)	1.436(6)
Fe(1)-N(1)#2	2.052(3)	C(4)-C(5)#3	1.395(5)
Fe(1)-N(1)#3	2.052(3)	C(5)-C(4)#2	1.395(5)
Fe(1)-N(1)#1	2.052(3)	C(5)-C(6)	1.497(5)
Fe(1)-Cl(1)	2.193(3)	C(6)-C(7)	1.366(4)
N(1)-C(4)	1.380(5)	C(6)-C(7)#4	1.366(4)
N(1)-C(1)	1.386(5)	C(7)-C(8)	1.388(5)
N(1)-Fe(1)#1	2.052(3)	C(8)-C(9)	1.363(5)
C(1)-C(5)	1.398(6)	C(9)-C(8)#4	1.363(5)
C(1)-C(2)	1.427(6)		

Symmetry transformations used to generate equivalent atoms:

#1 -x,-y,-z+1 #2 y,-x,-z+1 #3 -y,x,z #4 x,y,-z+1

Table B12. Anisotropic displacement parameters ($Å^2$ x 10^3) in **12** at 293(2) K. The anisotropic displacement factor exponent takes the form: $-2\pi^2 [h^2a^{*2}U^{11} + ... + 2\ hka^*b^*U^{12}]$

	U^{11}	U^{22}	U^{33}	U^{23}	U^{13}	U^{12}
Fe(1)	35(1)	35(1)	41(1)	0	0	0
Cl(1)	61(1)	61(1)	40(1)	0	0	0
N(1)	38(2)	38(2)	53(2)	0	0	0(1)
C(1)	47(2)	39(2)	53(2)	0	0	-2(2)
C(2)	55(2)	38(2)	76(3)	0	0	1(2)
C(3)	51(2)	42(2)	71(3)	0	0	8(2)
C(4)	44(2)	42(2)	51(2)	0	0	6(2)
C(5)	47(2)	39(2)	44(2)	0	0	-6(2)
C(6)	46(2)	39(2)	55(2)	0	0	-3(2)
C(7)	92(3)	67(2)	55(2)	1(2)	6(2)	-27(2)
C(8)	97(3)	66(2)	74(3)	15(2)	10(2)	-27(2)
C(9)	54(3)	41(2)	104(4)	0	0	-7(2)

Table B13. Atomic coordinates (x 10^4) and equivalent isotropic displacement parameters (Å^2 x 10^3) in **12** at 143(2) K in *I4/m* space group. *U*(eq) is defined as one third of the trace of the orthogonalized U^{ij} tensor

	x	y	z	*U*(eq)
Fe(1)	0	0	4593(2)	25(1)
Cl(1)	0	0	2342(3)	33(1)
N(1)	-370(3)	1449(3)	5000	29(1)
C(1)	261(3)	2252(3)	5000	30(1)
C(2)	-295(4)	3157(3)	5000	34(1)
C(3)	-1267(4)	2907(3)	5000	33(1)
C(4)	-1315(3)	1837(3)	5000	29(1)
C(5)	1297(3)	2198(3)	5000	30(1)
C(6)	1859(3)	3157(3)	5000	32(1)
C(7)	2125(3)	3604(3)	3788(4)	47(1)
C(8)	2667(4)	4478(3)	3788(5)	51(1)
C(9)	2941(4)	4917(4)	5000	39(1)

Table B14. Bond angles (°) in **12** at 143(2) K in *I4/m* space group

Angles			
Fe(1)#1-Fe(1)-N(1)	78.91(5)	C(4)-N(1)-Fe(1)#1	125.8(3)
Fe(1)#1-Fe(1)-N(1)#2	78.91(5)	N(1)-C(1)-C(5)	125.2(4)
N(1)-Fe(1)-N(1)#2	87.88(2)	N(1)-C(1)-C(2)	110.3(4)
Fe(1)#1-Fe(1)-N(1)#3	78.91(5)	C(5)-C(1)-C(2)	124.5(4)
N(1)-Fe(1)-N(1)#3	87.88(2)	C(3)-C(2)-C(1)	107.1(4)
N(1)#2-Fe(1)-N(1)#3	157.82(10)	C(2)-C(3)-C(4)	107.0(4)
Fe(1)#1-Fe(1)-N(1)#1	78.91(5)	N(1)-C(4)-C(5)#3	126.2(4)
N(1)-Fe(1)-N(1)#1	157.82(10)	N(1)-C(4)-C(3)	109.7(4)
N(1)#2-Fe(1)-N(1)#1	87.88(2)	C(5)#3-C(4)-C(3)	124.1(4)
N(1)#3-Fe(1)-N(1)#1	87.88(2)	C(4)#2-C(5)-C(1)	124.4(4)
Fe(1)#1-Fe(1)-Cl(1)	180.000(1)	C(4)#2-C(5)-C(6)	118.1(4)
N(1)-Fe(1)-Cl(1)	101.09(5)	C(1)-C(5)-C(6)	117.5(4)
N(1)#2-Fe(1)-Cl(1)	101.09(5)	C(7)-C(6)-C(7)#4	118.5(5)
N(1)#3-Fe(1)-Cl(1)	101.09(5)	C(7)-C(6)-C(5)	120.8(2)
N(1)#1-Fe(1)-Cl(1)	101.09(5)	C(7)#4-C(6)-C(5)	120.8(2)
C(1)-N(1)-C(4)	105.9(4)		
C(1)-N(1)-Fe(1)	126.7(3)		
C(4)-N(1)-Fe(1)	125.8(3)		
C(1)-N(1)-Fe(1)#1	126.7(3)		

Table B14. (continued)

Angles			
C(6)-C(7)-C(8)	120.8(4)	C(8)#4-C(9)-C(8)	118.7(5)
C(9)-C(8)-C(7)	120.6(4)		

Symmetry transformations used to generate equivalent atoms:

#1 -x,-y,-z+1 #2 y,-x,-z+1 #3 -y,x,z #4 x,y,-z+1

Table B15. Bond lengths (Å) in **12** at 143(2) K in *I4/m* space group

Lengths			
Fe(1)-Fe(1)#1	0.792(4)	C(2)-C(3)	1.355(7)
Fe(1)-N(1)	2.058(4)	C(3)-C(4)	1.446(6)
Fe(1)-N(1)#2	2.059(4)	C(4)-C(5)#3	1.398(6)
Fe(1)-N(1)#3	2.059(4)	C(5)-C(4)#2	1.398(6)
Fe(1)-N(1)#1	2.059(4)	C(5)-C(6)	1.501(6)
Fe(1)-Cl(1)	2.190(4)	C(6)-C(7)	1.372(5)
N(1)-C(1)	1.378(6)	C(6)-C(7)#4	1.372(5)
N(1)-C(4)	1.380(6)	C(7)-C(8)	1.390(5)
N(1)-Fe(1)#1	2.058(4)	C(8)-C(9)	1.371(5)
C(1)-C(5)	1.401(7)	C(9)-C(8)#4	1.371(5)
C(1)-C(2)	1.435(6)		

Symmetry transformations used to generate equivalent atoms:

#1 -x,-y,-z+1 #2 y,-x,-z+1 #3 -y,x,z #4 x,y,-z+1

Table B16. Anisotropic displacement parameters ($Å^2$ x 10^3) in **12** at 143(2) K in *I4/m* space group. The anisotropic displacement factor exponent takes the form: $-2\pi^2 [h^2a^{*2}U^{11} + ... + 2\ hka^*b^*U^{12}]$

	U^{11}	U^{22}	U^{33}	U^{23}	U^{13}	U^{12}
Fe(1)	22(1)	22(1)	30(1)	0	0	0
Cl(1)	36(1)	36(1)	27(2)	0	0	0
N(1)	25(2)	25(2)	37(2)	0	0	1(1)
C(1)	33(2)	26(2)	30(2)	0	0	0(2)
C(2)	37(2)	25(2)	40(3)	0	0	1(2)
C(3)	33(2)	27(2)	38(3)	0	0	2(2)
C(4)	29(2)	28(2)	31(2)	0	0	4(2)
C(5)	32(2)	25(2)	31(2)	0	0	-3(2)
C(6)	30(2)	24(2)	40(3)	0	0	-1(2)
C(7)	61(2)	45(2)	33(2)	-1(2)	4(2)	-19(2)
C(8)	67(3)	41(2)	44(2)	8(2)	10(2)	-16(2)
C(9)	31(2)	26(2)	59(4)	0	0	-2(2)

Table B17. Atomic coordinates (x 10^4) and equivalent isotropic displacement parameters (Å^2 x 10^3) in **12** at 143(2) K in *I4* space group. *U*(eq) is defined as one third of the trace of the orthogonalized U^{ij} tensor

	x	y	z	*U*(eq)
Fe(1)	0	0	4602(2)	24(1)
Fe(2)	0	0	5414(1)	24(1)
Cl(1)	0	0	2366(3)	32(1)
Cl(2)	0	0	7675(2)	32(1)
N(1)	-372(1)	1445(1)	4998(2)	28(1)
C(1)	-1318(1)	1841(1)	5001(3)	28(1)
C(2)	-1265(1)	2905(1)	4987(4)	33(1)
C(3)	-298(1)	3154(1)	4996(3)	33(1)
C(4)	264(1)	2247(1)	4992(3)	28(1)
C(5)	1293(1)	2199(1)	4997(3)	29(1)
C(6)	1862(1)	3155(1)	5004(3)	29(1)
C(7)	2086(3)	3629(3)	3785(3)	46(1)
C(8)	2633(3)	4498(2)	3791(3)	51(1)
C(9)	2939(1)	4914(1)	5006(4)	38(1)
C(10)	2692(2)	4464(2)	6217(2)	50(1)
C(11)	2159(2)	3577(2)	6219(2)	46(1)

Table B18. Bond angles (°) in **12** at 143(2) K in *I4* space group

Angles			
Fe(2)-Fe(1)-N(1)#1	79.17(10)	N(1)#2-Fe(2)-N(1)#3	87.77(3)
Fe(2)-Fe(1)-N(1)#2	79.17(10)	N(1)#1-Fe(2)-N(1)#3	87.77(3)
N(1)#1-Fe(1)-N(1)#2	158.3(2)	Fe(1)-Fe(2)-N(1)	78.63(8)
Fe(2)-Fe(1)-N(1)#3	79.17(10)	N(1)#2-Fe(2)-N(1)	87.78(3)
N(1)#1-Fe(1)-N(1)#3	87.98(4)	N(1)#1-Fe(2)-N(1)	87.77(3)
N(1)#2-Fe(1)-N(1)#3	87.98(4)	N(1)#3-Fe(2)-N(1)	157.27(16)
Fe(2)-Fe(1)-N(1)	79.17(10)	Fe(1)-Fe(2)-Cl(2)	180.0
N(1)#1-Fe(1)-N(1)	87.98(4)	N(1)#2-Fe(2)-Cl(2)	101.37(8)
N(1)#2-Fe(1)-N(1)	87.98(4)	N(1)#1-Fe(2)-Cl(2)	101.37(8)
N(1)#3-Fe(1)-N(1)	158.3(2)	N(1)#3-Fe(2)-Cl(2)	101.37(8)
Fe(2)-Fe(1)-Cl(1)	180.000(1)	N(1)-Fe(2)-Cl(2)	101.37(8)
N(1)#1-Fe(1)-Cl(1)	100.83(10)	C(4)-N(1)-C(1)	105.72(14)
N(1)#2-Fe(1)-Cl(1)	100.83(10)	C(4)-N(1)-Fe(1)	126.32(12)
N(1)#3-Fe(1)-Cl(1)	100.83(10)	C(1)-N(1)-Fe(1)	126.41(12)
N(1)-Fe(1)-Cl(1)	100.83(10)	C(4)-N(1)-Fe(2)	126.34(12)
Fe(1)-Fe(2)-N(1)#2	78.63(8)	C(1)-N(1)-Fe(2)	126.26(12)
Fe(1)-Fe(2)-N(1)#1	78.63(8)	Fe(1)-N(1)-Fe(2)	22.20(6)
N(1)#2-Fe(2)-N(1)#1	157.27(16)	N(1)-C(1)-C(5)#2	125.45(16)
Fe(1)-Fe(2)-N(1)#3	78.63(8)	N(1)-C(1)-C(2)	109.85(15)

Table B18. (continued)

Angles			
N(1)-C(4)-C(5)	125.75(15)	C(6)-C(7)-C(8)	120.4(3)
N(1)-C(4)-C(3)	109.80(15)	C(9)-C(8)-C(7)	120.7(3)
C(5)-C(4)-C(3)	124.46(16)	C(10)-C(9)-C(8)	119.14(19)
C(4)-C(5)-C(1)#1	124.53(17)	C(9)-C(10)-C(11)	120.52(13)
C(4)-C(5)-C(6)	118.06(15)	C(6)-C(11)-C(10)	120.38(12)
C(1)#1-C(5)-C(6)	117.41(16)	C(5)#2-C(1)-C(2)	124.70(16)
C(11)-C(6)-C(7)	118.87(18)	C(3)-C(2)-C(1)	107.28(15)
C(11)-C(6)-C(5)	120.7(2)	C(2)-C(3)-C(4)	107.35(15)
C(7)-C(6)-C(5)	120.4(3)		

Symmetry transformations used to generate equivalent atoms:

#1 -x,-y,z #2 -y,x,z #3 y,-x,z

Table B19. Bond lengths (Å) in **12** at 143(2) K in *I4* space group

Lengths			
Fe(1)-Fe(2)	0.791(2)	C(1)-C(5)#2	1.401(2)
Fe(1)-N(1)#1	2.0517(17)	C(1)-C(2)	1.439(2)
Fe(1)-N(1)#2	2.0517(17)	C(2)-C(3)	1.348(3)
Fe(1)-N(1)#3	2.0517(17)	C(3)-C(4)	1.441(2)
Fe(1)-N(1)	2.0518(17)	C(4)-C(5)	1.391(3)
Fe(1)-Cl(1)	2.175(5)	C(5)-C(1)#1	1.401(2)
Fe(2)-N(1)#2	2.0555(16)	C(5)-C(6)	1.502(2)
Fe(2)-N(1)#1	2.0555(16)	C(6)-C(11)	1.373(4)
Fe(2)-N(1)#3	2.0555(16)	C(6)-C(7)	1.382(5)
Fe(2)-N(1)	2.0555(16)	C(7)-C(8)	1.387(4)
Fe(2)-Cl(2)	2.200(3)	C(8)-C(9)	1.372(5)
N(1)-C(4)	1.382(2)	C(9)-C(10)	1.368(4)
N(1)-C(1)	1.384(2)	C(10)-C(11)	1.3964

Symmetry transformations used to generate equivalent atoms:

#1 -x,-y,z #2 -y,x,z #3 y,-x,z

Table B20. Anisotropic displacement parameters ($Å^2$ x 10^3) in **12** at 143(2) K in *I4* space group. The anisotropic displacement factor exponent takes the form: $-2\pi^2 [h^2a^{*2}U^{11} + ... + 2\ hka^*b^*U^{12}]$

	U^{11}	U^{22}	U^{33}	U^{23}	U^{13}	U^{12}
Fe(1)	22(1)	22(1)	28(1)	0	0	0
Fe(2)	22(1)	22(1)	28(1)	0	0	0
Cl(1)	34(1)	34(1)	27(1)	0	0	0
Cl(2)	34(1)	34(1)	27(1)	0	0	0
N(1)	25(1)	24(1)	36(1)	-1(1)	0(1)	1(1)
C(1)	26(1)	27(1)	30(1)	0(1)	1(1)	3(1)
C(2)	33(1)	25(1)	40(1)	-1(1)	1(1)	4(1)
C(3)	35(1)	24(1)	41(1)	1(1)	-1(1)	2(1)
C(4)	31(1)	24(1)	30(1)	0(1)	-1(1)	0(1)
C(5)	30(1)	25(1)	31(1)	-1(1)	1(1)	-3(1)
C(6)	27(1)	24(1)	36(1)	3(1)	0(1)	-1(1)
C(7)	59(2)	44(2)	36(2)	-1(1)	2(1)	-17(1)
C(8)	61(2)	42(2)	48(2)	8(1)	11(1)	-18(2)
C(9)	30(1)	25(1)	59(2)	-5(1)	-1(1)	-2(1)
C(10)	62(2)	41(2)	48(3)	-10(1)	-8(1)	-15(1)
C(11)	66(2)	42(2)	30(2)	2(1)	-2(1)	20(1)

Table B21. Atomic coordinates and equivalent isotropic displacement parameters ($Å^3$ x 10^3) in **12** at 20(2) K in *I4* space group. *U*(eq) is defined as one third of the trace of the orthogonalized U^{ij} tensor

	x	y	z	*U*(eq)
Fe(1)	0	0	4606(1)	9(1)
Cl(1)	0	0	2337(1)	11(1)
Fe(2)	0	0	5421(1)	9(1)
Cl(2)	0	0	7694(1)	11(1)
N(1)	366(1)	1455(1)	5000(1)	12(1)
C(5)	2198(1)	1315(1)	4997(1)	12(1)
C(4)	1310(1)	1855(1)	4999(1)	12(1)
C(1)	-278(1)	2254(1)	4995(1)	12(1)
C(2)	275(1)	3170(1)	4994(1)	14(1)
C(3)	1254(1)	2924(1)	5006(1)	14(1)
C(6)	3154(1)	1883(1)	4994(1)	11(1)
C(7)	3567(1)	2223(1)	3808(1)	14(1)
C(8)	4458(2)	2789(2)	3814(2)	14(1)
C(9)	4928(12)	2907(7)	5000(40)	14(1)
C(10)	4563(2)	2608(4)	6238(5)	18(1)
C(11)	3660(2)	2049(3)	6251(4)	16(1)
C(6B)	3154(1)	1883(1)	4994(1)	11(1)

Table B21. (continued)

	x	y	z	*U*(eq)
C(7B)	3662(1)	2035(1)	3739(1)	14(1)
C(8B)	4537(1)	2573(1)	3742(1)	14(1)
C(9B)	4932(7)	2988(4)	5010(20)	14(1)
C(10B)	4426(1)	2761(2)	6245(3)	18(1)
C(11B)	3544(1)	2250(1)	6235(2)	16(1)

Table B22. Bond angles (°) in **12** at 20(2) K in *I4* space group

Angles			
N(1)#1-Fe(1)-N(1)#2	88.030(8)	N(1)-Fe(2)-Cl(2)	101.39(2)
N(1)#1-Fe(1)-N(1)#3	88.030(8)	C(1)-N(1)-C(4)	105.91(3)
N(1)#2-Fe(1)-N(1)#3	158.63(4)	C(1)-N(1)-Fe(1)	126.24(3)
N(1)#1-Fe(1)-N(1)	158.63(4)	C(4)-N(1)-Fe(1)	126.31(3)
N(1)#2-Fe(1)-N(1)	88.030(8)	C(1)-N(1)-Fe(2)	126.24(3)
N(1)#3-Fe(1)-N(1)	88.030(8)	C(4)-N(1)-Fe(2)	126.22(3)
N(1)#1-Fe(1)-Cl(1)	100.69(2)	Fe(1)-N(1)-Fe(2)	22.080(9)
N(1)#2-Fe(1)-Cl(1)	100.69(2)	C(1)#2-C(5)-C(4)	124.36(3)
N(1)#3-Fe(1)-Cl(1)	100.69(2)	C(1)#2-C(5)-C(6)	117.69(3)
N(1)-Fe(1)-Cl(1)	100.69(2)	C(4)-C(5)-C(6)	117.95(3)
N(1)#1-Fe(2)-N(1)#3	87.763(8)	N(1)-C(4)-C(5)	125.73(3)
N(1)#1-Fe(2)-N(1)#2	87.763(8)	N(1)-C(4)-C(3)	109.94(3)
N(1)#3-Fe(2)-N(1)#2	157.21(4)	C(5)-C(4)-C(3)	124.33(3)
N(1)#1-Fe(2)-N(1)	157.21(4)	N(1)-C(1)-C(5)#3	125.81(3)
N(1)#3-Fe(2)-N(1)	87.763(8)	N(1)-C(1)-C(2)	110.07(3)
N(1)#2-Fe(2)-N(1)	87.763(8)	C(5)#3-C(1)-C(2)	124.12(3)
N(1)#1-Fe(2)-Cl(2)	101.39(2)	C(3)-C(2)-C(1)	106.94(3)
N(1)#3-Fe(2)-Cl(2)	101.39(2)	C(2)-C(3)-C(4)	107.14(3)
N(1)#2-Fe(2)-Cl(2)	101.39(2)	C(7)-C(6)-C(11)	118.49(14)

Table B22. (continued)

Angles			
C(8)-C(9)-C(10)	123.9(11)	C(11B)-C(10B)-C(9B)	121.5(6)
C(9)-C(10)-C(11)	118.1(9)	C(11)-C(6)-C(5)	119.61(15)
C(6)-C(11)-C(10)	119.1(3)	C(6)-C(7)-C(8)	121.67(10)
C(7B)-C(8B)-C(9B)	121.1(5)	C(9)-C(8)-C(7)	118.3(9)
C(10B)-C(9B)-C(8B)	117.2(6)		

Symmetry transformations used to generate equivalent atoms:

#1 -x,-y,z #2 -y,x,z #3 y,-x,z

Table B23. Bond lengths (Å) in **12** at 20(2) K in *I4* space group

Lengths			
Fe(1)-N(1)#1	2.0582(3)	C(4)-C(3)	1.4432(4)
Fe(1)-N(1)#2	2.0582(3)	C(1)-C(5)#3	1.3997(5)
Fe(1)-N(1)#3	2.0582(3)	C(1)-C(2)	1.4434(5)
Fe(1)-N(1)	2.0582(3)	C(2)-C(3)	1.3620(5)
Fe(1)-Cl(1)	2.1979(8)	C(6)-C(7)	1.3558
Fe(2)-N(1)#1	2.0631(3)	C(6)-C(11)	1.414(4)
Fe(2)-N(1)#3	2.0631(3)	C(7)-C(8)	1.423(2)
Fe(2)-N(1)#2	2.0631(3)	C(8)-C(9)	1.32(3)
Fe(2)-N(1)	2.0632(3)	C(9)-C(10)	1.36(3)
Fe(2)-Cl(2)	2.2011(5)	C(10)-C(11)	1.431(6)
N(1)-C(1)	1.3830(5)	C(7B)-C(8B)	1.3846(17)
N(1)-C(4)	1.3833(4)	C(8B)-C(9B)	1.453(18)
C(5)-C(1)#2	1.3997(5)	C(9B)-C(10B)	1.408(19)
C(5)-C(4)	1.4015(5)	C(10B)-C(11B)	1.375(3)
C(5)-C(6)	1.4991		

Symmetry transformations used to generate equivalent atoms:

#1 -x,-y,z #2 -y,x,z #3 y,-x,z

Table B24. Anisotropic displacement parameters ($Å^2$ x 10^3) in **12** at 20(2) K in *I4* space group. The anisotropic displacement factor exponent takes the form: $-2\pi^2 [h^2a^{*2}U^{11} + ... + 2\ hka^*b^*U^{12}]$

	U^{11}	U^{22}	U^{33}	U^{23}	U^{13}	U^{12}
Fe(1)	9(1)	9(1)	8(1)	0	0	0
Cl(1)	12(1)	12(1)	8(1)	0	0	0
Fe(2)	9(1)	9(1)	8(1)	0	0	0
Cl(2)	12(1)	12(1)	8(1)	0	0	0
N(1)	10(1)	10(1)	15(1)	0(1)	0(1)	0(1)
C(5)	11(1)	12(1)	12(1)	0(1)	0(1)	-1(1)
C(4)	11(1)	11(1)	14(1)	0(1)	0(1)	-1(1)
C(1)	12(1)	10(1)	14(1)	0(1)	0(1)	0(1)
C(2)	14(1)	11(1)	19(1)	0(1)	-1(1)	0(1)
C(3)	13(1)	11(1)	18(1)	0(1)	0(1)	-2(1)
C(6)	11(1)	14(1)	10(1)	0(1)	0(1)	-2(1)
C(7)	18(1)	15(1)	9(1)	-1(1)	1(1)	-5(1)
C(8)	18(1)	11(1)	14(1)	0(1)	3(1)	-4(1)
C(9)	11(1)	12(1)	19(1)	-1(2)	-1(1)	-1(1)
C(10)	11(1)	29(1)	15(1)	-6(1)	-2(1)	-3(1)
C(11)	14(1)	23(1)	10(1)	-4(1)	1(1)	-4(1)

Table B24. (continued)

	U^{11}	U^{22}	U^{33}	U^{23}	U^{13}	U^{12}
C(6B)	11(1)	14(1)	10(1)	0(1)	0(1)	-2(1)
C(7B)	18(1)	15(1)	9(1)	-1(1)	1(1)	-5(1)
C(8B)	18(1)	11(1)	14(1)	0(1)	3(1)	-4(1)
C(9B)	11(1)	12(1)	19(1)	-1(2)	-1(1)	-1(1)
C(10B)	11(1)	29(1)	15(1)	-6(1)	-2(1)	-3(1)
C(11B)	14(1)	23(1)	10(1)	-4(1)	1(1)	-4(1)

Table B25. Atomic coordinates (x 10^4) and equivalent isotropic displacement parameters (Å^2 x 10^3) in **13** •H_2O•$CHCl_3$ at 143(2) K. *U*(eq) is defined as one third of the trace of the orthogonalized U^{ij} tensor

	x	y	z	*U*(eq)
Fe(1)	10000	10000	5000	18(1)
Fe(2)	5000	5000	0	17(1)
N(1)	8887(1)	9968(1)	4307(1)	19(1)
N(2)	11180(1)	11066(1)	3983(1)	19(1)
N(3)	10939(2)	8792(1)	4701(1)	22(1)
N(4)	11471(2)	7159(2)	4700(1)	34(1)
N(5)	5208(2)	6379(1)	199(1)	20(1)
N(6)	5568(2)	4193(1)	1005(1)	19(1)
N(7)	3239(2)	4860(1)	720(1)	21(1)
N(8)	1593(2)	4899(2)	1773(1)	29(1)
C(1)	7796(2)	9334(2)	4570(1)	20(1)
C(2)	7316(2)	9484(2)	3872(1)	24(1)
C(3)	8103(2)	10206(2)	3186(1)	24(1)
C(4)	9088(2)	10513(2)	3456(1)	21(1)
C(5)	10110(2)	11215(2)	2911(1)	22(1)
C(6)	10164(2)	11719(2)	1997(1)	29(1)
C(7)	11107(2)	11478(2)	1369(2)	43(1)

Table B25. (continued)

	x	y	z	*U*(eq)
C(7)	11107(2)	11478(2)	1369(2)	43(1)
C(8)	11125(3)	11962(3)	524(2)	59(1)
C(9)	10206(3)	12670(3)	320(2)	62(1)
C(10)	9272(3)	12903(3)	930(2)	54(1)
C(11)	9246(2)	12437(2)	1768(2)	38(1)
C(12)	11083(2)	11473(2)	3170(1)	21(1)
C(13)	12122(2)	12232(2)	2626(1)	24(1)
C(14)	12842(2)	12289(2)	3107(1)	23(1)
C(15)	12269(2)	11560(2)	3945(1)	21(1)
C(16)	11992(2)	8863(2)	4025(2)	38(1)
C(17)	12317(2)	7857(2)	4023(2)	40(1)
C(18)	10660(2)	7742(2)	5095(2)	30(1)
C(19)	7239(2)	8618(2)	5385(1)	20(1)
C(20)	6061(2)	7991(2)	5522(1)	21(1)
C(21)	6142(2)	6942(2)	5505(1)	30(1)
C(22)	5069(3)	6391(2)	5570(2)	38(1)
C(23)	3921(2)	6873(2)	5653(2)	40(1)
C(24)	3823(2)	7907(2)	5686(2)	37(1)
C(25)	4889(2)	8467(2)	5621(1)	28(1)

Table B25. (continued)

	x	y	z	*U*(eq)
C(26)	4932(2)	7400(2)	-260(1)	21(1)
C(27)	5178(2)	8182(2)	84(1)	26(1)
C(28)	5582(2)	7638(2)	758(1)	25(1)
C(29)	5585(2)	6513(2)	836(1)	21(1)
C(30)	5895(2)	5684(2)	1483(1)	22(1)
C(31)	6230(2)	5957(2)	2157(1)	24(1)
C(32)	5303(2)	6252(2)	2764(1)	30(1)
C(33)	5611(3)	6454(2)	3411(2)	37(1)
C(34)	6831(3)	6356(2)	3456(2)	39(1)
C(35)	7765(3)	6075(2)	2853(2)	40(1)
C(36)	7467(2)	5881(2)	2201(2)	32(1)
C(37)	5880(2)	4599(2)	1550(1)	20(1)
C(38)	6195(2)	3731(2)	2213(1)	23(1)
C(39)	6113(2)	2809(2)	2054(1)	23(1)
C(40)	5722(2)	3093(2)	1305(1)	19(1)
C(41)	5528(2)	2340(2)	953(1)	20(1)
C(42)	5904(2)	1200(2)	1312(1)	22(1)
C(43)	5145(2)	456(2)	2038(2)	37(1)
C(44)	5552(3)	-585(2)	2358(2)	43(1)

Table B25. (continued)

	x	y	z	*U*(eq)
C(45)	6716(2)	-884(2)	1960(2)	36(1)
C(46)	7476(3)	-149(2)	1242(2)	43(1)
C(47)	7072(2)	890(2)	915(2)	36(1)
C(48)	2851(2)	4996(2)	1466(1)	25(1)
C(49)	1137(2)	4687(2)	1202(2)	31(1)
C(50)	2154(2)	4657(2)	553(1)	27(1)
C(51)	1142(3)	7772(3)	2190(2)	64(1)
Cl(1)	809(1)	5084(1)	3527(1)	81(1)
Cl(2)	2611(3)	8049(13)	1846(2)	87(3)
Cl(2A)	2653(2)	8681(7)	1822(2)	69(1)
Cl(3)	22(1)	8412(1)	2757(1)	75(1)
Cl(4)	694(1)	7726(1)	1329(1)	104(1)
O(1)	8299(3)	5060(2)	4939(2)	61(1)

Table B26. Bond angles (°) in **13**•H_2O•$CHCl_3$ at 143(2) K

Angles			
N(3)#1-Fe(1)-N(3)	179.999(1)	N(7)-Fe(2)-N(6)#2	89.61(7)
N(3)#1-Fe(1)-N(1)	90.64(7)	N(6)-Fe(2)-N(6)#2	180.00(6)
N(3)-Fe(1)-N(1)	89.36(7)	N(7)#2-Fe(2)-N(5)	91.09(7)
N(3)#1-Fe(1)-N(1)#1	89.36(7)	N(7)-Fe(2)-N(5)	88.91(7)
N(3)-Fe(1)-N(1)#1	90.64(7)	N(6)-Fe(2)-N(5)	89.07(7)
N(1)-Fe(1)-N(1)#1	179.999(1)	N(6)#2-Fe(2)-N(5)	90.93(7)
N(3)#1-Fe(1)-N(2)#1	90.10(7)	N(7)#2-Fe(2)-N(5)#2	88.91(7)
N(3)-Fe(1)-N(2)#1	89.90(7)	N(7)-Fe(2)-N(5)#2	91.09(7)
N(1)-Fe(1)-N(2)#1	90.39(7)	N(6)-Fe(2)-N(5)#2	90.92(7)
N(1)#1-Fe(1)-N(2)#1	89.61(7)	N(6)#2-Fe(2)-N(5)#2	89.08(7)
N(3)#1-Fe(1)-N(2)	89.90(7)	N(5)-Fe(2)-N(5)#2	180.0
N(3)-Fe(1)-N(2)	90.10(7)	C(4)-N(1)-C(1)	105.61(16)
N(1)-Fe(1)-N(2)	89.61(7)	C(4)-N(1)-Fe(1)	127.44(13)
N(1)#1-Fe(1)-N(2)	90.39(7)	C(1)-N(1)-Fe(1)	126.82(13)
N(2)#1-Fe(1)-N(2)	179.998(2)	C(15)-N(2)-C(12)	105.15(16)
N(7)#2-Fe(2)-N(7)	180.0	C(15)-N(2)-Fe(1)	127.10(13)
N(7)#2-Fe(2)-N(6)	89.61(7)	C(12)-N(2)-Fe(1)	127.76(13)
N(7)-Fe(2)-N(6)	90.39(7)	C(18)-N(3)-C(16)	105.41(19)
N(7)#2-Fe(2)-N(6)#2	90.39(7)	C(18)-N(3)-Fe(1)	127.13(15)

Table B26. (continued)

Angles			
C(16)-N(3)-Fe(1)	127.42(16)	C(5)-C(4)-C(3)	123.61(18)
C(18)-N(4)-C(17)	107.8(2)	C(4)-C(5)-C(12)	123.34(18)
C(29)-N(5)-C(26)	105.35(16)	C(4)-C(5)-C(6)	118.16(17)
C(29)-N(5)-Fe(2)	128.20(13)	C(12)-C(5)-C(6)	118.50(18)
C(26)-N(5)-Fe(2)	126.37(13)	C(7)-C(6)-C(11)	118.8(2)
C(40)-N(6)-C(37)	105.55(15)	C(7)-C(6)-C(5)	121.2(2)
C(40)-N(6)-Fe(2)	126.40(13)	C(11)-C(6)-C(5)	119.9(2)
C(37)-N(6)-Fe(2)	128.05(13)	C(6)-C(7)-C(8)	119.6(3)
C(48)-N(7)-C(50)	105.85(17)	C(9)-C(8)-C(7)	120.0(3)
C(48)-N(7)-Fe(2)	125.67(14)	C(10)-C(9)-C(8)	120.8(3)
C(50)-N(7)-Fe(2)	128.41(14)	C(9)-C(10)-C(11)	119.8(3)
C(48)-N(8)-C(49)	107.88(19)	C(10)-C(11)-C(6)	120.9(3)
N(1)-C(1)-C(19)	126.18(17)	N(2)-C(12)-C(5)	125.44(18)
N(1)-C(1)-C(2)	110.09(18)	N(2)-C(12)-C(13)	110.16(17)
C(19)-C(1)-C(2)	123.70(18)	C(5)-C(12)-C(13)	124.37(18)
C(3)-C(2)-C(1)	107.45(18)	C(14)-C(13)-C(12)	107.00(18)
C(2)-C(3)-C(4)	106.89(18)	C(13)-C(14)-C(15)	107.25(18)
N(1)-C(4)-C(5)	126.36(17)	N(2)-C(15)-C(19)#1	125.65(18)
N(1)-C(4)-C(3)	109.95(17)	N(2)-C(15)-C(14)	110.44(17)

Table B26. (continued)

Angles			
C(19)#1-C(15)-C(14)	123.91(18)	C(27)-C(28)-C(29)	106.90(18)
C(17)-C(16)-N(3)	109.3(2)	N(5)-C(29)-C(30)	125.50(18)
C(16)-C(17)-N(4)	106.6(2)	N(5)-C(29)-C(28)	110.34(17)
N(3)-C(18)-N(4)	110.9(2)	C(30)-C(29)-C(28)	124.14(18)
C(15)#1-C(19)-C(1)	123.80(18)	C(37)-C(30)-C(29)	123.14(18)
C(15)#1-C(19)-C(20)	119.28(18)	C(37)-C(30)-C(31)	117.75(17)
C(1)-C(19)-C(20)	116.90(17)	C(29)-C(30)-C(31)	119.09(18)
C(21)-C(20)-C(25)	119.06(19)	C(32)-C(31)-C(36)	118.81(19)
C(21)-C(20)-C(19)	119.95(18)	C(32)-C(31)-C(30)	120.55(19)
C(25)-C(20)-C(19)	120.91(19)	C(36)-C(31)-C(30)	120.60(19)
C(20)-C(21)-C(22)	119.9(2)	C(31)-C(32)-C(33)	120.2(2)
C(23)-C(22)-C(21)	120.7(2)	C(34)-C(33)-C(32)	120.4(2)
C(22)-C(23)-C(24)	119.9(2)	C(33)-C(34)-C(35)	120.2(2)
C(23)-C(24)-C(25)	120.0(2)	C(34)-C(35)-C(36)	119.8(2)
C(24)-C(25)-C(20)	120.4(2)	C(31)-C(36)-C(35)	120.6(2)
N(5)-C(26)-C(41)#2	126.09(18)	N(6)-C(37)-C(30)	125.98(18)
N(5)-C(26)-C(27)	110.17(17)	N(6)-C(37)-C(38)	110.01(17)
C(41)#2-C(26)-C(27)	123.74(18)	C(30)-C(37)-C(38)	124.01(18)
C(28)-C(27)-C(26)	107.21(18)	C(39)-C(38)-C(37)	107.03(18)

Table B26. (continued)

Angles			
C(38)-C(39)-C(40)	107.26(18)	C(45)-C(44)-C(43)	120.6(2)
N(6)-C(40)-C(41)	126.39(17)	C(46)-C(45)-C(44)	119.4(2)
N(6)-C(40)-C(39)	110.11(17)	C(45)-C(46)-C(47)	120.3(2)
C(41)-C(40)-C(39)	123.49(18)	C(42)-C(47)-C(46)	120.7(2)
C(26)#2-C(41)-C(40)	123.69(18)	N(7)-C(48)-N(8)	110.88(19)
C(26)#2-C(41)-C(42)	118.25(18)	C(50)-C(49)-N(8)	106.65(19)
C(40)-C(41)-C(42)	117.97(17)	C(49)-C(50)-N(7)	108.73(19)
C(43)-C(42)-C(47)	118.6(2)	Cl(2)-C(51)-Cl(3)	126.1(6)
C(43)-C(42)-C(41)	122.52(19)	Cl(2)-C(51)-Cl(4)	105.9(3)
C(47)-C(42)-C(41)	118.82(19)	Cl(3)-C(51)-Cl(4)	109.81(18)
C(42)-C(43)-C(44)	120.3(2)		

Symmetry transformations used to generate equivalent atoms:

#1 -x+2,-y+2,-z+1 #2 -x+1,-y+1,-z

Table B27. Bond lengths (Å) in **13**•H_2O•$CHCl_3$ at 143(2)

Lengths			
Fe(1)-N(3)#1	1.9774(17)	N(4)-C(17)	1.355(3)
Fe(1)-N(3)	1.9774(17)	N(5)-C(29)	1.378(2)
Fe(1)-N(1)	1.9911(16)	N(5)-C(26)	1.379(2)
Fe(1)-N(1)#1	1.9911(16)	N(6)-C(40)	1.378(2)
Fe(1)-N(2)#1	1.9999(19)	N(6)-C(37)	1.380(2)
Fe(1)-N(2)	1.9999(19)	N(7)-C(48)	1.326(3)
Fe(2)-N(7)#2	1.9616(18)	N(7)-C(50)	1.384(3)
Fe(2)-N(7)	1.9616(18)	N(8)-C(48)	1.332(3)
Fe(2)-N(6)	1.9896(16)	N(8)-C(49)	1.366(3)
Fe(2)-N(6)#2	1.9897(16)	C(1)-C(19)	1.396(3)
Fe(2)-N(5)	2.0020(17)	C(1)-C(2)	1.432(3)
Fe(2)-N(5)#2	2.0020(17)	C(2)-C(3)	1.347(3)
N(1)-C(4)	1.377(3)	C(3)-C(4)	1.444(3)
N(1)-C(1)	1.380(2)	C(4)-C(5)	1.391(3)
N(2)-C(15)	1.382(2)	C(5)-C(12)	1.391(3)
N(2)-C(12)	1.382(2)	C(5)-C(6)	1.503(3)
N(3)-C(18)	1.325(3)	C(6)-C(7)	1.384(3)
N(3)-C(16)	1.375(3)	C(6)-C(11)	1.396(3)
N(4)-C(18)	1.335(3)	C(7)-C(8)	1.400(4)

Table B27. (continued)

Lengths			
C(8)-C(9)	1.379(5)	C(28)-C(29)	1.439(3)
C(9)-C(10)	1.355(5)	C(29)-C(30)	1.392(3)
C(10)-C(11)	1.384(3)	C(30)-C(37)	1.392(3)
C(12)-C(13)	1.439(3)	C(30)-C(31)	1.502(3)
C(13)-C(14)	1.350(3)	C(31)-C(32)	1.388(3)
C(14)-C(15)	1.431(3)	C(31)-C(36)	1.391(3)
C(15)-C(19)#1	1.389(3)	C(32)-C(33)	1.394(3)
C(16)-C(17)	1.350(3)	C(33)-C(34)	1.372(4)
C(19)-C(15)#1	1.389(3)	C(34)-C(35)	1.377(4)
C(19)-C(20)	1.504(3)	C(35)-C(36)	1.392(3)
C(20)-C(21)	1.387(3)	C(37)-C(38)	1.438(3)
C(20)-C(25)	1.393(3)	C(38)-C(39)	1.349(3)
C(21)-C(22)	1.389(3)	C(39)-C(40)	1.435(3)
C(22)-C(23)	1.374(4)	C(40)-C(41)	1.394(3)
C(23)-C(24)	1.377(4)	C(41)-C(26)#2	1.391(3)
C(24)-C(25)	1.388(3)	C(41)-C(42)	1.500(3)
C(26)-C(41)#2	1.391(3)	C(42)-C(43)	1.381(3)
C(26)-C(27)	1.438(3)	C(42)-C(47)	1.382(3)
C(27)-C(28)	1.348(3)	C(43)-C(44)	1.392(3)

Table B27. (continued)

Lengths			
C(44)-C(45)	1.375(4)	C(51)-Cl(2)	1.576(6)
C(45)-C(46)	1.368(4)	C(51)-Cl(3)	1.715(3)
C(46)-C(47)	1.391(3)	C(51)-Cl(4)	1.756(3)
C(49)-C(50)	1.353(3)		

Symmetry transformations used to generate equivalent atoms:

#1 -x+2,-y+2,-z+1 #2 -x+1,-y+1,-z

Table B28. Anisotropic displacement parameters ($Å^2$ x 10^3) in **13**•H_2O•$CHCl_3$ at 143(2) K. The anisotropic displacement factor exponent takes the form: $-2\pi^2$ [$h(2a^{*2}U^{11}$ + ... + 2 hka*b*U^{12}]

	U^{11}	U^{22}	U^{33}	U^{23}	U^{13}	U^{12}
Fe(1)	15(1)	22(1)	16(1)	-5(1)	-5(1)	1(1)
Fe(2)	20(1)	18(1)	14(1)	-5(1)	-7(1)	2(1)
N(1)	16(1)	23(1)	18(1)	-6(1)	-6(1)	0(1)
N(2)	17(1)	24(1)	18(1)	-6(1)	-7(1)	0(1)
N(3)	20(1)	28(1)	21(1)	-10(1)	-9(1)	4(1)
N(4)	38(1)	31(1)	41(1)	-18(1)	-18(1)	10(1)
N(5)	24(1)	20(1)	16(1)	-6(1)	-8(1)	3(1)
N(6)	21(1)	20(1)	16(1)	-5(1)	-8(1)	2(1)
N(7)	24(1)	20(1)	19(1)	-6(1)	-8(1)	2(1)
N(8)	27(1)	32(1)	24(1)	-11(1)	-2(1)	3(1)
C(1)	17(1)	24(1)	21(1)	-8(1)	-6(1)	1(1)
C(2)	20(1)	30(1)	23(1)	-9(1)	-9(1)	-1(1)
C(3)	25(1)	31(1)	18(1)	-8(1)	-9(1)	0(1)
C(4)	21(1)	25(1)	17(1)	-7(1)	-7(1)	2(1)
C(5)	20(1)	28(1)	16(1)	-6(1)	-6(1)	1(1)
C(6)	27(1)	40(1)	18(1)	-3(1)	-7(1)	-12(1)

Table B28. (continued)

	U^{11}	U^{22}	U^{33}	U^{23}	U^{13}	U^{12}
C(7)	35(1)	67(2)	27(1)	-16(1)	-4(1)	-13(1)
C(8)	48(2)	99(3)	24(1)	-20(2)	5(1)	-31(2)
C(9)	60(2)	94(3)	25(1)	5(2)	-21(1)	-39(2)
C(10)	46(2)	67(2)	36(2)	13(1)	-26(1)	-25(1)
C(11)	33(1)	46(2)	29(1)	4(1)	-17(1)	-14(1)
C(12)	19(1)	24(1)	18(1)	-5(1)	-6(1)	3(1)
C(13)	21(1)	27(1)	18(1)	-2(1)	-4(1)	-2(1)
C(14)	19(1)	26(1)	21(1)	-4(1)	-5(1)	-3(1)
C(15)	18(1)	22(1)	21(1)	-7(1)	-6(1)	3(1)
C(16)	34(1)	37(1)	31(1)	-10(1)	2(1)	6(1)
C(17)	41(1)	45(2)	35(1)	-20(1)	-6(1)	15(1)
C(18)	27(1)	29(1)	33(1)	-11(1)	-10(1)	4(1)
C(19)	16(1)	21(1)	22(1)	-8(1)	-6(1)	1(1)
C(20)	22(1)	25(1)	16(1)	-3(1)	-8(1)	-3(1)
C(21)	33(1)	30(1)	27(1)	-10(1)	-9(1)	-2(1)
C(22)	58(2)	32(1)	23(1)	-5(1)	-12(1)	-17(1)
C(23)	39(1)	54(2)	22(1)	2(1)	-16(1)	-24(1)
C(24)	24(1)	47(2)	31(1)	3(1)	-13(1)	-7(1)

Table B28. (continued)

	U^{11}	U^{22}	U^{33}	U^{23}	U^{13}	U^{12}
C(25)	24(1)	27(1)	29(1)	-2(1)	-11(1)	0(1)
C(26)	22(1)	20(1)	18(1)	-5(1)	-6(1)	1(1)
C(27)	33(1)	21(1)	27(1)	-9(1)	-12(1)	2(1)
C(28)	34(1)	22(1)	24(1)	-10(1)	-13(1)	2(1)
C(29)	23(1)	23(1)	20(1)	-9(1)	-8(1)	3(1)
C(30)	23(1)	25(1)	20(1)	-9(1)	-8(1)	2(1)
C(31)	36(1)	20(1)	20(1)	-6(1)	-15(1)	3(1)
C(32)	40(1)	28(1)	25(1)	-11(1)	-15(1)	8(1)
C(33)	63(2)	29(1)	22(1)	-10(1)	-17(1)	7(1)
C(34)	68(2)	29(1)	31(1)	-11(1)	-31(1)	3(1)
C(35)	49(2)	42(1)	41(2)	-13(1)	-30(1)	1(1)
C(36)	35(1)	37(1)	30(1)	-14(1)	-16(1)	4(1)
C(37)	21(1)	24(1)	16(1)	-7(1)	-7(1)	2(1)
C(38)	27(1)	27(1)	19(1)	-7(1)	-12(1)	4(1)
C(39)	26(1)	23(1)	17(1)	-2(1)	-10(1)	3(1)
C(40)	19(1)	22(1)	16(1)	-4(1)	-6(1)	2(1)
C(41)	21(1)	20(1)	18(1)	-4(1)	-5(1)	1(1)
C(42)	30(1)	19(1)	22(1)	-6(1)	-14(1)	1(1)

Table B28. (continued)

	U^{11}	U^{22}	U^{33}	U^{23}	U^{13}	U^{12}
C(43)	34(1)	28(1)	39(1)	-1(1)	-7(1)	1(1)
C(44)	51(2)	24(1)	44(2)	4(1)	-16(1)	-3(1)
C(45)	56(2)	20(1)	43(2)	-8(1)	-34(1)	7(1)
C(46)	47(2)	35(1)	47(2)	-14(1)	-17(1)	18(1)
C(47)	39(1)	26(1)	36(1)	-4(1)	-7(1)	7(1)
C(48)	27(1)	27(1)	22(1)	-10(1)	-6(1)	2(1)
C(49)	25(1)	38(1)	31(1)	-10(1)	-9(1)	1(1)
C(50)	25(1)	34(1)	24(1)	-9(1)	-9(1)	1(1)
C(51)	78(2)	73(2)	41(2)	-27(2)	-16(2)	32(2)
Cl(1)	129(1)	88(1)	36(1)	-33(1)	-35(1)	55(1)
Cl(2)	38(1)	146(8)	61(1)	-21(2)	-7(1)	10(2)
Cl(2A)	49(1)	92(3)	56(1)	-27(1)	1(1)	6(1)
Cl(3)	52(1)	88(1)	103(1)	-69(1)	-7(1)	10(1)
Cl(4)	181(1)	87(1)	45(1)	-21(1)	-28(1)	-30(1)
O(1)	90(2)	47(1)	65(2)	-28(1)	-45(2)	27(1)

Table B29. Atomic coordinates (x 10^4) and equivalent isotropic displacement parameters (Å^2 x 10^3) in **13**•H_2O•$CHCl_3$ at 20(2) K. *U*(eq) is defined as one third of the trace of the orthogonalized U^{ij} tensor

	x	y	z	*U*(eq)
Fe(1)	10000	0	10000	5(1)
Fe(2)	5000	5000	5000	5(1)
N(1)	11776(1)	144(1)	9288(1)	8(1)
N(2)	13441(1)	94(1)	8241(1)	11(1)
N(3)	9794(1)	-1391(1)	9800(1)	7(1)
N(4)	9442(1)	800(1)	8988(1)	6(1)
N(5)	4068(1)	6212(1)	5309(1)	8(1)
N(6)	3541(1)	7858(1)	5310(1)	12(1)
N(7)	3814(1)	3923(1)	6021(1)	7(1)
N(8)	6131(1)	5033(1)	5690(1)	7(1)
C(1)	12856(1)	349(1)	9467(1)	12(1)
C(2)	13899(1)	315(1)	8818(1)	13(1)
C(3)	12169(1)	-3(1)	8541(1)	9(1)
C(4)	10066(1)	-2409(1)	10260(1)	7(1)
C(5)	9834(1)	-3207(1)	9916(1)	10(1)
C(6)	9430(1)	-2667(1)	9234(1)	11(1)
C(7)	9422(1)	-1534(1)	9159(1)	8(1)

Table B29. (continued)

	x	y	z	*U*(eq)
C(8)	9114(1)	-709(1)	8509(1)	9(1)
C(9)	8783(1)	-991(1)	7838(1)	11(1)
C(10)	9728(1)	-1283(1)	7226(1)	16(1)
C(11)	9422(2)	-1491(1)	6573(1)	21(1)
C(12)	8186(2)	-1403(1)	6522(1)	22(1)
C(13)	7235(2)	-1123(1)	7135(1)	20(1)
C(14)	7533(1)	-922(1)	7790(1)	15(1)
C(15)	9129(1)	385(1)	8443(1)	7(1)
C(16)	8809(1)	1246(1)	7778(1)	9(1)
C(17)	8892(1)	2185(1)	7936(1)	8(1)
C(18)	9290(1)	1903(1)	8687(1)	6(1)
C(19)	9480(1)	2666(1)	9040(1)	7(1)
C(20)	9103(1)	3803(1)	8681(1)	8(1)
C(21)	7938(1)	4123(1)	9101(1)	14(1)
C(22)	7526(1)	5163(1)	8772(1)	17(1)
C(23)	8286(1)	5899(1)	8023(1)	15(1)
C(24)	9455(1)	5587(1)	7603(1)	15(1)
C(25)	9864(1)	4542(1)	7928(1)	13(1)
C(26)	4345(1)	7272(1)	4903(1)	12(1)

Table B29. (continued)

	x	y	z	*U*(eq)
C(27)	2701(1)	7150(1)	6007(1)	16(1)
C(28)	3032(1)	6128(1)	6004(1)	16(1)
C(29)	2720(1)	3425(1)	6058(1)	7(1)
C(30)	2140(1)	2681(1)	6900(1)	8(1)
C(31)	2878(1)	2741(1)	7380(1)	9(1)
C(32)	3920(1)	3516(1)	6829(1)	8(1)
C(33)	4901(1)	3781(1)	7092(1)	10(1)
C(34)	4848(1)	3281(1)	8000(1)	14(1)
C(35)	3884(1)	3509(2)	8634(1)	21(1)
C(36)	3858(2)	3033(2)	9481(1)	30(1)
C(37)	4793(2)	2330(2)	9699(1)	32(1)
C(38)	5764(2)	2109(2)	9072(1)	27(1)
C(39)	5786(1)	2578(1)	8229(1)	19(1)
C(40)	5934(1)	4492(1)	6542(1)	9(1)
C(41)	6930(1)	4800(1)	6811(1)	10(1)
C(42)	7731(1)	5533(1)	6117(1)	9(1)
C(43)	7230(1)	5674(1)	5422(1)	7(1)
C(44)	7790(1)	6398(1)	4608(1)	7(1)
C(45)	8978(1)	7022(1)	4467(1)	8(1)

Table B29. (continued)

	x	y	z	*U*(eq)
C(46)	10153(1)	6534(1)	4369(1)	12(1)
C(47)	11242(1)	7093(1)	4305(1)	17(1)
C(48)	11162(1)	8150(1)	4334(1)	19(1)
C(49)	10001(1)	8644(1)	4418(1)	17(1)
C(50)	8910(1)	8087(1)	4481(1)	12(1)
C(52)	3805(2)	7171(2)	7815(1)	37(1)
Cl(1)	4043(2)	9779(1)	6535(1)	20(1)
Cl(2)	2324(1)	6258(1)	8202(1)	26(1)
Cl(3)	4100(3)	7314(1)	8688(1)	30(1)
Cl(4)	5009(1)	6544(1)	7264(1)	26(1)
O(1)	6680(2)	9904(1)	5076(1)	33(1)
Cl(2A)	2383(1)	6974(3)	8147(1)	47(1)
Cl(1A)	4485(3)	10073(2)	6415(1)	24(1)
Cl(3A)	4592(5)	7325(2)	8618(1)	23(1)
Fe(2A)	4448(13)	4915(19)	4981(15)	492(8)

Table B30. Bond angles (°) in **13**•H_2O•$CHCl_3$ at 20(2) K

Angles			
N(1)#1-Fe(1)-N(1)	179.999(1)	N(5)-Fe(2)-N(8)#2	91.03(3)
N(1)#1-Fe(1)-N(4)	89.79(3)	N(8)-Fe(2)-N(8)#2	179.999(1)
N(1)-Fe(1)-N(4)	90.21(3)	N(5)#2-Fe(2)-N(7)	90.03(3)
N(1)#1-Fe(1)-N(4)#1	90.21(3)	N(5)-Fe(2)-N(7)	89.97(3)
N(1)-Fe(1)-N(4)#1	89.79(3)	N(8)-Fe(2)-N(7)	89.64(3)
N(4)-Fe(1)-N(4)#1	180.00(4)	N(8)#2-Fe(2)-N(7)	90.36(3)
N(1)#1-Fe(1)-N(3)#1	88.97(3)	N(5)#2-Fe(2)-N(7)#2	89.97(3)
N(1)-Fe(1)-N(3)#1	91.03(3)	N(5)-Fe(2)-N(7)#2	90.03(3)
N(4)-Fe(1)-N(3)#1	91.25(3)	N(8)-Fe(2)-N(7)#2	90.36(3)
N(4)#1-Fe(1)-N(3)#1	88.75(3)	N(8)#2-Fe(2)-N(7)#2	89.64(3)
N(1)#1-Fe(1)-N(3)	91.03(3)	N(7)-Fe(2)-N(7)#2	179.999(1)
N(1)-Fe(1)-N(3)	88.97(3)	C(3)-N(1)-C(1)	106.57(8)
N(4)-Fe(1)-N(3)	88.75(3)	C(3)-N(1)-Fe(1)	125.35(7)
N(4)#1-Fe(1)-N(3)	91.25(3)	C(1)-N(1)-Fe(1)	127.98(6)
N(3)#1-Fe(1)-N(3)	180.00(5)	C(3)-N(2)-C(2)	108.03(8)
N(5)#2-Fe(2)-N(5)	179.999(1)	C(4)-N(3)-C(7)	105.21(7)
N(5)#2-Fe(2)-N(8)	91.03(3)	C(4)-N(3)-Fe(1)	126.20(6)
N(5)-Fe(2)-N(8)	88.97(3)	C(7)-N(3)-Fe(1)	128.51(5)
N(5)#2-Fe(2)-N(8)#2	88.97(3)	C(18)-N(4)-C(15)	105.75(7)

Table B30. (continued)

Angles			
C(18)-N(4)-Fe(1)	126.05(6)	C(5)-C(6)-C(7)	106.30(8)
C(15)-N(4)-Fe(1)	128.20(5)	N(3)-C(7)-C(8)	125.57(7)
C(26)-N(5)-C(28)	106.25(8)	N(3)-C(7)-C(6)	110.81(7)
C(26)-N(5)-Fe(2)	126.75(6)	C(8)-C(7)-C(6)	123.60(8)
C(28)-N(5)-Fe(2)	126.96(7)	C(7)-C(8)-C(15)	122.61(8)
C(26)-N(6)-C(27)	108.15(9)	C(7)-C(8)-C(9)	119.20(7)
C(32)-N(7)-C(29)	105.37(7)	C(15)-C(8)-C(9)	118.17(7)
C(32)-N(7)-Fe(2)	127.68(6)	C(14)-C(9)-C(10)	118.75(9)
C(29)-N(7)-Fe(2)	126.95(6)	C(14)-C(9)-C(8)	120.61(9)
C(40)-N(8)-C(43)	105.69(7)	C(10)-C(9)-C(8)	120.59(10)
C(40)-N(8)-Fe(2)	127.56(6)	C(9)-C(10)-C(11)	120.30(13)
C(43)-N(8)-Fe(2)	126.58(5)	C(12)-C(11)-C(10)	120.53(12)
C(2)-C(1)-N(1)	108.54(8)	C(11)-C(12)-C(13)	119.60(10)
C(1)-C(2)-N(2)	106.33(9)	C(12)-C(13)-C(14)	120.04(14)
N(1)-C(3)-N(2)	110.53(8)	C(13)-C(14)-C(9)	120.77(12)
N(3)-C(4)-C(19)#1	126.09(7)	N(4)-C(15)-C(8)	126.33(7)
N(3)-C(4)-C(5)	110.51(7)	N(4)-C(15)-C(16)	110.34(7)
C(19)#1-C(4)-C(5)	123.40(7)	C(8)-C(15)-C(16)	123.33(8)
C(6)-C(5)-C(4)	107.15(7)	C(17)-C(16)-C(15)	106.57(7)

Table B30. (continued)

Angles			
C(16)-C(17)-C(18)	107.24(7)	N(7)-C(29)-C(30)	110.65(7)
N(4)-C(18)-C(19)	126.58(7)	C(44)#2-C(29)-C(30)	123.27(7)
N(4)-C(18)-C(17)	110.07(7)	C(31)-C(30)-C(29)	106.73(7)
C(19)-C(18)-C(17)	123.36(7)	C(30)-C(31)-C(32)	106.83(7)
C(4)#1-C(19)-C(18)	123.70(7)	N(7)-C(32)-C(33)	125.78(8)
C(4)#1-C(19)-C(20)	118.12(7)	N(7)-C(32)-C(31)	110.41(7)
C(18)-C(19)-C(20)	118.07(7)	C(33)-C(32)-C(31)	123.79(8)
C(21)-C(20)-C(25)	119.52(8)	C(32)-C(33)-C(40)	123.03(8)
C(21)-C(20)-C(19)	118.50(8)	C(32)-C(33)-C(34)	118.64(8)
C(25)-C(20)-C(19)	121.96(8)	C(40)-C(33)-C(34)	118.32(8)
C(22)-C(21)-C(20)	120.46(10)	C(35)-C(34)-C(39)	118.63(11)
C(21)-C(22)-C(23)	119.93(11)	C(35)-C(34)-C(33)	121.49(12)
C(24)-C(23)-C(22)	119.93(9)	C(39)-C(34)-C(33)	119.88(10)
C(23)-C(24)-C(25)	120.24(10)	C(34)-C(35)-C(36)	120.41(16)
C(24)-C(25)-C(20)	119.92(10)	C(37)-C(36)-C(35)	120.27(16)
N(5)-C(26)-N(6)	110.47(9)	C(38)-C(37)-C(36)	119.71(12)
C(28)-C(27)-N(6)	106.29(9)	C(37)-C(38)-C(39)	120.01(17)
C(27)-C(28)-N(5)	108.84(10)	C(38)-C(39)-C(34)	120.96(14)
N(7)-C(29)-C(44)#2	126.08(7)	N(8)-C(40)-C(33)	126.25(8)

Table B30. (continued)

Angles			
N(8)-C(40)-C(41)	110.16(7)	C(46)-C(45)-C(44)	120.74(8)
C(33)-C(40)-C(41)	123.53(8)	C(50)-C(45)-C(44)	120.03(9)
C(42)-C(41)-C(40)	106.96(8)	C(45)-C(46)-C(47)	120.45(10)
C(41)-C(42)-C(43)	106.80(7)	C(46)-C(47)-C(48)	120.09(12)
N(8)-C(43)-C(44)	126.73(7)	C(49)-C(48)-C(47)	119.60(10)
N(8)-C(43)-C(42)	110.40(7)	C(48)-C(49)-C(50)	120.41(11)
C(44)-C(43)-C(42)	122.84(7)	C(45)-C(50)-C(49)	120.29(11)
C(29)#2-C(44)-C(43)	123.22(7)	Cl(3)-C(52)-Cl(4)	113.48(14)
C(29)#2-C(44)-C(45)	119.49(7)	Cl(3)-C(52)-Cl(2)	107.97(13)
C(43)-C(44)-C(45)	117.28(7)	Cl(4)-C(52)-Cl(2)	106.16(14)
C(46)-C(45)-C(50)	119.13(9)		

Symmetry transformations used to generate equivalent atoms:

#1 -x+2,-y,-z+2 #2 -x+1,-y+1,-z+1

Table B31. Bond lengths (Å) in **13**•H_2O•$CHCl_3$ at 20(2) K

Lengths			
Fe(1)-N(1)#1	1.9598(8)	N(4)-C(15)	1.3801(11)
Fe(1)-N(1)	1.9598(8)	N(5)-C(26)	1.3278(13)
Fe(1)-N(4)	1.9838(7)	N(5)-C(28)	1.3784(12)
Fe(1)-N(4)#1	1.9838(7)	N(6)-C(26)	1.3378(13)
Fe(1)-N(3)#1	2.0014(7)	N(6)-C(27)	1.3662(16)
Fe(1)-N(3)	2.0014(7)	N(7)-C(32)	1.3752(11)
Fe(2)-N(5)#2	1.9749(8)	N(7)-C(29)	1.3762(11)
Fe(2)-N(5)	1.9750(8)	N(8)-C(40)	1.3760(11)
Fe(2)-N(8)	1.9898(7)	N(8)-C(43)	1.3768(10)
Fe(2)-N(8)#2	1.9898(7)	C(1)-C(2)	1.3667(13)
Fe(2)-N(7)	2.0022(7)	C(4)-C(19)#1	1.3917(11)
Fe(2)-N(7)#2	2.0022(7)	C(4)-C(5)	1.4404(12)
N(1)-C(3)	1.3315(11)	C(5)-C(6)	1.3534(12)
N(1)-C(1)	1.3785(13)	C(6)-C(7)	1.4377(12)
N(2)-C(3)	1.3353(13)	C(7)-C(8)	1.3874(11)
N(2)-C(2)	1.3747(14)	C(8)-C(15)	1.3924(11)
N(3)-C(4)	1.3671(10)	C(8)-C(9)	1.4925(12)
N(3)-C(7)	1.3787(11)	C(9)-C(14)	1.3956(18)
N(4)-C(18)	1.3711(10)	C(9)-C(10)	1.3964(15)

Table B31. (continued)

Lengths			
C(10)-C(11)	1.3996(16)	C(30)-C(31)	1.3556(12)
C(11)-C(12)	1.382(3)	C(31)-C(32)	1.4440(12)
C(12)-C(13)	1.393(2)	C(32)-C(33)	1.3945(12)
C(13)-C(14)	1.3949(14)	C(33)-C(40)	1.3962(12)
C(15)-C(16)	1.4321(11)	C(33)-C(34)	1.4898(12)
C(16)-C(17)	1.3595(12)	C(34)-C(35)	1.3921(17)
C(17)-C(18)	1.4351(11)	C(34)-C(39)	1.3935(19)
C(18)-C(19)	1.3950(11)	C(35)-C(36)	1.3958(19)
C(19)-C(4)#1	1.3916(11)	C(36)-C(37)	1.386(3)
C(19)-C(20)	1.4868(11)	C(37)-C(38)	1.385(3)
C(20)-C(21)	1.3939(14)	C(38)-C(39)	1.3895(15)
C(20)-C(25)	1.3969(13)	C(40)-C(41)	1.4405(12)
C(21)-C(22)	1.3867(14)	C(41)-C(42)	1.3585(12)
C(22)-C(23)	1.3910(18)	C(42)-C(43)	1.4371(11)
C(23)-C(24)	1.3913(19)	C(43)-C(44)	1.3947(11)
C(24)-C(25)	1.3900(14)	C(44)-C(29)#2	1.3880(11)
C(27)-C(28)	1.3614(15)	C(44)-C(45)	1.4933(11)
C(29)-C(44)#2	1.3880(11)	C(45)-C(46)	1.3938(14)
C(29)-C(30)	1.4398(11)	C(45)-C(50)	1.3939(13)

Table B31. (continued)

Lengths			
C(46)-C(47)	1.3954(14)	C(52)-Cl(3)	1.731(2)
C(47)-C(48)	1.394(2)	C(52)-Cl(4)	1.7334(15)
C(48)-C(49)	1.384(2)	C(52)-Cl(2)	1.885(3)
C(49)-C(50)	1.3973(15)	Fe(2A)-Fe(2A)#2	1.27(3)

Symmetry transformations used to generate equivalent atoms:

#1 -x+2,-y,-z+2 #2 -x+1,-y+1,-z+1

Table B32. Anisotropic displacement parameters ($Å^2$ x 10^3) in **13**•H_2O•$CHCl_3$ at 20(2) K. The anisotropic displacement factor exponent takes the form: $-2\pi^2$ [$H(2a^{*2}U^{11}$ + ... + 2 hka*b*U^{12}]

	U^{11}	U^{22}	U^{33}	U^{23}	U^{13}	U^{12}
Fe(1)	7(1)	4(1)	3(1)	0(1)	-1(1)	2(1)
Fe(2)	4(1)	8(1)	4(1)	-2(1)	-1(1)	0(1)
N(1)	9(1)	8(1)	5(1)	-2(1)	-1(1)	2(1)
N(2)	10(1)	12(1)	7(1)	-4(1)	0(1)	2(1)
N(3)	10(1)	5(1)	4(1)	-1(1)	-3(1)	2(1)
N(4)	9(1)	5(1)	4(1)	-1(1)	-3(1)	2(1)
N(5)	8(1)	10(1)	7(1)	-4(1)	-2(1)	1(1)
N(6)	14(1)	12(1)	13(1)	-6(1)	-5(1)	4(1)
N(7)	6(1)	9(1)	5(1)	-2(1)	-1(1)	-1(1)
N(8)	6(1)	10(1)	5(1)	-2(1)	-1(1)	-1(1)
C(1)	10(1)	18(1)	7(1)	-4(1)	-3(1)	2(1)
C(2)	10(1)	20(1)	9(1)	-4(1)	-1(1)	2(1)
C(3)	10(1)	10(1)	6(1)	-3(1)	0(1)	1(1)
C(4)	11(1)	5(1)	5(1)	0(1)	-3(1)	2(1)
C(5)	18(1)	6(1)	8(1)	-2(1)	-6(1)	3(1)

Table B32. (continued)

	U^{11}	U^{22}	U^{33}	U^{23}	U^{13}	U^{12}
C(6)	20(1)	7(1)	8(1)	-3(1)	-8(1)	4(1)
C(7)	15(1)	6(1)	5(1)	-2(1)	-4(1)	3(1)
C(8)	16(1)	6(1)	5(1)	-2(1)	-5(1)	4(1)
C(9)	23(1)	8(1)	6(1)	-3(1)	-8(1)	6(1)
C(10)	31(1)	12(1)	8(1)	-5(1)	-8(1)	10(1)
C(11)	46(1)	12(1)	9(1)	-6(1)	-13(1)	10(1)
C(12)	51(1)	11(1)	13(1)	-5(1)	-20(1)	7(1)
C(13)	39(1)	13(1)	17(1)	-6(1)	-21(1)	5(1)
C(14)	26(1)	13(1)	13(1)	-6(1)	-13(1)	5(1)
C(15)	11(1)	6(1)	4(1)	-1(1)	-3(1)	2(1)
C(16)	13(1)	7(1)	6(1)	-1(1)	-5(1)	2(1)
C(17)	12(1)	6(1)	7(1)	1(1)	-5(1)	1(1)
C(18)	8(1)	5(1)	5(1)	0(1)	-3(1)	0(1)
C(19)	10(1)	4(1)	6(1)	0(1)	-3(1)	1(1)
C(20)	11(1)	5(1)	8(1)	0(1)	-5(1)	1(1)
C(21)	18(1)	9(1)	11(1)	-1(1)	-3(1)	5(1)
C(22)	24(1)	11(1)	15(1)	-4(1)	-8(1)	10(1)
C(23)	25(1)	6(1)	16(1)	-3(1)	-14(1)	5(1)

Table B32. (continued)

	U^{11}	U^{22}	U^{33}	U^{23}	U^{13}	U^{12}
C(24)	20(1)	6(1)	16(1)	3(1)	-9(1)	-2(1)
C(25)	14(1)	7(1)	13(1)	3(1)	-4(1)	-1(1)
C(26)	12(1)	10(1)	11(1)	-3(1)	-2(1)	3(1)
C(27)	16(1)	16(1)	14(1)	-9(1)	0(1)	4(1)
C(28)	15(1)	14(1)	14(1)	-7(1)	5(1)	0(1)
C(29)	6(1)	7(1)	6(1)	-1(1)	-2(1)	0(1)
C(30)	7(1)	9(1)	7(1)	0(1)	-2(1)	-2(1)
C(31)	7(1)	12(1)	6(1)	0(1)	-2(1)	-2(1)
C(32)	7(1)	12(1)	5(1)	-2(1)	-1(1)	-2(1)
C(33)	7(1)	16(1)	4(1)	-2(1)	-1(1)	-4(1)
C(34)	11(1)	26(1)	4(1)	-1(1)	-2(1)	-8(1)
C(35)	16(1)	39(1)	7(1)	-8(1)	1(1)	-9(1)
C(36)	24(1)	56(1)	6(1)	-8(1)	1(1)	-15(1)
C(37)	27(1)	56(1)	6(1)	2(1)	-5(1)	-21(1)
C(38)	21(1)	42(1)	10(1)	9(1)	-9(1)	-16(1)
C(39)	13(1)	29(1)	8(1)	4(1)	-6(1)	-9(1)
C(40)	7(1)	14(1)	4(1)	-2(1)	-2(1)	-3(1)
C(41)	10(1)	16(1)	5(1)	-2(1)	-2(1)	-4(1)

Table B32. (continued)

	U^{11}	U^{22}	U^{33}	U^{23}	U^{13}	U^{12}
C(42)	8(1)	12(1)	7(1)	-2(1)	-3(1)	-2(1)
C(43)	6(1)	8(1)	6(1)	-2(1)	-2(1)	-1(1)
C(44)	6(1)	7(1)	7(1)	-1(1)	-3(1)	-1(1)
C(45)	9(1)	7(1)	9(1)	0(1)	-5(1)	-2(1)
C(46)	8(1)	11(1)	13(1)	2(1)	-5(1)	-1(1)
C(47)	10(1)	22(1)	13(1)	5(1)	-6(1)	-6(1)
C(48)	20(1)	23(1)	10(1)	4(1)	-8(1)	-14(1)
C(49)	27(1)	13(1)	10(1)	0(1)	-8(1)	-10(1)
C(50)	18(1)	8(1)	11(1)	-2(1)	-7(1)	-2(1)
C(52)	43(1)	58(1)	13(1)	-18(1)	-11(1)	36(1)
Cl(1)	31(1)	23(1)	8(1)	-7(1)	-8(1)	13(1)
Cl(2)	16(1)	46(1)	16(1)	-14(1)	1(1)	2(1)
Cl(3)	60(1)	17(1)	9(1)	-5(1)	-4(1)	-10(1)
Cl(4)	17(1)	31(1)	34(1)	-27(1)	4(1)	-3(1)
O(1)	62(1)	19(1)	27(1)	-12(1)	-25(1)	17(1)
Cl(2A)	17(1)	97(3)	13(1)	-4(1)	0(1)	3(1)
Cl(1A)	42(1)	19(1)	6(1)	-4(1)	-4(1)	14(1)
Cl(3A)	30(1)	24(1)	9(1)	-2(1)	2(1)	-11(1)

Table B32. (continued)

	U^{11}	U^{22}	U^{33}	U^{23}	U^{13}	U^{12}
Fe(2A)	390(20)	558(15)	538(12)	-164(11)	-221(18)	190(20)

Table B33. Final coordinates and equivalent isotropic displacement parameters of the non-hydrogen atoms for the neutron structure of **13**•H_2O•$CHCl_3$. *U*(eq) is defined as one third of the trace of the orthogonalized U^{ij} tensor

	x	y	z	*U*(eq) (Å^2)
Fe(1)	0	0	0	0.0117
N(1)	0.11486	0.00368	0.06845	0.0057
N(2)	-0.11754	-0.10718	0.10209	0.0083
N(3)	-0.09168	0.12256	0.02998	0.0077
N(4)	-0.14381	0.28600	0.02943	0.0150
C(1)	0.22315	0.06760	0.04113	0.0073
C(2)	0.27481	0.05239	0.11215	0.0062
C(3)	0.19565	-0.02058	0.18054	0.0022
C(4)	0.09469	-0.05039	0.15341	0.0026
C(5)	-0.00910	-0.12115	0.20833	0.0060
C(6)	-0.01477	-0.17032	0.29960	0.0098
C(7)	0.07885	-0.24061	0.32262	0.0080
C(8)	0.07607	-0.28749	0.40680	0.0115
C(9)	-0.01995	-0.26518	0.46972	0.0153
C(10)	-0.11395	-0.19425	0.44868	0.0144
C(11)	-0.11136	-0.14704	0.36235	0.0104
C(12)	-0.11014	-0.15047	0.18345	0.0071

Table B33. (continued)

	x	y	z	U(eq) (Å^2)
C(13)	-0.21220	-0.22691	0.23808	0.0030
C(14)	-0.28852	-0.23193	0.18926	0.0062
C(15)	-0.22815	-0.15739	0.10536	0.0032
C(16)	-0.19434	0.11292	0.10002	0.0152
C(17)	-0.22808	0.21726	0.09959	0.0114
C(18)	-0.06245	0.22775	-0.01297	0.0071
C(19)	0.27952	0.13988	-0.03935	0.0030
C(20)	0.39932	0.20201	-0.05303	0.0059
C(21)	0.39070	0.30812	-0.05151	0.0097
C(22)	0.50036	0.36755	-0.05766	0.0105
C(23)	0.61890	0.31724	-0.06689	0.0155
C(24)	0.62627	0.20992	-0.06999	0.0161
C(25)	0.51653	0.15227	-0.06317	0.0024
Fe(2)	1/2	1/2	1/2	0.0032
N(5)	0.48032	0.36026	0.48021	0.0057
N(6)	0.44453	0.57991	0.39892	0.0079
N(7)	0.67751	0.51414	0.42928	0.0121
N(8)	0.84332	0.50923	0.32437	0.0082
C(26)	0.50552	0.25881	0.52580	0.0041

Table B33. (continued)

	x	y	z	*U*(eq) (Å^2)
C(27)	0.48331	0.17610	0.49221	0.0025
C(28)	0.44216	0.23315	0.42336	0.0132
C(29)	0.43989	0.34669	0.41617	0.0098
C(30)	0.41163	0.42838	0.35149	0.0132
C(31)	0.37940	0.39948	0.28295	0.0129
C(32)	0.47480	0.37003	0.22352	0.0081
C(33)	0.44288	0.35114	0.15698	0.0165
C(34)	0.31950	0.35915	0.15166	0.0160
C(35)	0.22480	0.38647	0.21263	0.0144
C(36)	0.25472	0.40734	0.27813	0.0158
C(37)	0.41194	0.53734	0.34514	0.0112
C(38	0.38041	0.62454	0.27574	0.0105
C(39)	0.38975	0.71722	0.29357	0.0125
C(40)	0.43049	0.68928	0.36879	0.0062
C(41)	0.55174	0.23152	0.59648	0.0100
C(42)	0.58777	0.11869	0.63254	0.0052
C(43)	0.51259	0.04651	0.70719	0.0086
C(44)	0.55311	-0.06023	0.74109	0.0120
C(45)	0.67117	-0.09081	0.69918	0.0073

Table B33. (continued)

	x	y	z	*U*(eq) (Å^2)
C(46)	0.74546	-0.01770	0.62420	0.0111
C(47)	0.70659	0.08991	0.58898	0.0106
C(48)	0.71642	0.49975	0.35316	0.0063
C(49)	0.89173	0.53192	0.38338	0.0100
C(50)	0.78833	0.53304	0.44751	0.0088
C(51)	0.87958	0.21423	0.28140	0.0188
Cl(1)	0.73318	0.13625	0.31655	0.0372
Cl(2)	1.00248	0.15417	0.22618	0.0205
Cl(3)	0.91611	0.23240	0.36781	0.0251
Cl(4)	0.91263	0.48497	0.15047	0.0238
O(1)	0.16784	0.48797	0.00768	0.0262

Table B34. Hydrogen atom positions and isotropic displacement parameters for the neutron structure of **13**•H_2O•$CHCl_3$

	x	y	z	*U*(iso) (Å^2)
H(2)	0.35919	0.09611	0.10855	0.0309
H(3)	0.20044	-0.05090	0.24599	0.0336
H(4N)	-0.14754	0.37923	0.00909	0.0270
H(7)	0.15462	-0.26035	0.27374	0.0246
H(8)	0.14715	-0.33784	0.42570	0.0401
H(8N)	0.88864	0.50103	0.26763	0.0207
H(9)	-0.02191	-0.30013	0.53447	0.0329
H(10)	-0.19038	-0.17692	0.49567	0.0445
H(11)	-0.18409	-0.09036	0.34509	0.0286
H(13)	-0.22316	-0.27039	0.30321	0.0221
H(14)	-0.37085	-0.28066	0.20829	0.0295
H(16)	-0.23556	0.03841	0.14296	0.0294
H(17)	-0.29505	0.24457	0.14208	0.0241
H(18)	0.00819	0.26507	-0.06764	0.0298
H(21)	0.30150	0.34470	-0.04405	0.0284
H(22)	0.49733	0.44332	-0.05490	0.0276
H(23)	0.69818	0.36172	-0.07090	0.0297

Table B34. (continued)

	x	y	z	*U*(iso) (Å^2)
H(24)	0.71618	0.17185	-0.07568	0.0351
H(25)	0.52284	0.07556	-0.06545	0.0364
H(27)	0.49824	0.09545	0.51724	0.0244
H(28)	0.41783	0.20226	0.38102	0.0247
H(32)	0.57019	0.36500	0.22554	0.0324
H(34)	0.30014	0.34572	0.09979	0.0296
H(35)	0.17775	0.42953	0.32746	0.0415
H(38)	0.35599	0.61721	0.22748	0.0216
H(39)	0.37504	0.80009	0.25604	0.0180
H(43)	0.42453	0.06799	0.73942	0.0300
H(44)	0.49526	-0.11886	0.79705	0.0382
H(45)	0.70206	-0.17056	0.72537	0.0240
H(46)	0.83734	-0.04084	0.59468	0.0479
H(47)	0.75809	0.14233	0.53419	0.0399
H(48)	0.65966	0.48273	0.32303	0.0257
H(49)	0.98757	0.54488	0.37319	0.0269
H(50)	0.78400	0.55056	0.50364	0.0203
H(51)	0.86866	0.29550	0.23681	0.0578
H(52)	0.14814	0.48281	-0.03643	0.0263

Table B34. (continued)

	x	y	z	*U*(iso) (Å^2)
H(53)	0.08858	0.46540	0.05665	0.0510

The Temperature Factor has the Form of Exp(-T) Where T =

8*(π**2)**U**(Sin(θ)/λ)**2 for Isotropic Atoms

Table B35. Bond angles (°) in the neutron structure of **13**•H_2O•$CHCl_3$

Angles			
N(1)-Fe(1)-N(1)	89.43	N(5)-Fe(2)-N(7B)	91.64
N(1)-Fe(1)-N(3)	89.43	N(6)-Fe(2)-N(7)	90.50
N(1)-Fe(1)-N(1A)	180.00	H(52)-O(1)-H(53)	106.00
N(1)-Fe(1)-N(1)A)	90.57	Fe(1)-N(1)-C(1)	126.14
N(1)-Fe(1)-N(3A)	90.57	Fe(1)-N(1)-C(4)	127.06
N(1)-Fe(1)-N(3)	90.50	C(1)-N(1)-C(4)	106.59
N(1A)-Fe(1)-N(1)	90.57	Fe(1)-N(1)-C(12)	130.11
N(1)-Fe(1)-N(1A)	180.00	Fe(1)-N(1)-C(15)	126.15
N(1)-Fe(1)-N(3A)	89.50	C(12)-N(1)-C(15)	103.73
N(1A)-Fe(1)-N(3)	90.57	C(16)-N(3)-C(18)	108.40
N(1A)-Fe(1)-N(3)	89.50	Fe(1)-N(3)-C(18)	125.75
N(3)-Fe(1)-N(3A)	180.00	Fe(1)-N(3)-C(16)	125.83
N(1A)-Fe(1)-N(1A)	89.43	C(17)-N(4)-C(18)	110.03
N(1A)-Fe(1)-N(3A)	89.43	C(18)-N(4)-H(4N)	127.00
N(1A)-Fe(1)-N(3A)	90.50	C(17)-N(4)-H(4N)	123.00
N(6)-Fe(2)-N(6B)	180.00	Fe(2)-N(5)-C(29)	127.29
N(6)-Fe(2)-N(7B)	89.50	C(26)-N(5)-C(29)	105.50
N(5B)-Fe(2)-N(7)	91.64	Fe(2)-N(5)-C(26)	127.21
N(6B)-Fe(2)-N(7)	89.50	Fe(2)-N(6)-C(40)	126.36

Table B35. (continued)

Angles			
N(7)-Fe(2)-N(7B)	180.00	Fe(2)-N(6)-C(37)	127.73
N(5B)-Fe(2)-N(6B)	89.36	C(37)-N(6)-C(40)	105.91
N(5B)-Fe(2)-N(7B)	88.36	Fe(2)-N(7)-C(50)	128.63
N(6B)-Fe(2)-N(7B)	90.50	Fe(2)-N(7)-C(48)	124.91
N(5B)-Fe(2)-N(6)	90.64	C(48)-N(7)-C(50)	106.33
N(5)-Fe(2)-N(6)	89.36	C(48)-N(8)-C(49)	109.15
N(5)-Fe(2)-N(7)	88.36	C(49)-N(8)-H(8N)	131.00
N(5)-Fe(2)-N(5B)	180.00	C(48)-N(8)-H(8N)	120.00
N(5)-Fe(2)-N(6B)	90.64	N(1)-C(1)-C(2)	109.47
C(2)-C(1)-C(19)	122.64	N(3)-C(18)-N(4)	108.18
N(1)-C(1)-C(19)	127.86	C(1)-C(19)-C(20)	117.37
C(1)-C(2)-C(3)	106.99	C(15A) -C(19)-C(20)	119.97
C(2)-C(3)-C(4)	106.69	C(1)-C(19)-C(15A)	122.65
N(1)-C(4)-C(5)	126.44	C(19)-C(20)-C(21)	118.48
C(3)-C(4)-C(5)	123.27	C(21)-C(20)-C(25)	120.95
N(1)-C(4)-C(3)	110.25	C(19)-C(20)-C(25)	120.51
C(4)-C(5)-C(12)	124.31	C(20)-C(21)-C(22)	120.56
C(4)-C(5)-C(6)	118.23	C(21)-C(22)-C(23)	118.76
C(6)-C(5)-C(12)	117.46	C(22)-C(23)-C(24)	119.85

Table B35. (continued)

Angles			
C(7)-C(6)-C(11)	119.14	C(23)-C(24)-C(25)	120.50
C(5)-C(6)-C(11)	121.20	C(20)-C(25)-C(24)	119.36
C(5)-C(6)-C(7)	119.66	C(1)-C(2)-H(2)	125.00
C(6)-C(7)-C(8)	120.96	C(3)-C(2)-H(2)	128.00
C(7)-C(8)-C(9)	120.32	C(4)-C(3)-H(3)	125.00
C(8)-C(9)-C(10	120.09	C(2)-C(3)-H(3)	129.00
C(9)-C(10)-C(11)	119.41	C(6)-C(7)-H(7)	120.00
C(6)-C(11)-C(10)	120.06	C(8)-C(7)-H(7)	119.00
C(5)-C(12)-C(13)	124.50	C(7)-C(8)-H(8)	123.00
N(1)-C(12)-C(5)	122.55	C(9)-C(8)-H(8)	117.00
N(1)-C(12)-C(13)	112.95	C(10)-C(9)-H(9)	119.00
C(12)-C(13)-C(14)	106.06	C(8)-C(9)-H(9)	121.00
C(13)-C(14)-C(15)	105.99	C(9)-C(10)-H(10)	122.00
C(14)-C(15)-C(19A)	122.19	C(11)-C(10)-H(10)	119.00
N(1)-C(15)-C(14)	111.26	C(10)-C(11)-H(11)	120.00
N(1)-C(15)-C(19A)	126.53	C(6)-C(11)-H(11)	120.00
N(3)-C(16)-C(17)	108.12	C(12)-C(13)-H(13)	125.00
N(4)-C(17)-C(16)	105.26	C(14)-C(13)-H(13)	129.00

Table B35. (continued)

Angles			
C(13)-C(14)-H(14)	127.00	C(31)-C(30)-C(37)	117.88
C(15)-C(14)-H(14)	127.00	C(32)-C(31)-C(36)	120.59
C(17)-C(16)-H(16)	129.00	C(30)-C(31)-C(32)	119.88
N(3)-C(16)-H(16)	123.00	C(30)-C(31)-C(36)	119.47
C(16)-C(17)-H(17)	132.00	C(31)-C(32)-C(33)	118.29
N(4)-C(17)-H(17)	123.00	C(32)-C(33)-C(34)	121.41
N(3)-C(18)-H(18)	130.00	C(33)-C(34)-C(35)	119.51
N(4)-C(18)-H(18)	122.00	C(34)-C(35)-C(36)	120.02
C(20)-C(21)-H(21)	120.00	C(31)-C(36)-C(35)	120.17
C(22)-C(21)-H(21)	119.00	N(6)-C(37)-C(38)	110.91
C(23)-C(22)-H(22)	118.00	N(6)-C(37)-C(30)	126.28
C(21)-C(22)-H(22)	123.00	C(30)-C(37)-C(38)	122.78
C(24)-C(23)-H(23)	122.00	C(37)-C(38)-C(39)	104.24
C(22)-C(23)-H(23)	118.00	C(38)-C(39)-C(40)	108.62
C(25)-C(24)-H(24)	120.00	N(6)-C(40)-C(41B)	127.74
C(23)-C(24)-H(24)	119.00	C(39)-C(40)-C(41B)	122.00
C(24)-C(25)-H(25)	120.00	N(6)-C(40)-C(39)	110.25
C(20)-C(25)-H(25)	121.00	C(40B) -C(41)-C(42)	119.39

Table B35. (continued)

Angles			
N(5)-C(26)-C(41)	126.47	C(26)-C(41)-C(42)	119.13
C(27)-C(26)-C(41)	121.09	C(41)-C(42)-C(47)	116.59
C(26)-C(27)-C(28)	104.35	C(43)-C(42)-C(47)	121.31
C(27)-C(28)-C(29)	108.12	C(41)-C(42)-C(43)	122.02
N(5)-C(29)-C(30)	126.08	C(42)-C(43)-C(44)	120.12
C(28)-C(29)-C(30)	124.12	C(43)-C(44)-C(45)	119.71
N(5)-C(29)-C(28)	109.61	C(44)-C(45)-C(46)	119.55
C(29)-C(30)-C(37)	123.15	C(45)-C(46)-C(47)	121.66
C(29)-C(30)-C(31)	118.97	C(42)-C(47)-C(46)	117.62
N(7)-C(48)-N(8)	109.49	C(42)-C(43)-H(43)	121.00
N(8)-C(49)-C(50)	105.23	C(43)-C(44)-H(44)	122.00
N(7)-C(50)-C(49)	109.78	C(45)-C(44)-H(44)	118.00
C(26)-C(27)-H(27)	124.00	C(46)-C(45)-H(45)	121.00
C(28)-C(27)-H(27)	132.00	C(44)-C(45)-H(45)	120.00
C(29)-C(28)-H(28)	124.00	C(45)-C(46)-H(46)	119.00
C(27)-C(28)-H(28)	128.00	C(47)-C(46)-H(46)	120.00
C(31)-C(32)-H(32)	122.00	C(46)-C(47)-H(47)	122.00
C(33)-C(32)-H(32)	120.00	C(42)-C(47)-H(47)	120.00

Table B35. (continued)

Angles			
C(34)-C(33)-H(33)	119.00	N(7)-C(48)-H(48)	126.00
C(32)-C(33)-H(33)	120.00	N(8)-C(48)-H(48)	125.00
C(33)-C(34)-H(34)	119.00	C(50)-C(49)-H(49)	132.00
C(35)-C(34)-H(34)	122.00	N(8)-C(49)-H(49)	123.00
C(36)-C(35)-H(35)	122.00	N(7)-C(50)-H(50)	122.00
C(34)-C(35)-H(35)	118.00	C(49)-C(50)-H(50	129.00
C(35)-C(36)-H(36)	120.00	Cl1)-C(51)-Cl(3)	110.60
C(31)-C(36)-H(36)	120.00	Cl(2)-C(51)-Cl(3)	111.14
C(37)-C(38)-H(38)	128.00	Cl(1)-C(51)-Cl(2)	110.98
C(39)-C(38)-H(38)	128.00	Cl(2)-C(51)-H(51)	107.00
C(38)-C(39)-H(39)	127.00	Cl(3)-C(51)-H(51)	109.00

Table B36. Bond lengths (Å) in the neutron structure of **13**•H_2O•$CHCl_3$

Lengths			
Fe(1)-N(1)	1.9984	N(6)-C(37)	1.3821
Fe(1)-N(2)	1.9944	N(6)-C(40)	1.3632
Fe(1)-N(3)	1.9866	N(7)-C(50)	1.4018
Fe(1)-N(1A)	1.9984	N(7) -C(48)	1.3556
Fe(1)-N(1A)	1.9944	N(8)-C(48)	1.3338
Fe(1)-N(3A)	1.9866	N(8)-C(49)	1.4145
Fe(2)-N(7)	1.9609	N(8)-H(8N)	1.0200
Fe(2)-N(5B)	2.0032	C(1)-C(19)	1.3862
Fe(2)-N(6B)	1.9867	C(1)-C(2)	1.4714
Fe(2)-N(7B)	1.9609	C(2)-C(3)	1.3446
Fe(2)-N(5)	2.0032	C(3)-C(4)	1.4477
Fe(2)-N(6)	1.9867	C(4)-C(5)	1.3951
Cl(1)-C(51)	1.7802	C(5)-C(12)	1.4206
Cl(2)-C(51)	1.7373	C(5)-C(6)	1.4985
Cl(3)-C(51)	1.7737	C(6)-C(11)	1.3939
O(1)-H(53)	1.0000	C(6)-C(7)	1.4015
O(1)-H(52)	0.8900	C(7)-C(8)	1.3907
N(1)-C(4)	1.3754	C(8)-C(9)	1.3870

Table B36. (continued)

Lengths			
N(1)-C(1)	1.3567	C(9)-C(10)	1.3997
N(2)-C(12)	1.3764	C(10-C(11)	1.4261
N(2)-C(15)	1.3889	C(12)-C(13)	1.4185
N(3)-C(16)	1.3784	C(13)-C(14)	1.3845
N(3)-C(18)	1.3275	C(14)-C(15)	1.4446
N(4)-C(17)	1.3609	C(15)-C(19A)	1.3843
N(4)-C(18)	1.3623	C(16)-C(17)	1.3916
N(4)-H(4N)	1.1500	C(19)-C(40)	1.4980
N(5)-C(49)	1.3924	C(20)-C(25)	1.4043
N(5)-C(26)	1.3604	C(20)-C(21)	1.3927
C(21)-C(22)	1.4255	C(31)-C(36)	1.3953
C(22)-C(23)	1.4201	C(31)-C(32)	1.3879
C(23)-C(24)	1.4180	C(32)-C(33)	1.4153
C(24)-C(25)	1.4091	C(33)-C(34)	1.3839
C(2)-H(2)	1.0900	C(34)-C(35)	1.3876
C(3)-H(3)	1.1000	C(35)-C(36)	1.3991
C(7)-H(7)	1.1000	C(37)-C(38)	1.4759
C(8)-H(8)	1.0500	C(38)-C(39)	1.3646
C(9)-H(9)	1.0700	C(39)-C(40)	1.4470

Table B36. (continued)

Lengths			
C(10)-H(10)	1.0700	C(40)-C(41B)	1.4143
C(11)-H(11)	1.1000	C(41)-C(42)	1.4788
C(13)-H(13)	1.0700	C(42)-C(47)	1.4108
C(14)-H(14)	1.0400	C(42)-C(43)	1.3791
C(16)-H(16)	1.0300	C(43)-C(44)	1.4241
C(17)-H(17)	1.0300	C(44)-C(45)	1.4038
C(18)-H(18)	1.0200	C(45)-C(46)	1.3837
C(21)-H(21)	1.0600	C(46)-C(47)	1.4308
C(22)-H(22)	1.0100	C(49)-C(50)	1.3493
C(23)-H(23)	1.0400	C(27)-H(27)	1.0200
C(24)-H(24)	1.0800	C(28)-H(28)	1.0600
C(25)-H(25)	1.0100	C(32)-H(32)	1.0600
C(26)-C(27)	1.4560	C(33)-H(33)	1.1300
C(26)-C(41)	1.4101	C(34)-H(34)	1.0700
C(27)-C(28)	1.3811	C(35)-H(35)	1.1000
C(28)-C(29)	1.4443	C(36)-H(36)	1.1300
C(29)-C(30)	1.3728	C(38)-H(38)	1.0000
C(30)-C(31)	1.5158	C(39)-H(39)	1.0900

Table B36. (continued)

Lengths			
C(30)-C(37)	1.3891	C(43)-H(43)	1.0500
C(44)-H(44)	1.0600	C(48)-H(48)	1.0000
C(45)-H(45)	1.0700	C(49)-H(49)	1.0300
C(46)-H(46)	1.0700	C(50)-H(50)	1.0700
C(47)-H(47)	1.0000	C(51)-H(51)	1.1100

Table B37. (An)isotropic displacement parameters for the neutron structure of **13**•H_2O•$CHCl_3$

	U^{11}	U^{22}	U^{33}	U^{23}	U^{13}	U^{12}
Cl(1)	0.0170	0.0726	0.0225	-0.0198	-0.0010	-0.0039
Cl(2)	0.0203	0.0184	0.0319	-0.0229	-0.0034	-0.0028
C(3)	0.0523	0.0118	0.0107	-0.0060	-0.0049	-0.0059
H(51)	0.0677	0.0487	0.0417	0.0066	-0.0238	0.0305
H(52)	0.0286	0.0378	0.0114	-0.0158	0.0045	0.0007
H(53)	0.0496	0.0477	0.0637	-0.0205	-0.0254	-0.0039
Cl(4)	0.0415	0.0229	0.0154	-0.0133	-0.0153	0.0171

The temperature factor has the form of exp(-T) where $T = 8\pi^2 U(\text{Sin}\ \theta/\lambda)^2$ for isotropic atoms for isotropic atoms, and $T = 2\pi^2 \sum_{ij} [h(i)\ h(j)\ U(i,j)\ A^*(i)\ A^*(j)]$ for anisotropic atoms. $A^*(i)$ are reciprocal axial lengths, and $h(i)$ are the reflection indices.

Table B38. Atomic coordinates (x 10^4) and equivalent isotropic displacement parameters (Å^2 x 10^3) in **14-*d*$_{30}$**. *U*(eq) is defined as one third of the trace of the orthogonalized U^{ij} tensor

	x	y	z	*U*(eq)
N(1)	1296(2)	-108(1)	-1448(1)	44(1)
N(2)	2647(2)	1374(1)	773(1)	44(1)
C(1)	206(3)	-802(2)	-2443(1)	45(1)
C(2)	1426(3)	-396(2)	-3250(2)	55(1)
D(2)	1078	-713	-3998	66
C(3)	3183(3)	529(2)	-2744(2)	55(1)
D(3)	4245	961	-3084	66
C(4)	3120(3)	727(2)	-1600(1)	45(1)
C(5)	4544(3)	1666(2)	-793(1)	45(1)
C(6)	6360(3)	2526(2)	-1168(1)	46(1)
C(7)	7915(3)	2016(2)	-1599(2)	59(1)
D(7)	7864	1119	-1648	71
C(8)	9563(3)	2821(2)	-1962(2)	68(1)
D(8)	10594	2460	-2260	81
C(9)	9671(3)	4143(2)	-1881(2)	65(1)
D(9)	10773	4680	-2126	78
C(10)	8142(3)	4680(2)	-1435(2)	65(1)

Table B38. (continued)

	x	y	z	*U*(eq)
D(10)	8230	5581	-1368	78
C(11)	6488(3)	3879(2)	-1092(2)	56(1)
C(12)	4340(3)	1912(2)	308(1)	45(1)
C(13)	5959(3)	2810(2)	1139(2)	54(1)
D(13)	7272	3286	1035	65
C(14)	5212(3)	2824(2)	2081(2)	54(1)
D(14)	5901	3318	2753	64
C(15)	3124(3)	1924(2)	1858(1)	44(1)
C(16)	1804(3)	1681(2)	2638(1)	45(1)
C(17)	2589(3)	2381(2)	3786(1)	51(1)
C(18)	4457(3)	2210(2)	4429(2)	67(1)
D(18)	5241	1634	4153	81
C(19)	5169(4)	2888(3)	5481(2)	83(1)
D(19)	6446	2781	5900	99
C(20)	4006(5)	3717(3)	5910(2)	92(1)
D(20)	4487	4168	6618	110
C(21)	2148(5)	3877(2)	5295(2)	90(1)
D(21)	1345	4427	5591	108

Table B38. (continued)

	x	y	z	*U*(eq)
C(22)	1439(4)	3231(2)	4235(2)	71(1)
D(22)	181	3366	3818	85
D(11)	5390	4252	-835	85

Table B39. Bond angles (°) in **14-d_{30}**

Angles			
H(1)-N(1)-C(1)	125.4(14)	C(9)-C(8)-C(7)	120.09(19)
H(1)-N(1)-C(4)	125.0(14)	C(8)-C(9)-C(10)	119.98(18)
C(1)-N(1)-C(4)	109.46(14)	C(11)-C(10)-C(9)	119.92(19)
C(12)-N(2)-C(15)	106.37(13)	C(10)-C(11)-C(6)	120.68(18)
N(1)-C(1)-C(16)#1	126.48(15)	N(2)-C(12)-C(5)	126.83(14)
N(1)-C(1)-C(2)	107.07(14)	N(2)-C(12)-C(13)	109.58(14)
C(16)#1-C(1)-C(2)	126.33(15)	C(5)-C(12)-C(13)	123.59(15)
C(3)-C(2)-C(1)	108.33(15)	C(14)-C(13)-C(12)	107.30(15)
C(2)-C(3)-C(4)	108.11(16)	C(13)-C(14)-C(15)	107.11(15)
N(1)-C(4)-C(5)	126.08(15)	N(2)-C(15)-C(16)	125.88(14)
N(1)-C(4)-C(3)	107.02(14)	N(2)-C(15)-C(14)	109.62(14)
C(5)-C(4)-C(3)	126.72(15)	C(16)-C(15)-C(14)	124.49(15)
C(12)-C(5)-C(4)	125.50(15)	C(15)-C(16)-C(1)#1	125.36(15)
C(12)-C(5)-C(6)	117.78(14)	C(15)-C(16)-C(17)	118.39(14)
C(4)-C(5)-C(6)	116.61(15)	C(1)#1-C(16)-C(17)	116.23(15)
C(7)-C(6)-C(11)	118.38(16)	C(18)-C(17)-C(22)	118.05(17)
C(7)-C(6)-C(5)	121.56(16)	C(18)-C(17)-C(16)	121.75(17)
C(11)-C(6)-C(5)	120.05(15)	C(22)-C(17)-C(16)	120.20(17)
C(6)-C(7)-C(8)	120.93(18)	C(17)-C(18)-C(19)	120.6(2)

Table B39. (continued)

Angles			
C(20)-C(19)-C(18)	120.4(2)	C(20)-C(21)-C(22)	120.7(2)
C(21)-C(20)-C(19)	119.7(2)	C(21)-C(22)-C(17)	120.6(2)

Symmetry transformations used to generate equivalent atoms:

#1 -x,-y,-z

Table B40. Bond lengths (Å) in **14-d_{30}**

Lengths			
N(1)-H(1)	0.910(15)	C(8)-C(9)	1.367(3)
N(1)-C(1)	1.374(2)	C(9)-C(10)	1.382(3)
N(1)-C(4)	1.374(2)	C(10)-C(11)	1.378(3)
N(2)-C(12)	1.368(2)	C(12)-C(13)	1.453(2)
N(2)-C(15)	1.373(2)	C(13)-C(14)	1.336(2)
C(1)-C(16)#1	1.404(2)	C(14)-C(15)	1.451(2)
C(1)-C(2)	1.421(2)	C(15)-C(16)	1.400(2)
C(2)-C(3)	1.354(2)	C(16)-C(1)#1	1.404(2)
C(3)-C(4)	1.425(2)	C(16)-C(17)	1.496(2)
C(4)-C(5)	1.402(2)	C(17)-C(18)	1.383(3)
C(5)-C(12)	1.399(2)	C(17)-C(22)	1.390(3)
C(5)-C(6)	1.501(2)	C(18)-C(19)	1.383(3)
C(6)-C(7)	1.374(2)	C(19)-C(20)	1.370(4)
C(6)-C(11)	1.398(2)	C(20)-C(21)	1.358(4)
C(7)-C(8)	1.389(3)	C(21)-C(22)	1.380(3)

Symmetry transformations used to generate equivalent atoms:

#1 -x,-y,-z

Table B41. Anisotropic displacement parameters ($Å^2$ x 10^3) in **14-*d*$_{30}$**. The anisotropic displacement factor exponent takes the form: $-2\pi^2 [h^2a^{*2}U^{11} + ... + 2 hka^* b^*U^{12}]$

	U^{11}	U^{22}	U^{33}	U^{23}	U^{13}	U^{12}
N(1)	41(1)	41(1)	46(1)	0(1)	8(1)	2(1)
N(2)	42(1)	40(1)	46(1)	0(1)	6(1)	3(1)
C(1)	44(1)	41(1)	46(1)	-2(1)	7(1)	6(1)
C(2)	55(1)	57(1)	48(1)	-5(1)	13(1)	2(1)
C(3)	52(1)	54(1)	54(1)	-1(1)	16(1)	-1(1)
C(4)	41(1)	40(1)	51(1)	2(1)	10(1)	4(1)
C(5)	40(1)	40(1)	52(1)	3(1)	8(1)	4(1)
C(6)	41(1)	44(1)	47(1)	3(1)	5(1)	2(1)
C(7)	50(1)	47(1)	82(1)	11(1)	16(1)	12(1)
C(8)	45(1)	70(2)	90(2)	11(1)	20(1)	9(1)
C(9)	53(1)	62(1)	71(1)	12(1)	10(1)	-8(1)
C(10)	69(1)	44(1)	76(1)	8(1)	12(1)	-3(1)
C(11)	56(1)	45(1)	65(1)	2(1)	13(1)	8(1)
C(12)	40(1)	39(1)	51(1)	2(1)	6(1)	2(1)
C(13)	44(1)	54(1)	55(1)	0(1)	5(1)	-7(1)
C(14)	49(1)	52(1)	48(1)	-2(1)	1(1)	-5(1)

Table B41. (continued)

	U^{11}	U^{22}	U^{33}	U^{23}	U^{13}	U^{12}
C(15)	44(1)	37(1)	46(1)	0(1)	4(1)	4(1)
C(16)	45(1)	40(1)	46(1)	-1(1)	4(1)	6(1)
C(17)	53(1)	47(1)	46(1)	0(1)	6(1)	-4(1)
C(18)	60(1)	77(2)	56(1)	6(1)	2(1)	5(1)
C(19)	76(2)	98(2)	56(1)	17(1)	-12(1)	-10(1)
C(20)	121(2)	84(2)	49(1)	-7(1)	4(1)	-14(2)
C(21)	119(2)	79(2)	62(1)	-16(1)	10(2)	17(2)
C(22)	83(2)	64(1)	59(1)	-11(1)	6(1)	15(1)

Table B42. Atomic coordinates (x 10^4) and equivalent isotropic displacement parameters (Å^2 x 10^3) in **12**-$\boldsymbol{d_{28}}$ at 293(2) K. *U*(eq) is defined as one third of the trace of the orthogonalized U^{ij} tensor

	x	y	z	*U*(eq)
Fe(1)	0	0	394(1)	38(1)
Cl(1)	0	0	2628(1)	55(1)
N(1)	379(1)	1440(1)	0	46(1)
C(1)	-250(1)	2240(1)	0	47(1)
C(2)	314(2)	3140(2)	0	56(1)
D(2A)	62	3779	0	68
C(3)	1274(2)	2886(1)	0	56(1)
D(3A)	1808	3317	0	67
C(4)	1324(1)	1824(1)	0	47(1)
C(5)	2196(1)	1281(1)	0	46(1)
C(6)	3151(1)	1840(1)	0	48(1)
C(7)	3598(1)	2102(2)	1199(2)	74(1)
D(7A)	3316	1914	2024	89
C(8)	4466(2)	2644(2)	1194(2)	82(1)
D(8A)	4759	2821	2016	98
C(9)	4894(2)	2919(2)	0	69(1)

Table B42. (continued)

	x	y	z	*U*(eq)
D(9A)	5472	3289	0	82

Table B43. Bond angles (°) in **12-d_{28}** at 293(2) K

Angles			
Fe(1)#1-Fe(1)-N(1)	79.136(18)	C(4)-N(1)-Fe(1)#1	126.10(12)
Fe(1)#1-Fe(1)-N(1)#1	79.136(18)	N(1)-C(1)-C(5)#2	125.75(17)
Fe(1)#1-Fe(1)-N(1)#2	79.136(18)	N(1)-C(1)-C(2)	109.70(17)
N(1)-Fe(1)-N(1)#2	87.964(7)	C(5)#2-C(1)-C(2)	124.55(18)
N(1)#1-Fe(1)-N(1)#2	87.964(7)	C(3)-C(2)-C(1)	107.28(17)
Fe(1)#1-Fe(1)-N(1)#3	79.136(18)	C(2)-C(3)-C(4)	107.56(17)
N(1)-Fe(1)-N(1)#3	87.964(7)	N(1)-C(4)-C(5)	126.00(17)
N(1)#1-Fe(1)-N(1)#3	87.964(7)	N(1)-C(4)-C(3)	109.38(17)
N(1)#2-Fe(1)-N(1)#3	158.27(4)	C(5)-C(4)-C(3)	124.62(18)
Fe(1)#1-Fe(1)-Cl(1)	180.0	C(4)-C(5)-C(1)#3	124.34(18)
N(1)-Fe(1)-Cl(1)	100.864(18)	C(4)-C(5)-C(6)	117.75(17)
N(1)#1-Fe(1)-Cl(1)	100.864(18)	C(1)#3-C(5)-C(6)	117.91(17)
N(1)#2-Fe(1)-Cl(1)	100.864(18)	C(7)#4-C(6)-C(7)	118.4(2)
N(1)#3-Fe(1)-Cl(1)	100.864(18)	C(7)#4-C(6)-C(5)	120.79(10)
C(1)-N(1)-C(4)	106.08(15)	C(7)-C(6)-C(5)	120.79(10)
C(1)-N(1)-Fe(1)	126.28(12)	C(6)-C(7)-C(8)	120.56(17)
C(4)-N(1)-Fe(1)	126.10(12)	C(9)-C(8)-C(7)	120.67(17)
C(1)-N(1)-Fe(1)#1	126.28(12)	C(8)-C(9)-C(8)#4	119.1(2)

Symmetry transformations used to generate equivalent atoms:
#1 -x,-y,-z #2 -y,x,z #3 y,-x,-z #4 x,y,-z

Table B44. Bond lengths (Å) in **12**-d_{28} at 293(2) K

Lengths			
Fe(1)-Fe(1)#1	0.7742(12)	C(2)-C(3)	1.344(3)
Fe(1)-N(1)	2.0537(16)	C(3)-C(4)	1.439(3)
Fe(1)-N(1)#1	2.0538(16)	C(4)-C(5)	1.391(3)
Fe(1)-N(1)#2	2.0538(16)	C(5)-C(1)#3	1.398(3)
Fe(1)-N(1)#3	2.0538(16)	C(5)-C(6)	1.498(3)
Fe(1)-Cl(1)	2.1925(14)	C(6)-C(7)#4	1.3701(19)
N(1)-C(1)	1.379(2)	C(6)-C(7)	1.3702(19)
N(1)-C(4)	1.381(2)	C(7)-C(8)	1.387(3)
N(1)-Fe(1)#1	2.0537(16)	C(8)-C(9)	1.359(2)
C(1)-C(5)#2	1.398(3)	C(9)-C(8)#4	1.359(2
C(1)-C(2)	1.438(3)		

Symmetry transformations used to generate equivalent atoms:
#1 -x,-y,-z #2 -y,x,z #3 y,-x,-z #4 x,y,-z

Table B45. Anisotropic displacement parameters (Å^2 x 10^3) **12-*d*$_{28}$** at 293(2) K. The anisotropic displacement factor exponent takes the form: $-2\pi^2$ [$h^2a^{*2}U^{11}$ + ... + 2 hka* b*U^{12}]

	U^{11}	U^{22}	U^{33}	U^{23}	U^{13}	U^{12}
Fe(1)	36(1)	36(1)	43(1)	0	0	0
Cl(1)	60(1)	60(1)	44(1)	0	0	0
N(1)	41(1)	40(1)	56(1)	0	0	-1(1)
C(1)	48(1)	40(1)	54(1)	0	0	1(1)
C(2)	56(1)	38(1)	75(1)	0	0	-1(1)
C(3)	51(1)	41(1)	75(1)	0	0	-7(1)
C(4)	44(1)	42(1)	54(1)	0	0	-5(1)
C(5)	42(1)	48(1)	50(1)	0	0	-5(1)
C(6)	41(1)	46(1)	58(1)	0	0	-3(1)
C(7)	68(1)	96(1)	59(1)	-6(1)	-1(1)	-28(1)
C(8)	68(1)	94(1)	83(1)	-12(1)	-16(1)	-26(1)
C(9)	43(1)	56(1)	107(2)	0	0	-8(1)

Table B46. Atomic coordinates (x 10^4) and equivalent isotropic displacement parameters ($Å^2$ x 10^3) in **13**-$\boldsymbol{d_{36}}$•D_2O•$CDCl_3$ at 293(2) K. *U*(eq) is defined as one third of the trace of the orthogonalized U^{ij} tensor

	x	y	z	*U*(eq)
Fe(1)	10000	10000	5000	34(1)
Fe(2)	5000	5000	0	32(1)
N(1)	8922(1)	9969(1)	4301(1)	37(1)
N(2)	11168(1)	11059(1)	3988(1)	38(1)
N(3)	10965(2)	8811(1)	4702(1)	43(1)
N(4)	11526(2)	7212(2)	4681(2)	66(1)
N(5)	5212(1)	6354(1)	198(1)	36(1)
N(6)	5572(1)	4182(1)	999(1)	36(1)
N(7)	3254(2)	4867(1)	732(1)	39(1)
N(8)	1632(2)	4890(2)	1797(1)	56(1)
O(1)	1755(4)	5021(2)	4992(2)	112(1)
C(1)	10184(2)	11724(2)	2000(1)	57(1)
C(2)	11098(3)	11477(3)	1377(2)	89(1)
D(2)	11708	10992	1513	106
C(3)	11110(4)	11965(4)	528(2)	121(2)
D(3)	11728	11802	101	145

Table B46. (continued)

	x	y	z	*U*(eq)
C(4)	10209(4)	12676(4)	334(2)	123(2)
D(4)	10218	12991	-226	148
C(5)	9312(4)	12927(3)	942(2)	105(1)
D(5)	8706	13412	801	126
C(6)	9293(3)	12459(2)	1777(2)	73(1)
D(6)	8676	12640	2195	88
C(7)	6141(2)	8023(2)	5504(1)	42(1)
C(8)	6231(3)	6993(2)	5484(2)	60(1)
D(8)	7000	6661	5426	72
C(9)	5178(3)	6454(2)	5548(2)	74(1)
D(9)	5246	5763	5529	89
C(10)	4043(3)	6928(3)	5641(2)	78(1)
D(10)	3342	6563	5680	93
C(11)	3937(2)	7936(3)	5677(2)	72(1)
D(11)	3161	8256	5743	87
C(12)	4977(2)	8486(2)	5616(2)	56(1)
D(12)	4894	9169	5651	67
C(13)	10695(2)	7785(2)	5064(2)	59(1)

Table B46. (continued)

	x	y	z	*U*(eq)
D(13)	10005	7492	5532	71
C(14)	12386(3)	7901(3)	4048(2)	84(1)
D(14)	13083	7730	3669	100
C(15)	12053(3)	8884(2)	4062(2)	76(1)
D(15)	12493	9516	3694	91
C(16)	6241(2)	5904(2)	2140(1)	46(1)
C(17)	7462(3)	5842(2)	2167(2)	70(1)
D(17)	8091	5671	1750	84
C(18)	7759(3)	6033(3)	2815(2)	88(1)
D(18)	8583	5979	2832	106
C(19)	6849(4)	6300(2)	3421(2)	81(1)
D(19)	7051	6426	3852	97
C(20)	5657(3)	6382(2)	3396(2)	74(1)
D(20)	5040	6573	3808	89
C(21)	5337(3)	6183(2)	2758(2)	60(1)
D(21)	4508	6238	2750	72
C(22)	5882(2)	1226(2)	1303(1)	45(1)
C(23)	7060(3)	919(2)	949(2)	76(1)

Table B46. (continued)

	x	y	z	*U*(eq)
C(24)	7442(4)	-116(3)	1275(2)	91(1)
D(23)	7610	1412	484	92
D(24)	8246	-308	1031	110
C(25)	6656(4)	-843(2)	1942(2)	80(1)
D(25)	6903	-1543	2149	96
C(26)	5517(4)	-548(2)	2302(3)	104(1)
D(26)	4982	-1045	2772	125
C(27)	5114(3)	487(2)	1988(2)	87(1)
D(27)	4316	673	2248	104
C(28)	2871(2)	4984(2)	1481(1)	49(1)
D(28)	3402	5115	1752	59
C(29)	1183(2)	4693(2)	1231(2)	62(1)
D(29)	346	4587	1285	75
C(30)	2184(2)	4679(2)	574(1)	54(1)
D(30)	2154	4562	93	65
C(31)	1077(4)	7687(4)	2195(3)	119(1)
D(31)	938	6938	2567	143
C(1A)	7849(2)	9344(2)	4558(1)	40(1)

Table B46. (continued)

	x	y	z	*U*(eq)
C(2A)	9126(2)	10511(2)	3450(1)	41(1)
C(3A)	11082(2)	11465(2)	3176(1)	42(1)
C(4A)	12231(2)	11540(2)	3957(1)	40(1)
C(5A)	4942(2)	7368(2)	-257(1)	39(1)
C(6A)	5591(2)	6471(2)	835(1)	39(1)
C(7A)	5879(2)	4573(2)	1542(1)	38(1)
C(8A)	5722(2)	3096(2)	1294(1)	38(1)
C(1B)	7388(2)	9502(2)	3857(1)	48(1)
D(1B)	6682	9169	3869	57
C(2B)	8164(2)	10218(2)	3180(1)	49(1)
D(2B)	8092	10477	2636	59
C(3B)	12103(2)	12207(2)	2638(1)	48(1)
D(3B)	12252	12583	2064	58
C(4B)	12808(2)	12259(2)	3117(1)	47(1)
D(4B)	13531	12680	2938	56
C(5B)	5193(2)	8130(2)	87(1)	50(1)
D(5B)	5096	8865	-114	60
C(6B)	5595(2)	7579(2)	755(1)	48(1)

Table B46. (continued)

	x	y	z	*U*(eq)
D(6B)	5831	7864	1101	58
C(7B)	6194(2)	3709(2)	2198(1)	46(1)
D(7B)	6414	3764	2648	55
C(8B)	6110(2)	2806(2)	2042(1)	45(1)
D(8B)	6274	2120	2359	54
C(1M)	10128(2)	11210(2)	2915(1)	44(1)
C(2M)	7295(2)	8638(2)	5370(1)	40(1)
C(3M)	5899(2)	5644(2)	1475(1)	40(1)
C(4M)	5519(2)	2362(2)	945(1)	40(1)
Cl(1)	453(6)	7904(9)	1341(5)	183(3)
Cl(2)	2627(4)	8639(12)	1822(3)	156(3)
Cl(3)	73(1)	8358(2)	2769(1)	172(1)
Cl(4)	700(1)	5006(1)	3567(1)	143(1)
Cl(1A)	852(15)	7676(6)	1312(4)	209(3)
Cl(2A)	2572(3)	7845(9)	1862(3)	155(3)
D(32)	1450(50)	5060(40)	4430(40)	180(20)
D(33)	990(40)	4860(30)	5440(30)	116(16)
D(8N)	1240(20)	4930(20)	2310(13)	76(9)

Table B46. (continued)

	x	y	z	*U*(eq)
D(4N)	11450(30)	6495(15)	4820(20)	94(11)

Table B47. Bond angles (°) in **13-*d*$_{36}$**•D_2O•$CDCl_3$ at 293(2) K

Angles			
N(3)-Fe(1)-N(3)#1	180.00(9)	N(7)#2-Fe(2)-N(6)	89.70(6)
N(3)-Fe(1)-N(1)#1	90.51(6)	N(6)#2-Fe(2)-N(6)	180.0
N(3)#1-Fe(1)-N(1)#1	89.49(6)	N(7)-Fe(2)-N(5)#2	90.81(6)
N(3)-Fe(1)-N(1)	89.49(6)	N(7)#2-Fe(2)-N(5)#2	89.19(6)
N(3)#1-Fe(1)-N(1)	90.51(6)	N(6)#2-Fe(2)-N(5)#2	89.26(6)
N(1)#1-Fe(1)-N(1)	180.00(5)	N(6)-Fe(2)-N(5)#2	90.74(6)
N(3)-Fe(1)-N(2)	90.06(7)	N(7)-Fe(2)-N(5)	89.19(6)
N(3)#1-Fe(1)-N(2)	89.94(7)	N(7)#2-Fe(2)-N(5)	90.81(6)
N(1)#1-Fe(1)-N(2)	90.28(6)	N(6)#2-Fe(2)-N(5)	90.74(6)
N(1)-Fe(1)-N(2)	89.72(6)	N(6)-Fe(2)-N(5)	89.26(6)
N(3)-Fe(1)-N(2)#1	89.94(7)	N(5)#2-Fe(2)-N(5)	180.0
N(3)#1-Fe(1)-N(2)#1	90.06(7)	C(2A)-N(1)-C(1A)	105.40(15)
N(1)#1-Fe(1)-N(2)#1	89.72(6)	C(2A)-N(1)-Fe(1)	127.56(13)
N(1)-Fe(1)-N(2)#1	90.28(6)	C(1A)-N(1)-Fe(1)	126.92(12)
N(2)-Fe(1)-N(2)#1	179.999(1)	C(3A)-N(2)-C(4A)	105.31(16)
N(7)-Fe(2)-N(7)#2	180.0	C(3A)-N(2)-Fe(1)	127.66(13)
N(7)-Fe(2)-N(6)#2	89.70(6)	C(4A)-N(2)-Fe(1)	127.03(12)
N(7)#2-Fe(2)-N(6)#2	90.30(6)	C(13)-N(3)-C(15)	104.8(2)
N(7)-Fe(2)-N(6)	90.30(6)	C(13)-N(3)-Fe(1)	127.72(16)

Table B47. (continued)

Angles			
C(15)-N(3)-Fe(1)	127.46(17)	C(5)-C(6)-C(1)	120.9(3)
C(13)-N(4)-C(14)	107.2(2)	C(8)-C(7)-C(12)	118.7(2)
C(5A)-N(5)-C(6A)	105.44(14)	C(8)-C(7)-C(2M)	120.25(19)
C(5A)-N(5)-Fe(2)	126.47(12)	C(12)-C(7)-C(2M)	120.99(19)
C(6A)-N(5)-Fe(2)	128.01(12)	C(9)-C(8)-C(7)	120.1(3)
C(8A)-N(6)-C(7A)	105.72(14)	C(10)-C(9)-C(8)	120.5(3)
C(8A)-N(6)-Fe(2)	126.50(12)	C(11)-C(10)-C(9)	120.0(2)
C(7A)-N(6)-Fe(2)	127.77(12)	C(10)-C(11)-C(12)	120.3(3)
C(28)-N(7)-C(30)	105.48(17)	C(11)-C(12)-C(7)	120.3(2)
C(28)-N(7)-Fe(2)	125.94(14)	N(3)-C(13)-N(4)	111.7(2)
C(30)-N(7)-Fe(2)	128.53(14)	N(4)-C(14)-C(15)	107.0(2)
C(28)-N(8)-C(29)	107.55(19)	C(14)-C(15)-N(3)	109.3(3)
C(2)-C(1)-C(6)	119.0(3)	C(21)-C(16)-C(17)	118.2(2)
C(2)-C(1)-C(1M)	121.2(3)	C(21)-C(16)-C(3M)	120.8(2)
C(6)-C(1)-C(1M)	119.9(2)	C(17)-C(16)-C(3M)	121.0(2)
C(1)-C(2)-C(3)	119.5(4)	C(16)-C(17)-C(18)	120.4(3)
C(4)-C(3)-C(2)	119.9(4)	C(19)-C(18)-C(17)	120.3(3)
C(5)-C(4)-C(3)	121.0(3)	C(20)-C(19)-C(18)	120.0(2)
C(4)-C(5)-C(6)	119.8(4)	C(19)-C(20)-C(21)	120.7(3)

Table B47. (continued)

Angles			
C(16)-C(21)-C(20)	120.4(3)	N(1)-C(2A)-C(2B)	109.91(17)
C(27)-C(22)-C(23)	117.8(2)	C(1M)-C(2A)-C(2B)	124.13(18)
C(27)-C(22)-C(4M)	123.0(2)	N(2)-C(3A)-C(1M)	125.22(18)
C(23)-C(22)-C(4M)	119.1(2)	N(2)-C(3A)-C(3B)	110.20(17)
C(22)-C(23)-C(24)	120.9(3)	C(1M)-C(3A)-C(3B)	124.56(18)
C(25)-C(24)-C(23)	120.4(3)	N(2)-C(4A)-C(2M)#1	125.90(18)
C(24)-C(25)-C(26)	119.2(3)	N(2)-C(4A)-C(4B)	110.23(16)
C(25)-C(26)-C(27)	121.4(3)	C(2M)#1-C(4A)-C(4B)	123.87(18)
C(22)-C(27)-C(26)	120.3(3)	N(5)-C(5A)-C(4M)#2	126.04(17)
N(7)-C(28)-N(8)	111.2(2)	N(5)-C(5A)-C(5B)	110.12(16)
C(30)-C(29)-N(8)	106.8(2)	C(4M)#2-C(5A)-C(5B)	123.84(17)
C(29)-C(30)-N(7)	109.0(2)	N(5)-C(6A)-C(3M)	125.58(17)
Cl(2A)-C(31)-Cl(1A)	98.3(6)	N(5)-C(6A)-C(6B)	110.09(16)
Cl(2A)-C(31)-Cl(3)	125.5(5)	C(3M)-C(6A)-C(6B)	124.31(17)
Cl(1A)-C(31)-Cl(3)	118.9(6)	N(6)-C(7A)-C(3M)	126.06(16)
N(1)-C(1A)-C(2M)	126.12(16)	N(6)-C(7A)-C(7B)	109.92(16)
N(1)-C(1A)-C(1B)	110.02(17)	C(3M)-C(7A)-C(7B)	124.02(16)
C(2M)-C(1A)-C(1B)	123.84(18)	N(6)-C(8A)-C(4M)	126.43(16)
N(1)-C(2A)-C(1M)	125.93(17)	N(6)-C(8A)-C(8B)	109.86(16)

Table B47. (continued)

Angles			
C(4M)-C(8A)-C(8B)	123.70(17)	C(3A)-C(1M)-C(1)	118.26(18)
C(2B)-C(1B)-C(1A)	107.28(18)	C(4A)#1-C(2M)-C(1A)	123.71(18)
C(1B)-C(2B)-C(2A)	107.38(17)	C(4A)#1-C(2M)-C(7)	119.20(17)
C(4B)-C(3B)-C(3A)	107.23(18)	C(1A)-C(2M)-C(7)	117.07(16)
C(3B)-C(4B)-C(4A)	107.02(18)	C(6A)-C(3M)-C(7A)	123.25(16)
C(6B)-C(5B)-C(5A)	107.17(18)	C(6A)-C(3M)-C(16)	118.87(17)
C(5B)-C(6B)-C(6A)	107.14(17)	C(7A)-C(3M)-C(16)	117.86(16)
C(8B)-C(7B)-C(7A)	107.14(16)	C(5A)#2-C(4M)-C(8A)	123.70(17)
C(7B)-C(8B)-C(8A)	107.34(17)	C(5A)#2-C(4M)-C(22)	118.12(16)
C(2A)-C(1M)-C(3A)	123.87(18)	C(8A)-C(4M)-C(22)	118.10(16
C(2A)-C(1M)-C(1)	117.87(17)		

Symmetry transformations used to generate equivalent atoms:

#1 -x+2,-y+2,-z+1 #2 -x+1,-y+1,-z

Table B48. Bond lengths (Å) in **13-*d*$_{36}$**•D_2O•$CDCl_3$ at 293(2) K

Lengths			
Fe(1)-N(3)	1.9789(16)	N(4)-C(14)	1.338(4)
Fe(1)-N(3)#1	1.9789(16)	N(5)-C(5A)	1.378(2)
Fe(1)-N(1)#1	1.9897(14)	N(5)-C(6A)	1.380(2)
Fe(1)-N(1)	1.9897(14)	N(6)-C(8A)	1.373(2)
Fe(1)-N(2)	2.0029(16)	N(6)-C(7A)	1.378(2)
Fe(1)-N(2)#1	2.0030(16)	N(7)-C(28)	1.323(2)
Fe(2)-N(7)	1.9681(16)	N(7)-C(30)	1.373(3)
Fe(2)-N(7)#2	1.9681(16)	N(8)-C(28)	1.327(3)
Fe(2)-N(6)#2	1.9927(14)	N(8)-C(29)	1.357(3)
Fe(2)-N(6)	1.9927(14)	C(1)-C(2)	1.370(4)
Fe(2)-N(5)#2	2.0006(14)	C(1)-C(6)	1.390(4)
Fe(2)-N(5)	2.0006(14)	C(1)-C(1M)	1.506(3)
N(1)-C(2A)	1.379(2)	C(2)-C(3)	1.412(5)
N(1)-C(1A)	1.382(2)	C(3)-C(4)	1.367(7)
N(2)-C(3A)	1.379(2)	C(4)-C(5)	1.346(6)
N(2)-C(4A)	1.377(2)	C(5)-C(6)	1.384(4)
N(3)-C(13)	1.309(3)	C(7)-C(8)	1.382(3)
N(3)-C(15)	1.369(3)	C(7)-C(12)	1.386(3)
N(4)-C(13)	1.329(3)	C(7)-C(2M)	1.500(3)

Table B48. (continued)

Lengths			
C(8)-C(9)	1.385(4)	C(29)-C(30)	1.348(3)
C(9)-C(10)	1.364(5)	C(31)-Cl(2A)	1.601(5)
C(10)-C(11)	1.362(4)	C(31)-Cl(1A)	1.664(8)
C(11)-C(12)	1.384(3)	C(31)-Cl(3)	1.693(4)
C(14)-C(15)	1.341(4)	C(1A)-C(2M)	1.392(3)
C(16)-C(21)	1.378(3)	C(1A)-C(1B)	1.431(3)
C(16)-C(17)	1.379(3)	C(2A)-C(1M)	1.389(3)
C(16)-C(3M)	1.497(2)	C(2A)-C(2B)	1.435(3)
C(17)-C(18)	1.394(4)	C(3A)-C(1M)	1.395(3)
C(18)-C(19)	1.361(5)	C(3A)-C(3B)	1.433(3)
C(19)-C(20)	1.346(5)	C(4A)-C(2M)#1	1.389(3)
C(20)-C(21)	1.396(3)	C(4A)-C(4B)	1.437(3)
C(22)-C(27)	1.358(4)	C(5A)-C(4M)#2	1.391(3)
C(22)-C(23)	1.373(4)	C(5A)-C(5B)	1.437(3)
C(22)-C(4M)	1.502(3)	C(6A)-C(3M)	1.389(3)
C(23)-C(24)	1.387(4)	C(6A)-C(6B)	1.436(3)
C(24)-C(25)	1.346(5)	C(7A)-C(3M)	1.393(3)
C(25)-C(26)	1.335(5)	C(7A)-C(7B)	1.434(3)
C(26)-C(27)	1.393(4)	C(8A)-C(4M)	1.391(3)

Table B48. (continued)

Lengths			
C(8A)-C(8B)	1.436(2)	C(7B)-C(8B)	1.343(3)
C(1B)-C(2B)	1.343(3)	C(2M)-C(4A)#1	1.389(3)
C(3B)-C(4B)	1.346(3)	C(4M)-C(5A)#2	1.391(3)
C(5B)-C(6B)	1.347(3)		

Symmetry transformations used to generate equivalent atoms:

#1 -x+2,-y+2,-z+1 #2 -x+1,-y+1,-z

Table B49. Anisotropic displacement parameters (Å^2 x 10^3) in **13**-***d*$_{36}$•D_2O•$CDCl_3$ at 293(2) K. The anisotropic displacement factor exponent takes the form: $-2\pi^2 [h^2a^{*2}U^{11} + ... + 2\ hka^*\ b^*U^{12}]$

	U^{11}	U^{22}	U^{33}	U^{23}	U^{13}	U^{12}
Fe(1)	32(1)	41(1)	31(1)	-10(1)	-12(1)	4(1)
Fe(2)	38(1)	34(1)	27(1)	-10(1)	-13(1)	4(1)
N(1)	35(1)	44(1)	32(1)	-10(1)	-13(1)	1(1)
N(2)	35(1)	46(1)	32(1)	-10(1)	-13(1)	2(1)
N(3)	42(1)	50(1)	41(1)	-18(1)	-18(1)	9(1)
N(4)	73(1)	58(1)	80(2)	-35(1)	-34(1)	22(1)
N(5)	44(1)	36(1)	31(1)	-11(1)	-16(1)	3(1)
N(6)	43(1)	37(1)	30(1)	-11(1)	-16(1)	5(1)
N(7)	41(1)	42(1)	34(1)	-12(1)	-13(1)	4(1)
N(8)	49(1)	66(1)	46(1)	-21(1)	-2(1)	2(1)
O(1)	150(3)	90(2)	116(2)	-49(2)	-63(2)	42(2)
C(1)	51(1)	80(2)	34(1)	-6(1)	-14(1)	-20(1)
C(2)	71(2)	146(3)	49(2)	-34(2)	-10(1)	-16(2)
C(3)	99(3)	210(5)	45(2)	-40(2)	2(2)	-53(3)
C(4)	112(3)	195(5)	46(2)	7(2)	-35(2)	-75(3)
C(5)	100(2)	128(3)	64(2)	27(2)	-51(2)	-45(2)

Table B49. (continued)

	U^{11}	U^{22}	U^{33}	U^{23}	U^{13}	U^{12}
C(6)	68(2)	88(2)	52(1)	8(1)	-35(1)	-17(1)
C(7)	45(1)	46(1)	35(1)	-7(1)	-17(1)	-4(1)
C(8)	68(2)	56(1)	57(1)	-21(1)	-19(1)	-4(1)
C(9)	108(2)	65(2)	53(2)	-17(1)	-23(2)	-32(2)
C(10)	80(2)	101(2)	48(1)	-2(1)	-29(1)	-43(2)
C(11)	50(1)	92(2)	65(2)	-2(2)	-28(1)	-12(1)
C(12)	47(1)	55(1)	58(1)	-5(1)	-21(1)	-1(1)
C(13)	58(1)	53(1)	67(2)	-22(1)	-19(1)	10(1)
C(14)	84(2)	79(2)	77(2)	-35(2)	-7(2)	31(2)
C(15)	67(2)	68(2)	70(2)	-22(1)	6(1)	14(1)
C(16)	62(1)	44(1)	38(1)	-14(1)	-25(1)	4(1)
C(17)	67(2)	96(2)	66(2)	-38(2)	-34(1)	5(1)
C(18)	95(2)	108(2)	89(2)	-35(2)	-63(2)	-3(2)
C(19)	139(3)	67(2)	62(2)	-25(1)	-62(2)	4(2)
C(20)	126(3)	64(2)	49(1)	-29(1)	-40(2)	16(2)
C(21)	79(2)	64(1)	48(1)	-28(1)	-30(1)	16(1)
C(22)	62(1)	37(1)	43(1)	-10(1)	-28(1)	5(1)
C(23)	77(2)	53(2)	80(2)	-10(1)	-16(2)	17(1)

Table B49. (continued)

	U^{11}	U^{22}	U^{33}	U^{23}	U^{13}	U^{12}
C(24)	98(2)	68(2)	110(3)	-30(2)	-42(2)	37(2)
C(25)	125(3)	42(1)	93(2)	-19(2)	-69(2)	20(2)
C(26)	111(3)	48(2)	111(3)	18(2)	-26(2)	-5(2)
C(27)	76(2)	51(2)	93(2)	6(2)	-6(2)	1(1)
C(28)	49(1)	60(1)	39(1)	-21(1)	-10(1)	1(1)
C(29)	42(1)	79(2)	61(2)	-20(1)	-12(1)	-2(1)
C(30)	45(1)	73(2)	46(1)	-21(1)	-16(1)	0(1)
C(31)	121(3)	143(4)	107(3)	-66(3)	-36(3)	42(3)
C(1A)	38(1)	45(1)	38(1)	-13(1)	-16(1)	2(1)
C(2A)	38(1)	52(1)	33(1)	-11(1)	-14(1)	2(1)
C(3A)	38(1)	49(1)	34(1)	-9(1)	-13(1)	2(1)
C(4A)	36(1)	44(1)	38(1)	-10(1)	-13(1)	2(1)
C(5A)	48(1)	36(1)	36(1)	-11(1)	-16(1)	4(1)
C(6A)	46(1)	41(1)	36(1)	-16(1)	-17(1)	4(1)
C(7A)	44(1)	43(1)	31(1)	-13(1)	-16(1)	6(1)
C(8A)	42(1)	38(1)	31(1)	-7(1)	-14(1)	3(1)
C(1B)	46(1)	58(1)	43(1)	-14(1)	-21(1)	-5(1)
C(2B)	47(1)	65(1)	38(1)	-13(1)	-19(1)	-5(1)

Table B49. (continued)

	U^{11}	U^{22}	U^{33}	U^{23}	U^{13}	U^{12}
C(3B)	46(1)	56(1)	37(1)	-4(1)	-14(1)	-5(1)
C(4B)	42(1)	53(1)	40(1)	-6(1)	-14(1)	-5(1)
C(5B)	70(1)	37(1)	50(1)	-15(1)	-29(1)	4(1)
C(6B)	66(1)	43(1)	47(1)	-19(1)	-27(1)	3(1)
C(7B)	60(1)	48(1)	35(1)	-12(1)	-25(1)	8(1)
C(8B)	57(1)	43(1)	35(1)	-7(1)	-23(1)	7(1)
C(1M)	42(1)	56(1)	32(1)	-10(1)	-14(1)	0(1)
C(2M)	38(1)	44(1)	40(1)	-12(1)	-15(1)	2(1)
C(3M)	47(1)	45(1)	34(1)	-15(1)	-18(1)	4(1)
C(4M)	46(1)	36(1)	36(1)	-8(1)	-16(1)	3(1)
Cl(1)	132(4)	302(9)	128(3)	-63(4)	-64(2)	-4(3)
Cl(2)	111(2)	212(8)	143(3)	-85(4)	-11(2)	22(3)
Cl(3)	133(1)	202(2)	221(2)	-150(2)	-27(1)	38(1)
Cl(4)	201(1)	173(1)	64(1)	-59(1)	-46(1)	68(1)
Cl(1A)	410(10)	131(4)	97(3)	-43(2)	-77(5)	-36(4)
Cl(2A)	81(2)	203(7)	178(3)	-76(3)	-25(2)	15(2)

Table B50. Atomic coordinates (x 10^4) and equivalent isotropic displacement parameters (Å^2 x 10^3) in **13**-$\boldsymbol{d_{36}}$•D_2O•$CDCl_3$ at 173(2) K. *U*(eq) is defined as one third of the trace of the orthogonalized U^{ij} tensor

	x	y	z	*U*(eq)
Fe(1)	10000	10000	5000	20(1)
Fe(2)	5000	5000	0	19(1)
N(1)	8892(2)	9968(2)	4307(1)	22(1)
N(2)	11181(2)	11068(2)	3983(1)	22(1)
N(3)	10942(2)	8799(2)	4699(1)	26(1)
N(4)	11486(2)	7159(2)	4696(2)	36(1)
N(5)	5209(2)	6374(2)	199(1)	22(1)
N(6)	5562(2)	4189(2)	1007(1)	21(1)
N(7)	3239(2)	4861(2)	719(1)	24(1)
N(8)	1589(2)	4901(2)	1775(1)	33(1)
O(1)	1728(4)	4952(2)	5046(2)	66(1)
C(1)	10161(3)	11722(3)	1999(2)	35(1)
C(2)	11110(3)	11483(3)	1371(2)	50(1)
D(2)	11729	11007	1508	60
C(3)	11119(4)	11969(4)	528(2)	69(1)
D(3)	11751	11816	103	83

Table B50. (continued)

	x	y	z	*U*(eq)
C(4)	10205(4)	12671(4)	322(2)	74(1)
D(4)	10225	12986	-241	89
C(5)	9273(4)	12908(3)	931(2)	59(1)
D(5)	8654	13380	786	71
C(6)	9248(3)	12443(3)	1772(2)	44(1)
D(6)	8616	12614	2189	53
C(7)	6071(2)	7996(2)	5518(2)	24(1)
C(8)	6151(3)	6949(2)	5503(2)	33(1)
D(8)	6919	6612	5452	40
C(9)	5076(3)	6405(3)	5566(2)	43(1)
D(9)	5130	5703	5550	52
C(10)	3934(3)	6885(3)	5653(2)	44(1)
D(10)	3223	6510	5689	53
C(11)	3836(3)	7917(3)	5686(2)	42(1)
D(11)	3060	8241	5751	51
C(12)	4899(3)	8469(2)	5622(2)	32(1)
D(12)	4835	9167	5648	38
C(13)	10674(3)	7754(2)	5087(2)	33(1)
D(13)	10002	7462	5573	40

Table B50. (continued)

	x	y	z	*U*(eq)
C(14)	12329(3)	7869(3)	4025(2)	47(1)
D(14)	13007	7693	3637	57
C(15)	12005(3)	8880(3)	4022(2)	45(1)
D(15)	12427	9523	3631	54
C(16)	6223(3)	5948(2)	2156(2)	27(1)
C(17)	7455(3)	5872(3)	2202(2)	37(1)
D(17)	8088	5687	1793	45
C(18)	7752(4)	6068(3)	2852(2)	49(1)
D(18)	8579	6012	2880	59
C(19)	6817(4)	6347(3)	3456(2)	46(1)
D(19)	7011	6471	3896	55
C(20)	5606(3)	6440(2)	3411(2)	42(1)
D(20)	4983	6640	3815	50
C(21)	5294(3)	6238(2)	2762(2)	34(1)
D(21)	4466	6298	2738	41
C(22)	5899(3)	1204(2)	1311(2)	26(1)
C(23)	7060(3)	894(3)	918(2)	43(1)
D(23)	7584	1384	427	51
C(24)	7455(4)	-147(3)	1248(2)	50(1)

Table B50. (continued)

	x	y	z	*U*(eq)
D(24)	8244	-346	979	60
C(25)	6703(3)	-872(2)	1957(2)	44(1)
D(25)	6968	-1569	2173	53
C(26)	5548(4)	-575(3)	2357(2)	52(1)
D(26)	5032	-1072	2847	63
C(27)	5140(3)	463(2)	2036(2)	44(1)
D(27)	4353	656	2313	52
C(28)	2846(3)	4995(2)	1466(2)	29(1)
D(28)	3380	5136	1739	35
C(29)	1142(3)	4687(2)	1199(2)	36(1)
D(29)	298	4580	1244	43
C(30)	2160(3)	4661(2)	551(2)	30(1)
D(30)	2136	4529	70	37
C(31)	1112(5)	7748(4)	2188(3)	74(1)
C(1A)	7801(2)	9334(2)	4569(2)	23(1)
C(2A)	9090(2)	10512(2)	3453(2)	24(1)
C(3A)	11075(2)	11477(2)	3172(2)	24(1)
C(4A)	12264(2)	11560(2)	3948(2)	23(1)
C(5A)	4932(2)	7395(2)	-260(2)	23(1)

Table B50. (continued)

	x	y	z	*U*(eq)
C(6A)	5580(2)	6505(2)	839(2)	24(1)
C(7A)	5874(2)	4593(2)	1553(1)	23(1)
C(8A)	5717(2)	3089(2)	1306(1)	22(1)
C(1B)	7320(3)	9487(2)	3873(2)	27(1)
D(1B)	6595	9149	3891	32
C(2B)	8109(2)	10211(2)	3188(2)	28(1)
D(2B)	8030	10466	2644	33
C(3B)	12112(2)	12234(2)	2632(2)	27(1)
D(3B)	12256	12617	2059	33
C(4B)	12838(2)	12289(2)	3107(2)	27(1)
D(4B)	13575	12718	2924	32
C(5B)	5182(3)	8171(2)	86(2)	30(1)
D(5B)	5086	8915	-116	36
C(6B)	5582(3)	7628(2)	758(2)	28(1)
D(6B)	5815	7926	1105	34
C(7B)	6191(3)	3733(2)	2209(2)	26(1)
D(7B)	6413	3799	2659	32
C(8B)	6110(2)	2811(2)	2052(2)	26(1)
D(8B)	6277	2120	2370	32

Table B50. (continued)

	x	y	z	*U*(eq)
C(1M)	10109(2)	11217(2)	2915(2)	25(1)
C(2M)	7246(2)	8616(2)	5384(2)	22(1)
C(3M)	5890(2)	5673(2)	1486(2)	24(1)
C(4M)	5521(2)	2341(2)	954(2)	23(1)
Cl(1)	479(9)	7837(12)	1337(7)	95(3)
Cl(2)	2640(3)	8657(10)	1823(2)	86(2)
Cl(3)	32(1)	8404(1)	2759(1)	90(1)
Cl(4)	780(1)	5070(1)	3530(1)	88(1)
Cl(1A)	830(20)	7679(8)	1316(4)	117(3)
Cl(2A)	2604(3)	7973(14)	1846(3)	88(3)
D(33)	1020(50)	4840(40)	5450(30)	79(17)
D(32)	1500(40)	4930(30)	4660(30)	61(13)
D(31)	1100(50)	6960(50)	2580(30)	120(20)

Table B51. Bond angles (°) in **13-d_{36}**•D_2O•$CDCl_3$ at 173(2) K

Angles			
N(3)-Fe(1)-N(3)#1	179.999(1)	N(7)-Fe(2)-N(5)#2	91.23(9)
N(3)-Fe(1)-N(1)	89.66(9)	N(5)-Fe(2)-N(5)#2	180.00(10)
N(3)#1-Fe(1)-N(1)	90.34(9)	N(7)#2-Fe(2)-N(6)	89.58(9)
N(3)-Fe(1)-N(1)#1	90.34(9)	N(7)-Fe(2)-N(6)	90.42(9)
N(3)#1-Fe(1)-N(1)#1	89.66(9)	N(5)-Fe(2)-N(6)	89.24(8)
N(1)-Fe(1)-N(1)#1	180.000(1)	N(5)#2-Fe(2)-N(6)	90.76(8)
N(3)-Fe(1)-N(2)#1	90.15(9)	N(7)#2-Fe(2)-N(6)#2	90.42(9)
N(3)#1-Fe(1)-N(2)#1	89.86(9)	N(7)-Fe(2)-N(6)#2	89.58(9)
N(1)-Fe(1)-N(2)#1	90.45(8)	N(5)-Fe(2)-N(6)#2	90.76(8)
N(1)#1-Fe(1)-N(2)#1	89.55(8)	N(5)#2-Fe(2)-N(6)#2	89.24(8)
N(3)-Fe(1)-N(2)	89.85(9)	N(6)-Fe(2)-N(6)#2	180.0
N(3)#1-Fe(1)-N(2)	90.15(9)	C(1A)-N(1)-C(2A)	105.3(2)
N(1)-Fe(1)-N(2)	89.54(8)	C(1A)-N(1)-Fe(1)	126.78(16)
N(1)#1-Fe(1)-N(2)	90.46(8)	C(2A)-N(1)-Fe(1)	127.76(17)
N(2)#1-Fe(1)-N(2)	179.998(1)	C(4A)-N(2)-C(3A)	105.5(2)
N(7)#2-Fe(2)-N(7)	180.0	C(4A)-N(2)-Fe(1)	127.00(16)
N(7)#2-Fe(2)-N(5)	91.23(9)	C(3A)-N(2)-Fe(1)	127.45(17)
N(7)-Fe(2)-N(5)	88.77(9)	C(13)-N(3)-C(15)	105.4(2)
N(7)#2-Fe(2)-N(5)#2	88.77(9)	C(13)-N(3)-Fe(1)	127.33(18)

Table B51. (continued)

Angles			
C(15)-N(3)-Fe(1)	127.2(2)	C(5)-C(6)-C(1)	120.8(3)
C(13)-N(4)-C(14)	106.6(3)	C(8)-C(7)-C(12)	119.1(3)
C(6A)-N(5)-C(5A)	105.7(2)	C(8)-C(7)-C(2M)	119.6(2)
C(6A)-N(5)-Fe(2)	127.99(17)	C(12)-C(7)-C(2M)	121.3(2)
C(5A)-N(5)-Fe(2)	126.20(16)	C(7)-C(8)-C(9)	119.4(3)
C(8A)-N(6)-C(7A)	105.2(2)	C(10)-C(9)-C(8)	121.0(3)
C(8A)-N(6)-Fe(2)	126.72(16)	C(9)-C(10)-C(11)	120.2(3)
C(7A)-N(6)-Fe(2)	128.08(17)	C(10)-C(11)-C(12)	119.4(3)
C(28)-N(7)-C(30)	105.6(2)	C(11)-C(12)-C(7)	120.9(3)
C(28)-N(7)-Fe(2)	125.93(19)	N(3)-C(13)-N(4)	111.9(3)
C(30)-N(7)-Fe(2)	128.45(17)	N(4)-C(14)-C(15)	107.5(3)
C(28)-N(8)-C(29)	107.1(2)	C(14)-C(15)-N(3)	108.6(3)
C(2)-C(1)-C(6)	119.1(3)	C(21)-C(16)-C(17)	119.0(2)
C(2)-C(1)-C(1M)	120.9(3)	C(21)-C(16)-C(3M)	120.3(3)
C(6)-C(1)-C(1M)	119.9(3)	C(17)-C(16)-C(3M)	120.6(2)
C(1)-C(2)-C(3)	119.0(4)	C(18)-C(17)-C(16)	120.7(3)
C(4)-C(3)-C(2)	120.8(4)	C(19)-C(18)-C(17)	119.7(3)
C(5)-C(4)-C(3)	120.7(3)	C(20)-C(19)-C(18)	120.1(3)
C(4)-C(5)-C(6)	119.6(4)	C(19)-C(20)-C(21)	120.7(3)

Table B51. (continued)

Angles			
C(16)-C(21)-C(20)	119.8(3)	N(1)-C(2A)-C(2B)	110.0(2)
C(23)-C(22)-C(27)	118.6(3)	C(1M)-C(2A)-C(2B)	124.1(2)
C(23)-C(22)-C(4M)	119.2(2)	C(1M)-C(3A)-N(2)	125.7(2)
C(27)-C(22)-C(4M)	122.2(2)	C(1M)-C(3A)-C(3B)	124.6(2)
C(22)-C(23)-C(24)	120.6(3)	N(2)-C(3A)-C(3B)	109.7(2)
C(25)-C(24)-C(23)	120.5(3)	N(2)-C(4A)-C(2M)#1	125.8(2)
C(24)-C(25)-C(26)	119.6(3)	N(2)-C(4A)-C(4B)	110.2(2)
C(25)-C(26)-C(27)	120.6(3)	C(2M)#1-C(4A)-C(4B)	124.0(2)
C(22)-C(27)-C(26)	120.1(3)	N(5)-C(5A)-C(4M)#2	126.5(2)
N(7)-C(28)-N(8)	111.5(2)	N(5)-C(5A)-C(5B)	109.7(2)
C(30)-C(29)-N(8)	106.8(3)	C(4M)#2-C(5A)-C(5B)	123.8(2)
C(29)-C(30)-N(7)	109.0(2)	N(5)-C(6A)-C(3M)	125.7(2)
Cl(2A)-C(31)-Cl(1A)	100.2(8)	N(5)-C(6A)-C(6B)	109.9(2)
Cl(2A)-C(31)-Cl(3)	126.7(7)	C(3M)-C(6A)-C(6B)	124.3(2)
Cl(1A)-C(31)-Cl(3)	116.4(8)	N(6)-C(7A)-C(3M)	125.7(2)
N(1)-C(1A)-C(2M)	126.0(2)	N(6)-C(7A)-C(7B)	110.3(2)
N(1)-C(1A)-C(1B)	110.1(2)	C(3M)-C(7A)-C(7B)	124.0(2)
C(2M)-C(1A)-C(1B)	123.9(2)	N(6)-C(8A)-C(4M)	126.1(2)
N(1)-C(2A)-C(1M)	125.8(2)	N(6)-C(8A)-C(8B)	110.1(2)

Table B51. (continued)

Angles			
C(4M)-C(8A)-C(8B)	123.8(2)	C(2A)-C(1M)-C(1)	117.8(2)
C(2B)-C(1B)-C(1A)	107.5(2)	C(4A)#1-C(2M)-C(1A)	123.9(2)
C(1B)-C(2B)-C(2A)	107.1(2)	C(4A)#1-C(2M)-C(7)	119.5(2)
C(4B)-C(3B)-C(3A)	107.4(2)	C(1A)-C(2M)-C(7)	116.6(2)
C(3B)-C(4B)-C(4A)	107.2(2)	C(7A)-C(3M)-C(6A)	123.2(2)
C(6B)-C(5B)-C(5A)	107.5(2)	C(7A)-C(3M)-C(16)	117.8(2)
C(5B)-C(6B)-C(6A)	107.2(2)	C(6A)-C(3M)-C(16)	119.0(2)
C(8B)-C(7B)-C(7A)	107.2(2)	C(8A)-C(4M)-C(5A)#2	123.6(2)
C(7B)-C(8B)-C(8A)	107.2(2)	C(8A)-C(4M)-C(22)	117.7(2)
C(3A)-C(1M)-C(2A)	123.7(2)	C(5A)#2-C(4M)-C(22)	118.6(2)
C(3A)-C(1M)-C(1)	118.5(2)		

Symmetry transformations used to generate equivalent atoms:
#1 -x+2,-y+2,-z+1 #2 -x+1,-y+1,-z

Table B52. Bond lengths (Å) in **13**-d_{36}•D_2O•$CDCl_3$ at 173(2) K

Lengths			
Fe(1)-N(3)	1.973(2)	N(4)-C(14)	1.353(4)
Fe(1)-N(3)#1	1.973(2)	N(5)-C(6A)	1.376(3)
Fe(1)-N(1)	1.987(2)	N(5)-C(5A)	1.381(3)
Fe(1)-N(1)#1	1.987(2)	N(6)-C(8A)	1.378(3)
Fe(1)-N(2)#1	1.999(2)	N(6)-C(7A)	1.378(3)
Fe(1)-N(2)	1.999(2)	N(7)-C(28)	1.325(3)
Fe(2)-N(7)#2	1.963(2)	N(7)-C(30)	1.375(3)
Fe(2)-N(7)	1.963(2)	N(8)-C(28)	1.332(4)
Fe(2)-N(5)	1.990(2)	N(8)-C(29)	1.367(4)
Fe(2)-N(5)#2	1.990(2)	C(1)-C(2)	1.388(4)
Fe(2)-N(6)	1.992(2)	C(1)-C(6)	1.396(4)
Fe(2)-N(6)#2	1.992(2)	C(1)-C(1M)	1.505(3)
N(1)-C(1A)	1.378(3)	C(2)-C(3)	1.400(5)
N(1)-C(2A)	1.383(3)	C(3)-C(4)	1.373(6)
N(2)-C(4A)	1.373(3)	C(4)-C(5)	1.356(6)
N(2)-C(3A)	1.385(3)	C(5)-C(6)	1.390(4)
N(3)-C(13)	1.314(4)	C(7)-C(8)	1.381(4)
N(3)-C(15)	1.381(3)	C(8)-C(9)	1.384(4)
N(4)-C(13)	1.343(4)	C(9)-C(10)	1.369(5)

Table B52. (continued)

Lengths			
C(10)-C(11)	1.373(5)	C(31)-Cl(1A)	1.689(9)
C(11)-C(12)	1.378(4)	C(31)-Cl(3)	1.711(4)
C(14)-C(15)	1.353(4)	C(1A)-C(2M)	1.395(3)
C(16)-C(21)	1.385(4)	C(1A)-C(1B)	1.428(4)
C(16)-C(17)	1.389(4)	C(2A)-C(1M)	1.385(4)
C(16)-C(3M)	1.492(3)	C(2A)-C(2B)	1.430(4)
C(17)-C(18)	1.389(4)	C(3A)-C(1M)	1.383(4)
C(18)-C(19)	1.378(5)	C(3A)-C(3B)	1.433(4)
C(19)-C(20)	1.365(5)	C(4A)-C(2M)#1	1.386(3)
C(20)-C(21)	1.397(4)	C(4A)-C(4B)	1.435(3)
C(22)-C(23)	1.377(4)	C(5A)-C(4M)#2	1.387(3)
C(22)-C(27)	1.378(4)	C(5A)-C(5B)	1.431(3)
C(22)-C(4M)	1.497(4)	C(6A)-C(3M)	1.397(4)
C(23)-C(24)	1.392(4)	C(6A)-C(6B)	1.432(4)
C(24)-C(25)	1.351(5)	C(7A)-C(3M)	1.384(4)
C(25)-C(26)	1.368(5)	C(7A)-C(7B)	1.428(4)
C(26)-C(27)	1.391(4)	C(8A)-C(8B)	1.432(3)
C(29)-C(30)	1.352(4)	C(8A)-C(4M)	1.386(3)
C(31)-Cl(2A)	1.590(7)	C(1B)-C(2B)	1.346(4)

Table B52. (continued)

Lengths			
C(3B)-C(4B)	1.344(4)	C(2M)-C(4A)#1	1.386(3)
C(5B)-C(6B)	1.344(4)	C(4M)-C(5A)#2	1.387(3)
C(7B)-C(8B)	1.344(4)		

Symmetry transformations used to generate equivalent atoms:
#1 -x+2,-y+2,-z+1 #2 -x+1,-y+1,-z

Table B53. Anisotropic displacement parameters ($Å^2$ x 10^3) in **13-*d*$_{36}$•D_2O•$CDCl_3$** at 173(2) K. The anisotropic displacement factor exponent takes the form: $-2\pi^2$ [$h^2a^{*2}U^{11}$ + ... + 2 hka^* b^*U^{12}]

	U^{11}	U^{22}	U^{33}	U^{23}	U^{13}	U^{12}
Fe(1)	18(1)	24(1)	18(1)	-6(1)	-6(1)	1(1)
Fe(2)	24(1)	19(1)	15(1)	-5(1)	-7(1)	2(1)
N(1)	21(1)	24(1)	20(1)	-7(1)	-6(1)	1(1)
N(2)	19(1)	25(1)	20(1)	-5(1)	-8(1)	1(1)
N(3)	23(1)	33(1)	25(1)	-12(1)	-11(1)	6(1)
N(4)	36(1)	40(2)	42(1)	-20(1)	-20(1)	12(1)
N(5)	25(1)	22(1)	19(1)	-6(1)	-9(1)	2(1)
N(6)	26(1)	20(1)	18(1)	-5(1)	-9(1)	1(1)
N(7)	27(1)	24(1)	20(1)	-7(1)	-7(1)	2(1)
N(8)	32(1)	34(1)	29(1)	-10(1)	-4(1)	4(1)
O(1)	94(3)	52(2)	71(2)	-31(2)	-48(2)	32(2)
C(1)	31(2)	51(2)	20(1)	-5(1)	-9(1)	-13(1)
C(2)	38(2)	80(3)	31(2)	-20(2)	-5(1)	-11(2)
C(3)	57(3)	114(4)	30(2)	-24(2)	3(2)	-38(2)
C(4)	66(3)	115(4)	30(2)	5(2)	-23(2)	-46(3)
C(5)	55(2)	70(3)	41(2)	14(2)	-30(2)	-25(2)

Table B53. (continued)

	U^{11}	U^{22}	U^{33}	U^{23}	U^{13}	U^{12}
C(6)	39(2)	55(2)	32(2)	4(1)	-21(1)	-15(2)
C(7)	24(1)	27(1)	21(1)	-5(1)	-9(1)	-3(1)
C(8)	36(2)	32(2)	31(1)	-10(1)	-10(1)	-1(1)
C(9)	67(2)	33(2)	30(1)	-6(1)	-15(1)	-20(2)
C(10)	46(2)	56(2)	27(1)	2(1)	-17(1)	-27(2)
C(11)	26(2)	56(2)	35(2)	3(1)	-15(1)	-4(1)
C(12)	30(2)	29(2)	31(1)	-1(1)	-11(1)	0(1)
C(13)	33(2)	32(2)	38(2)	-15(1)	-13(1)	7(1)
C(14)	51(2)	47(2)	43(2)	-22(2)	-8(2)	21(2)
C(15)	42(2)	46(2)	35(2)	-13(1)	2(1)	7(2)
C(16)	39(2)	24(1)	23(1)	-8(1)	-17(1)	3(1)
C(17)	41(2)	45(2)	34(1)	-18(1)	-18(1)	3(1)
C(18)	58(2)	55(2)	49(2)	-18(2)	-35(2)	2(2)
C(19)	79(3)	36(2)	34(2)	-13(1)	-32(2)	4(2)
C(20)	70(2)	34(2)	26(1)	-14(1)	-20(1)	11(2)
C(21)	46(2)	30(2)	29(1)	-12(1)	-16(1)	10(1)
C(22)	35(2)	24(1)	26(1)	-8(1)	-18(1)	2(1)
C(23)	47(2)	33(2)	38(2)	-5(1)	-6(1)	10(1)

Table B53. (continued)

	U^{11}	U^{22}	U^{33}	U^{23}	U^{13}	U^{12}
C(25)	67(2)	21(2)	54(2)	-9(1)	-40(2)	7(1)
C(24)	57(2)	38(2)	56(2)	-16(2)	-22(2)	21(2)
C(26)	61(2)	29(2)	50(2)	9(2)	-19(2)	-3(2)
C(27)	40(2)	28(2)	48(2)	0(1)	-9(1)	2(1)
C(28)	32(2)	32(2)	23(1)	-11(1)	-7(1)	0(1)
C(29)	26(2)	42(2)	37(2)	-12(1)	-10(1)	0(1)
C(30)	30(2)	35(2)	28(1)	-10(1)	-12(1)	0(1)
C(31)	80(3)	93(4)	50(2)	-36(2)	-15(2)	36(3)
C(1A)	19(1)	27(1)	25(1)	-10(1)	-8(1)	3(1)
C(2A)	22(1)	31(1)	19(1)	-7(1)	-8(1)	3(1)
C(3A)	24(1)	27(1)	21(1)	-6(1)	-7(1)	2(1)
C(4A)	21(1)	24(1)	24(1)	-8(1)	-7(1)	2(1)
C(5A)	28(1)	18(1)	22(1)	-6(1)	-7(1)	1(1)
C(6A)	26(1)	26(1)	22(1)	-9(1)	-9(1)	2(1)
C(7A)	24(1)	29(1)	17(1)	-9(1)	-8(1)	3(1)
C(8A)	22(1)	24(1)	18(1)	-4(1)	-6(1)	3(1)
C(1B)	25(1)	30(2)	27(1)	-9(1)	-10(1)	-2(1)
C(2B)	26(1)	36(2)	22(1)	-9(1)	-10(1)	-2(1)

Table B53. (continued)

	U^{11}	U^{22}	U^{33}	U^{23}	U^{13}	U^{12}
C(3B)	25(1)	30(1)	22(1)	-2(1)	-8(1)	-1(1)
C(4B)	20(1)	32(2)	24(1)	-4(1)	-6(1)	-2(1)
C(5B)	42(2)	22(1)	29(1)	-9(1)	-15(1)	3(1)
C(6B)	37(2)	27(1)	27(1)	-12(1)	-15(1)	1(1)
C(7B)	33(2)	29(2)	20(1)	-7(1)	-13(1)	3(1)
C(8B)	30(1)	26(1)	22(1)	-3(1)	-12(1)	4(1)
C(1M)	22(1)	32(2)	20(1)	-7(1)	-8(1)	2(1)
C(2M)	20(1)	23(1)	24(1)	-7(1)	-8(1)	3(1)
C(3M)	27(1)	28(1)	21(1)	-10(1)	-10(1)	4(1)
C(4M)	23(1)	21(1)	22(1)	-5(1)	-7(1)	1(1)
Cl(1)	80(7)	142(8)	62(3)	-29(3)	-24(2)	-9(3)
Cl(2)	57(1)	122(5)	70(1)	-39(2)	2(1)	8(2)
Cl(3)	66(1)	105(1)	121(1)	-81(1)	-10(1)	14(1)
Cl(4)	137(1)	100(1)	39(1)	-37(1)	-37(1)	55(1)
Cl(1A)	229(7)	76(3)	50(2)	-27(2)	-38(4)	-20(4)
Cl(2A)	44(2)	132(8)	76(2)	-29(2)	-10(1)	12(2)

Table B54. Calculation of MALDI MS intensity[a] in the sample $[H_2(TPP\text{-}d_n)+H]^+$ $[\mathbf{15}\text{-}\boldsymbol{d}_n+H]^+$

$[M+H]^+$	Intensity Ratio	Intensity (I)[a] (%)
636.281	179.508	0.909
637.218	307.211	1.556
638.307	460.817	2.336
639.347	2610.69	13.227
640.337	6476.73	32.814
641.353	13389	67.834
642.344	19738	100
643.361	17664	89.492
644.354	7117.05	36.058
645.373	3072.11	15.564

[a] The intensity percentage is based out of 19738 from the 642.344 *m/z* peak.

Table B55. Mass spectrum of H_2(TPP-d_{23}) (**15-d_{23}**) used in the simulation.

Charge number	*m/z*	Isotope Abundance	Contribution in the Current Spectrum	Isotope Abundance in the Sample	Weighted Contribution
1	637.391	100	2.336	2.336	1.9188
1	638.395	49.1472		1.148078592	
1	639.398	11.8171		0.276047456	
1	640.401	1.8526		0.043276736	
1	641.404	0.2129		0.004973344	
1	642.407	0.0191		0.000446176	
1	643.41	0.0014		0.000032704	

Table B56. Standard mass spectrum of H_2(TPP-d_{28}) (**15-d_{28}**) used in the simulation

Charge number	*m/z*	Isotope Abundance	Overall Contribution	Contribution of $H_2(TPP\text{-}d_{28})^+$
1	642.423	100	Overall - $H_2(TPP\text{-}d_{27})^+$ - $H_2(TPP\text{-}d_{26})^+$	48.10586
1	643.426	49.0896	$H_2(TPP\text{-}d_{25})^+$ - $H_2(TPP\text{-}d_{24})^+$ - $H_2(TPP\text{-}d_{23})^+$ =	23.61498
1	644.429	11.7889	89.4974 - 34.56218 - 6.320184 -	5.671152
1	645.432	1.8458	0.482138 - 0.02569 - 0.000446 = 48.10586	0.887938
1	646.435	0.2119		0.101936
1	647.439	0.019		0.00914
1	648.442	0.0014		0.000673

VITA

Brenda Ann Dougan was born in Canton, Ohio, to the parents of Donald Ray and Elise Ann Dougan. In 1998 she graduated from Jackson Massillon High School in Massillon, Ohio. In August 1998 she enrolled at Kent State University, Kent, Ohio, where she conducted research under the supervision of Dr. Nicola Brasch. She studied the synthesis and characterization of vandium(III)/carboxylate derivatives with water, which resulted in three publications. Finally in May 2005 she graduated with a Bachelor of Science degree in chemistry. In August 2005, she enrolled at The University of Tennessee. Under the guidance of Dr. Zi-Ling (Ben) Xue, she studied the thermodynamic and kinetic studies of tungsten(VI) alkylidynes with phosphines and water. In addition, she also pursued the spin density and structural studies of Fe(III) porphyrin derivatives by polarized neutron diffraction and X-ray diffraction.